The Dynamic Behaviour of Rail Vehicles operating at High Speeds for Manriding in British Coal Mines

by

P. van Manen

The behaviour of trains used at high speeds for transporting men along mine railways is examined using a number of mathematical models. These models predict the responses of different rail vehicles to typical irregularities in the track, and are used to examine the guidance, the ride, and the likelihood of derailment of the main classes of manriding trains used in British coal mines. The outcome of the modelling compares favourably with the results of tests carried out on actual vehicles.

The investigation has shown that the safe speed at which trains may operate is ultimately restricted by the condition of the track,but changes in the design of the vehicles can lead to an improved performance. The use of conventional wheelsets, for example, can reduce flange wear significantly and so allows higher speeds to be reached. Guidelines for the design of vehicles intended for high speed use are included in this thesis.

THAMES POLY.

PhD Thesis by VAN MANEN, P

We have given the above thesis the Lending Division identification number:

D54350/85

In your notification to Aslib please show this number, so that it can be included in their published 'Index to Theses...' and 'Abstracts of Theses', respectively.

DAB

J P CHILLAG
Theses Officer

Summary

The behaviour of trains used at high speeds for transporting men along mine railways is examined using a number of mathematical models. These models predict the responses of different rail vehicles to typical irregularities in the track, and are used to examine the guidance, the ride, and the likelihood of derailment of the main classes of manriding trains used in British coal mines. The outcome of the modelling compares favourably with the results of tests carried out on actual vehicles.

The investigation has shown that the safe speed at which trains may operate is ultimately restricted by the condition of the track, but changes in the design of the vehicles can lead to an improved performance. The use of conventional wheelsets, for example, can reduce flange wear significantly and so allows higher speeds to be reached. Guidelines for the design of vehicles intended for high speed use are included in this thesis.

Acknowledgements

I wish to thank Dr B.V. Brickle for both instigating and supervising this research, Mr J.A.N. Currie for his help and advice on behalf of the National Coal Board, and Mr I.R. Bittle who has been my mentor throughout.

Many employees of the National Coal Board have helped with various aspects of the work, but particular thanks are due to Mr R.L. Bell for his assistance in carrying out the test work and Mr P. Clemson for his help in the work concerning unbalanced wheels.

The work is partially funded by the National Coal Board and acknowledgement is made for that contribution. Acknowledgment is also made for the provision of equipment by the Mining Research and Development Establishment, and for the use of vehicles and track in the North East and Nottinghamshire Areas.

My special thanks to Mrs A. Pearson for doing an excellent job of typing and to Miss V.S. North for proof-reading the thesis.

Author's Note

The work presented is the original work of the author except where stated otherwise. The views expressed are not necessarily those of the National Coal Board.

Contents

Chapter 1

Outline of Study

1.1 Introduction

1.1.1 Reasons for the research

Rail vehicles are used extensively for manriding in British Coal mines, often travelling long distances along the underground railways (the average distance from the shaft to the coal face is 4.5 km (see Curl (1))). It is important from a point of view of productivity to get the men to their places of work quickly, and so faster trains are being introduced into many mines. Trains are already operating at speeds up to 25 mph and, at such speeds, there are kinetic effects which alter the manner in which the vehicles behave: the motion is affected by the suspension, inertia of components, forces generated between the wheels and the rails, and the resilience of the track. This dynamic behaviour affects the ride of the train and, under certain conditions, could lead to derailment. It will become even more significant as the speeds are increased in the future.

Although there has been an extensive study of the dynamics of mainline trains, no parallel study of rail vehicles operating in mines has been carried out. The manriding trains are small in comparison, and are generally equipped with fairly primitive suspension systems (see Fig 1.1). They operate on narrow gauge track (see Fig 1.2), which is often of a poor standard, and at speeds that are significantly lower than for mainline trains. Much of the work which has been done for high speed rail vehicles concerns stability and curving, which is largely inappropriate in the study of manriding trains. Other work concerned with vehicle ride can only be of limited use because of the differences in the vehicles and the track. This research has been carried out in order to gain an insight into the behaviour of manriding trains as they travel at speed along underground railways in order to identify any design changes that are required.

1.1.2 Railways in coal mines

Coal mines are used to extract coal from an underground seam. A shaft is sunk to the level of the seam and roads are constructed that radiate out towards the coal faces (see Fig 1.3). In British

vehicles. There is no standard gauge, but 2 ft, 2 ft 6 in, and 3 ft gauges are commonly used.

1.1.3 Rail vehicles used for manriding

The rail vehicles used for manriding are generally either gondola type or two axle cars (see Figs 1.4 and 1.5) which are hauled by locomotives or by rope. These vehicles have evolved from the minecar (see Fig 1.6), and insufficient consideration seems to have been given to problems which arise when travelling at speed: this is particularly apparent with respect to guidance.

The wheels on a conventional mainline train have a tapered profile, and each pair of wheels is rigidly fitted to an axle. This arrangement, usually referred to as a wheelset, ensures that the wheels revolve at the same speed. If the wheelset is displaced laterally there will be a difference in the rolling radii of the wheels which will cause the wheelset to yaw, and so move back towards the track centreline, thus providing guidance to the middle of the track without the flange coming into contact with the rail. This behaviour was first described by Stephenson in 1821 (see Stephenson (2)) and is known as the kinematic oscillation. The majority of manriding vehicles, however, are fitted with wheels that revolve independently on a fixed axle. With this arrangement, which will be referred to as a "pair of wheels", the wheels are able to revolve at different speeds and so guidance will only occur if there is a net lateral component of the normal force beween the wheel and the rail acting to push a displaced pair of wheels back towards the track centreline. Because the profiles of the wheels are tapered, lateral displacement causes the axle to rotate slightly about a longitudinal axis, and this leads to the development of a small lateral restoring force. This force only becomes significant as the flange touches the rail and the contact angle between the wheel and the rail gets large. The guidance with this type of wheel arrangement is generally accompanied by flange contact, which can lead to excessive wear of the wheels and rails when operating at high speeds.

The suspension on manriding vehicles is generally very stiff with little or no damping and, as a result, there is only limited isolation from motion due to rail irregularities. In addition to this, the

travel in the suspension is small and this does not always allow all the wheels of a vehicle to remain in contact with the rail when travelling over large irregularities in the track. The safety of the train, as well as its ride, is therefore affected.

Finally, there is no requirement in the specfications used for manriding by the National Coal Board (NCB) for wheels to be dynamically balanced and, as a result, vibrations due to out-of-balance forces can occur when the vehicles travel at high speeds.

1.1.4 Types of vehicles used at high speeds.

There are four main types of vehicle which are used for high speed manriding in British coal mines, these being: gondola vehicles, unit trains, two axle vehicles, and locomotives.

A gondola vehicle is made up of a car body suspended on a pair of bogies (see Fig 1.4), and has both primary and secondary suspensions. The primary suspension is between the wheels and the bogie, and the secondary suspension is between the bogie and car-body.

These vehicles are used in the arterial roads, and are hauled by locomotives in trains of up to eleven cars. The maximum operating speed of these cars is currently 25 mph.

Unit trains are permanently coupled trains made up of several cars (see Fig 1.7). Unlike gondola vehicles, these trains are used to transport men along the gate roads as well as arterial roads. The use of unit trains is a fairly recent development and so there are few in operation. These trains generally have a softer primary suspension than more conventional manriders and, in some cases, also have limited secondary suspension. Unit trains currently operate at speeds up to 25 mph.

The two axle vehicle (see Fig 1.5) is widely used for manriding, although at operating speeds which are generally lower than those achieved by the gondola cars and unit trains. These vehicles have no secondary suspension, and are hauled by either locomotives or rope.

The locomotives used for hauling manriding vehicles are of three types, these being: diesel, electric overhead trolley, and battery electric locomotives. The first two types are suited for hauling trains over long distances, and these are the types generally used for high speed manriding (see Figs 1.8 and 1.9).

1.2 Object of the research

The object of the research is to explain the dynamic behaviour of manriding trains travelling at high speeds along mining railways in order to assess the ride and the likelihood of derailment.

This is achieved by the development of mathematical models of different types of rail vehicles which are used to study the response of the vehicles to typical rail irregularities. The results of the modelling are compared with measurements made on manriding trains, and then evaluated against suitable criteria to assess the acceptability of the ride, and the safety of the vehicles. Recommendations about the design of vehicles for high speed use are made on the basis of these evaluations.

1.3 Synopsis of thesis

The geometry of the track, the interaction between the wheels and rails, the principal modelling technique, and the computer programs used, are all described in Chapter 2. The measurement of track geometry is discussed in Chapter 3, and results are presented in a suitable form to use in the models. Mine railways are compared with mainline railways in this chapter. A set of criteria to assess the outcome of the modelling is proposed in Chapter 4.

On the basis of these early chapters, a number of mathematical models are proposed. These are compared with results obtained from tests on all the main classes of rail vehicles used for high speed manriding in British coal mines. The models are of the following: a single wheelset (Chapter 5), a gondola car hauled by a Bo-bo locomotive (Chapter 6), a unit train (Chapter 7), and cars and locomotives with two axles (Chapter 8).

Conclusions, and some guidelines for the design of high speed rail transport systems, are made in Chapter 9. This chapter also contains some suggestions for further work.

Chapter 2

Mathematical Modelling of Rail Vehicles

2.1 Introduction

2.1.1 Concept of modelling

The interaction of the component parts of a rail vehicle may be expressed in mathematical terms and, if the resultant model is sufficiently explicit, it can be used to study the motion of the vehicle under a variety of operating conditions. The object of developing such a model is to permit assessment of certain aspects of the behaviour of the vehicle, such as its ride and its likelihood of derailment, and so the manner in which the model is constructed, and its complexity, are dictated by this goal. It is inappropriate to make the mathematical models too elaborate for the sake of exact representation of the physical system. However, it is important to include all the essential features of the system.

The motion of rail vehicles is affected by the geometry and resilience of the track, the interaction between wheels and rails, the suspension, and the inertia of component parts. These are the important variables used in the construction of the mathematical models. The vehicles are modelled as a set of rigid bodies interconnected by stiffness and damping elements, with the positions of the rigid bodies being represented by co-ordinates, and the relationships between these co-ordinates being provided by mathematical equations. Modelling in this way allows the equations of motion to be written in a consistent form: the equations are then suitable for solution by a general purpose computer program.

2.1.1 Vehicle co-ordinates

The co-ordinate system used to describe the positions of the rigid bodies is shown in Fig 2.1.

2.1.3 Synopsis of chapter

The chapter describes the technique used to model a rail vehicle travelling along a section of straight track and, in conjunction with this, it explains some of the fundamental variables that affect the dynamic behaviour. The method used to solve the equations of motion is introduced, and general purpose computer programs that can

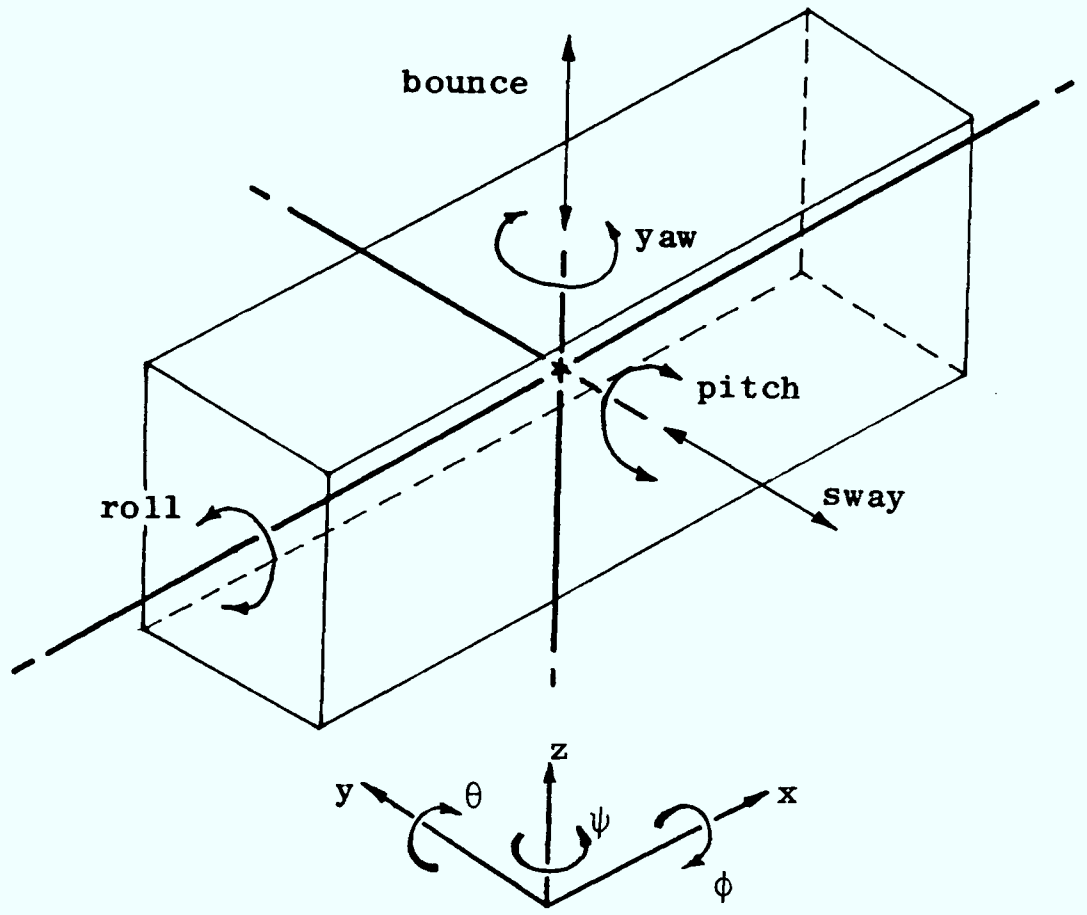

Fig 2.1 Vehicle co-ordinates

be used to carry out this solution are described.

The concepts behind the modelling technique are discussed in section 2.1, and important variables affecting the motion of the vehicle are introduced. The co-ordinate system which is used in the modelling is defined (see Fig 2.1).

The geometry of the track is defined in section 2.2 in a way which is convenient for use in the models. The track is discussed in greater detail in Chapter 3.

The interaction of the wheel and the rail, which is fundamental to vehicle behaviour, is examined in section 2.3. The geometry of the wheel and the rail are described, and the forces that arise where the wheel and rail touch are explained. Much of the discussion in this section is the basis for any investigation of the motion of rail vehicles and, as such, is widely documented. A noteworthy summary has been produced by British Rail (see Wickens and Gilchrist (3)).

The approach used to model the rail vehicles is explained in section 2.4, and the form in which the equations of motion are written

is proposed (see equation (2.33)). A decision regarding the treatment of track resilience in the models is taken in this section. A simple model of a two axle vehicle is also introduced (see Fig 2.12): this is used as an example in the remainder of the chapter.

In section 2.5 the method used to solve the equations of motion is determined. The technique is developed for a single, easily defined, track input (a sinusoidal input), and extended to accommodate a random input (which is available from measurement of actual track (see Chapter 3). The format of the solution is suitable to use directly with the acceptability criteria chosen in Chapter 4.

Finally, the computer programs which have been written to carry out the solution of the equations of motion are explained in section 2.6.

2.2 Track geometry

An ideal section of track is made up of smooth rails which remain straight, level and with a uniform gauge. Deviations from this ideal, such as undulations and twist in a section of track, affect the motion of vehicles which travel upon it, and so these irregularities are important variables to consider in the modelling of rail vehicles. The positions of the two rails at a given point along the track may be described using the co-ordinate system shown in Fig 2.2.

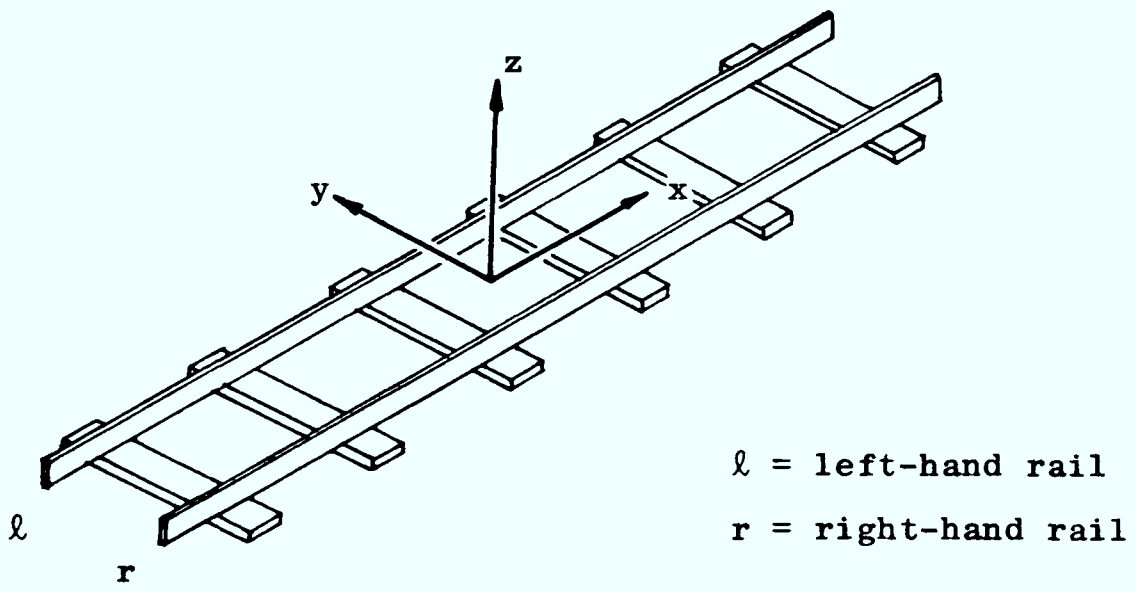

Fig 2.2 Track co-ordinates

The geometry is usually described in terms of the vertical profile, lateral alignment, cross-level and gauge (see ISO (4)). The first two quantities describe the position of the track centreline,

$$\text{vertical profile} = \frac{z_\ell + z_r}{2} \tag{2.1}$$

$$\text{lateral alignment} = \frac{y_\ell + y_r}{2} \tag{2.2}$$

and the latter quantities describe the relative position of the two rails,

$$\text{cross-level} = z_\ell - z_r \tag{2.3}$$

$$\text{gauge} = y_\ell - y_r \tag{2.4}$$

These four quantities are used as the inputs to the mathematical models. The way in which they are measured and described is discussed in Chapter 3.

2.3 Interaction between wheel and rail

2.3.1 Geometry of the wheel and rail

The way in which the wheel and rail interact is dependent upon their mutual geometry and the position of the point of contact. When a wheel is displaced laterally the point of contact changes as illustrated in Fig 2.3, and because railway wheels are profiled, this leads to a rotation of the axle about a longitudinal (x) axis. The geometry of the wheel at the contact point may be defined in terms of the radius at the point of contact (the rolling radius), and the angle of the common tangent at the point of contact (the contact angle): these are both shown in Fig 2.3. For a pair of wheels it is convenient to express the geometry in terms of the rolling radii difference and contact angle difference between the two wheels: these quantities are plotted against lateral displacement in Fig 2.4.

2.3.2 Gravitational stiffness forces

When a pair of wheels is displaced laterally the axis of the axle rotates slightly about a longitudinal (x) axis as a result of the

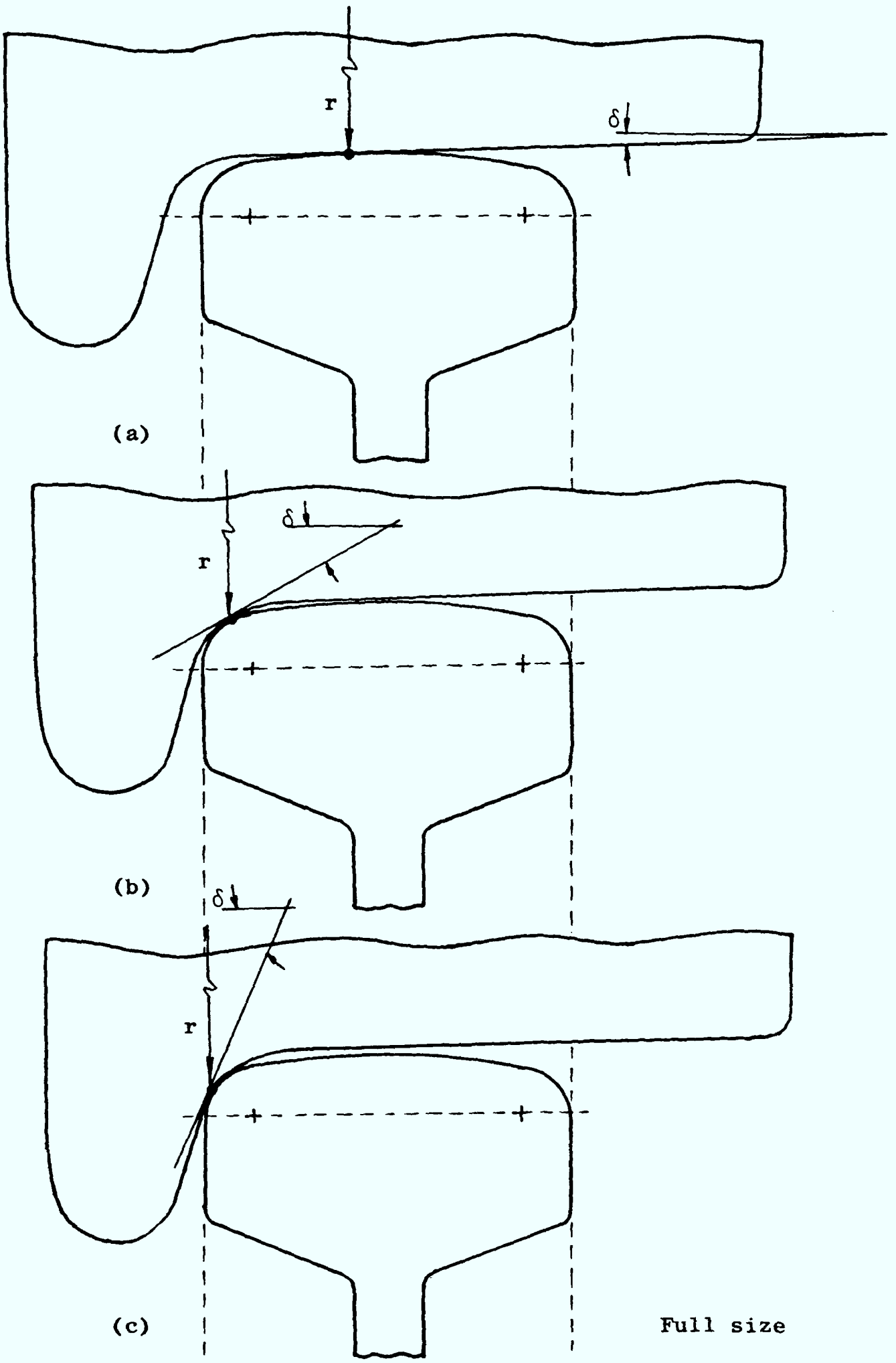

Fig 2.3 New 14 in dia mine car wheel (see BS4854:1972 (5)) on a section of 30 kg/m rail, showing:
(a) undisplaced wheel
(b) wheel displaced laterally by 4 mm
(c) wheel displaced laterally by 5 mm

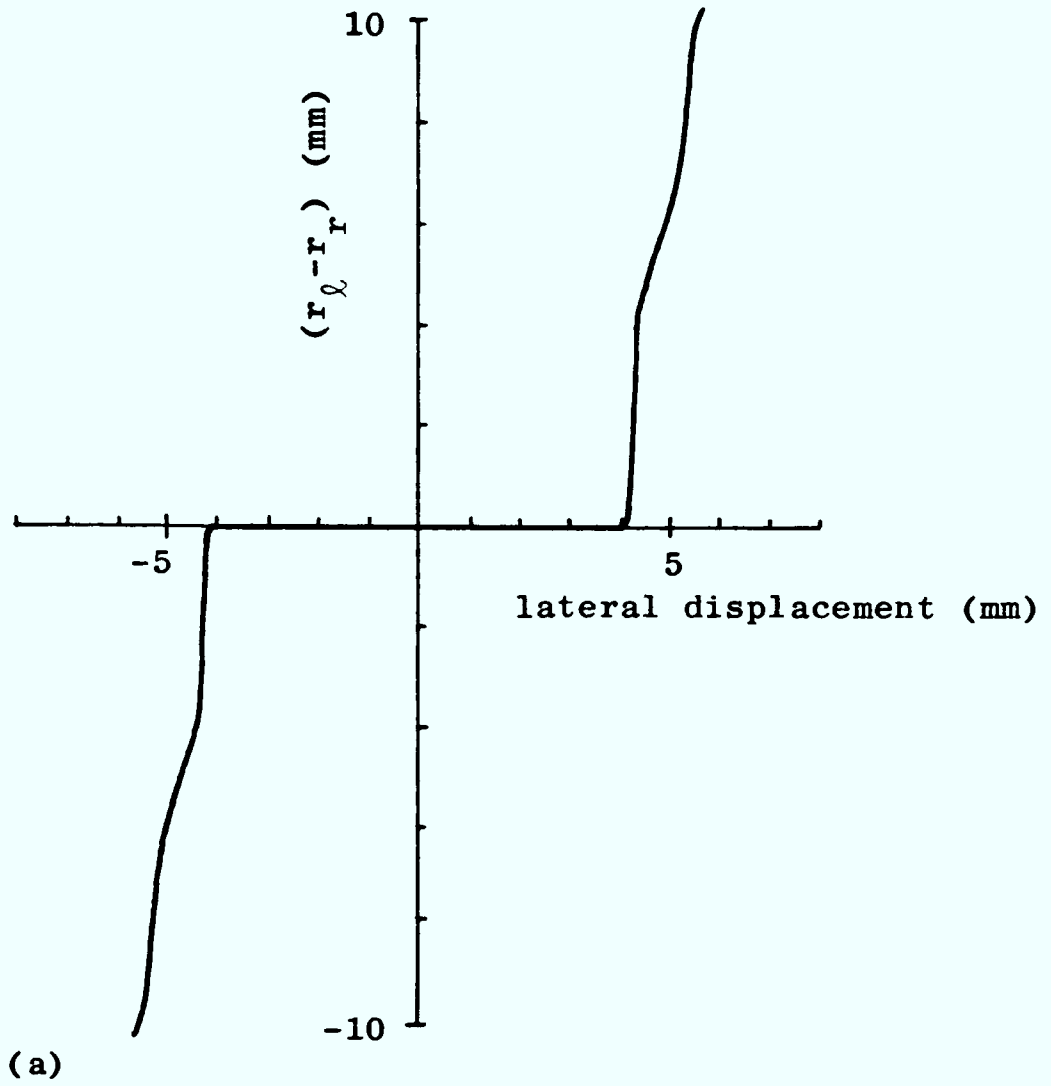

(a)

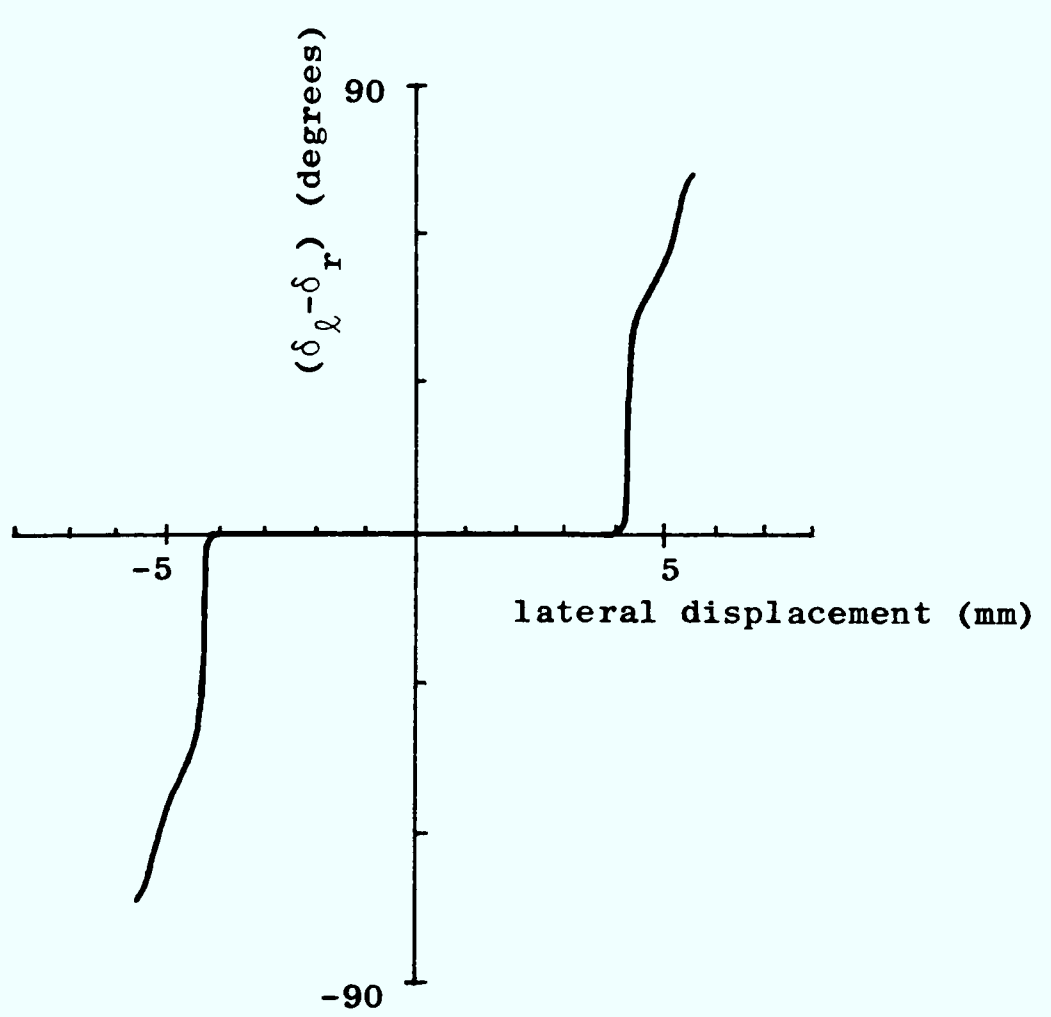

(b)

Fig 2.4 (a) Difference in rolling radii
(b) Difference in contact angles

(New 14 in dia mine car wheel)

difference in rolling radii of the wheels. This gives rise to a small lateral force which is the resultant of the normal forces acting between the wheels and the rails. When the flange touches the rail this rotation increases; in addition, there is a sharp increase in the contact angle difference between the wheels. These effects combine to produce a significant increase in the net lateral force, which pushes the displaced pair of wheels back towards the middle of the track. This force is known as the gravitational stiffness force. The magnitude of this force may be calculated in the following manner.

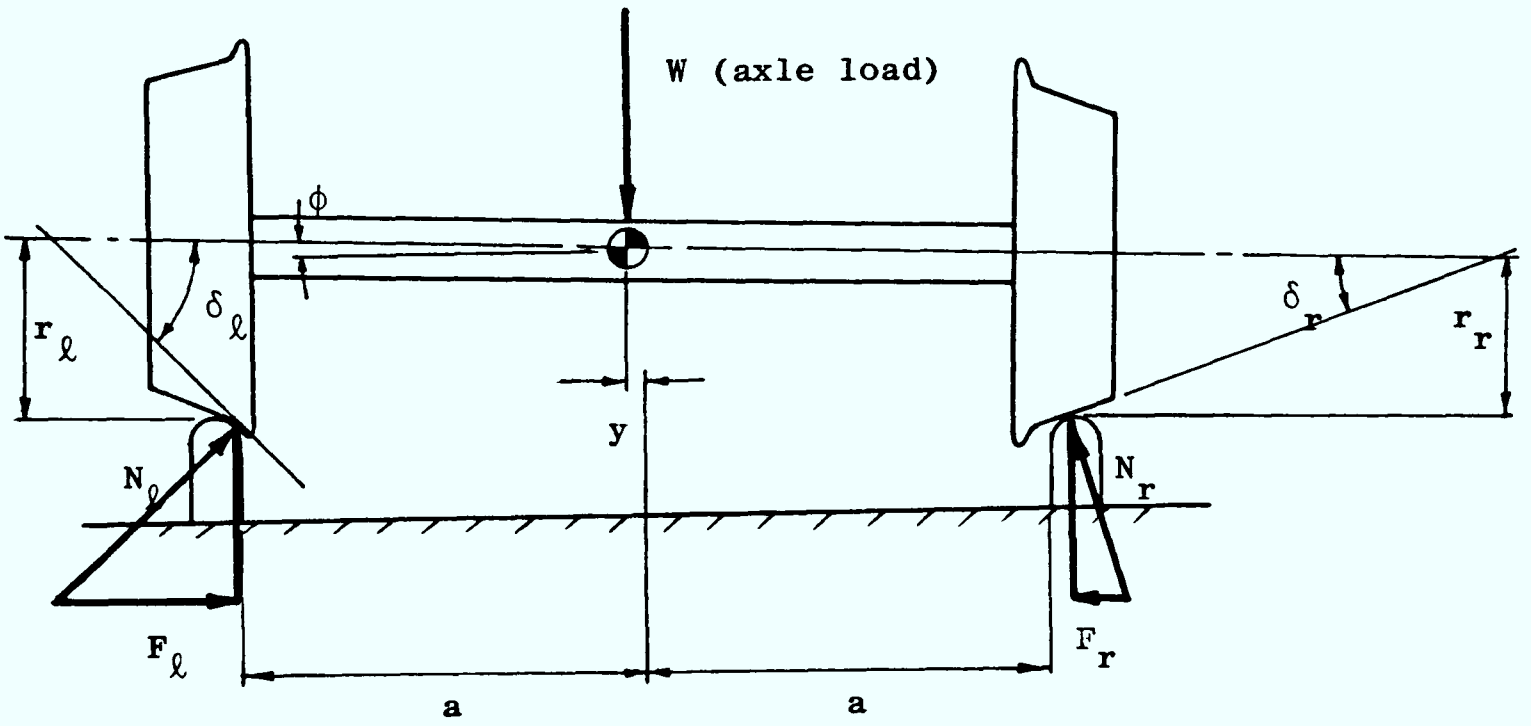

Fig 2.5 Normal wheel/rail forces for a displaced pair of wheels

A displaced pair of wheels is shown in Fig 2.5. The lateral component of the normal force for each of the wheels may be expressed as:

$$F_\ell = N_\ell \sin(\delta_\ell + \phi)$$
$$F_r = N_r \sin(\delta_r - \phi) \qquad (2.5)$$

where,

N_ℓ & N_r = normal wheel/rail forces

F_ℓ & F_r = lateral components

δ_ℓ & δ_r = contact angles

ϕ = axle roll angle

The vertical components of the normal forces combine to balance the axle load, W:

$$W = N_\ell \tan(\delta_\ell + \phi) + N_r \tan(\delta_r - \phi) \qquad (2.6)$$

If these vertical components are taken to be equal, which is reasonable for a pair of wheels travelling along straight track, equations (2.5) and (2.6) can be equated to give an expression for gravitational stiffness force, F_g:

$$F_g = F_\ell - F_r = \frac{W}{2}(\tan(\delta_\ell + \phi) - \tan(\delta_r - \phi)) \qquad (2.7)$$

The axle roll angle may be expressed in terms of the rolling radii difference and the distance between the contact points,

$$\phi \simeq \frac{r_\ell - r_r}{2a} \qquad (2.8)$$

where,

r_ℓ & r_r = rolling radii

$2a$ = track gauge

Equation (2.7) shows that the gravitational stiffness force is a function of the axle load, and of the rolling radii and contact angles. The axle loads are quite small for mine vehicles, and so this force only starts to become significant when the flange contacts the rail. The effect of the difference in rolling radii is small compared to the effect of the difference in contact angles (see Fig 2.4: for a track gauge of 2 ft 6 in, the axle roll angle for a pair of wheels displaced 6 mm is less than 1 degree when calculated using equation (2.8)), and so equation (2.7) may be re-written as:

$$F_g = \frac{W}{2}(\tan\delta_\ell - \tan\delta_r) \qquad (2.9)$$

Equations (2.7) and (2.9) have been used to calculate the variation of gravitational stiffness force as a pair of wheels is displaced laterally from the middle of a track, and the results are shown in Fig 2.6.

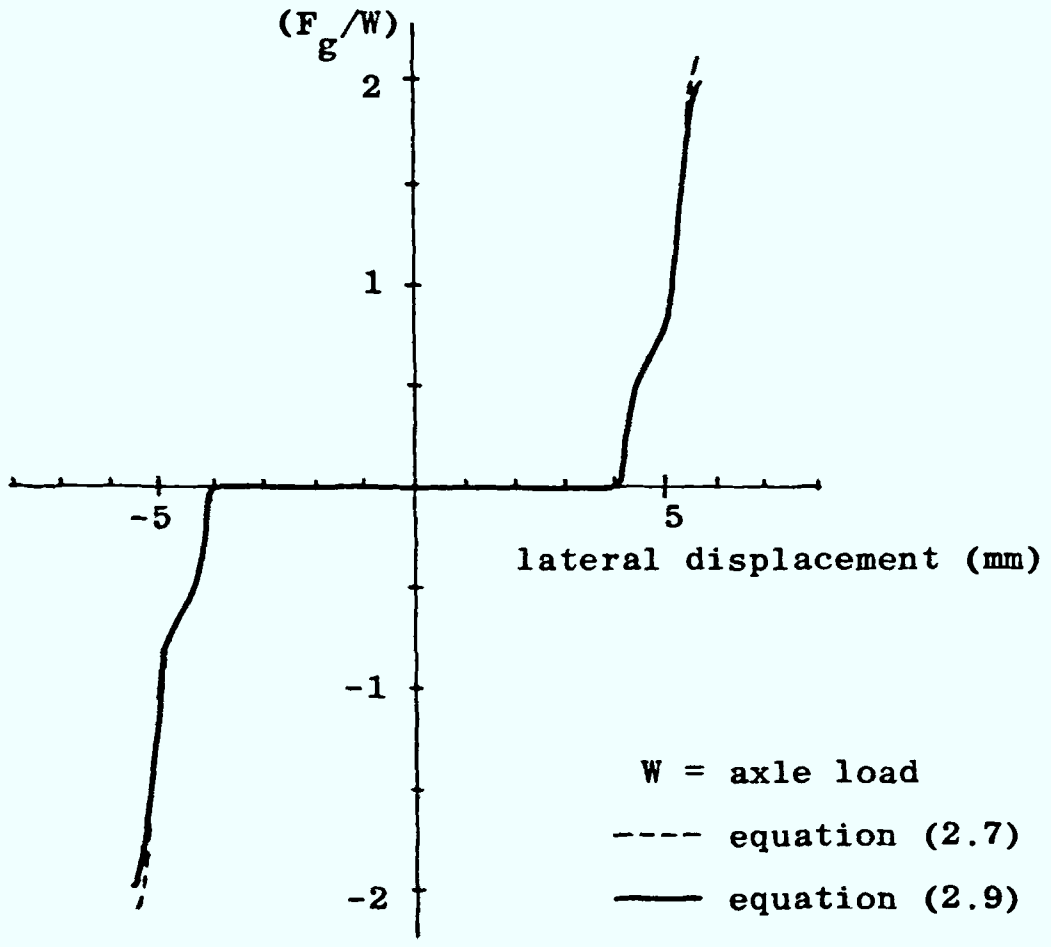

Fig 2.6 Variation of gravitational stiffness force with lateral displacement for new 14in dia. mine car wheels (see BS 4854:1972(5)) on 2 ft 6 in gauge track with 30 kg/m rails.

It is clear that in the region where the flange is in contact with the rail the gravitational stiffness is approximately uniform with displacement, whereas it is nearly zero when both wheels are running on their treads.

2.3.3 Creep forces

In addition to the normal force at the area of contact of the wheel and rail, there are also tangential forces that become significant whenever the motion of the wheel deviates from pure rolling (eg driving, braking, curving). These forces lead to an infinitesimal distortion of the wheel and rail at the area of contact which is known as creep: the tangential forces are known as the creep forces.

The analysis of this phenomenon was first carried out in connection with the driving wheels of locomotives (see Carter (6)), by considering a cylinder rolling along a thick plate. The creep was defined in terms of the difference between the distance travelled by the cylinder when it was transmitting a force, and the distance travelled

when it was not, and this was related to the traction. This relation -ship is shown in Fig 2.7.

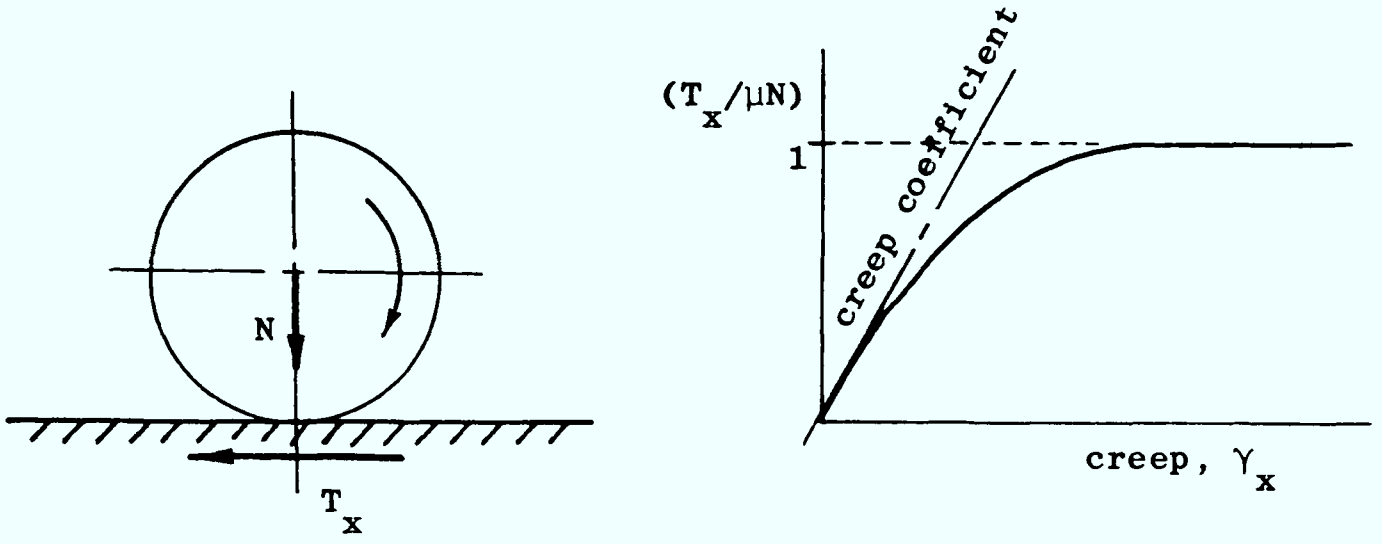

Fig 2.7 Relationship between creep and traction (Carter (6))

For small values of creep there is a linear relationship between the creep and the traction and these quantities may be related by a coefficient.

For the case of a stationary cylinder pressed against a flat plate the area of contact will appear as a strip along the length of the cylinder. As a cylinder rolls along it can exert a tangential force on the plate, and this will be accompanied by some slipping at the trailing edge of the contact area. If the tangential force is increased the area of slip gets larger and, eventually, the entire contact area slips. When this occurs the cylinder no longer rolls, but slides, and the creep is said to be saturated. For the case of a railway wheel pressed against a rail the contact area is no longer simply a strip and has a shape which is close to that of an ellipse.

The relationship between creep and creep force for general point contact has been studied extensively (see Kalker (7)), resulting in explanations based upon Hertz's theory of contact (see Hertz (8)), and the Coulomb law of dry friction. Hertz treated the problem of two curved elastic bodies being pressed together, and developed expressions which related the pressure distributions over the area of contact to the force normal to the plane of contact, to the radii of curvature, and to the modulii of elasticity of the bodies. The theory is dependent upon a decision to treat the contact area as being elliptical, a proposition that appears to have been suggested by observation. The Coulomb law of dry friction is an empirical law

that uses a coefficient of friction to relate the normal force between two bodies in contact to the tangential force required to initiate sliding.

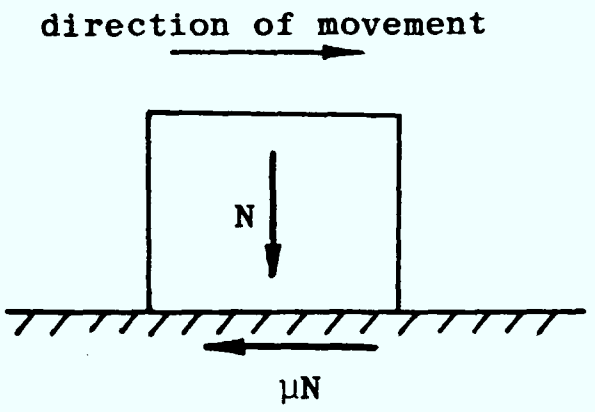

Fig 2.8 Coulomb law of dry friction

The coefficient of friction is obtained by measuring the two forces at the initiation of sliding. The coefficient is found to be dependent not only on the material properties of the bodies in contact, but also on such things as the surface roughness, presence of lubricant, humidity, and method of loading of the bodies. It is clear that the variation in measured coefficients will be considerable.

Kalker's "exact" theory of rolling contact (see Kalker (9)) proposes that the tangential traction is limited by the product of the coefficient of friction and the pressure in the region of slip. The elliptical contact area and pressure distribution are both determined according to the theory of Hertz, and a numerical method is used to calculate the relationships between creep and creep forces in both the direction of rolling (longitudinal creep) and transverse to this direction (lateral creep). Kalker's results for longitudinal creep have been compared with experimental results (see Hobbs (10)), and this comparison is reproduced in Fig 2.9. The variation in the results is quite considerable, and so the accuracy of using Kalker's theory in general application is limited.

In this work, only the initial slope of the curve shown in Fig 2.9 will be used. This simplification allows creep coefficients to be used to relate the creep force to the creep. The creep coefficients can be determined using Kalker's linear theory (see Kalker (9)) which calculates coefficients for the special case when no slip occurs in the contact ellipse. This simplification, which

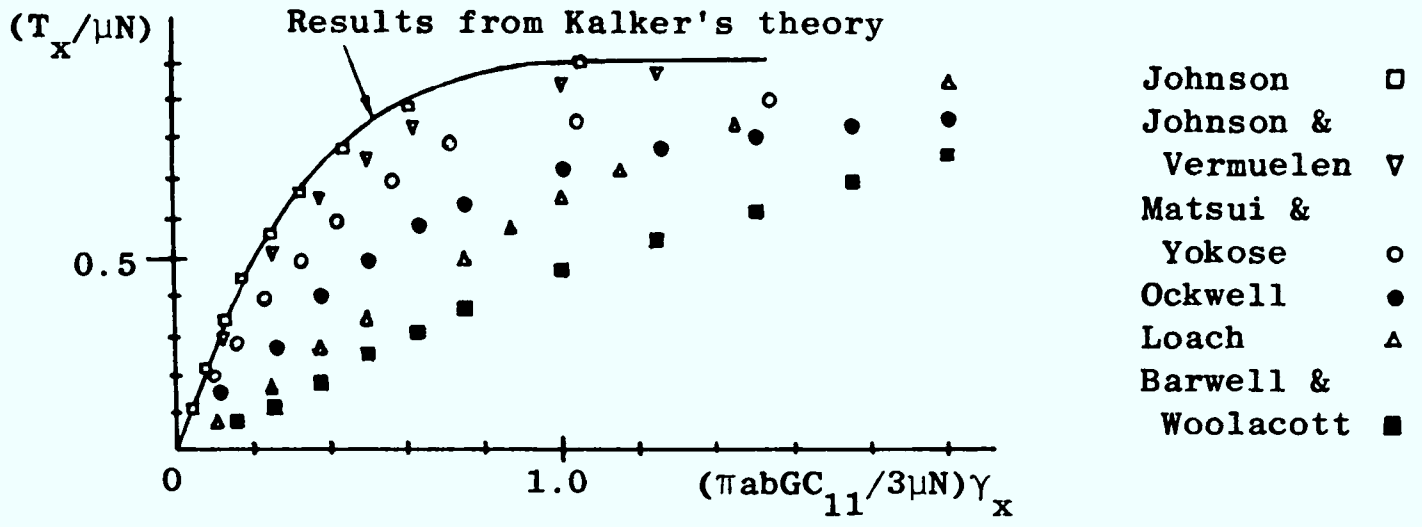

Fig 2.9 Kalker's, and experimental creep force laws (from Hobbs (10))

implies a situation in which the coefficient of friction is infinite, is only valid for very small amounts of creep.

The creep can be considered in terms of longitudinal (x) and lateral (y) components, and these may be defined in terms of the wheel velocity as shown below:

$$\text{longitudinal creep} = \gamma_x = \frac{\Delta V_x}{V} \qquad (2.10)$$

where,

ΔV_x = longitudinal component of the diffence between actual velocity and pure rolling velocity. The pure rolling velocity refers to the wheel velocity when no creep occurs.

V = forward speed

$$\text{lateral creep} = \gamma_y = \frac{\Delta V_y}{V} \qquad (2.11)$$

where,

ΔV_y = lateral component of the difference between actual velocity and pure rolling velocity

These creep components are then related to the components of the creep forces by the expressions:

$$T_x = - f_{11}\, \gamma_x$$
$$T_y = - f_{22}\, \gamma_y \qquad (2.12)$$

where,

T_x & T_y = components of the creep force

f_{11} = longitudinal creep coefficient

f_{22} = lateral creep coefficient

The creep coefficients in equation (2.12) are related to tabulated coefficients (see Kalker (7)) using the expressions:

$$f_{11} = G(ab)C_{11}$$
$$f_{22} = G(ab)C_{22} \qquad (2.13)$$

where,

C_{11} & C_{22} = Kalker's creep coefficients

G = shear modulus of elasticity

a & b = dimensions of contact ellipse (lengths of major and minor axes)

The dimensions of the contact ellipse can be calculated using Hertz's theory of contact (this is treated in Timoshenko and Goodier (11)): it can be noted that the product (ab) is proportional to $N^{2/3}$ (where N is the normal force between the surfaces in contact).

2.3.4 Creep forces for a displaced wheelset

When a conventional wheelset is displaced laterally or yawed there is creep between the wheels and the rails. Relationships between the displacement and the components of creep are well established (see Wickens and Gilchrist (3) for example) and these are reproduced below:

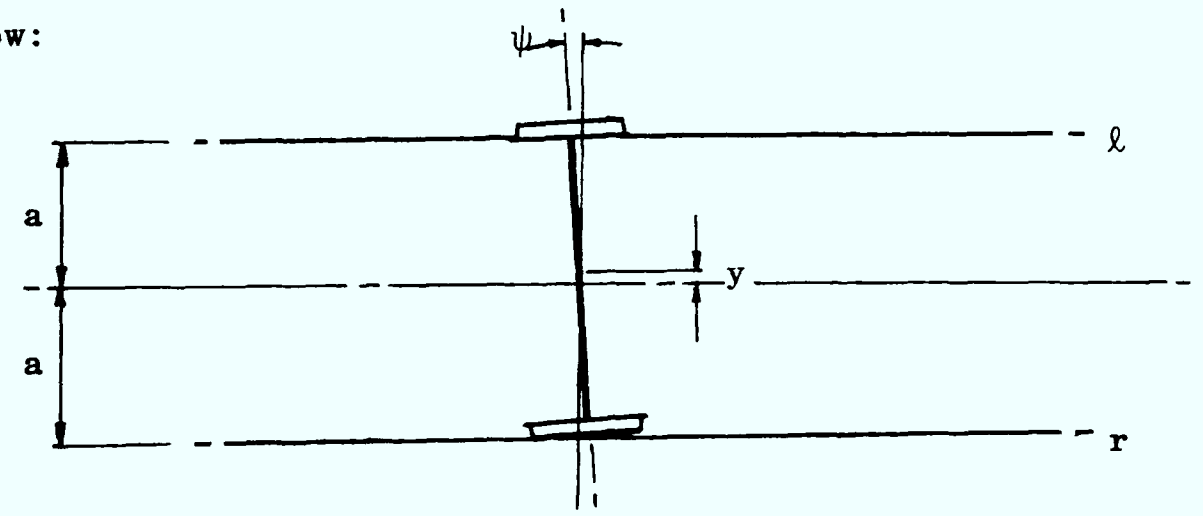

Fig 2.10 Displaced wheelset

The velocity of the left wheel will be given by:

$$V_{\ell,x} = V - a\dot{\psi}$$
$$V_{\ell,y} = \dot{y} \qquad (2.14)$$

The velocity of the right wheel is:

$$V_{r,x} = V + a\dot{\psi}$$
$$V_{r,y} = \dot{y} \qquad (2.15)$$

The pure rolling velocity, U, of the left wheel is:

$$U_{\ell,x} = \omega\, r_{\ell}$$
$$U_{\ell,y} = \psi V \qquad (2.16)$$

where,

r_{ℓ} = rolling radius of the left wheel

ω = angular velocity of wheelset

By making the substitution,

$$r = r_o + \lambda_o y \qquad (2.17)$$

where,

r = rolling radius for wheelset displaced a distance, y

λ_o = rate of change of wheel contact radius with lateral displacement. This is usually called the conicity, and corresponds to the gradient of the curve shown in Fig 2.4(a).

Equation (2.16) becomes:

$$U_{\ell,x} = V\left(1 + \frac{\lambda_o}{r_o}\, y\right)$$
$$U_{\ell,y} = \psi V \qquad (2.18)$$

The pure rolling velocity of the right wheel is:

$$U_{r,x} = V(1 - \frac{\lambda o}{r_o} y)$$

$$U_{r,y} = \psi V \qquad (2.19)$$

Equations (2.10) and (2.11) can now be used to calculate the components of the creep.

For the left wheel,

$$\gamma_{\ell,x} = -\frac{a\dot{\psi}}{V} - \frac{\lambda_o}{r_o} y$$

$$\gamma_{\ell,y} = \frac{\dot{y}}{V} - \psi \qquad (2.20)$$

For the right wheel,

$$\gamma_{r,x} = \frac{a\dot{\psi}}{V} + \frac{\lambda_o}{r_o} y$$

$$\gamma_{r,y} = \frac{\dot{y}}{V} - \psi \qquad (2.21)$$

The creep forces can now be determined using equation (2.12).

For the left wheel,

$$T_{\ell,x} = f_{11}(\frac{a\dot{\psi}}{V} + \frac{\lambda_o}{r_o} y)$$

$$T_{\ell,y} = - f_{22}(\frac{\dot{y}}{V} - \psi) \qquad (2.22)$$

For the right wheel,

$$T_{r,x} = - f_{11}(\frac{a\dot{\psi}}{V} + \frac{\lambda_o}{r_o} y)$$

$$T_{r,y} = - f_{22}(\frac{\dot{y}}{V} - \psi) \qquad (2.23)$$

These forces are shown on Fig 2.11.

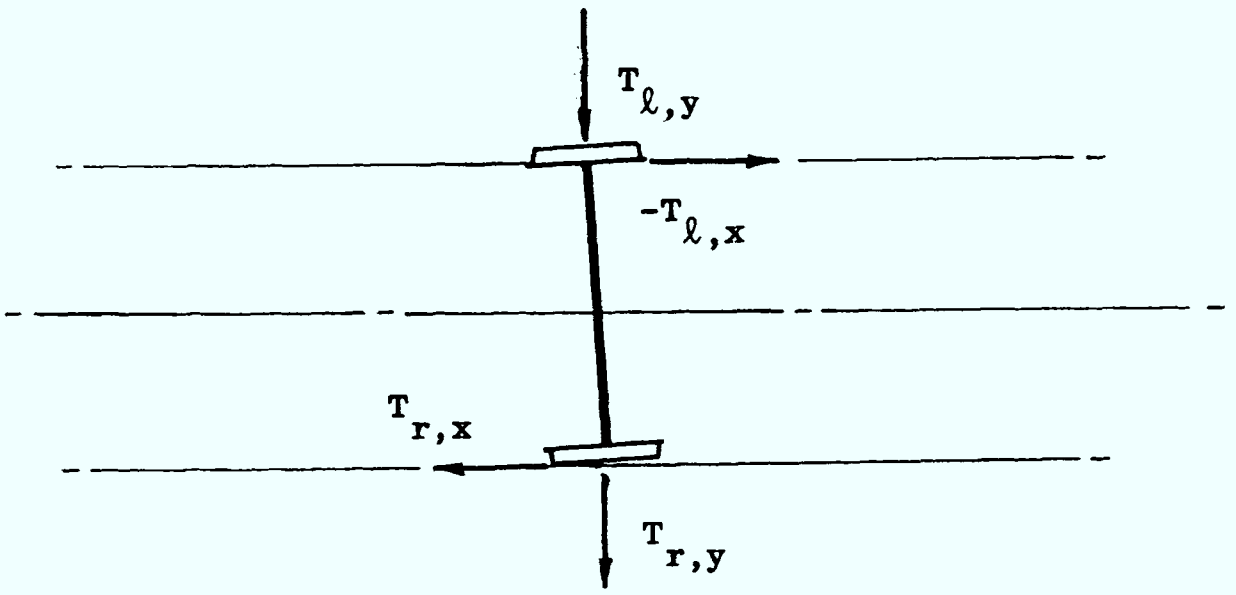

Fig 2.11 Displaced wheelset: creep forces

For the displaced wheelset there is a lateral force acting to push the wheelset back towards the middle of the track given by:

$$(T_{\ell,y} + T_{r,y}) = -\frac{2f_{22}\dot{y}}{V} + 2f_{22}\psi \qquad (2.24)$$

There is also a couple acting to steer the wheelset back towards the middle of the track.

$$a(-T_{\ell,x} + T_{r,x}) = -\frac{2f_{11}a^2}{V}\dot{\psi} - \frac{2f_{11}a\lambda_o}{r_o}y \qquad (2.25)$$

For the case of a pair of wheels that revolve independently on the axle, equation (2.24) is still applicable (although the yaw term will become negligible), but there will be no couple to steer the wheels. This is because the angular velocities for the wheels no longer need to be equal. Thus the only effect of creep for a pair of wheels that revolve independently is to damp out any lateral oscillations.

2.4 Equations of motion

2.4.1 General modelling decisions

Each rail vehicle has been treated as being symmetrical about a vertical plane through its longitudinal centreline (xz plane). The pitch and bounce are motions in the vertical plane, and roll, yaw and sway are motions in the lateral direction: these terms have been defined previously by Fig 2.1.

The inputs to the models are the track vertical profile, lateral alignment, and cross-level (the gauge is considered to remain uniform), and each of these is considered to be independent of the others. This decision simplifies the modelling by uncoupling the vertical and lateral movements of the vehicle, which allows them to be treated separately. In the lateral models the output is the response to lateral alignment and cross-level inputs when the interaction between the wheels and rails is modelled as described in section 2.3. In the vertical models the output is the response to vertical profile inputs when the wheels are considered to follow the profile of the track exactly.

Measurements of the resilience of the track to vertical loads (see Appendix 4) indicate that it has a stiffness of a similar magnitude to that of the primary suspensions of many manriding vehicles and, as such, cannot be ignored in vertical models. The resilience is incorporated by representing the track as a series of parallel vertical springs.

The lateral resilience of the track becomes important only as the wheel flange comes into contact with the rail, and it is therefore only incorporated in models where flange contact is being considered. The damping which occurs as the track moves laterally in its ballast is small in comparison with the damping due to creep of the wheel on the rail, and so it is ignored in the modelling.

For the most part linear equations have been used to describe the motion of the vehicles, which leads to solution by quite simple mathematical techniques (see section 2.5). In some cases (eg flange contact, creep saturation) the models are altered slightly to incorporate non-linearities, and these are discussed in the thesis as they arise.

2.4.2 Method used for representing a vehicle

The rail vehicles are modelled by considering the various parts, such as the car body, bogie frames, and wheels, as rigid bodies which are interconnected by stiffness and damping elements. The motion of each of the bodies is expressed in the co-ordinate system of Fig 2.1 and the equations are derived using these co-ordinates. In this way the equations of motion can be expressed in a general form (see

Wickens and Gilchrist (3)):

$$(As^2 + (\frac{B}{V} + D)s + (C + E))\underset{\sim}{q} = \underset{\sim}{Q} \qquad (2.26)$$

where,

A = inertia matrix

B = creep damping matrix

C = creep stiffness matrix

D = viscous damping matrix

E = elastic stiffness matrix

$\underset{\sim}{q}$ = vehicle co-ordinate vector

$\underset{\sim}{Q}$ = input force vector

V = forward speed of vehicle

s = differential operator

The general form of the equations of motion which is used for this work is:

$$(Ms^2 + Ls + K)\underset{\sim}{q} = (Cs + D)\underset{\sim}{u} \qquad (2.27)$$

where,

M = inertia matrix

L = damping matrix

K = stiffness matrix

C & D = input matrices

$\underset{\sim}{q}$ = vehicle co-ordinate vector

$\underset{\sim}{u}$ = track co-ordinate vector

s = differential operator

The representation of a vehicle by this method is illustrated here with a simple model of the vertical motion of a two axle vehicle (see Fig 2.12).

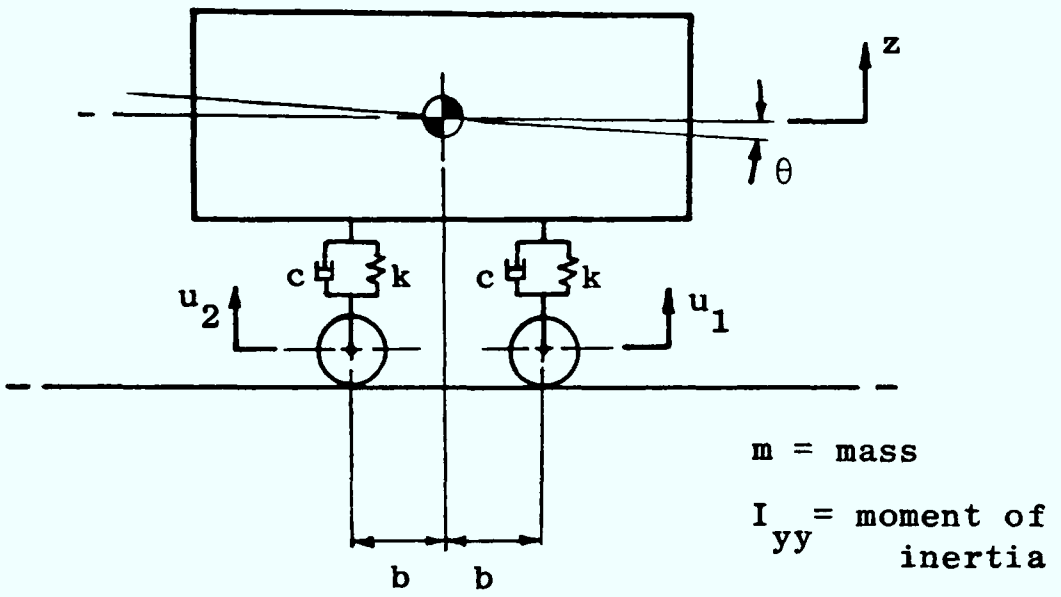

Fig 2.12 Simple model of the vertical motion of a two axle vehicle

The equations of motion may be written as:

$$m\ddot{z} + 2c\dot{z} + 2kz = c(\dot{u}_1 + \dot{u}_2) + k(u_1 + u_2)$$

$$I_{yy}\ddot{\theta} + 2b^2c\dot{\theta} + 2b^2k\theta = b^2c(\dot{u}_2 - \dot{u}_1) + b^2k(u_2 - u_1)$$

(2.28)

which can be re-written in the form of equation (2.27) by putting:

$$M = \begin{bmatrix} m & 0 \\ 0 & I \end{bmatrix} \qquad L = \begin{bmatrix} c & 0 \\ 0 & 2b^2c \end{bmatrix}$$

$$K = \begin{bmatrix} k & 0 \\ 0 & 2b^2k \end{bmatrix} \qquad C = \begin{bmatrix} c & c \\ -b^2c & b^2c \end{bmatrix}$$

$$D = \begin{bmatrix} k & k \\ -b^2k & b^2k \end{bmatrix} \qquad \underset{\sim}{q} = \begin{bmatrix} z \\ \theta \end{bmatrix} \qquad \underset{\sim}{u} = \begin{bmatrix} u_1 \\ u_2 \end{bmatrix}$$

(2.29)

If the vehicle is travelling at a constant speed the inputs to the front and rear pair of wheels will be related by a time delay, and so may be expressed in terms of a single input at the front wheels:

$$u_1 = u(t)$$

$$u_2 = u(t - \frac{2b}{v}) \qquad (2.30)$$

This can be re-written in terms of the differential operator, s, by using a Laplace transform (see Raven (12)).

$$u_1 = u(s)$$

$$u_2 = e^{-2b/v\ s} \cdot u(s) \qquad (2.31)$$

Equation (2.30) can now be expressed in the form:

$$\underset{\sim}{u} = T(s)\ u \qquad (2.32)$$

where,

$$T(s) = \begin{bmatrix} 1 \\ e^{-2b/v\ s} \end{bmatrix} = \text{time delay vector}$$

u = u(s) = scalar representing track co-ordinate at front set of wheels

In general, equation (2.27) can be expressed in the form:

$$(Ms^2 + Ls + K)\underset{\sim}{q} = (Cs + D)\ T(s)\ u \qquad (2.33)$$

This modification of the general form of the equations of motion is valid for constant forward speed.

2.5 Solution of equations of motion

2.5.1 General considerations

The models are constructed to explain the dynamic behaviour of man-riding vehicles travelling along typical underground railways in order to enable decisions to be made regarding their design for high speed operation. The decisions are taken on the basis of criteria relating to the ride and safety of the vehicles (see Chapter 4), and so it is necessary for the solution to be in a form which is compatible

with these criteria.

The inputs to the models are the track irregularities which are defined in equations (2.1) to (2.4). There are examples of irregularities that can be defined precisely (such as points and dipped joints) but, more often, these irregularities vary in a random manner. The solution technique is developed for a deterministic input, and extended to accept random inputs.

2.5.2 Solution for a sinusoidal input

Consider the case of a vehicle travelling at constant speed along track in which both of the rails have equal sinusoidal undulations which are in phase (see Fig 2.13).

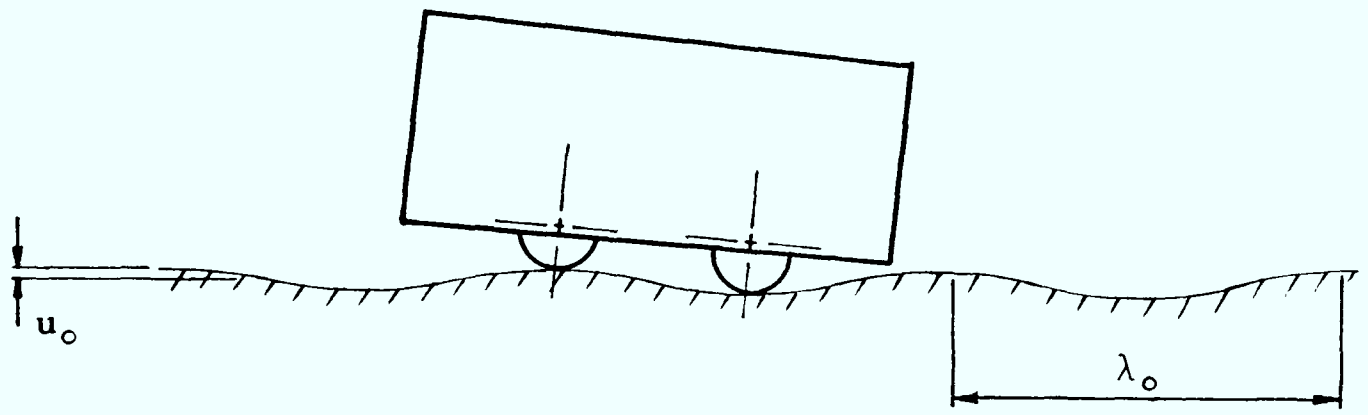

Fig 2.13 Vehicle travelling along track which undulates sinusoidally

The track co-ordinates at the front pair of wheels at a position, x, along the track may be expressed as:

$$u(x) = u_o \sin(\Omega x) \qquad (2.34)$$

where,

$\Omega = {}^{2\pi}/\lambda$ = spatial frequency

λ = wavelength

The vehicle is travelling at constant speed, and so this may be re-written to give:

$$u(x) = u_o \sin(\omega t) \qquad (2.35)$$

where,

$\omega = \Omega V$ = temporal frequency

V = forward speed

Modelling the vehicle in the manner described in section 2.4.2 means that the motion of the vehicle will be described in the form of equation (2.33). The input is sinusoidal, so this may be solved algebraically by substituting $j\omega$ for s (see Raven (12)). This leads to a complex form of equation (2.33) as shown below:

$$(K - M\omega^2 + jL\omega)\underset{\sim}{q}(\omega) = (D + jC\omega)\ T(\omega)\ u_o \qquad (2.36)$$

This can be re-written to give:

$$A(\omega)\ \underset{\sim}{q}(\omega) = B(\omega)u_o \qquad (2.37)$$

where,

$A(\omega) = (K - M\omega^2 + jL\omega)$

$B(\omega) = (D + jC\omega)\ T(\omega)$

$\underset{\sim}{q}(\omega)$ = complex vehicle co-ordinate vector

Making the substitution:

$$H(\omega) = A^{-1}(\omega)\ B(\omega) \qquad (2.38)$$

then gives the result:

$$\underset{\sim}{q}(\omega) = H(\omega)u_o \qquad (2.39)$$

The complex matrix $H(\omega)$ relates the output variables to the input and is the transfer function for the vehicle. It can be used to describe completely the response of the vehicle. In general,

$$H(\omega) = E(\omega) + jF(\omega) \qquad (2.40)$$

where,

$E(\omega)$ = real matrix

$F(\omega)$ = real matrix

The magnitude of the transfer function is:

$$|H(\omega)| = \sqrt{E^2(\omega) + F^2(\omega)} \qquad (2.41)$$

The phase relationship between the output variables and the input is:

$$\angle H(\omega) = \tan^{-1}(F(\omega)/E(\omega)) \qquad (2.42)$$

It can be seen in the derivation that the transfer function is dependent on the physical properties of the model, the forward speed (which affects the time delay vector, $T(\omega)$), and the frequency of the undulation.

Equation (2.38) can be solved over a range of frequencies, and the magnitude and phase of the transfer function then describes the frequency response of the system. The magnitude of the transfer function is shown in Fig 2.14 for the model of a two axle vehicle introduced in section 2.4.2 (see Fig 2.12 and equations (2.29) to (2.33)).

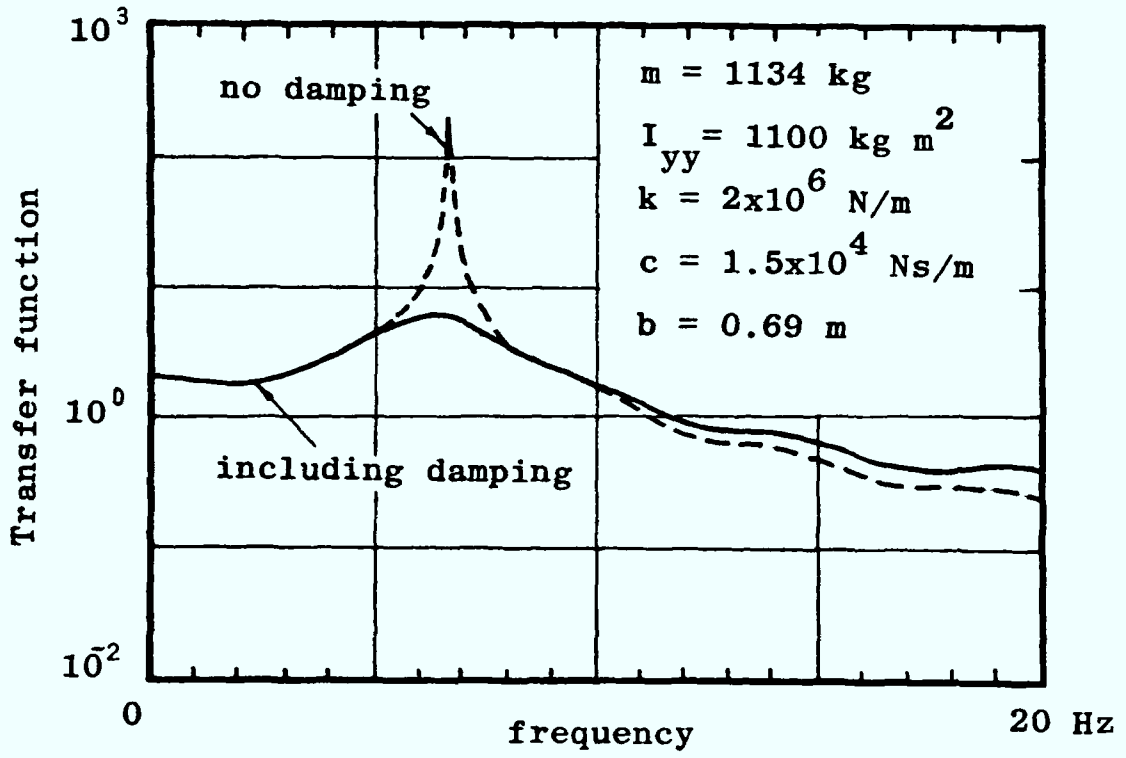

Fig 2.14 Transfer function, $H(\omega)$, for two axle vehicle: frequency response at front of vehicle to track vertical input (speed = 15 mph).

Alternatively, the frequency response may be expressed in terms of the displacement of the vehicle by using equation (2.39) in conjunction with equation (2.38).

The technique which has been explained can be used to describe the response of a vehicle to any sinusoidal input (eg vertical profile, lateral alignment, cross-level). The equations of motion must be linear to use this method.

2.5.3 Solution for an arbitrary periodic input (see Newland (13))

The response of a vehicle to an arbitrary input can be investigated by first considering its impulse response.

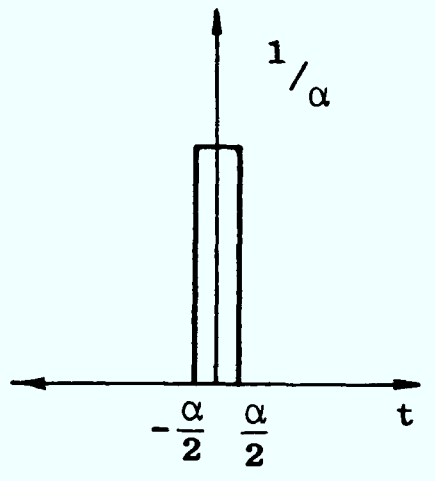

$$\lim_{\alpha \to 0} \int \delta(t)dt = 1$$

Fig 2.15 Delta impulse function, $\delta(t)$

For the input,

$$u(t) = A_1 \cdot \delta(t) \qquad (2.43)$$

where,

A_1 = a constant

$\delta(t)$ = delta impulse function (see Fig 2.15)

the response will be:

$$\underset{\sim}{q}(t) = A_1 \cdot \underset{\sim}{h}(t) \qquad (2.44)$$

Similarly, for an input at a later time, τ ,

$$u(t) = A_2 \cdot \delta(t - \tau) \tag{2.45}$$

The response will be:

$$\underset{\sim}{q}(t) = A_2 \cdot \underset{\sim}{h}(t - \tau) \tag{2.46}$$

If a linear relationship exists between $\underset{\sim}{q}$ and u, the principle of superposition can be applied.
For the input,

$$u(t) = A_1\, \delta(t) + A_2\, \delta(t - \tau) \tag{2.47}$$

the response is given by:

$$\underset{\sim}{q}(t) = A_1\, \underset{\sim}{h}(t) + A_2\, \underset{\sim}{h}(t - \tau) \tag{2.48}$$

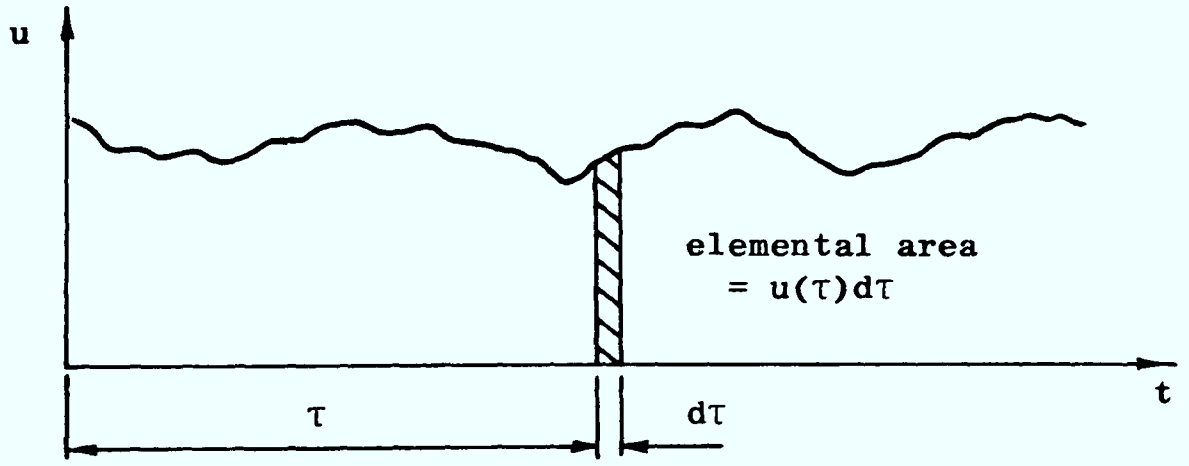

Fig 2.16 Arbitrary input, u(t)

Consider the response to an arbitrary input (see Fig 2.16). An element of the input at time, τ may be expressed as:

$$u(t) = u(\tau)d\tau \cdot \delta(t - \tau) \tag{2.49}$$

The response will be:

$$q(t) = u(\tau)d\tau \cdot \underset{\sim}{h}(t - \tau) \tag{2.50}$$

Again the response of the system to the arbitrary input can be obtained by using principle of superposition. This leads to the result:

$$\underset{\sim}{q}(t) = \int_{-\infty}^{\infty} u(\tau) \,.\, \underset{\sim}{h}(t - \tau)d\tau \qquad (2.51)$$

This is known as the convolution integral: it is an expression of the time-variable response of the system. If the input is periodic, the frequency-variable response can be obtained by taking Fourier Transforms (see Appendix 1) of equation (2.51).

$$\underset{\sim}{q}(f) = \int_{-\infty}^{\infty}\int_{-\infty}^{\infty} u(\tau) \,.\, \underset{\sim}{h}(t - \tau)d\tau \,.\, e^{-j2\pi ft}dt \qquad (2.52)$$

$$= \int_{-\infty}^{\infty} \underset{\sim}{h}(\sigma)e^{-j2\pi f\sigma}d\sigma \int_{-\infty}^{\infty}u(\tau)e^{-j2\pi f\tau}d\tau \qquad (2.53)$$

$$= H(f).\, u(f) \qquad (2.54)$$

where,

$\sigma = t - \tau$

$\underset{\sim}{q}(f)$ = Fourier transform of $\underset{\sim}{q}(t)$

$u(f)$ = Fourier transform of $u(t)$

$f = \omega/2\pi$ = temporal frequency

Equation (2.54) is equivalent to equation (2.38) and may be applied to find the response of a linear system to any periodic input. The equation can also be used for a non-periodic input when a Fourier transform can be taken (eg transients). The condition which must be met is:

$$\int_{-\infty}^{\infty} |u(t)|dt < \infty \qquad (2.55)$$

2.5.4 Solution for a random input

An input is considered to be random when it is non-periodic and has a zero mean value when considered over a long period of time. A sample taken of such an input will also be non-periodic, but will have a finite mean value. The two cases are illustrated in Fig 2.17.

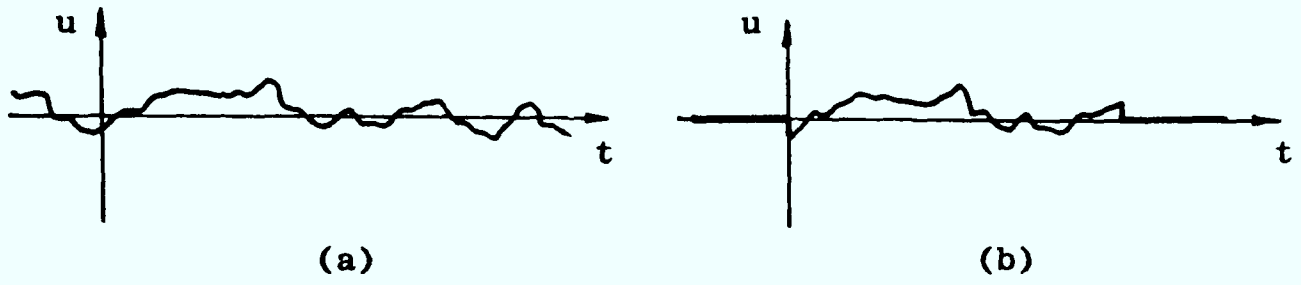

(a) (b)

Fig 2.17 (a) Random input, u(t)
(b) Sample of input, $u_s(t)$

For the second case the condition of equation (2.55) can be met, and as such can be transformed using a Fourier transform. This allows the results of section 2.5.3 to be applied.

It is clear that to describe the input adequately either a long sample, or a number of shorter samples, needs to be taken. Whichever approach is taken a statistical description of the input will need to be used, as deterministic quantities such as amplitude, period, and phase will be inappropriate. The input will therefore be defined in terms of statistical quantities such as the mean value, mean square value, and variance. For this work it will be convenient to deal with the mean square value as it can be easily related to the chosen acceptability criteria (see Chapter 4).

The mean square value for a single sample is given by:

$$\langle u_s^2(t)\rangle = \frac{1}{T}\int_o^T u_s^2(t)dt$$

$$= \frac{1}{T}\int_{-\infty}^{\infty} u_s^2(t)dt \qquad (2.56)$$

By using Fourier transforms (see Appendix 1) this can be re-arranged as shown:

$$\langle u_s^2(t)\rangle = \frac{1}{T}\int_{-\infty}^{\infty} u_s(t)\int_{-\infty}^{\infty} u_s(f)e^{j2\pi ft}df.\ dt$$

$$= \frac{1}{T}\int_{-\infty}^{\infty} u_s(f)\int_{-\infty}^{\infty} u_s(t)e^{j2\pi ft}dt.\ df$$

$$= \frac{1}{T}\int_{-\infty}^{\infty} |u_s(f)|^2 df \qquad (2.57)$$

The function $|u_s(f)|^2$ is even, which allows equation (2.57) to be re-written as:

$$\langle u_s^2(t)\rangle = \int_0^\infty \frac{2}{T} |u_s(f)|^2 df \qquad (2.58)$$

This can be expressed in the form:

$$\langle u_s^2(t)\rangle = \int_0^\infty S_u(f) df \qquad (2.59)$$

where,

$$S_u(f) = \frac{2}{T} |u_s(f)|^2 \qquad (2.60)$$

The quantity $S_u(f)$ is the spectral density, and it describes the harmonic content of the sample over a frequency range from zero to infinity. The mean square value in a narrow band of frequency is given by the expression:

$$\langle u^2(t)\rangle = S_u(f)\Delta f \qquad (2.61)$$

Successive sampling acts to improve the accuracy of the spectral density, and so a better description of the input can result.

The spectral density is measured using either an analog or digital technique. The analog technique is to use a number of filters with different centre frequencies, measure the mean square values corresponding to each of the frequency bands, and construct the spectral density using equation (2.61). The digital technique uses a discrete form of the Fourier Transform and determines the spectral density using equation (2.60): this method is explained in greater detail in section 3.3.2.

It can be shown (see Newland (13)) that:

$$S_{\underset{\sim}{q}}(f) = |H(f)|^2 S_u(f) \qquad (2.62)$$

where,

$S_q(f)$ = spectral density describing output
$S_{\tilde{u}}(f)$ = spectral density describing input
$H(f)$ = transfer function (see equation (2.33))

It is thus possible to find the harmonic content of the response of a linear system to a random input using equation (2.62), provided that the spectral density of the input and the transfer function are known. Spectral densities describing track vertical profile, lateral alignment, and cross-level have been measured (using a digital technique) in a number of coal mines, and an analytical expression that closely models these is established in section 3.3.7. This expression (equation (3.38)) is shown below:

$$S_u(f) = \frac{AV^{n-1}}{f^n}$$

where,

A = roughness coefficient

n = integer exponent (2, 3 or 4)

The transfer function can be determined algebraically for a linear model using equation (2.33).

In addition to describing the vehicle response by equation (2.62), the acceleration spectral density in response to track input can also be determined by using the expression:

$$S_{\underset{\sim}{\ddot{q}}}(f) = \left|H(f) \cdot \omega^2\right|^2 S_u(f)$$

$$= \left|H(f)\right|^2 \omega^4 S_u(f) \qquad (2.63)$$

where,

$S_{\underset{\sim}{\ddot{q}}}$ = acceleration spectral density

$\omega = 2\pi f$ = temporal frequency

This acceleration spectral density can be examined over narrow frequency bands by using a variation of equation (2.61):

$$\langle \underset{\sim}{q}^2(t) \rangle = S_{\underset{\sim}{\ddot{q}}}(f)\, \Delta f \qquad (2.64)$$

The root mean square (rms) accelerations, which can be used to establish a measure of the ride quality of a vehicle (see Chapter 4) can be obtained for these frequency bands by taking the square root

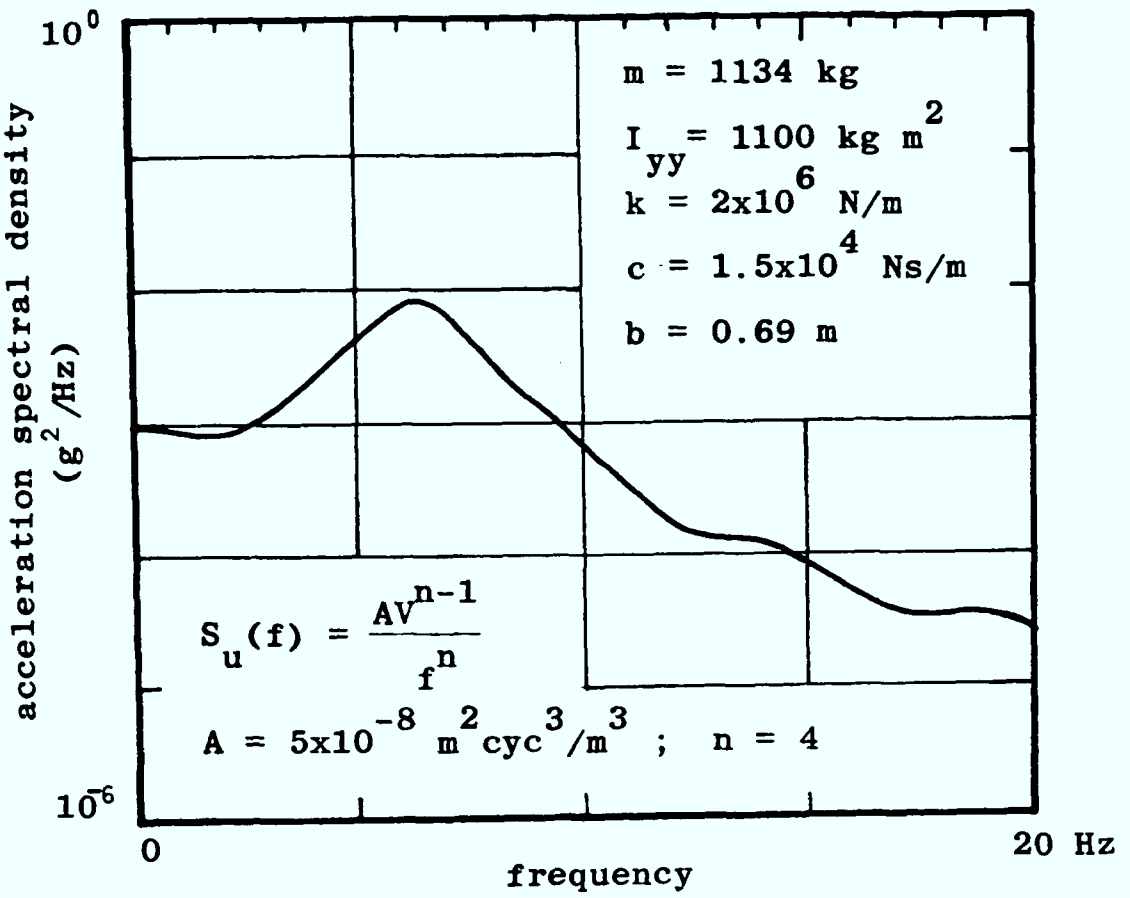

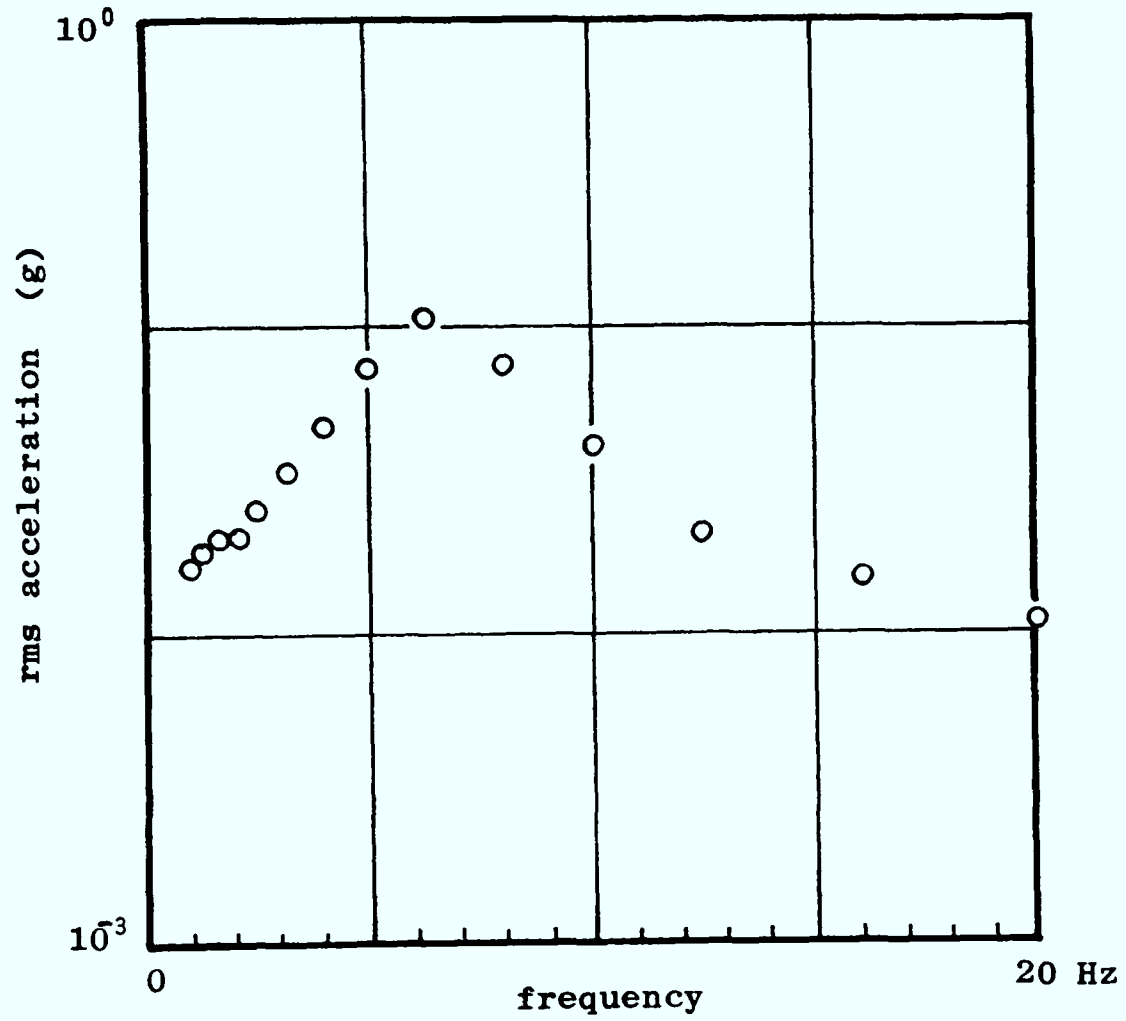

Fig 2.18 (a) Acceleration spectral density
(b) Rms accelerations

Two axle vehicle - response at front of vehicle to track vertical input (speed = 15 mph)

of equation (2.64).

The acceleration spectral density, and the rms accelerations measured over third octave bands, are shown in Fig 2.18 for the model of a two axle vehicle introduced in section 2.4.2. The input to the model is an analytical representation of measured vertical profile (equation (3.38)).

2.6 General purpose computer programs

2.6.1 Program for determining transfer functions

The transfer function, H(f), which describes the response of a vehicle to an input from the track, is calculated using the program TF.F77 (see Fig 2.19).

Equations of motion are written in the form of equation (2.33), and the parameter values are stored in the subroutines PARAM and INPUT. The program transforms the equations of motion into the form of equation (2.37), and then solves this at discrete intervals (0.1 Hz) over a pre-set frequency range (0 to 20 Hz) using a standard library subroutine (see NAG (14)). The transfer function, expressed in the form of real and imaginary vectors E and jF (see equation (2.40), is written into an output file for each frequency interval. The program is written in FORTRAN 77: a listing of the main program and the subroutines is included in Appendix 2.

2.6.2 Plotting program

The plotting program is used to plot the transfer function data using three different formats, these being: acceleration spectral densities and rms accelerations (these are plotted after the track input is defined in the form of a displacement spectral density), and as a transfer function. The program PLOT.F77 (see Fig 2.20) reads the transfer function data obtained with the program TF.F77 (see section 2.6.1), calls for the user to nominate a particular vehicle co-ordinate of interest, and then plots the data using one of the subroutines SPEC, RMS, or TRANS. These subroutines are discussed in more detail below.

The subroutine SPEC multiplies the squared transfer function by the spectral density describing the track input (which is defined by the user in the main program before the subroutine is entered)

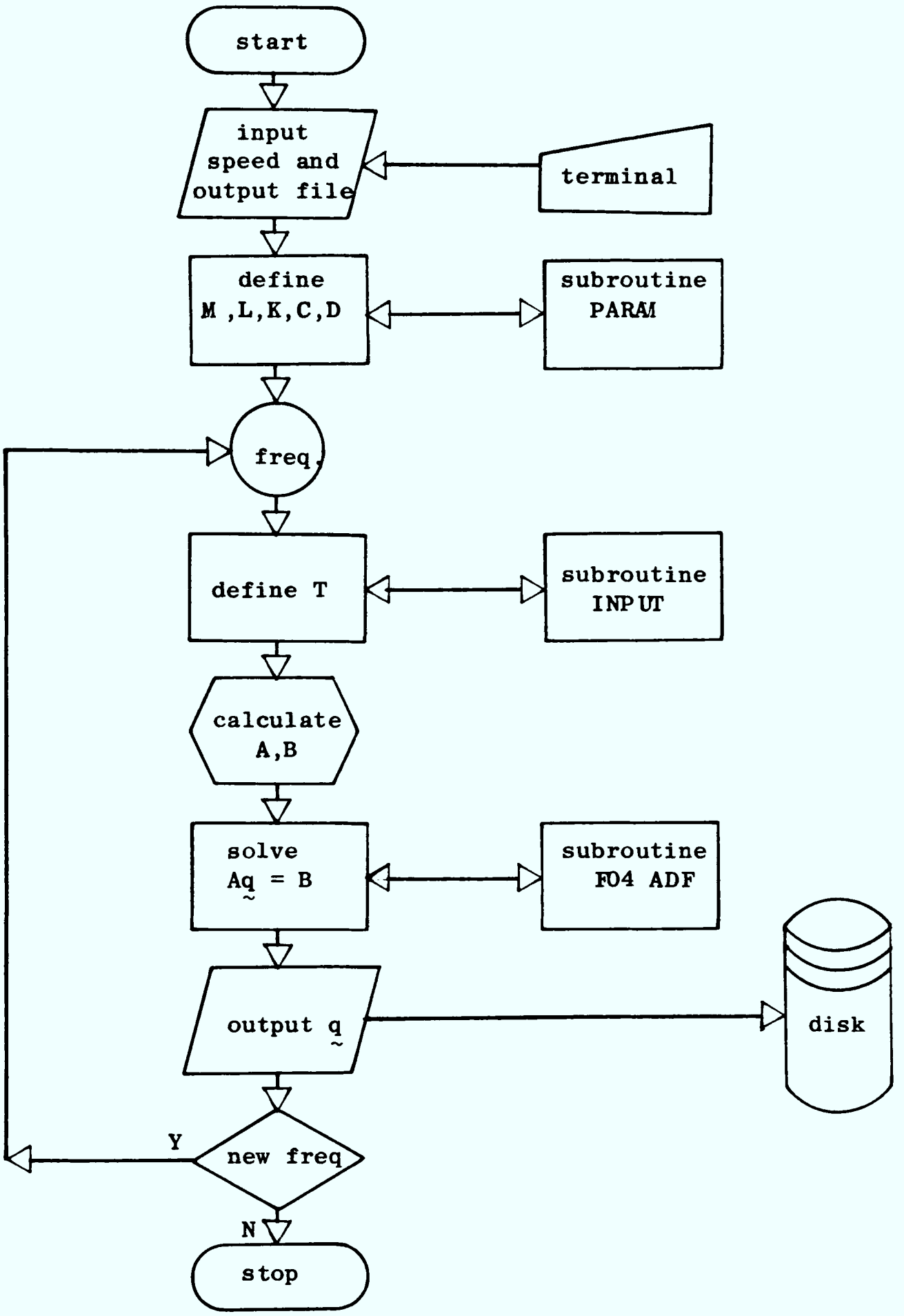

Fig 2.19 Flow chart describing the program TF.F77

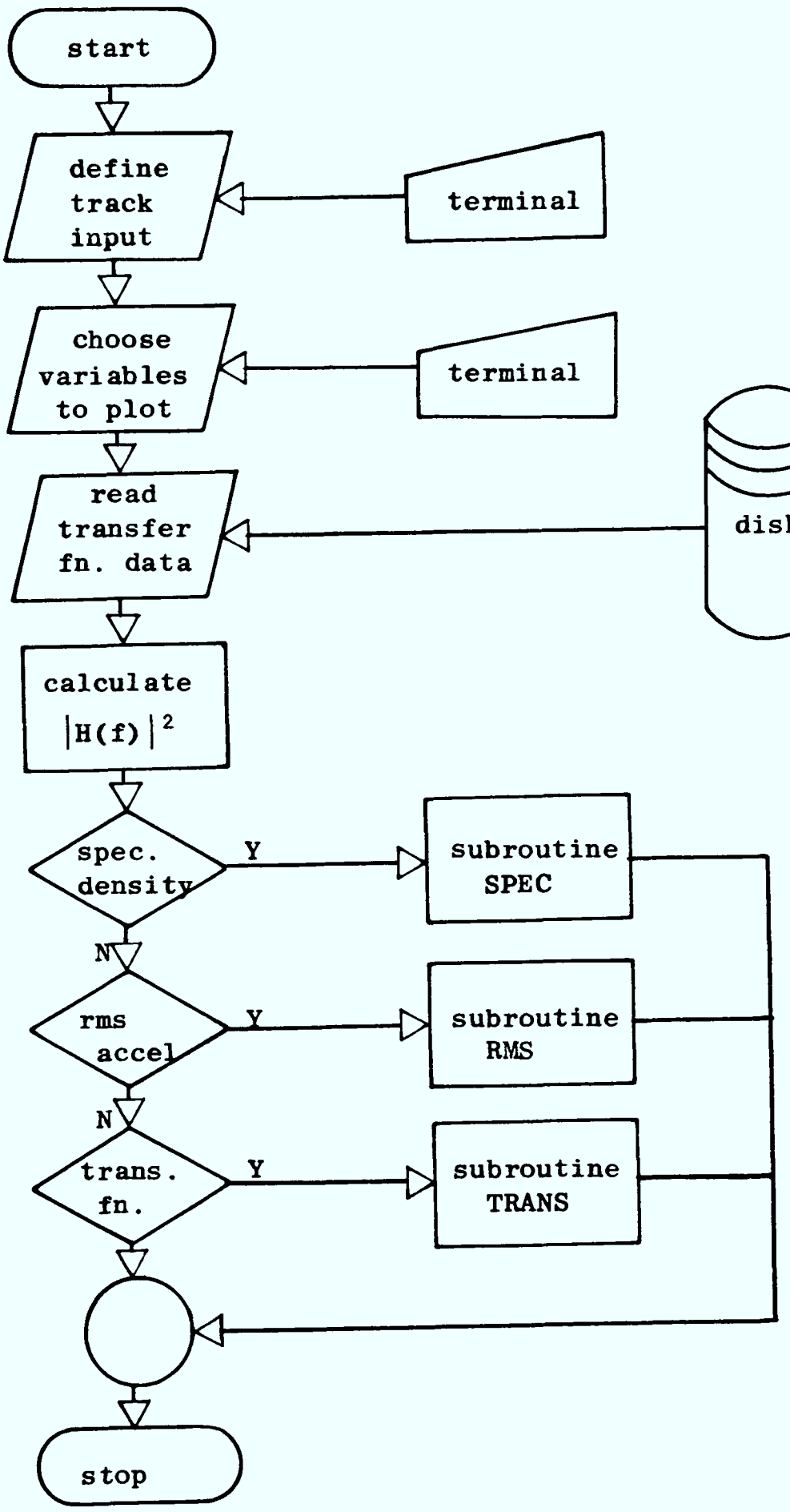

Fig 2.20 Flow chart describing the program PLOT.F77

according to equation (2.63). The resultant acceleration spectral density is plotted against frequency.

The subroutine RMS calculates the acceleration spectral density in the same manner, and then calculates rms accelerations over third octave bands by taking the square root of equations (2.64). The rms accelerations are plotted discretely at the centre frequencies of these bands.

The subroutine TRANS plots the magnitude of the transfer function against frequency. This subroutine ignores the track input defined in the main program.

The program is written in FORTRAN 77: a listing of the main program and the subroutines in included in Appendix 2.

Chapter 3

Measurement of Track Geometry

3.1 Introduction

3.1.1 General considerations

The ride and the likelihood of derailment of a rail vehicle are highly dependent upon the state of the track it runs on, particularly in the case of a mining vehicle, as it only has limited suspension to isolate it from irregularities. Any deviations from an ideal track (see section 2.2) will have an effect on the motion of a vehicle, and so an adequate description of these deviations is crucial to the explanation of dynamic behaviour. Throughout this work the track geometry is described in terms of the quantities defined in section 2.2, and these are summarised in Fig 3.1.

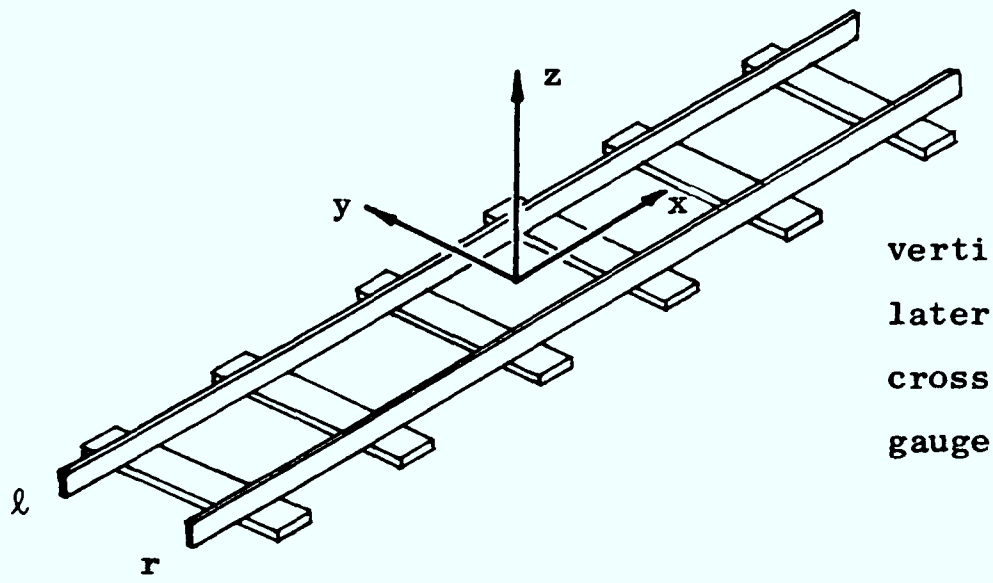

vertical profile = $\frac{1}{2}(z_\ell + z_r)$

lateral alignment = $\frac{1}{2}(y_\ell + y_r)$

cross-level = $z_\ell - z_r$

gauge = $y_\ell - y_r$

Fig 3.1 Definition of track geometry (see section 2.2)

The track geometry can either be measured by surveying, or by using a track monitoring vehicle. Measuring geometry from a vehicle moving along the track provides greater flexibility and is less time consuming, and so is widely used in the characterisation of mainline track: British Rail have developed a high speed track recording coach specifically for this task (see Lewis, et al (15)). The same technique is also used in the present work, and is described in section 3.2.

The measured data will usually be recorded for a length of track on either a chart or magnetic tape, and this recording may be processed further if required. The method of presentation of the

data is dictated largely by the application; for this work the track geometry is presented in the form of spectral densities describing the magnitude of each irregularity over a range of spatial frequencies. These spectral densities can be related to temporal frequencies and used as inputs to the mathematical models, provided the speed of the vehicle being modelled remains constant. The description of track geometry is explained in section 3.3. This method is employed widely for mainline track and results are well documented (see ISO (4)): some of these results are compared with those obtained for railways in coal mines in section 3.4.

3.1.2 Instrumentation in coal mines

Much of the electronic equipment which has been developed for measuring the geometry of mainline track cannot be taken into coal mines because of the safety risk. The types of instrumentation which are allowed in British coal mines are restricted severely, and must be approved by HM Inspectorate of Mines. Instrumentation which has been classed as "intrinsically safe (IS)" (see BS 1259:1958 (16)) is constructed in such a way that any electrical sparking that occurs is incapable of igniting flammable gases, and this type can be used generally in mines. Other instrumentation must be approved by the Inspectorate for use in a specific area of a particular mine.

3.2 Measurement of track geometry

3.2.1 Measurement from a moving vehicle

In order to measure the geometry of a section of track from a moving vehicle, the track displacement is measured relative to that vehicle and then related to absolute co-ordinates on the ground. Different techniques exist to carry out this measurement, and these are described below. Examples that illustrate the measurement of vertical profile are used to explain the methods.

The most common type of measuring instrument is the "mid-chord" type which is illustrated in Fig 3.2. The principle of this method is that the displacement of the central measuring wheel will be related to the profile of the track at the location of the wheel, and at the location of the front and rear wheels. For the vehicle shown in Fig 3.2, this may be expressed as shown in equation (3.1).

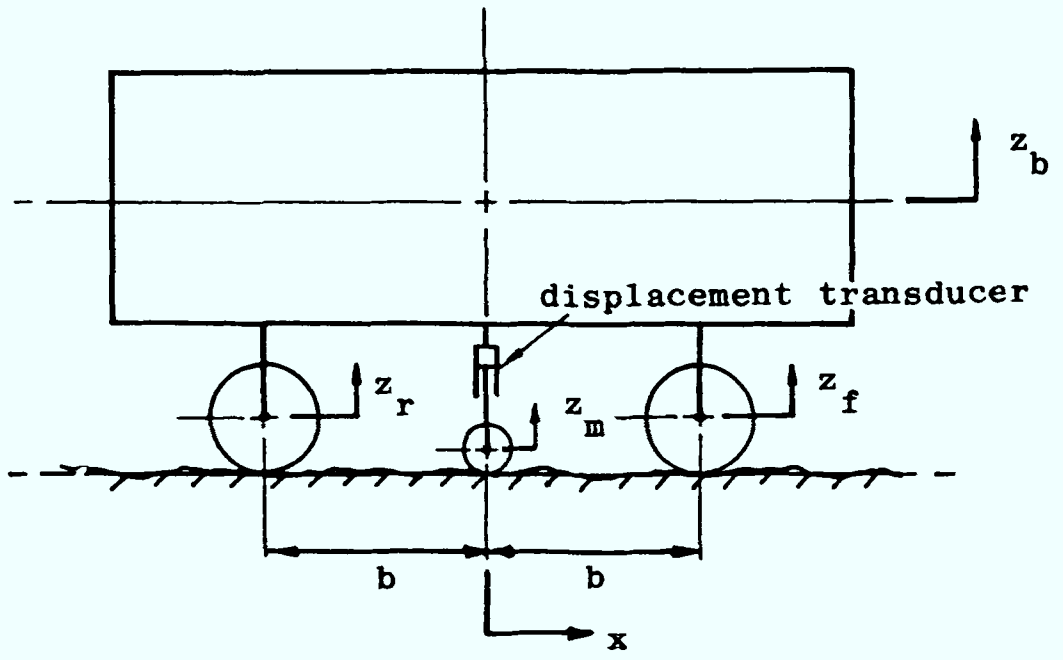

Fig 3.2 Mid-chord measuring vehicle

$$z_m = z_t - z_b \qquad (3.1)$$

where,

z_m = displacement of measuring wheel

z_t = displacement of track relative to an absolute co-ordinate system on the ground

z_b = displacement of vehicle body

which can be re-written in the form:

$$z_m = z_t - \tfrac{1}{2}(z_f + z_r) \qquad (3.2)$$

where,

z_f and z_r = displacement of the front and rear wheels.

At a given position, x, along the track, equation (3.2) can be expressed in the form:

$$z_m(x) = z_t(x) - \tfrac{1}{2}(z_t(x + b) + z_t(x - b)) \qquad (3.3)$$

where,

2b = wheelbase

The spatial frequency response of the measuring wheel can be determined by taking Laplace transforms (see Raven (12)) of equation (3.3), giving the result:

$$z_m(s) = z_t(s)(1 - \tfrac{1}{2}(e^{bs} + e^{-bs})) \qquad (3.4)$$

where,

s = Laplace differential operator

By making the substitution of $j(2\pi\Omega)$ for s in equation (3.4), it can be written as:

$$z_m = z_t \cdot (1 - \cos(2\pi\Omega b))$$

$$= z_t \cdot (2 \sin^2(\pi\Omega b)) \qquad (3.5)$$

where,

Ω = spatial frequency = $1/\lambda$

λ = wavelength of irregularity

$e^{j\theta} = \cos\theta + j \sin\theta$

The frequency response of the measuring device, as determined by equation (3.5), is shown in Fig 3.3.

It is clear that the displacement of the measuring wheel does not, in itself, give an accurate representation of the track as certain wavelengths of irregularities are emphasized. The results shown in Fig 3.3 can, however, be used in the processing of measured data to provide an adequate description of the track. If equation (3.5) is re-written in the following way:

$$z_m/z_t = H_m(\Omega) = 2 \sin^2(\pi\Omega\, b) \qquad (3.6)$$

where,

$H_m(\Omega)$ = transfer function of the measuring wheel

the spectral density describing the magnitude of the irregularity will be given by the expression:

$$S_u(\Omega) = |1/H_m(\Omega)|^2 S_m(\Omega) \qquad (3.7)$$

where,

$S_u(\Omega)$ = spectral density describing track irregularity

$S_m(\Omega)$ = spectral density obtaining from measured data

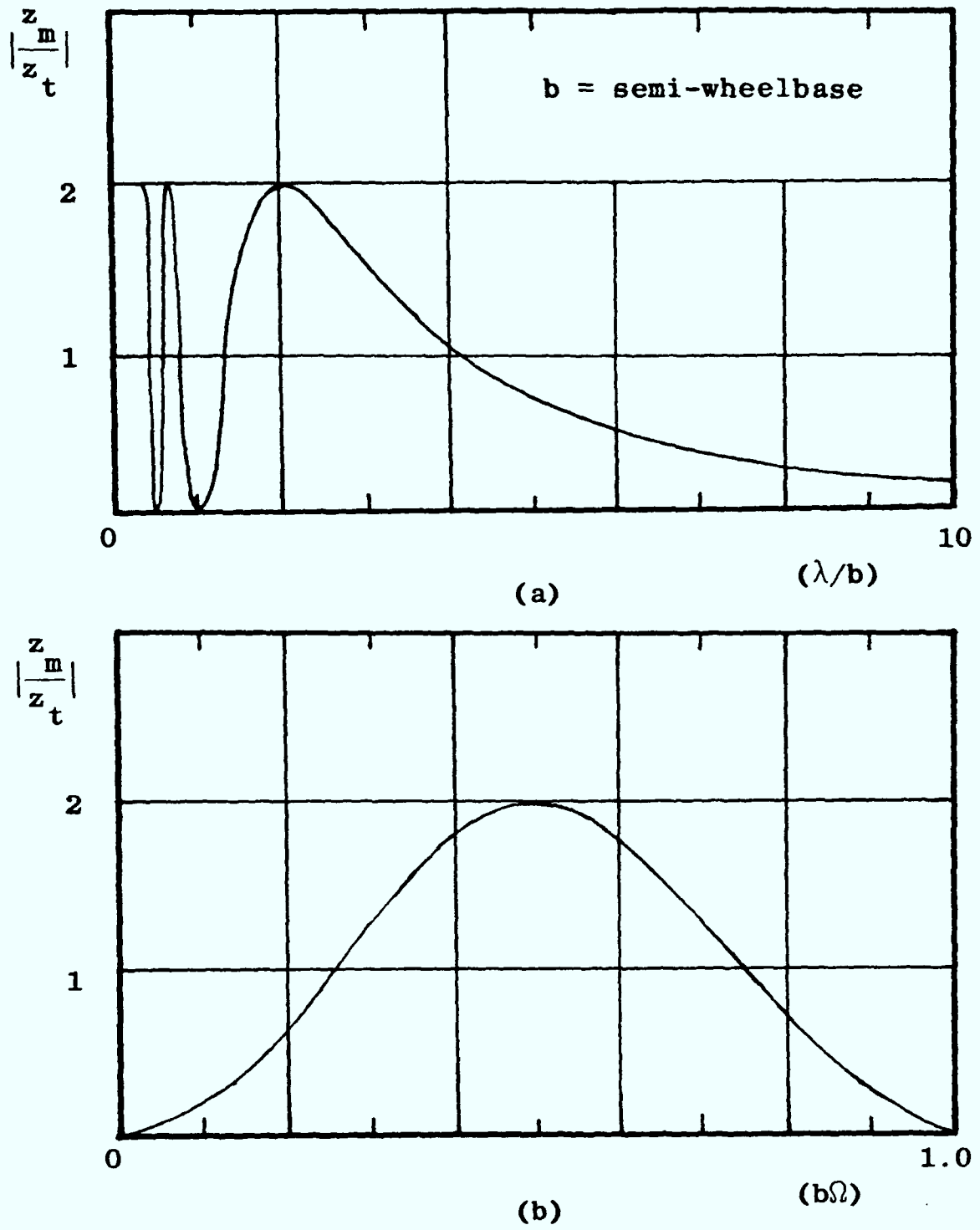

Fig 3.3 Frequency response of mid-chord measuring device:
(a) in terms of wavelengths of irregularity
(b) in terms of spatial frequency.

The method of obtaining the spectral density, $S_m(\Omega)$, from measured data is described in section 3.3, and the relationships between spectral density and transfer functions have been discussed in section 2.5.4. It can be noted from examination of equation (3.6) that equation (3.7) will be undefined whenever,

$$\Omega = \frac{n}{b} \quad (n = 0, 1, 2, ...) \tag{3.8}$$

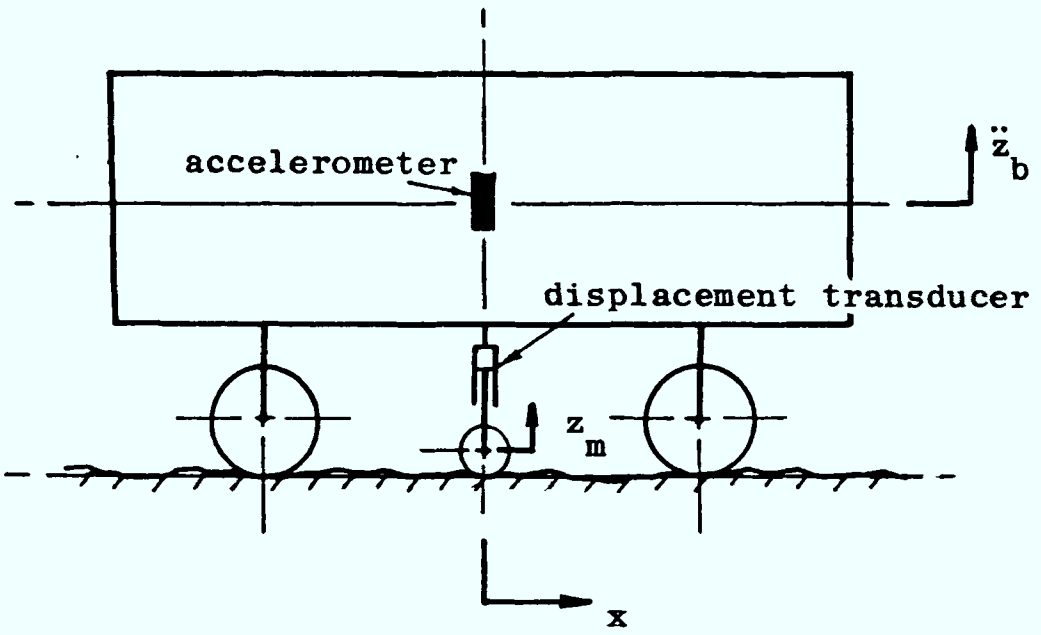

Fig 3.4 Inertial measurement

Another method which is used to measure track geometry is the "inertial" measurement technique which is illustrated in Fig 3.4. The displacement of the measuring wheel is still related to the profile of the track by equation (3.1),

$$z_m = z_t - z_b$$

but the displacement of the vehicle body, z_b, is now determined by independent measurement. This is done by measuring the acceleration of the vehicle body and integrating the measured data twice to give displacement. The spatial frequency response of such a system is dependent on the frequency response of the measuring and processing equipment. Most accelerometers and electronic integrators (eg operational amplifiers) exhibit a relatively poor response at very low frequencies and, for this reason, inertial measurement techniques are found to work best at fairly high vehicle speeds (note: $f = \Omega V$, where V = speed).

3.2.2 Existing track monitoring equipment

Monitoring equipment has already been developed to measure certain aspects of track geometry (see Clibborn (17)) in order to locate sections of track where there is a danger of derailment due to kinematic effects. If there is excessive twisting (rate of change

of cross-level) a wheel can leave the track. If the gradient is too large a locomotive, which commonly has a short wheelbase and a long overhang, can bump the track. The equipment is designed to measure three quantities: cross-level, gauge, and track gradient, and can either be fitted into a purpose built vehicle, or mounted within the floor section of a standard two axle manriding car.

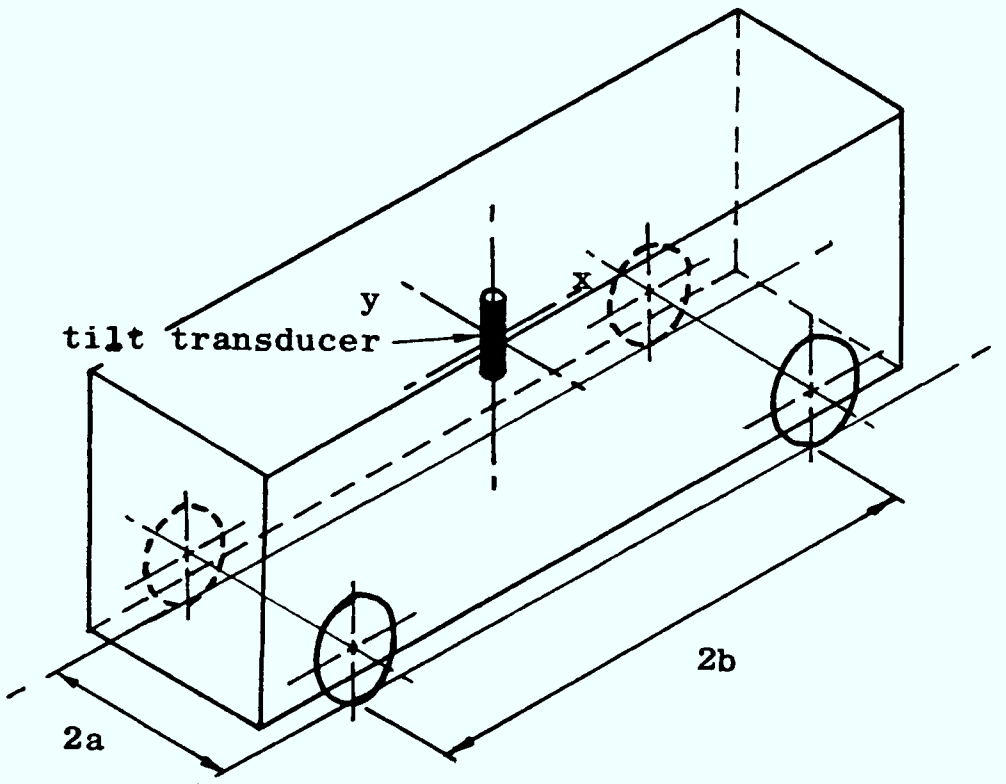

Fig 3.5 Measurement of cross-level and track gradient

The cross-level is measured with a tilt transducer which is mounted near the middle of the vehicle (see Fig 3.5). The sensing element is a pendulum which is pivoted on a piece of flat spring steel on which strain gauges are attached. The pendulum is immersed in a damping fluid. As the vehicle travels along the track the presence of any twist causes the pendulum to swing and the angle of rotation is recorded on a chart (examples of the chart recordings of cross-level are included in Appendix 3). This measurement technique is essentially a "mid-chord" type and is explained below.

The measured angle of roll, ϕ_m, is related to the roll angles of the front and rear wheels by the expression:

$$\phi_m = \tfrac{1}{2}(\phi_f + \phi_r) \qquad (3.9)$$

For a given position, x, along the track, this can be re-written as:

$$\phi_m = \tfrac{1}{2}(\phi_t(x + b) + \phi_t(x - b)) \qquad (3.10)$$

where,

$$\phi_t = (z_\ell - z_r)/2a \qquad (3.11)$$

Equation (3.11) is a definition of the cross-level (see Fig 3.1). Using the method of Laplace transforms that was described in section 3.2.1, an expression for the spatial frequency response can be obtained.

$$\phi_m = \phi_t(\cos(2\pi\Omega b)) \qquad (3.12)$$

Combining equations (3.11) and (3.12) then gives the result:

$$|\phi_m/(z_\ell - z_r)| = |H_c(\Omega)| = \sqrt{\cos^2(2\pi\Omega\, b)}/2a \qquad (3.13)$$

where,

$H_c(\Omega)$ = transfer function of the transducer measuring cross-level

The frequency response of the transducer, as determined by equation (3.13), is shown in Fig 3.7(a).

The transfer function, $H_c(\Omega)$, can be used to relate measured data to the cross-level by using equation (3.7), which yields results in the form of a spectral density. The measured data is used untreated in Clibborn's work (see (17)) and, as a result, he underestimates the magnitude of cross-level for most spatial frequencies. He uses the data to locate sections of track where the twist is excessive, rejecting those sections where the twist causes a wheel of a suspensionless vehicle to clear the rail (the criterion is explained in section 4.3.8). By underestimating the magnitude of the cross-level the track will always appear to be better than it actually is, and so the rejection criterion is relaxed.

The track gradient is measured using the same transducer (see Fig 3.5) turned so that the pendulum swings about a y axis (examples of the chart recordings of track gradient are included in Appendix 3). The track gradient is measured as an angle, θ_m, which can be related

to the vertical profile of the track at the position of the front and rear wheels. In this way the device is again a "mid-chord" type.

$$\theta_m = (z_R - z_F)/2b \qquad (3.14)$$

where,

z_R and z_F = vertical profile at the position of the front and rear wheels

This can be re-written as:

$$\theta_m(x) = (z_t(x - b) - z_t(x + b))/2b \qquad (3.15)$$

where,

$$z_t = \frac{z_\ell + z_r}{2}$$

= vertical profile (see Fig 3.1)

Again the use of Laplace Transforms gives the result:

$$\theta_m = z_t(- j\sin(2\pi\Omega b))/b \qquad (3.16)$$

which can be rearranged to give:

$$|\theta_m/z_t| = |H_v(\Omega)| = (2\sqrt{\sin^2(2\pi\Omega b)})/2b \qquad (3.17)$$

where,

$H_v(\Omega)$ = transfer function of the transducer measuring vertical profile

The frequency response of the transducer, as determined by equation (3.17), is shown in Fig 3.7(b).

The gauge is measured using a pair of small flanged cylindrical wheels that follow the lateral position of each of the rails (see Fig 3.7). The wheels are attached to vertical legs which pivot about their centres, and the difference in the movement of the two

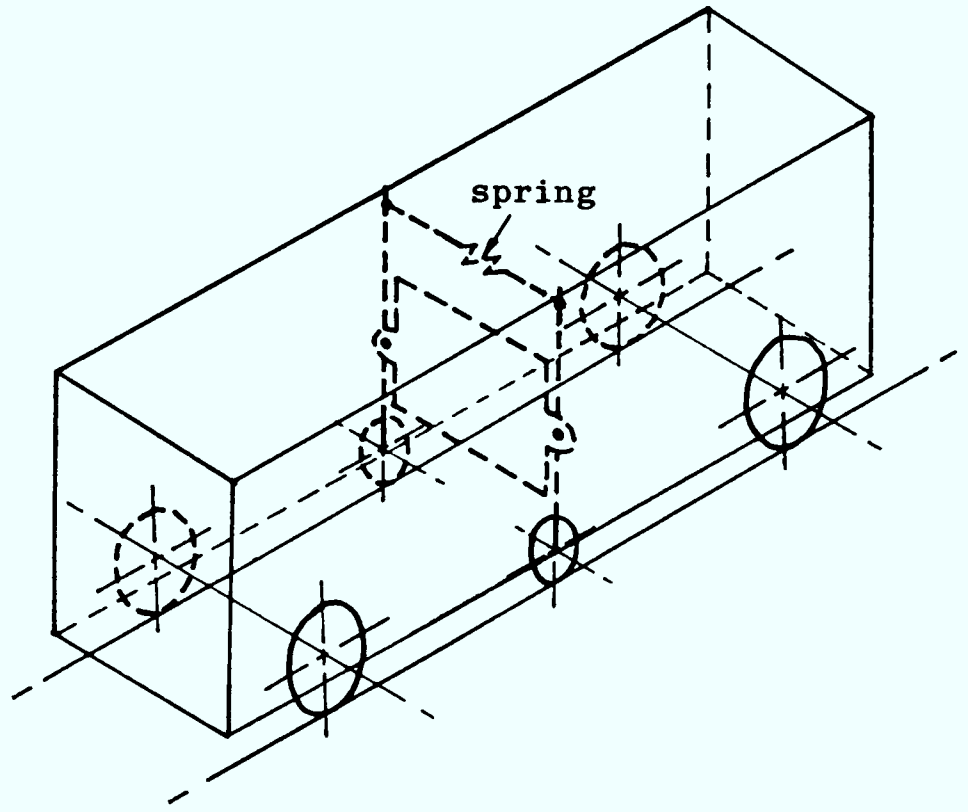

Fig 3.6 Measurement of gauge

legs is monitored using a single linear potentiometer. This gives an absolute measurement of the gauge,

$$\text{ie gauge} = y_\ell - y_r \quad \text{(see Fig 3.1)}$$

By using two potentiometers it would be possible to measure the absolute movement of each of the legs, which would enable the device to be used in the measurement of lateral alignment. The measurement would be based upon the "mid-chord" method that was explained previously in section 3.2.1. Using equation (3.6), this gives the result:

$$|y_{am}/y_a| = |H_a(\Omega)| = 2\sin^2(\pi\Omega b) \qquad (3.18)$$

where,

$y_a = \dfrac{y_\ell + y_r}{2}$ = lateral alignment (see Fig 3.1)

$y_{am} = \dfrac{y_{\ell m} + y_{rm}}{2}$ = measured lateral alignment

$H_a(\Omega)$ = transfer function of device measuring lateral alignment

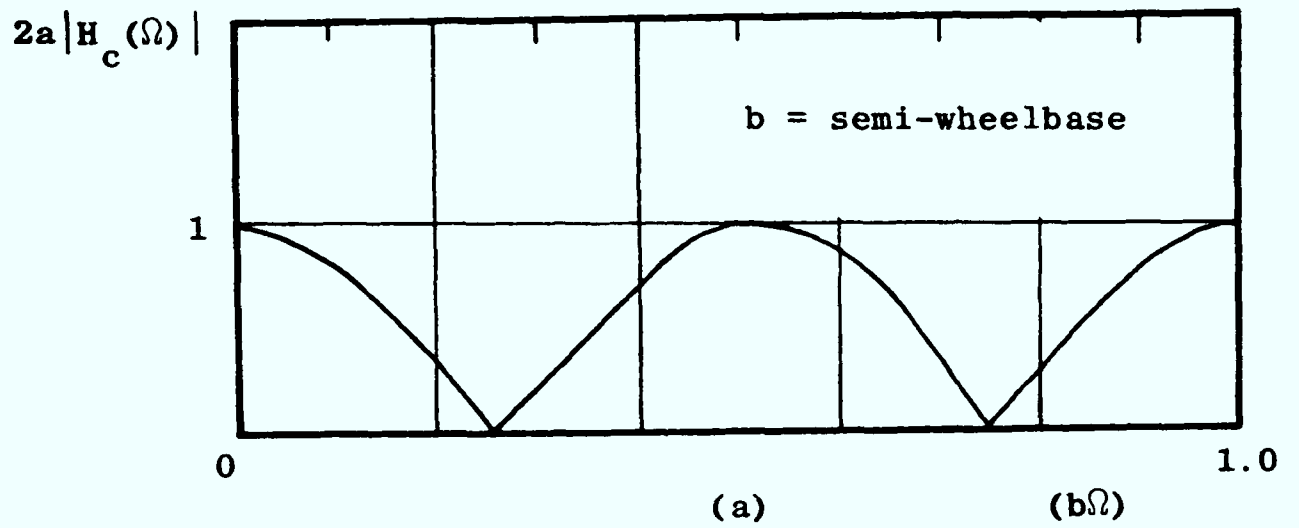

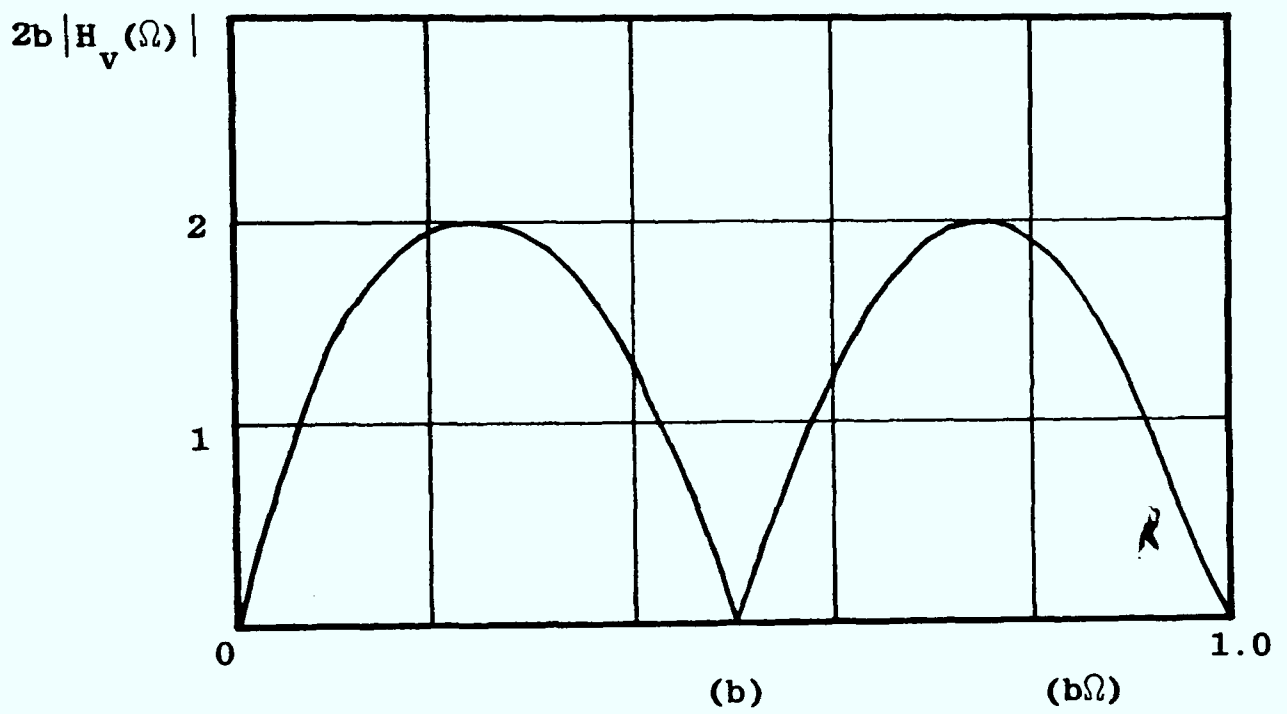

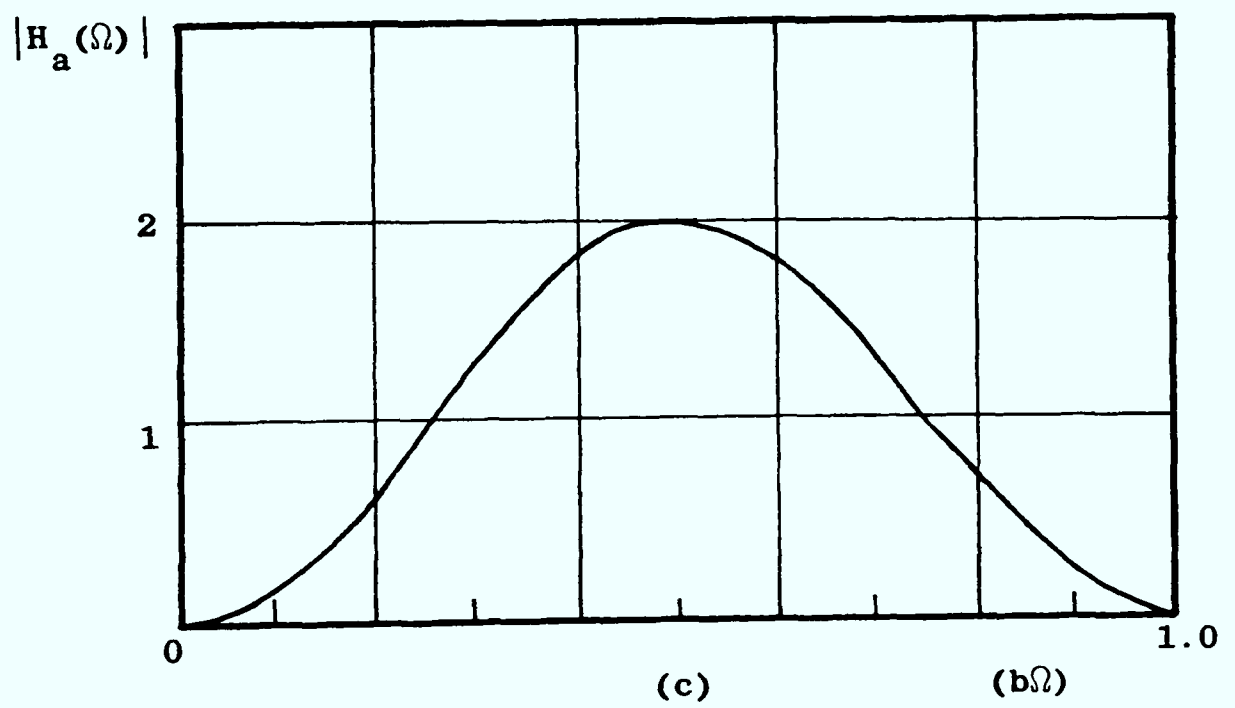

Fig 3.7 Spatial frequency response curves for transducers
(a) cross-level (equation (3.13))
(b) vertical profile (equation (3.17))
(c) lateral alignment (equation (3.18))

The frequency response of the device, as determined by equation (3.18) is shown in Fig 3.7(c).

The instrumentation associated with the existing track monitoring equipment is intrinsically safe (see section 3.1.2), and so can be used universally. As yet, no measurements of lateral alignment have been obtained with this equipment, but examples of cross-level and track gradient data are included in Appendix 3. The processing of the measured data to yield spectral densities is described in section 3.3.

3.2.3 Vertical profile by measuring axle acceleration

In addition to measuring the profile with specialised track monitoring equipment, it is also possible to obtain a measurement from the movement of a pair of wheels on a vehicle in service. This can be done using a variation of the "inertial" technique introduced in Fig 3.4. An accelerometer placed in the middle of an axle can be used to measure the average acceleration of the two wheels, and this can be integrated twice to give displacement. Due to the restrictions in permissible instrumentation (see section 3.1.2) this integration is best done outside the mine using a mathematical technique.

If the measured data are processed to give the acceleration spectral density (see section 2.5.4), this can be related to the spectral density describing track vertical profile using the expression:

$$S_z(f) = \frac{1}{\omega^4} S_z^{\cdot\cdot}(f) \qquad (3.19)$$

This can be expressed in terms of spatial frequency as:

$$S_z(\Omega) = V \cdot S_z(f) = \frac{V}{(2\pi f)^4} S_z(V\Omega) \qquad (3.20)$$

where,

V = forward speed of the vehicle

$f = V\Omega$

It is thus possible to obtain the spectral density by solving equation (3.20) over a range of spatial frequencies.

The results obtained from measuring axle movement give an indication of the magnitude of the vertical profile, although the effects of resonance of component parts will introduce inaccuracies: this is illustrated below.

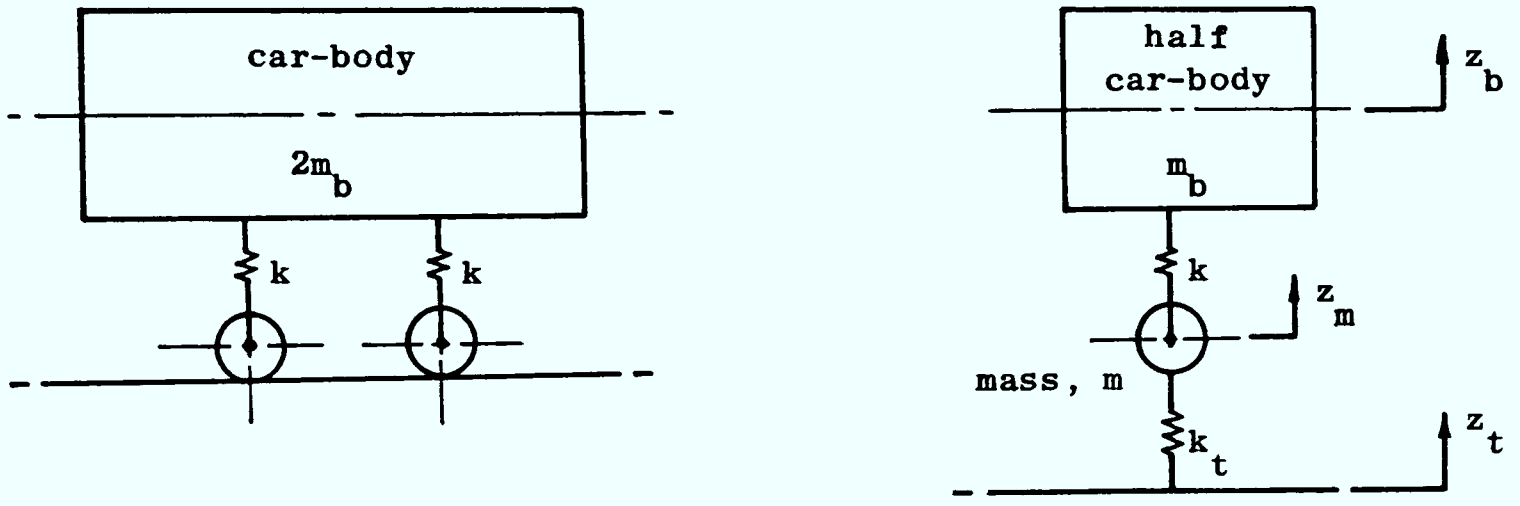

Fig 3.8 (a) Two axle vehicle

(b) Model of two axle vehicle (half car-body)

A two axle vehicle is modelled as shown in Fig 3.8. The motion of the vehicle can be described by the equations:

$$m_b \ddot{z}_b + kz_b = kz_m$$

$$m\ddot{z}_m + (k + k_t)z_m - kz_b = k_t z_t \qquad (3.21)$$

where,

k = primary suspension stiffness

k_t = track stiffness

$\ddot{z}_m$ = measured acceleration

z_t = track vertical profile

z_b = car-body movement

Using the method of Laplace Transforms (see Raven (12)) allows equation (3.21) to be re-written in the form:

$$z_t(s)/z_m(s) = \frac{s^2}{\omega_t^2} + 1 + \left(\frac{\omega_m}{\omega_t}\right)^2 \left(1 - \frac{\omega_b^2}{(s^2 + \omega_b^2)}\right) \qquad (3.22)$$

where,

s = Laplace differential operator

$\omega_b^2 = k/m_b$ = resonant frequency of car-body

$\omega_m^2 = k/m$

$\omega_t^2 = k_t/m$

By substituting $j\omega$ for s, this can be re-written as:

$$|z_m(\omega)/z_t(\omega)| = |H_{vp}(\omega)| = \sqrt{\left(1 + \left(\frac{\omega_m}{\omega_t}\right)^2 \left(1 + \frac{(\omega_b/\omega)^2}{1-(\omega_b/\omega)^2}\right) - \left(\frac{\omega}{\omega_t}\right)^2\right)^{-2}} \qquad (3.23)$$

where,

$H_{vp}(\omega)$ = transfer function of the accelerometer

For $\omega^2 >> \omega_b^2$ this becomes:

$$|H_{vp}(\omega)| = \sqrt{\left(1 + \left(\frac{\omega_m}{\omega_t}\right)^2 - \left(\frac{\omega}{\omega_t}\right)^2\right)^{-2}} \qquad (3.24)$$

For a typical two axle manriding vehicle,

m = 150 kg (mass of pair of wheels)

m_b = 1000 kg (mass of half car-body)

k = 2×10^6 N/m (primary suspension stiffness)

k_t = 5×10^6 N/m (track stiffness)

Substituting these values into equations (3.23) and (3.24) gives the results shown in Fig 3.9.

The effect of resonance is to reduce the accuracy with which the measured displacement represents the actual profile of the track. It is clear that this method of measurement is suited best to a vehicle with a fairly soft primary suspension travelling on track with little resilience, as this gives a wider range of frequencies for which the measurements are valid. For the example shown, the measurements are within 50% of the actual profile for the frequency range of 10 Hz to 25 Hz. When the track and primary suspension

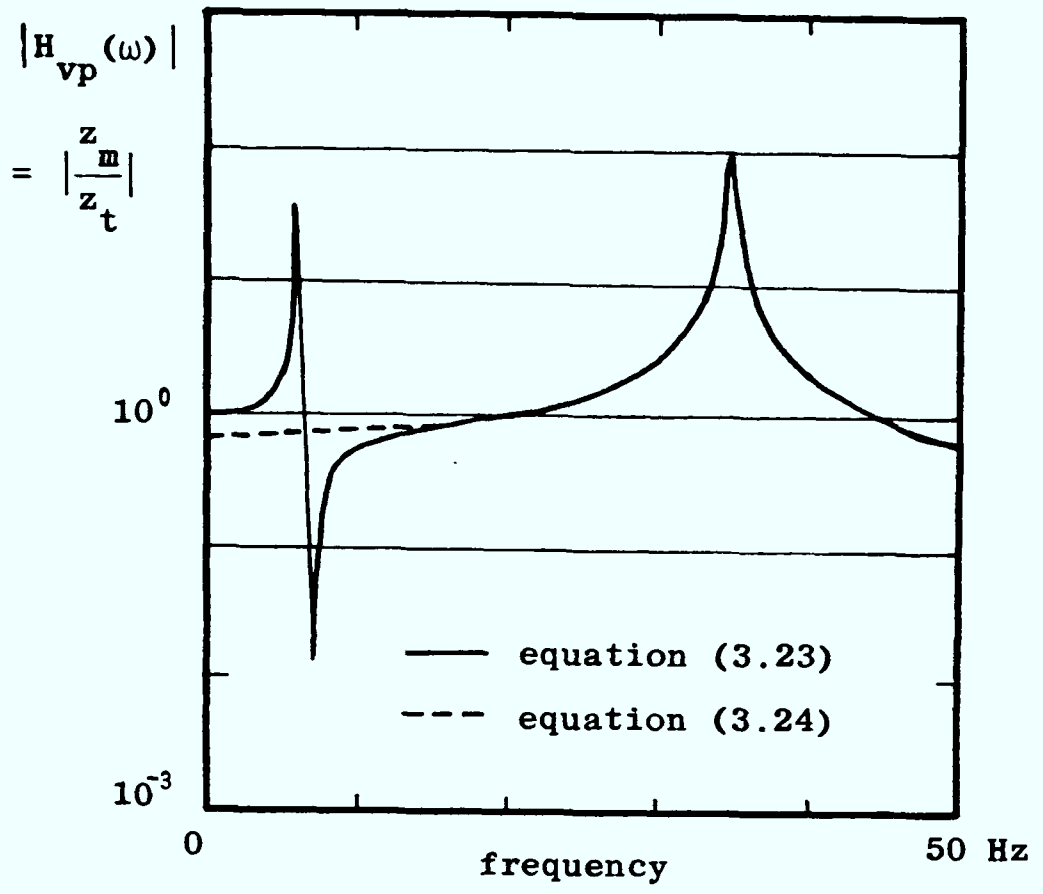

Fig 3.9 Frequency response of measured profile

stiffnesses are comparable, the $(\omega_m/\omega_t)^2$ term in equations (3.23) and (3.24) becomes significant, and the measurements underestimate the actual profile.

Measuring the vertical profile by the method described can be done in conjunction with vehicle tests and, although inaccurate, it gives a good indication of the magnitude of the irregularities. The results of a number of such tests, in the form of acceleration spectral densities, are included in Appendix 4 and these can be processed using equation (3.20) to give spectral densities describing vertical profile. The results of this process for the track in the arterial road at Ellington Colliery are shown in Fig 3.10. This section of track is laid in concrete, and the measurements were made from the axle of a locomotive. The resonant frequency of the car-body is quite low and the track resilience is small, and, as a result, the measurements are of a reasonable accuracy.

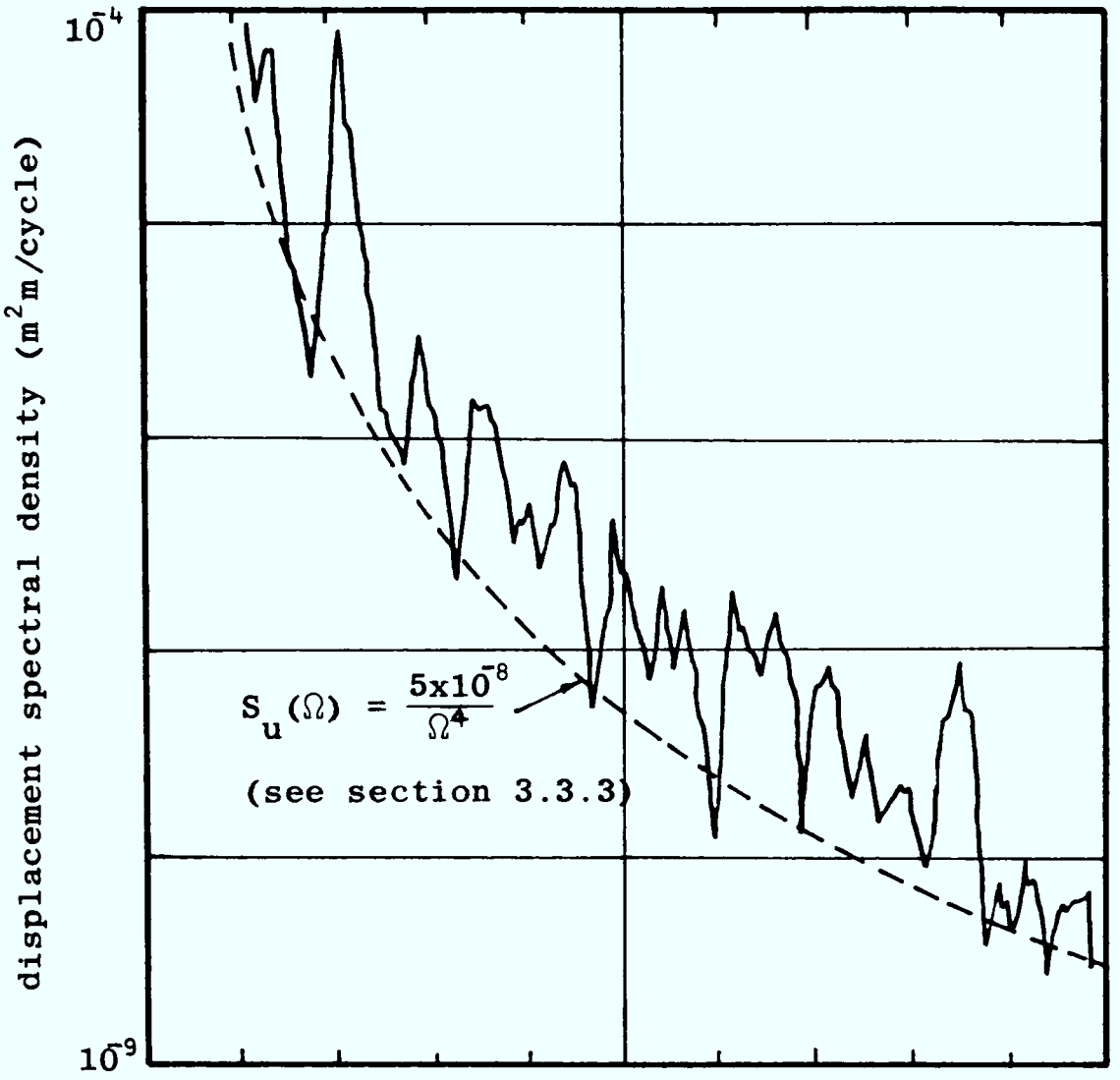

Fig 3.10 Spectral density describing vertical profile for arterial road at Ellington Colliery (4.10.83)

3.3 Description of track geometry

3.3.1 Format for presentation of data

Spectral densities can be used to describe the magnitudes of irregularities over a range of spatial frequencies, and are chosen as the format for presenting track geometry data in this work (see Fig 3.10). This method provides a convenient description of both the random and periodic irregularities that occur in a section of any track and, as a result, is used widely in the description of mainline railways (see ISO (4)). It should be noted that the spectral density, being a statistical quantity, cannot provide information about specific irregularities (such as a bad rail joint): it describes the average state of the track.

For a vehicle travelling at a constant speed, the spectral densities can be expressed in terms of temporal frequencies (see section 3.3.7), and may be used as inputs to the mathematical models (see section 2.5.4).

3.3.2 Data processing technique.

The equipment that is used to measure track irregularities has been described previously (see section 3.2.2), and provides data in the form of a chart recording of the variation of a particular irregularity over a length of track (see Appendix 3). To obtain the spectral density from this data, a sample from the recording is taken and a Fourier Transform Technique is used to process the sample. The spectral density obtained by this process is the "measured" spectral density, and is related to the spectral density describing the track irregularity by using equation (3.7). Each of the pieces of measuring equipment has an associated transfer function describing its frequency response, and these are used in this equation; the transfer functions are described in section 3.2.2. This method of processing the data is explained in detail below.

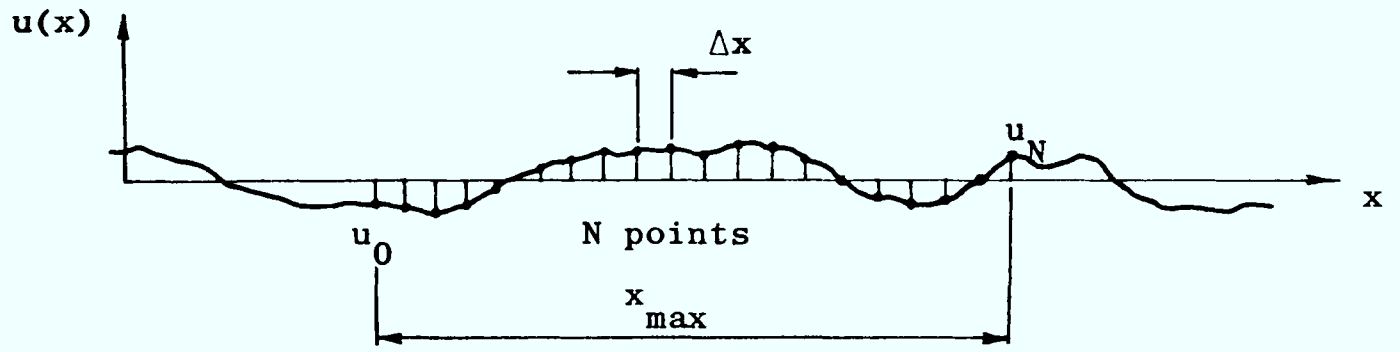

Fig 3.11 Sample of recording of track irregularity

Consider a sample taken from a recording of a track irregularity. The sample can be described approximately by a series of points as shown in Fig 3.11: in this example, the sample is described by N points equally spaced by a distance, Δx.

A discrete Fourier Transform (see Appendix 1) can be taken of the data when described in this manner, giving the result:

$$U_k = \frac{1}{N} \sum_{r=0}^{N-1} u_r \, e^{-j(2\pi kr/N)} \qquad (k = \text{any integer}) \qquad (3.25)$$

where,

U_k = Fourier coefficient

($U_k(\Omega)$ is located at the frequency, $\Omega = {}^{k}/_{N\Delta x}$)

The exponential term in equation (3.25) leads to two interesting characteristics which are described below. Firstly, the case when k = N + m (k and m = any integers),

$$e^{-j(2\pi r(N + m)/N)} = e^{-j2\pi r} \cdot e^{-j2\pi rm/N}$$

$$= e^{-j2\pi rm/N} \qquad (3.26)$$

indicates that equation (3.25) is periodic. Secondly, if the following cases are examined:

$$U_{\frac{N}{2} + m} = \frac{1}{N} \sum_{r=0}^{N-1} U_r (e^{-j\pi r} \cdot e^{-j\pi rm/N})$$

$$= \frac{1}{N} \sum_{r=0}^{N-1} U_r \, (-1)^r \cdot e^{-j\pi rm/N} \qquad (3.27)$$

$$U_{\frac{N}{2} - m} = \frac{1}{N} \sum_{r=0}^{N-1} U_r \, (e^{-j\pi r} \cdot e^{j\pi rm/N})$$

$$= \frac{1}{N} \sum_{r=0}^{N-1} U_r \, (-1)^r \cdot e^{j\pi rm/N} \qquad (3.28)$$

It can be seen that,

$$U_{\frac{N}{2} + m} = \overline{U}_{\frac{N}{2} - m} \qquad (3.29)$$

where,

$\overline{U}$ = complex conjugate of U.

These characteristics are features of the mathematics which are not reflected in the physical system: they act to limit the range of frequencies over which equation (3.25) may be applied.

The spectral density is determined from equation (3.25) using the expression,

$$S_m(\Omega) \simeq S_k = \frac{1}{\Delta\Omega} U_k \cdot \overline{U}_k \qquad (3.30)$$

where,

$S_m(\Omega)$ = spectral density of sample
S_k = discrete spectral density
$\Delta\Omega$ = frequency interval between Fourier coefficients

This is illustrated in Fig 3.12.

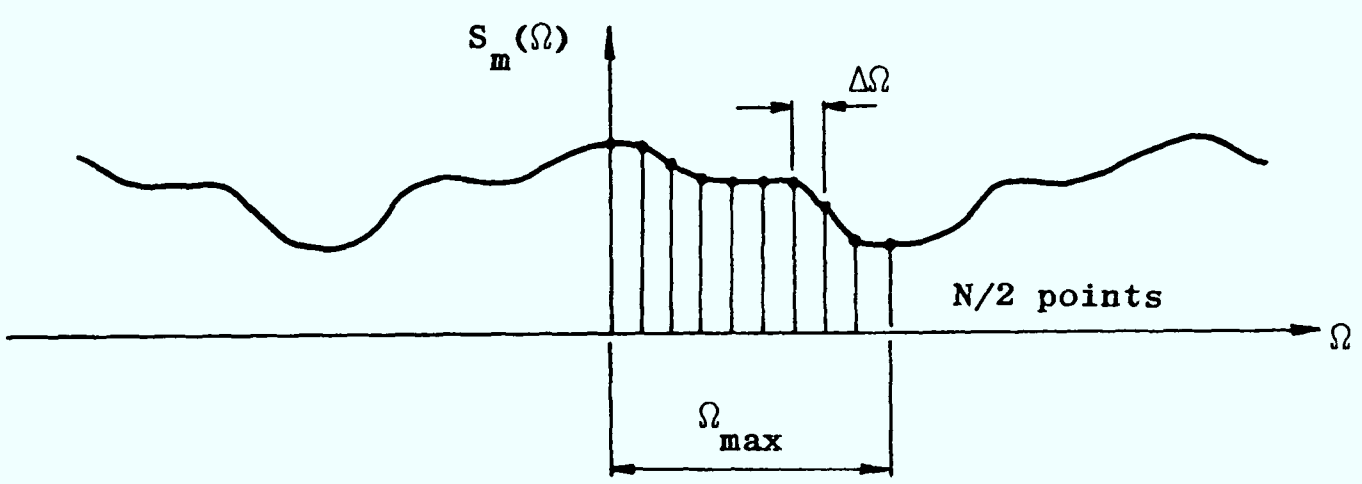

Fig 3.12 Spectral density of sample

The results of equations (3.26) and (3.29) act to limit the frequency range because the calculated spectral density will be symmetrical about a frequency, Ω_{max}. This is called the "Nyquist" or folding frequency. The following relationships can be used to describe the range over which results are valid:

N = number of points used to describe signal
Δ_x = spacing between points
x_{max} = $(N - 1)\,\Delta x \simeq N\Delta x$
= sample length
$\Delta\Omega \simeq 1/N\Delta x$
= frequency interval between Fourier coefficients

$$\Omega_{max} = (\frac{N}{2} - 1)\Delta\Omega \simeq 1/2\Delta x$$

$$= \text{maximum frequency that can be determined} \quad (3.31)$$

The fast Fourier Transform (or FFT) has been developed to solve equation (3.25), and can be implemented simply on a computer. The FFT treats the special case when $N = 2^n$ (n = positive integer), and splits the original sequence, U_r, into a series of single term sequences. Discrete Fourier Transforms (DFTs) of single term sequences equal the terms themselves (this is the case when N = 1 in equation (3.25)), and so are easily determined, and these can be combined to yield the Fourier coefficients of the original sequence. The FFT calculates the Fourier coefficients for the first half of the sequence, U_r, by this method, and then uses equation (3.29) to determine the remaining coefficients. A listing of the FFT computer program used in the work (see Newland (13)) is included in Appendix 1.

The result of equation (3.30), the "measured" spectral density, is processed using equation (3.7),

$$S_u(\Omega) = |{}^1/H_m(\Omega)|^2 \cdot S_m(\Omega)$$

where,

$$H_m(\Omega) = \text{transfer function of measuring device}$$

to give the spectral density, $S_u(\Omega)$, describing the track irregularity. The transfer functions for the measuring devices are given in equation (3.13) (cross-level), equation (3.17) (vertical profile), and equation (3.18) (lateral alignment).

The accuracy of the spectral density will depend upon the length of the sample and the spacing between the points. Clearly, if the spacing between the points is reduced, the discrete representation of the sample will improve, and so the frequency range that can be described is extended. If a long sample, or a series of shorter samples, is used the characteristics of the samples reflect those of the actual irregularity more closely. Successive sampling will only improve the accuracy of the representation if the statistical properties

describing the irregularity remain uniform along the length of the track. When this is the case the irregularity is said to be stationary.

3.3.3 Analytical expression of spectral densities

A great deal of work has been carried out in the characterisation of mainline railways (see ISO (4)), and on the basis of measured data the following general relationship is found to provide an adequate description of the track geometry:

$$S_u(\Omega) = {}^{A}/_{\Omega^n} \qquad (3.32)$$

where,

$S_u(\Omega)$ = spectral density describing irregularity (vertical profile, cross-level, lateral alignment, gauge)

A = roughness coefficient

n = integer exponent (2, 3 or 4)

Tests on a number of British mainline railways (see Pollard (18)) confirm this general relationship and suggest that, over a wide range of spatial frequencies, the variation of track geometry is such that $S_u(\Omega) \propto {}^{1}/_{\Omega^3}$. A more accurate description of the track is given in this work as being:

$$S_u(\Omega) = {}^{A}/_{\Omega^2} \text{ when } \Omega < \Omega_c$$
$$S_u(\Omega) = {}^{A\Omega_c^2}/_{\Omega^4} \text{ when } \Omega > \Omega_c$$

where,

Ω_c = break frequency (= 0.2 cyc/metre) (3.33)

The analytical expression shown in equation (3.32) will be used to describe the measured spectral densities determined in this work, and will be the basis of comparison of underground mining and mainline tracks in section 3.4.

3.3.4 Cross-level

In this section the spectral densities describing cross-level are presented for two sections of underground track, one being a recently laid track designed for high speed travel, and the other a track of inferior quality. These examples were chosen in order to illustrate the range over which track quality varies.

The chart recordings, which are included in Appendix 3, were processed using the technique described in section 3.3.2. In each case a single sample was taken, and the details of the sampling are shown below:

$$\begin{aligned} N &= 256 \\ \Delta x &= 0.36 \text{ metres} \\ x_{max} &= 92 \text{ metres} \\ \Delta\Omega &= 0.011 \text{ cyc/metre} \\ \Omega_{max} &= 1.39 \text{ cyc/metre} \end{aligned} \qquad (3.34)$$

The spectral densities describing the cross-level for both sections of track are shown in Fig 3.13. It can be seen that equation (3.32) can be used to describe the cross-level and, in particular,

$$S_u(\Omega) = A/\Omega^2 \qquad (3.35)$$

The roughness coefficient, A varies from 3×10^{-8} m^2cyc/m for the newly laid track to 2×10^{-7} m^2cyc/m for the inferior quality track. The magnitude of the cross-level is thus 2.6 ($\sqrt{6.7}$) times bigger for the inferior track.

3.3.5 Vertical profile

The spectral density describing vertical profile is presented in Fig 3.14 for the recently laid track introduced in section 3.3.4. The chart recordings, which are included in Appendix 3, were processed using the technique described in section 3.3.2, and the details of the sampling are given in equation (3.34).

The spectral density presented in this figure can be described using equation (3.32), and in particular,

$$S_u(\Omega) = A/\Omega^4 \qquad (3.36)$$

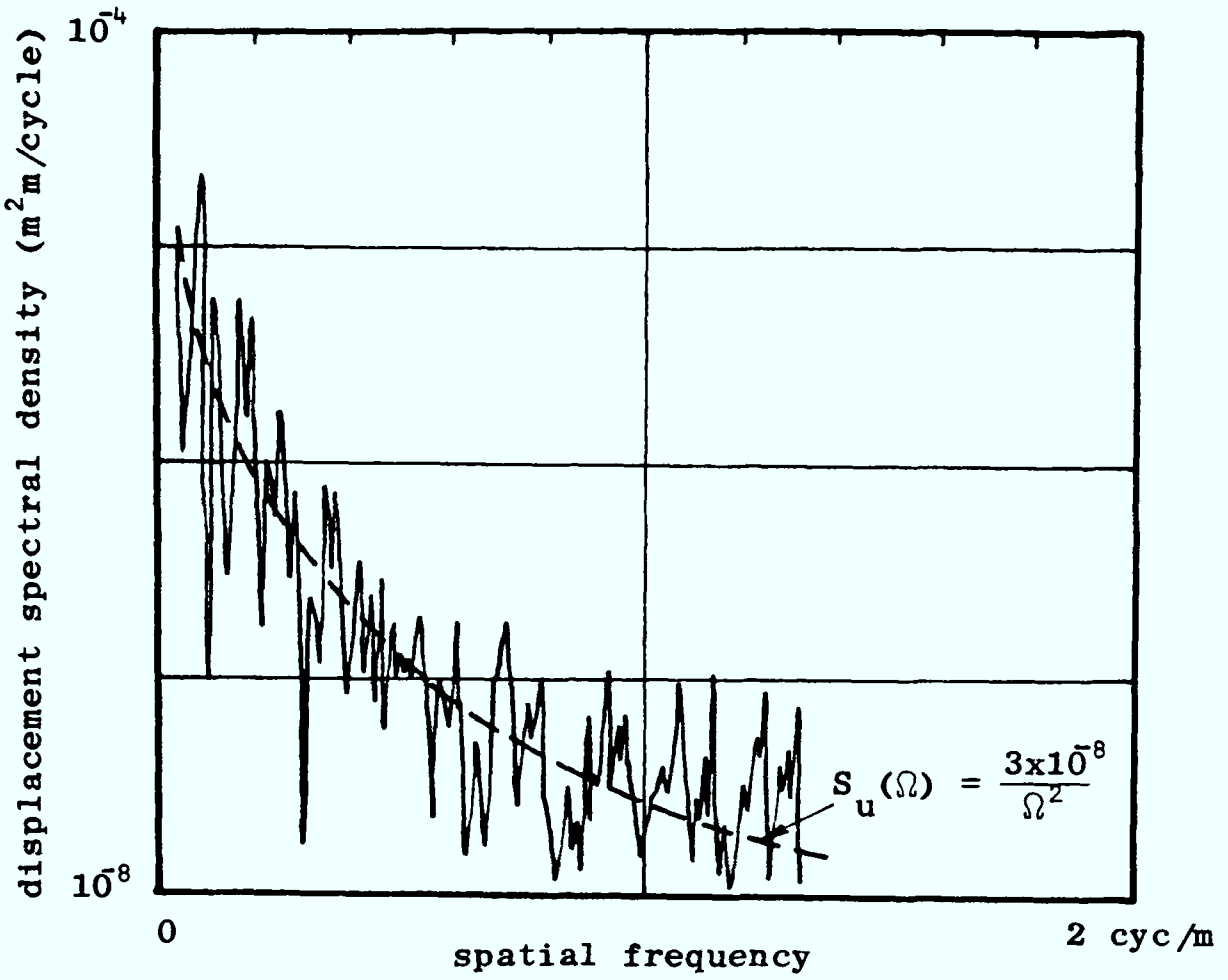

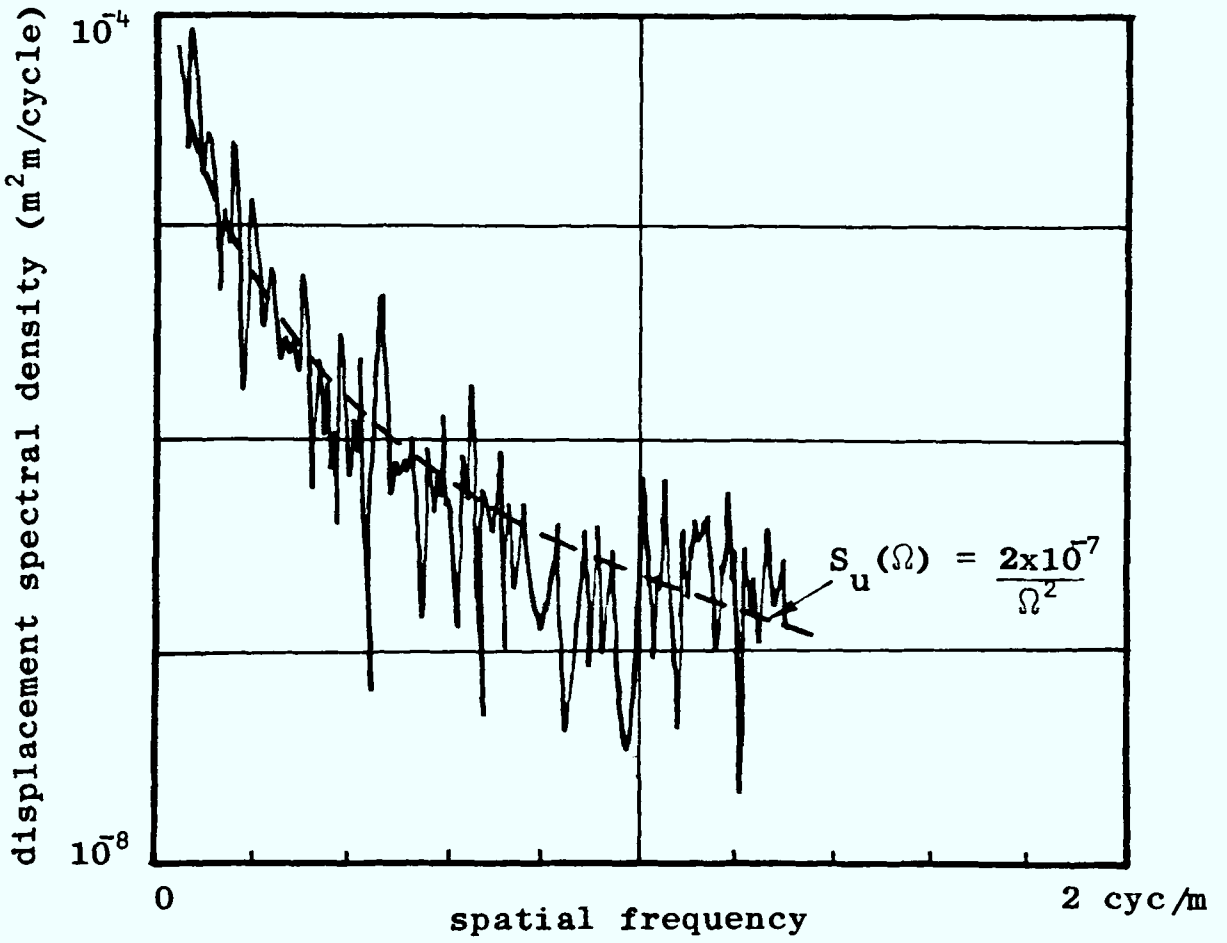

Fig 3.13 Spectral densities describing cross-level for the following railways:
(a) Abdy seam at Blidworth Colliery (3.8.82)
(b) Drift road at Shireoaks Colliery (23.6.83)

The spectral density for a track laid in concrete, as determined by the "inertial" technique described in section 3.2.3, is shown in Fig 3.10, and this may also be described by equation (3.36). The roughness coefficient, A, is 2 x 10^{-8} $m^2 cyc^3/m^3$ for the newly laid track, and 5 x 10^{-8} $m^2 cyc^3/m^3$ for the track laid in concrete.

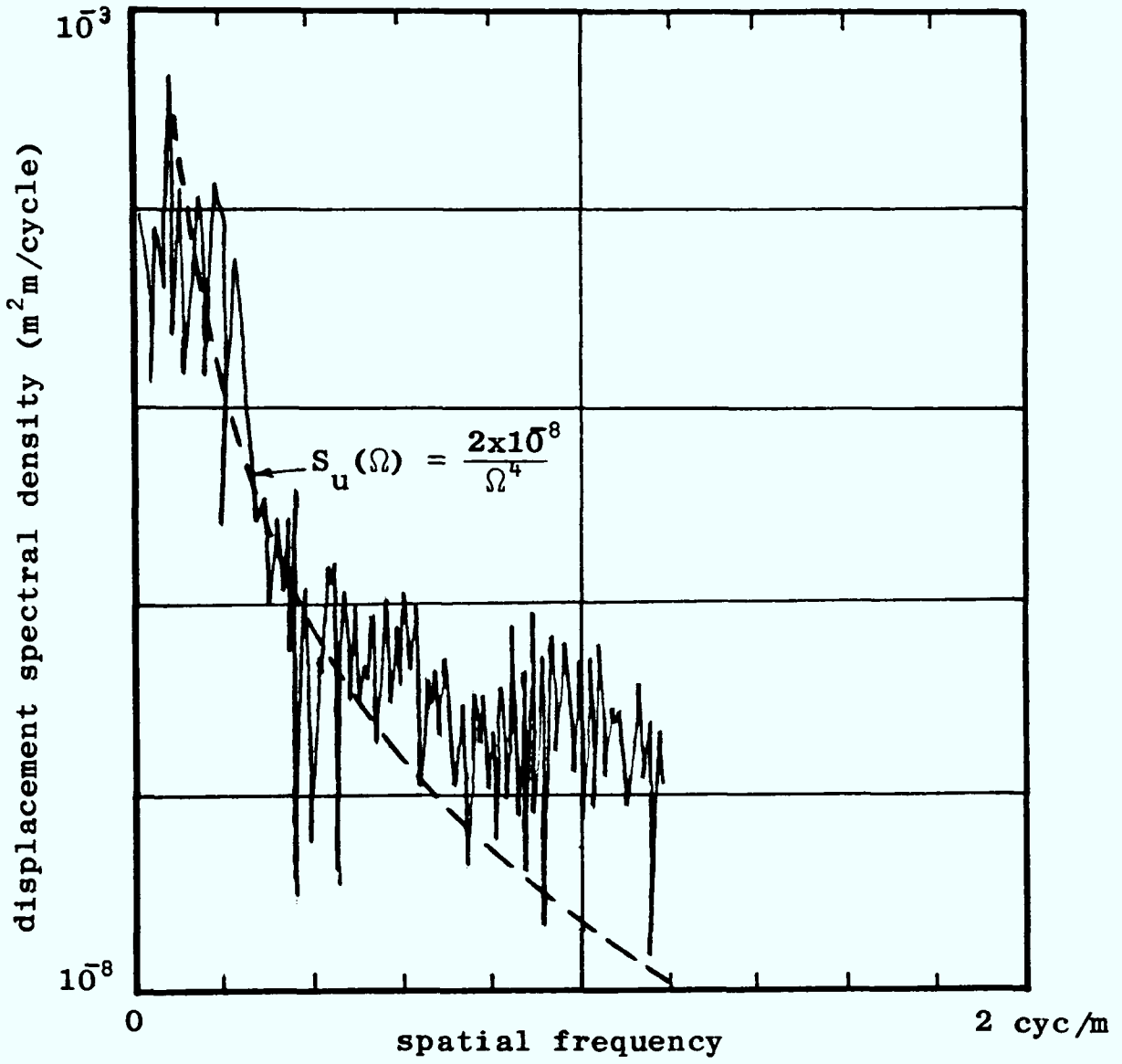

Fig 3.14 Spectral density describing vertical profile for railway in Abdy seam at Blidworth Colliery (3.8.82)

3.3.6 Lateral alignment

The equipment for measuring lateral alignment is being developed and, as yet, no measurements of underground track have been taken. In this work the spectral densities will be treated in a similar manner to cross-level (ie $S_u(\Omega) = A/\Omega^2$) and estimates for the roughness coefficient will be used (see section 3.4).

3.3.7 Application of data for mathematical modelling

Spectral densities have been determined by taking measurements of underground railways (see Figs 3.10, 3.13 and 3.14), and these describe the track geometry over a range of spatial frequencies. The spectral densities can also be described in terms of temporal frequencies with respect to a vehicle moving along the track at constant speed, and in this form they are suitable to use as inputs to the mathematical models (see section 2.5.4). If the vehicle is travelling along at a speed, V, then,

$$S_u(f) = \frac{1}{V} S_u(\Omega)$$

$$= \frac{1}{V} S_u(\frac{f}{V}) \qquad (3.37)$$

where,

$f = V\Omega$ = temporal frequency

Ω = spatial frequency

Using the analytical expression proposed in equation (3.32), this may be re-written as:

$$S_u(f) = \frac{AV^{n-1}}{f^n} \qquad (3.38)$$

where,

A = roughness coefficient

n = integer exponent (2, 3, or 4)

This expression of the spectral density can be used directly in equations (2.62) and (2.63) to yield the response of the vehicle.

3.4 Comparison of mining and mainline railways

The geometry of mainline track is described using spectral densities by many railway administrations and results are well documented. It has already been shown in section 3.3.3 how an analytical expression may be applied in the description of measured data and this provides a convenient way of comparing mining and mainline railways.

If equation (3.32) is used in the form,

$$S_u(\Omega) = A/\Omega^3 \qquad (3.39)$$

the values of the roughess coefficient, A, form a basis of comparison.

British Rail has carried out measurements on many sections of track in connection with the "Advanced Passenger Train" project (see Pollard (18)), and the results obtained for five sections of jointed track are used to present typical values of the roughness coefficient. These values are compared with those obtained for a newly laid section of track in a coal mine (see Figs 3.13 and 3.14) in Table 3.1.

	Roughness coefficient, A ($m^2 cyc^2/m^2$)		
	Vertical profile	Lateral alignment	Cross-level
BR jointed track	12×10^{-9}	4×10^{-9}	7×10^{-9}
Newly laid NCB track	3×10^{-8}	5×10^{-6} (estimate)	5×10^{-8}

Table 3.1 Comparison of mining and mainline railways

The comparison shows that the magnitudes of vertical profile are similar, but the amount of cross-level is considerably greater for track in coal mines (the lateral alignment is discussed later in this section).

Pollard's results also show a close similarity in the shape of cross-level and lateral alignment spectral densities, which indicate that the ways in which these irregularities come into existence are closely related. These features are explained below.

Consider the effects of vertical and lateral loading by a train travelling along a section of track. Vertical loads act to compress the ballast (see Fig 3.15 (a)), and lateral loads cause the track to move sideways and rotate slightly about a longitudinal (x) axis (see Fig 3.15 (b)). This latter point immediately establishes the basis of a relationship between lateral alignment and cross-level. Ideally the original position of the track is restored after the

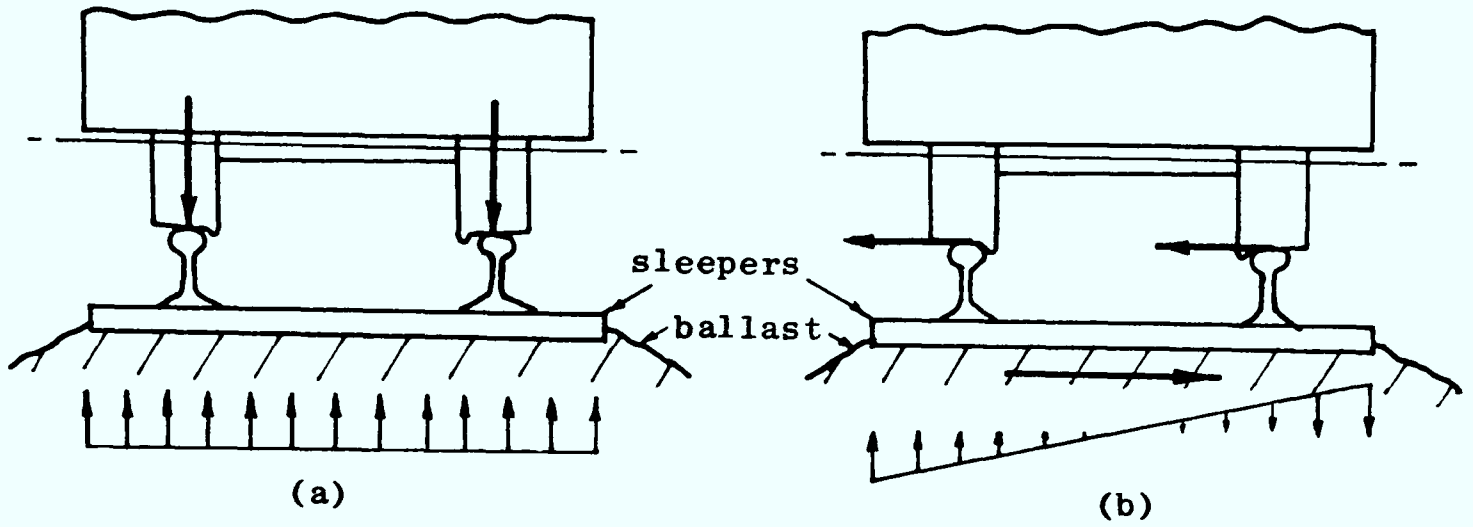

Fig 3.15 Loading of track by a vehicle

train passes, however, some residual displacement is inevitable, and this leads to track irregularities. It is clear from the above discussion that the magnitudes of irregularities reflect the manner in which the track is loaded and the quality of the bed upon which it is laid.

In the case of mining railways the main traffic will be trains made up of minecars (as shown in Fig 1.4) carrying materials and coal. The wheels of these minecars revolve independently on fixed axles and so rely upon the gravitational stiffness force associated with the flanges touching the rails to provide guidance (see section 2.32). When this occurs the magnitude of the lateral loading of the track is comparable with the vertical loading. Mainline railways, however, are used by trains fitted with conventional wheelsets and the magnitude of lateral loading is significantly less than the vertical loading. On the basis of the model shown in Fig 3.15 it is clear that the lateral alignment and cross-level will both be larger for railways in coal mines.

The roughness coefficient for track lateral alignment in Table 3.1 is estimated on the basis of a decision to treat lateral alignment irregularities as being ten times larger than cross-level irregularities. This decision, although based on the previous discussion, is quite arbitrary and should be confirmed with measured data when suitable track monitoring equipment is available.

Chapter 4

Acceptability Criteria

4.1 Introduction

In the preceding chapters a mathematical modelling technique has been developed which can be used to predict the motion of a rail vehicle. In order to exploit this technique for use in the design of vehicles for high speed operation, and to determine the suitability of the track, it is necessary to introduce criteria which relate to the ride and the likelihood of derailment.

There are no established ways of assessing the ride of vehicles used in British coal mines, and only informal guidelines exist to assess derailment (see section 4.3.8). In this chapter criteria are proposed which are based on quantities that can be evaluated using the mathematical models. Suitable acceptability limits are established and the methods of comparing these limits with the outcome of the modelling is explained. The ride is discussed in section 4.2 and this represents the more stringent of the two criteria for judging the suitability of vehicle behaviour. Derailment is discussed in section 4.3.

4.2 Ride criteria

4.2.1 General considerations

The way in which a person perceives the ride of a vehicle is affected by many factors, such as the levels of vibration, the noise and the general environmental conditions. The physiological response is difficult to quantify, and so any technique developed to assess it can only provide general guidelines. In this work the problem is simplified with a decision to consider vibrations as the primary factor influencing physiological response, and this can either be measured directly or evaluated using the mathematical models. The response to this vibration is assessed on the basis of data gathered from various field and laboratory tests (see ISO (19)).

4.2.2 Physiological response to vibration

A convenient measure of the physiological response to a known level of vibration is the duration of time that can be tolerated without ill effect and this may be evaluated on the basis of such things as

the reduction in comfort, the onset of fatigue or the impairment of health. It is clear that each of these conditions is open to interpretation. However the ambiguity can be removed if a large sample of individual responses is considered. This statistical approach ultimately provides general guidelines for allowable exposure times to vibration.

An international standard (see ISO (19)) has been established on this basis wherein limiting daily exposure times are proposed for vibration over a range of frequencies from 1 Hz to 80 Hz. Measured data from various unattributed field and laboratory tests have been gathered together and averaged to establish limits for preserving comfort, working efficiency and health. The volume of data, the experimental techniques, and the methods used to average are all unspecified in the standard, and this should be taken into account when the standard is used in any specific application.

The vibration is described in terms of rms accelerations measured over third octave bands, and these are considered to occur either along a longitudinal axis through the buttocks and head of a man travelling in a vehicle (z axis), or in a plane which is transverse to this axis (xy plane) (the co-ordinate system is shown in Fig 2.1). The limiting daily exposure times for the conservation of working efficiency are shown in Fig 4.1 on the basis of this description.

The decision to specify amplitude in terms of rms accelerations allows a relatively simple treatment of broad-band vibration, as rms accelerations can be evaluated directly from the spectral density. This is done by taking the square root of equation (2.64):

$$a_{rms} = \sqrt{S_{\ddot{q}}(f)\ \Delta f} \qquad (4.1)$$

where,

a_{rms} = rms acceleration
$S_{\ddot{q}}(f)$ = acceleration spectral density
Δf = frequency band (third octave)

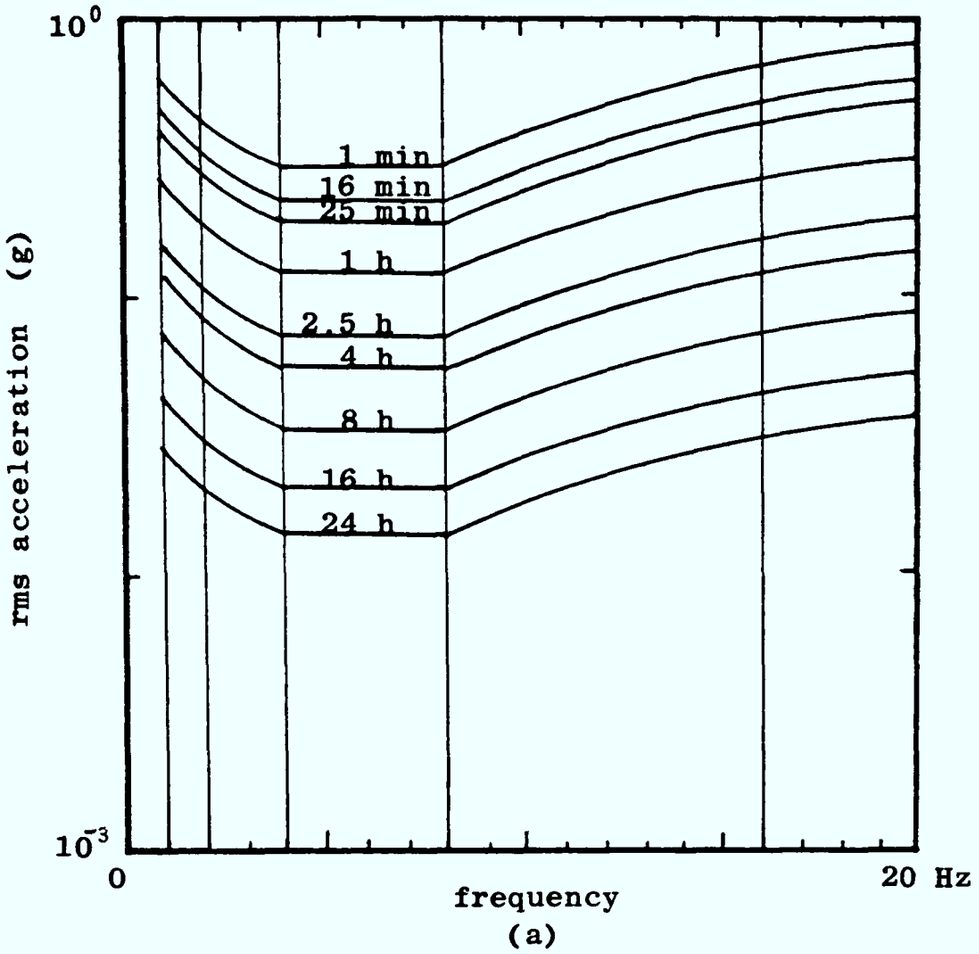

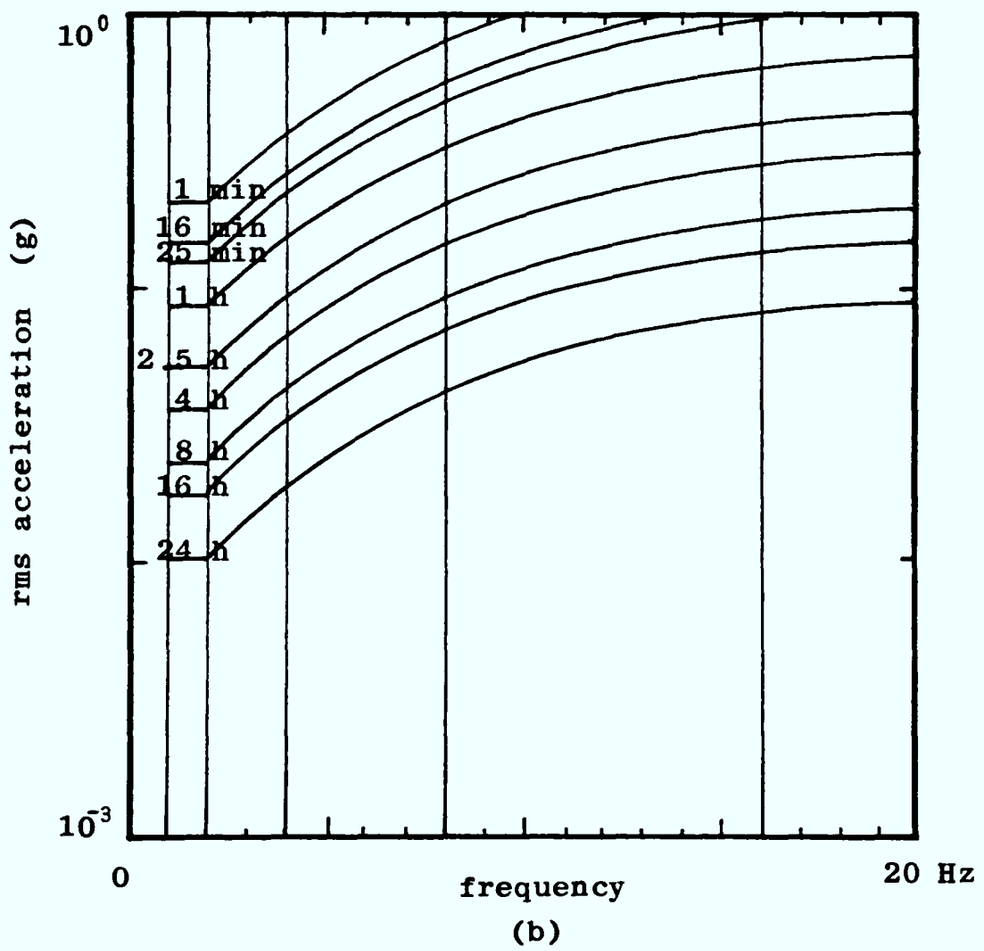

Fig 4.1 Permissible acceleration limits for the preservation of working efficiency (see ISO (19))
(a) Longitudinal (z) direction
(b) Transverse (xy) direction

The exposure limits are based on sinusoidal oscillation, and so in cases in which the ratio of peak to rms accelerations is large the standard cannot be considered to be applicable.

This standard takes no account of any factors other than vibration, and is derived from experimental data which have been obtained in environments which are different from coal mines. Despite these limitations, it provides a useful general guide to the physiological response to ride and will be used in this work.

4.2.3 Ride criterion for railways in coal mines

The acceptability of the ride of trains operating along underground railways is assessed on the basis of permitted times of exposure to vibration. The acceptance levels are the ISO guidelines for the preservation of working efficiency (see section 4.2.2), and these are determined for two specific conditions: the ride as perceived by a coal face worker and the ride as perceived by a driver.

A face worker rarely travels the entire journey from the pit bottom to his place of work in a single manriding train: he will usually travel along an arterial road by train, and then continue along subsidiary roads by foot, manriding conveyor, or in cars hauled by rope. The journey itself rarely takes longer than about twenty minutes, however, he will be subject to additional vibration and noise during his shift which will effectively increase his daily exposure. The ride of the manriding trains should not cause a loss in efficiency due to fatigue, and so a slightly conservative limit of one hour exposure is proposed. This choice can be revised in the light of more detailed knoweldge as it becomes available.

A driver will generally operate both manriding and materials haulage trains and, as a result, will be exposed to vibration for a large proportion of his shift. It is crucial from a point of view of safety that a driver does not become fatigued, and so a fairly stringent limit of four hours exposure is proposed. Clearly the operating speed, and even the locomotive being driven, is unlikely to remain the same throughout the shift. This exposure limit should, however, only be increased after careful consideration.

4.2.4 Application of ride criterion

The way in which the criterion can be applied to determine the acceptability of the ride is illustrated here using the model of a two axle vehicle introduced in section 2.4.2. The model may be used to predict the response of the vehicle to changes in track vertical profile, and the equations of motion can be solved to give the transfer function of the vehicle (see section 2.5.2).

The track profile can be described with respect to the moving vehicle using equation (3.38),

$$S_u(f) = \frac{AV^{n-1}}{f^n}$$

where,

$S_u(f)$ = spectral density describing track input
A = roughness coefficient
n = integer component (n = 4 for vertical profile (see section 3.3.5))

The acceleration spectral density that describes the response of the vehicle is then determined using equation (2.63),

$$S_{\ddot{q}}(f) = |H(f)|^2 \omega^4 S_u(f)$$

where,

$H(f)$ = transfer function (see Fig 2.14)
$S_{\ddot{q}}(f)$ = acceleration spectral density

The rms accelerations, in third octave bands, are obtained using equation (4.1),

$$a_{rms} = \sqrt{S_{\ddot{q}}(f)\ \Delta f}$$

where,

Δf = third octave band

The result of this process is a plot of rms accelerations over a band of frequencies (Fig 2.18 (b)) which is shown, with the exposure

limits superimposed, in Fig 4.2.

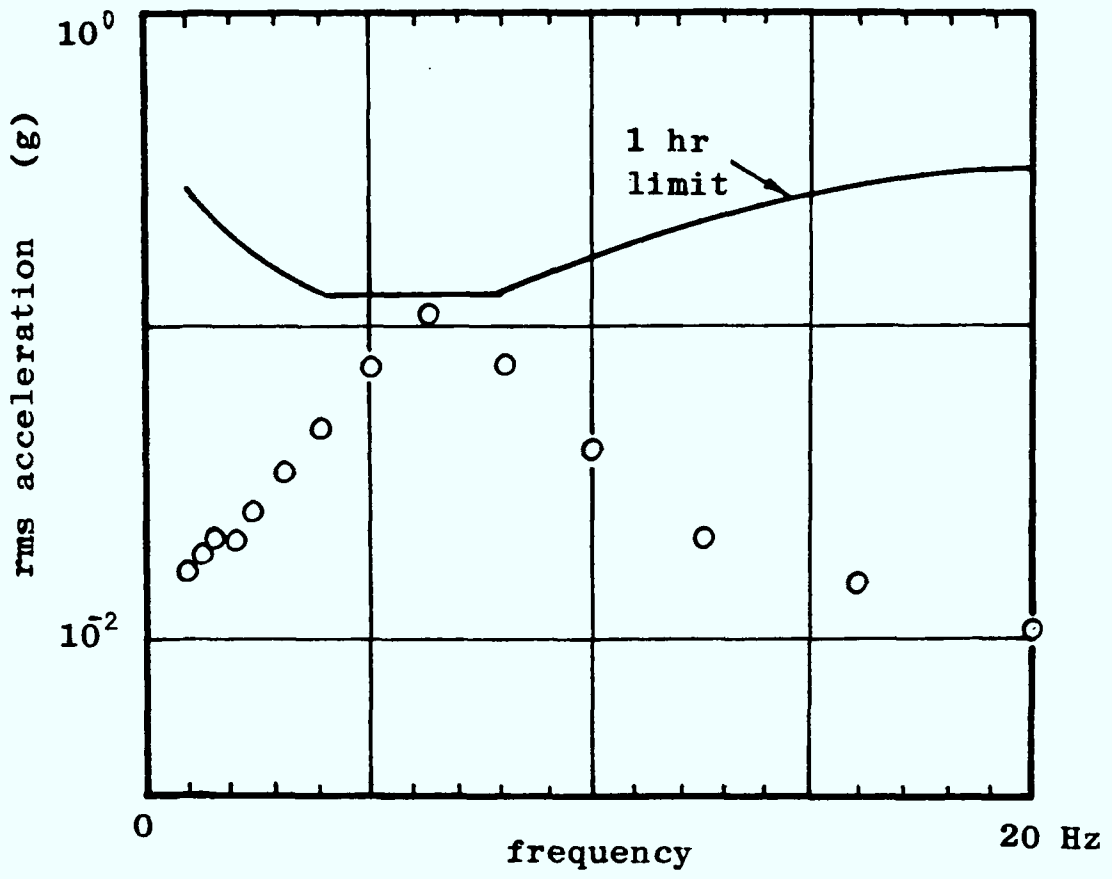

Fig 4.2 Rms accelerations at front of two axle vehicle travelling at 15 mph.

The ride of this vehicle is acceptable when travelling along this particular section of track.

4.2.5 Ride of a suspensionless vehicle

There are many vehicles operating in coal mines that have little or no suspension and here the ride is a direct reflection of the state of the track. The effects of lateral alignment and cross-level irregularities on ride will be closely dependent on the interaction of the wheels and rails and this is discussed in Chapter 5. The ride of a suspensionless vehicle can be described approximately without considering vehicle characteristics.

Equations (3.38), (2.63) and (4.1) (see section 4.2.3) combine to yield and expression of the rms accelerations:

$$a_{rms} = \sqrt{(2\pi)^4 \, AV^3 \, \Delta f} \qquad (4.2)$$

where,

A = roughness coefficient

V = forward speed

Δf = third octave band

This equation is solved for a range of frequencies from 1 to 20 Hz, and the solutions are shown in Fig 4.3.

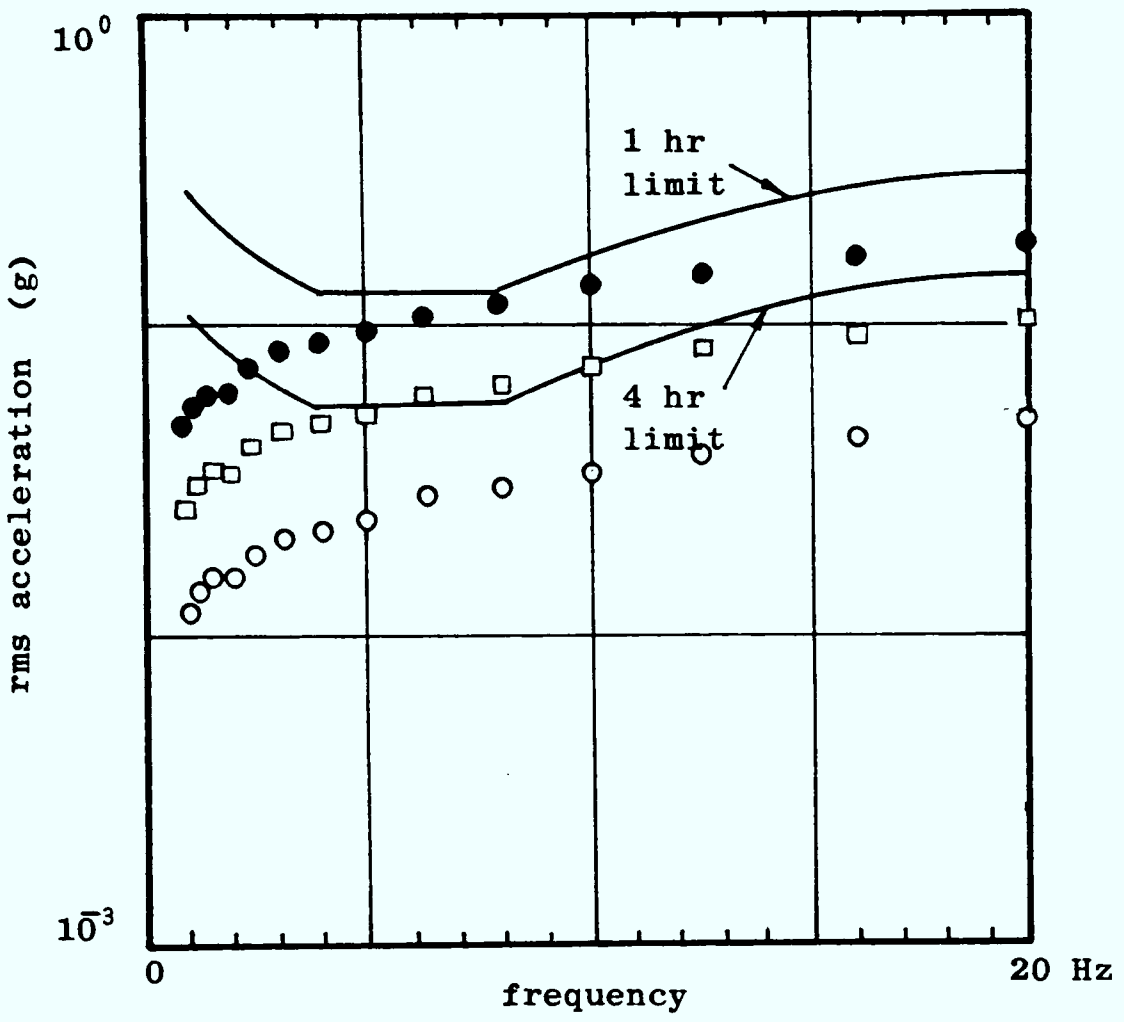

Fig 4.3 Rms accelerations for a suspensionless vehicle travelling along track of different standards

○ A = 5 x 10^{-8} $m^2 cyc^3/m^3$ (speed = 15 mph)
□ A = 5 x 10^{-8} $m^2 cyc^3/m^3$ (speed = 25 mph)
● A = 2 x 10^{-7} $m^2 cyc^3/m^3$ (speed = 15 mph)

The results indicate that the ride of a suspensionless vehicle is satisfactory when it travels along track of a reasonable standard ($A = 5 \times 10^{-8}$ $m^2 cyc^3/m^3$: see section 3.3.5). On inferior track the ride becomes unacceptable for the driver.

4.2.6 Ride of a two axle locomotive

The two axle locomotive is not of prime concern in this work, but it is interesting to consider because of its unusual geometry. The vehicle has a short wheelbase and a long overhang and, as a result, pitching motion of large amplitude is the most significant mode of vibration affecting the driver.

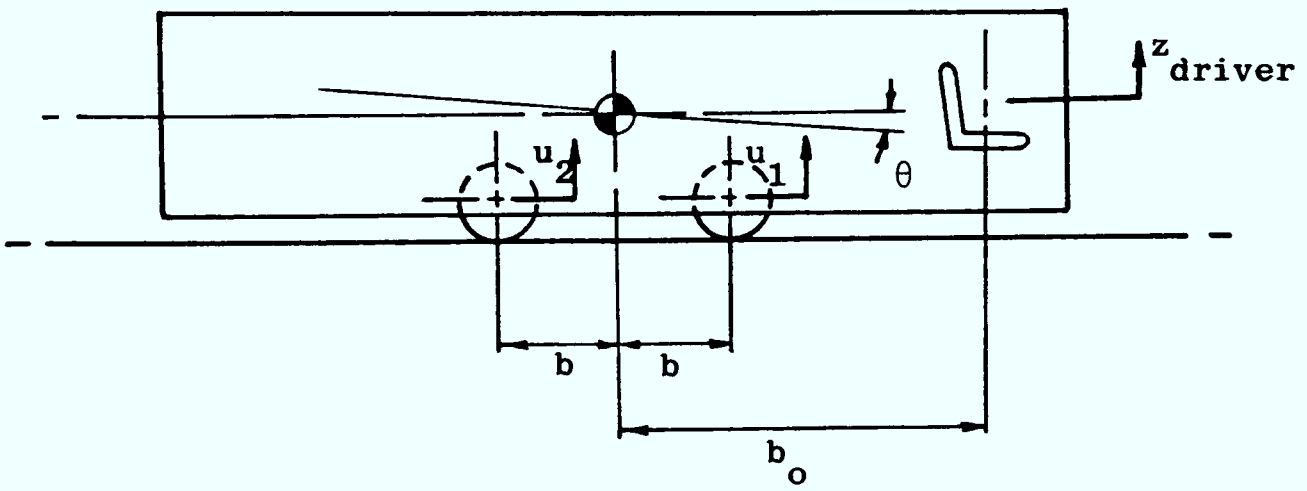

Fig 4.4 Two axle locomotive

If the effect of primary suspension is neglected, the motion of the driver due to the pitching of the locomotive will be:

$$z_{driver} = \frac{b_o}{2b}(u_2 - u_1) \qquad (4.3)$$

By using Laplace transforms and substituting $j\omega$ for the differential operator, s, equation (4.3) may be rewritten in the form:

$$z_{driver} = \frac{b_o}{2b}(e^{-j2b\omega/V} - 1)u_1 \qquad (4.4)$$

Which can be rearranged further to yield:

$$\left| \frac{z_{driver}}{u_1} \right| = |H_d(\omega)| = \frac{b_o}{b}(1 - \cos\frac{2b}{V}\omega) \qquad (4.5)$$

where,

$H_d(\omega)$ = transfer function of the driver

For a typical two axle locomotive,

$$b = 0.6$$
$$b_o = 2.26 \text{ m}$$
$$V = 15 \text{ mph } (6.7 \text{ m/s})$$

Equation (4.5) becomes:

$$|H_d(\omega)| = 3.8 \, (1 - \cos \, (0.36 \, \pi f)) \qquad (4.6)$$

Equation (4.6) combines with equations (2.63) and (4.1) (see section 4.2.4) to give the results shown in Fig 4.5.

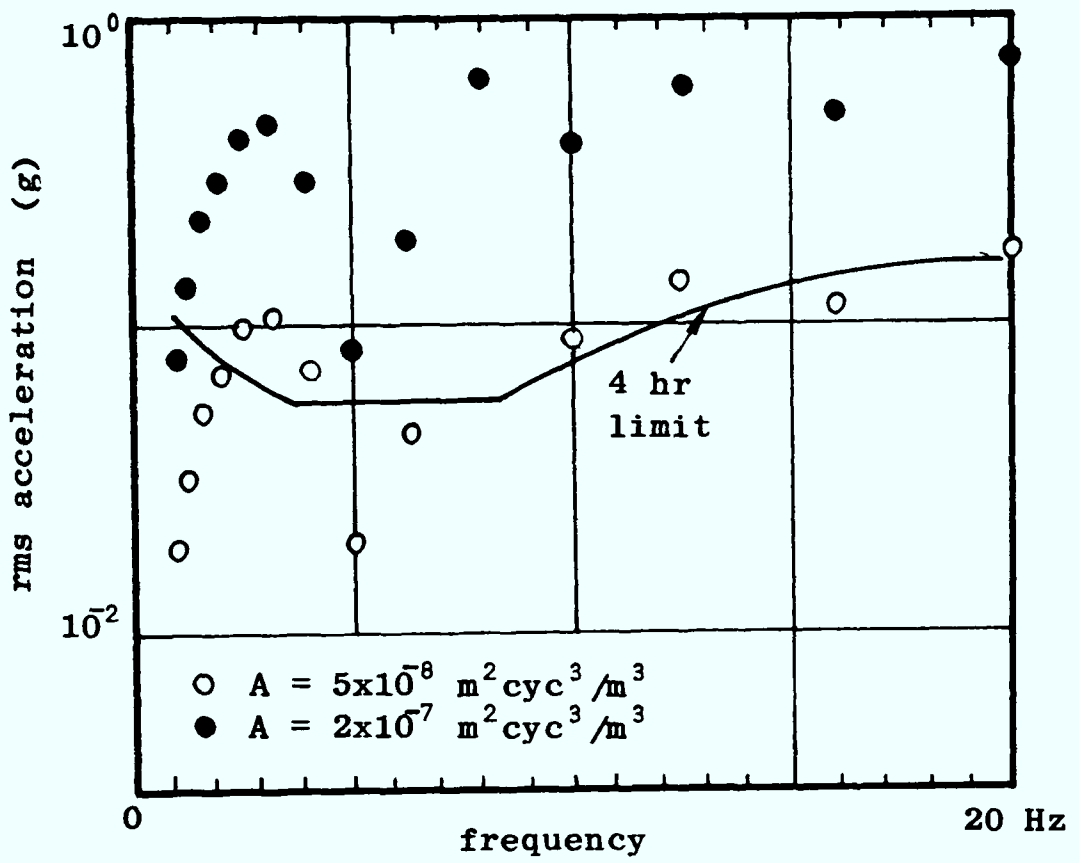

Fig 4.5 Rms accelerations at driver's position for suspensionless locomotive travelling at a speed of 15 mph. (Dimensions of locomotive are the same as the dimensions of a Hunslet 90 hp diesel locomotive).

It is clear that for this type of locomotive the ride is unacceptable in the absence of adequate suspension. This is the case even when travelling along track of a reasonable standard.

The effect of the suspension is examined in section 8.6.

4.3 Derailment criteria

4.3.1 Modes of derailment

When any of the wheels of a vehicle loses contact with the rails, the vehicle is likely to leave the track. If the flange of a wheel moves laterally beyond the rail the derailment is known as "wheel climb" (see Fig 4.6 (a)), and if it moves vertically above the rail it is known as "wheel lift" (see Fig 4.6 (b)).

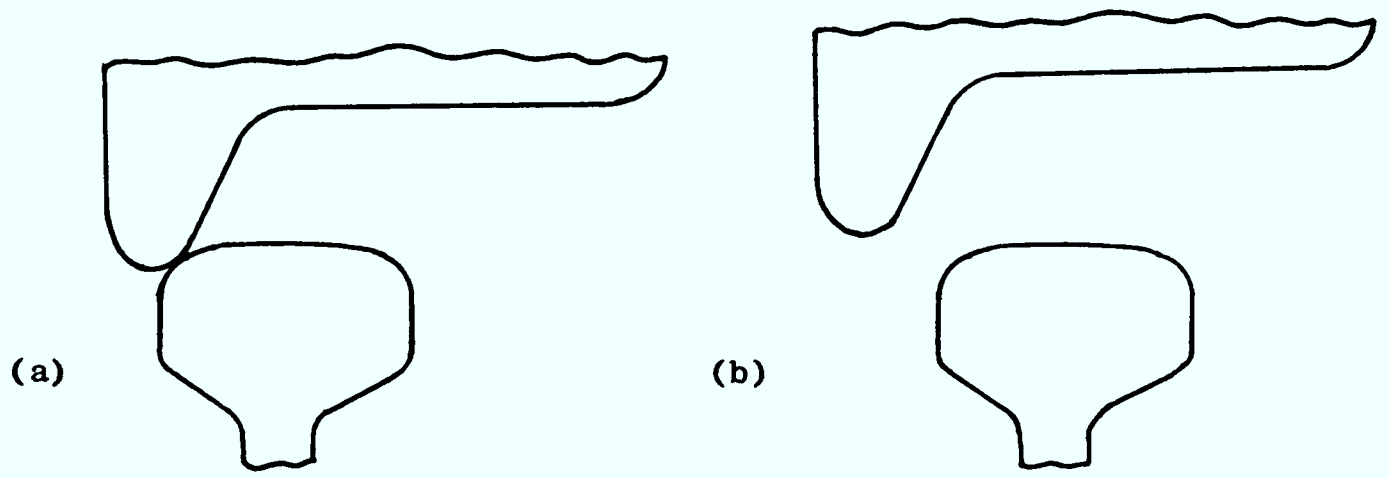

Fig 4.6 Modes of derailment

(a) wheel climb

(b) wheel lift

In addition to these modes, derailment can also occur due to sudden failure of either the track or the vehicle. This last mode of derailment is not considered in this work.

4.3.2 Wheel climb resulting from steady lateral force

When a wheel is subject to a lateral force the flange moves towards the rail. If the load is large enough the flange presses against the rail, contact at the tread is lost, and the wheel begins to "climb". In this situation the probability of derailment is high. The forces acting at the point of contact will be as shown in Fig 4.7.

The occurence of wheel climb is clearly dependent on the relative magnitudes of the lateral and vertical forces. The limiting case, when a derailment is imminent, can be evaluated on the basis of the forces shown in Fig 4.7. This leads to the result:

$$\begin{aligned} Q &= N\sin\delta - T_y\cos\delta \\ P &= N\cos\delta + T_y\sin\delta \end{aligned} \qquad (4.7)$$

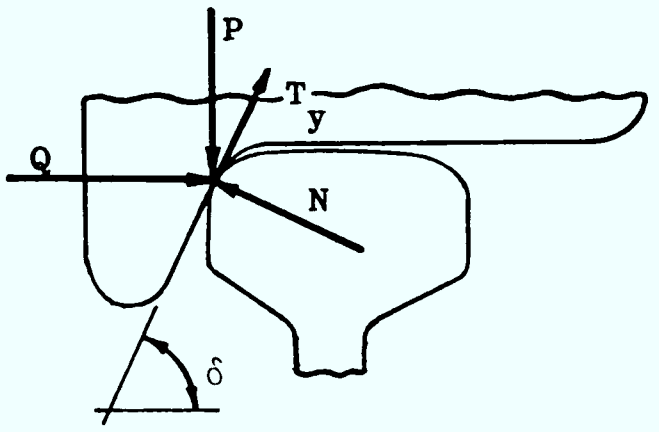

Q = applied lateral force
P = wheel load
N = normal force at contact point
T_y = lateral creep force

Fig 4.7 Forces acting at point of contact during flange contact

The lateral creep force, T_y, will be related to the creep of the wheel over the rail which, for a displaced pair of wheels, is given by equation (2.20) (see section 2.3.4). This equation can be simplified by ignoring the term dealing with the lateral velocity of the axle, leading to the result:

$$\gamma_y = -\psi \qquad (4.8)$$

where,

ψ = angle of attack.

The relationship between lateral creep force and angle of attack in the absence of longitudinal creep is shown in Fig 4.8.

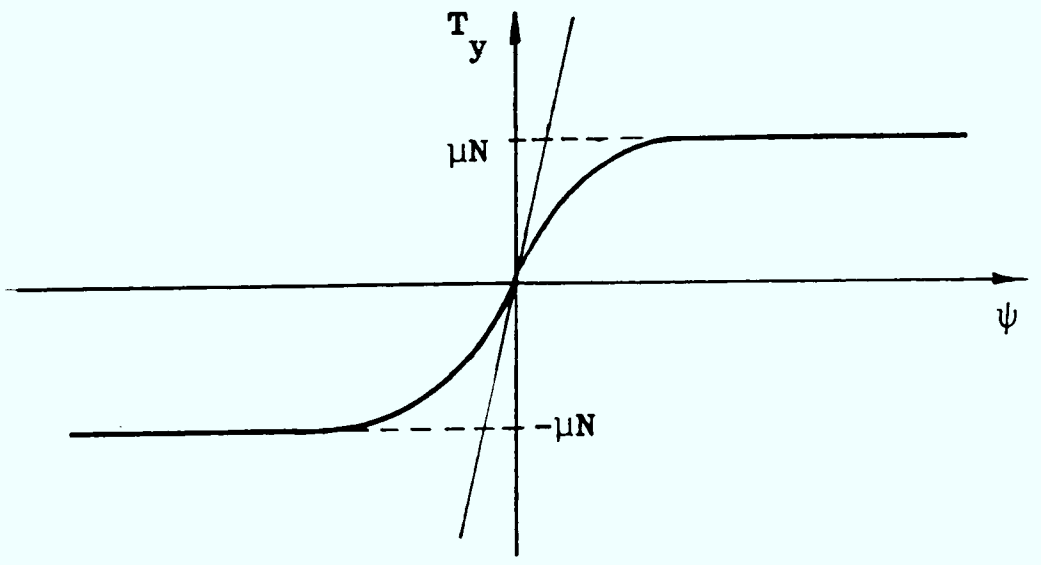

Fig 4.8 Relationship between lateral creep force and angle of attack (zero longitudinal creep)

This relationship indicates a limiting value for the creep force for all but very small angles of attack. This relationship may be simplified by using the model shown in Fig 4.9.

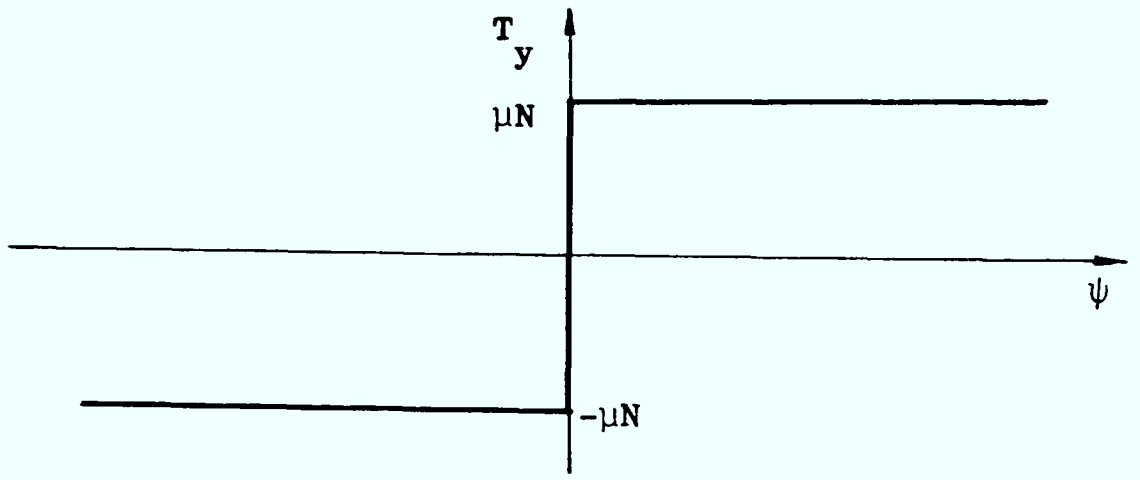

Fig 4.9 Simple model of relationship between lateral creep and angle of attack (zero longitudinal creep)

Equation (4.7) can now be rewritten in terms of the normal force, N, and the coefficient of friction, μ.

For positive angles of attack:

$$Q = N\sin\delta - \mu N\cos\delta$$
$$P = N\cos\delta + \mu N\sin\delta \qquad (4.9)$$

For negative angles of attack:

$$Q = N\sin\delta + \mu N\cos\delta$$
$$P = N\cos\delta - \mu N\sin\delta \qquad (4.10)$$

These equations can be rearranged to yield the result:

$$\frac{Q}{P} = \frac{\tan\delta \mp \mu}{1 \pm \mu\tan\delta} = \tan(\delta \mp \lambda) \qquad (4.11)$$

where,

$\mp$ indicates positive and negative angles of attack

$\lambda = \tan\mu$

This equation was first derived in 1896 and is known as the Nadal derailment ratio (see Nadal (20)). In the original derivation the creep of the wheel on the rail was not considered and the tangential force, T_y, was treated as being due to sliding friction. This

decision results in an identical model of the tangential force as shown in Fig 4.9. If a more precise model of the force is used, such as Kalker's "exact" theory of rolling contact (see section 2.3.3), the ratio is modified for very small angles of attack (see Gilchrist and Brickle (21)). However, the difficulties in providing representative values for the quantities used in such a model make it difficult to use in general application.

The ratio provides a value for imminent derailment: if the ratio of applied lateral force to wheel load exceeds this value a derailment is considered likely. It should be noted that the ratio is highly dependent on the coefficient of friction and this varies widely in different operating environments. It can also be seen that when the wheel creeps longitudinally, during braking for instance, the limiting value of lateral creep force (as shown in Fig 4.9) will be reduced for a wheel with a positive angle of attack, and so the likelihood of derailment is decreased. On this basis, and on the basis of the mechanism of guidance described in section 2.3.4, it becomes evident that a conventional wheelset is less likely to derail than a pair of wheels that revolve freely on an axle.

The validity of Nadal's ratio in predicting derailment has been tested by the Japanese National Railways (JNR) in a series of experiments with scale models of wheelsets (see Matsui (22)), and the results of the tests are reproduced in Fig 4.10.

It is clear that the ratio may be used to predict derailment for angles of attack greater than 1^{o}, although it is somewhat conservative when the angle of attack approaches zero. When the angle of attack is zero the lateral creep force will also be zero (see Fig 4.8), and so equation (4.11) becomes:

$$\frac{Q}{P} = \tan \delta \qquad (4.12)$$

This relationship is confirmed by the JNR test results.

When applied to full scale wheelsets the Nadal derailment ratio will be applicable for a wider range of angles of attack. This is because the creep coefficient is larger, and so the model shown in Fig 4.9 is more representative of the relationship between creep force and angle of attack (see Fig 4.8).

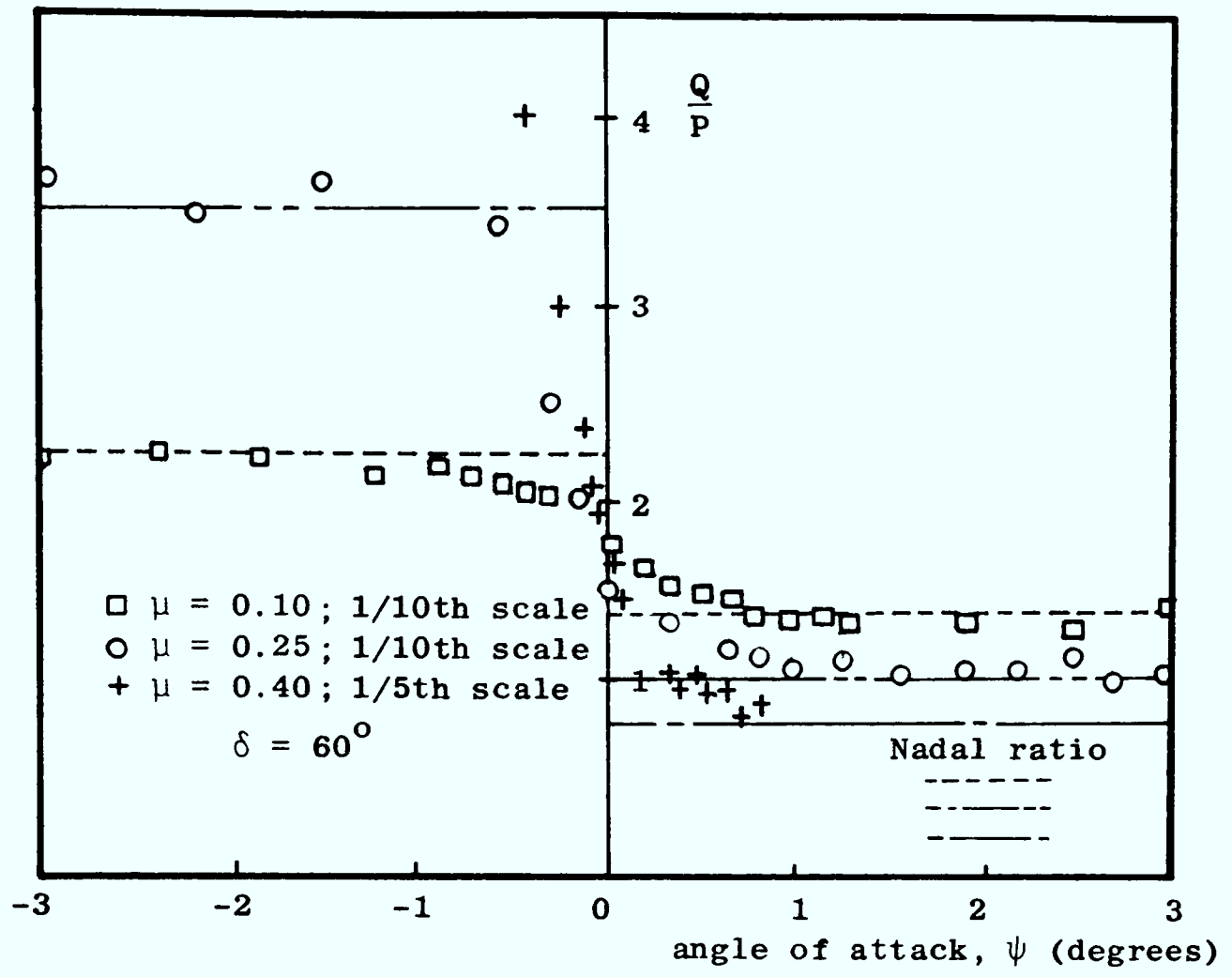

Fig 4.10 JNR derailment tests with 1/5th and 1/10th scale models of wheelsets (see Matsui (22))

4.3.3 Wheel climb resulting from a lateral impulse

When a wheel is subject to a lateral impulse it will not "climb" in the same manner as explained in section 4.3.1, but act to rebound away from the rail after the impact. This phenomenon has been observed and modelled by JNR (see Matsui (22)) leading to an extension of Nadal's derailment ratio which takes account of lateral impulses.

When the wheel hits the rail the forces at the point of impact are treated in the same manner as shown in equation (4.11). After the impact the wheel "jumps" and the wheelset is considered to rotate about a point on the other wheel. By using the conservation of momentum, and deciding to relate the normal components of velocity before and after impact by a coefficient of restitution, an expression is obtained relating the height of the jump to the lateral velocity of the wheel before impact (see equation (4.13)).

$$z = \left(\frac{K_w}{2a}\right)^2 \left(\frac{P_w}{P}\right) \left(\frac{(1 + C_r)C}{1 + C\cot\delta}\right)^2 \frac{V_y^2}{g} \qquad (4.13)$$

where,

z = height of jump

K_w = radius of gyration of wheelset about point of contact

$2a$ = gauge

P_w = $\frac{1}{2}$ mg (m = mass of wheelset)

P = wheel load

C_r = coefficient of restitution

$$C = \left(\frac{2a}{K_w}\right)^2 \frac{1 + \mu\tan\delta}{\tan\delta - \mu} \qquad (4.14)$$

(for positive angle of attack)

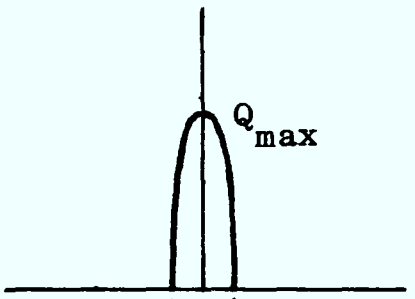

Fig 4.11 Model of impulse

The impulse is modelled as a half sine wave as shown in Fig 4.11, which leads to an expression relating the impulsive force and duration of impulse to the lateral velocity before impact:

$$V_y = \frac{1}{m}\left(\frac{1 + \cos\delta}{1 + C_r}\right)\frac{2}{\pi} Q_{max}\, t_1 \qquad (4.15)$$

The height of the jump is set as being equal to the depth of flange, and equations (4.13), (4.14) and (4.15) are equated to give,

$$\frac{Q_{max}}{P} = \frac{\tan\delta - \mu}{1 + \mu\tan\delta}\left(\frac{\pi}{2}\left(\frac{K_w}{2a}\right)\sqrt{\frac{P_w h}{P g}}\right)\frac{1}{t_1} \qquad (4.16)$$

where,

h = depth of flange

Equation (4.16) extends the Nadal derailment ratio to take account of impact forces.

It should be noted that an arithmetic error occurs in Matsui's derivation which leads to a permissible impulse which is twice the magnitude of that indicated by equation (4.16): this error is carried over into some other JNR documents and leads to a limiting value which is less safe.

The decision to treat the forces at the point of impact in the manner described by equation (4.11) is a simplification which ignores the effect of the wheel velocity on the creep of the wheel over the rail. The lateral creep is given by equation (2.20),

$$\gamma_y = \frac{v_y}{V} - \psi \qquad (4.17)$$

where,

V = forward speed of wheelset

This may be combined with equation (4.15) to give,

$$\gamma_y = \frac{1}{mV}\left(\frac{1 + C\cot\delta}{1 + C_r}\right)\frac{2}{\pi} Q_{max}\, t_1 - \psi$$

$$\simeq \frac{1}{mV}\,\frac{2}{\pi} Q_{max}\, t_1 - \psi \qquad (4.18)$$

Equation (4.18) shows that the creep due to the lateral velocity of the wheelset acts to offset the creep that occurs as a result of the angle of attack. When the wheelset has a positive angle of attack this equation suggests that a wheelset is less likely to derail from an impulse when the running speed is low. Equation (4.16) also indicates that errors may occur in scale model testing as the mass of the wheelset and the forward speed will both be small. The simplification will tend to make equation (4.16) conservative for such cases, which implies an additional margin of safety.

Experiments have been carried out by JNR (see Arai & Yokose (23)) to test the validity of using equation (4.16) as an indicator of derailment. A 1/5th scale model of a wheelset was made to hunt and the relationship between the impact time and the derailment ratio was plotted for conditions in which a derailment took place: the

results are reproduced in Fig 4.12.

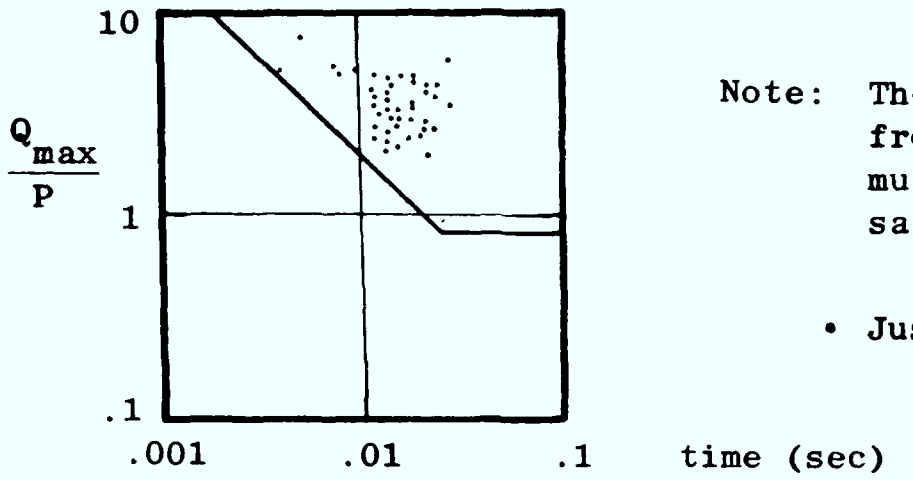

Fig 4.12 Relationship between impact time and derailment ratio (see Arai & Yokose (23))

The results indicate that the derailments all occur with ratios that are in excess of those determined by equation (4.16), and so this equation successfully predicts the safety of the models. The equation will be less conservative as an indicator of wheel climb for larger wheels travelling at higher speeds. However for the wheels used on manriding vehicles the use of this equation is justifiable.

4.3.4 Wheel climb criterion for railways in coal mines

The criterion for assessing the likelihood of derailment as a result of a wheel climbing the rail will be the ratio of the lateral force and the vertical force at the point of contact (Q/P ratio). The results of the preceding sections, and specifically equations (4.11) and (4.16), provide limiting values of this ratio for which a vehicle may be considered safe, and these equations are evaluated for a typical manriding vehicle (a fully laden gondola car) in this section. The results are obtained for a trailing wheel with a positive angle of attack.

The contact angle, δ, during flange contact is between 65^{o} and 75^{o} for the wheels used on manriding vehicles (see Figs 2.3 and 2.4 (b): these figures show the contact angles for a new 14 in. diameter mine car wheel), and measurements by British Rail (see Hobbs (10)) indicate a variation in the coefficient of friction from 0.125 to 0.39. For $\delta = 70^{o}$ and $\mu = 0.3$, equation (4.11) can be

rewritten as:

$$\frac{Q}{P} = 1.34 \qquad (4.19)$$

On the basis of extensive empirical studies JNR use a limit which is 80% of this value to provide a margin of safety. Adopting this same philosophy leads to the result:

$$\frac{Q}{P} = 1.07 \simeq 1 \qquad (4.20)$$

This is the limiting value for safety under the influence of a steady lateral force.

Under the influence of a lateral impulse, the limiting derailment ratio is obtained using equation (4.16). For a fully laden gondola car the quantities used in this equation are:

$$\begin{aligned} \gamma &= 70^{o} \\ \mu &= 0.3 \\ K_{w} &\simeq 2a \\ P_{w} &= 750\ N \\ P &= 11600\ N \\ h &= 0.02\ m \end{aligned} \qquad (4.21)$$

Using these values, equation (4.19) can be rewritten as:

$$\frac{Q}{P} = \frac{0.024}{t_1} \qquad (4.22)$$

Again, by considering the limit to be 80% of this value leads to the result:

$$\frac{Q}{P} = \frac{0.02}{t_1} \qquad (4.23)$$

Derailment ratios, as determined by equations (4.20) and (4.23), are shown in Fig 4.13: this figure represents the limiting values against which results will be compared to assess the likelihood of wheel climb derailment.

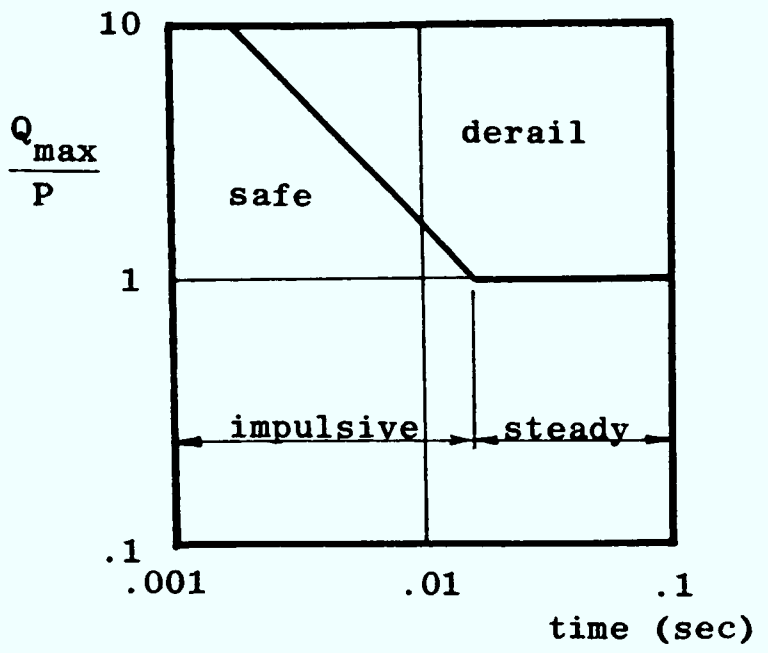

Fig 4.13 Likelihood of derailment for vehicles travelling along railways in coal mines

4.3.5 Application of wheel climb criterion

Wheel climb occurs when the flange comes into contact with the rail and, more specifically, when a large lateral force exists at the point of contact.

A derailment of this kind can result from purely geometric considerations, such as the tightening of the track gauge in a curve or the misalignment of the axles of a vehicle, as a result of impact forces at points, or because of the behaviour of a vehicle as it travels along the track. The last of these causes will be treated here.

A mathematical modelling technique (see Chapter 2) may be used to describe the behaviour of a vehicle in terms of acceleration spectral densities of component parts. Large lateral forces are detected by examination of the spectral density describing a pair of wheels in sway, and these forces will be associated with such things as: component resonance (eg car-body roll), vehicle guidance (for a pair of wheels rotating independently on an axle), and the use of unbalanced wheels. All of the above phenomena will cause peaks in the acceleration spectral densities, $S_{\ddot{q}}(f)$, and each peak can be processed using equation (4.1),

$$a_{rms} = \sqrt{S_{\ddot{q}}(f)\ \Delta f}$$

to give an associated rms acceleration. This acceleration is evaluated by considering the frequency band, Δf, to be equal to the width of the peak. If the oscillations associated with the phenomenon are considered as being sinusoidal, which is a reasonable simplification in the case of resonance, the peak accelerations will be given by,

$$a_{peak} = \sqrt{2} \cdot a_{rms} \qquad (4.24)$$

where,

a_{peak} = peak acceleration
a_{rms} = rms acceleration

To obtain the lateral force from this acceleration the following relationship can be used:

$$Q = m \cdot a_{peak} \qquad (4.25)$$

where,

m = mass of pair of wheels
Q = lateral force

The derailment ratio is obtained from equation (4.25) by dividing the lateral force by the vertical wheel load. In the absence of car-body (or bogie) roll, pitch, or bounce, this wheel load has a nominal value of half of the axle load and, unless otherwise stated, this is the value that is used in this work. The likelihood of derailment is assessed by comparing this ratio with the limiting value shown in Fig. 4.13: if it exceeds the limiting value the vehicle is considered to be unsafe. Fig 4.13 can be redrawn in terms of frequency by making the substitution,

$$f = \frac{1}{2t_1} \qquad (4.26)$$

in equation (4.23), with the substitution being based on a decision to treat the oscillation as being approximately sinusoidal. The results of this are shown in Fig 4.14.

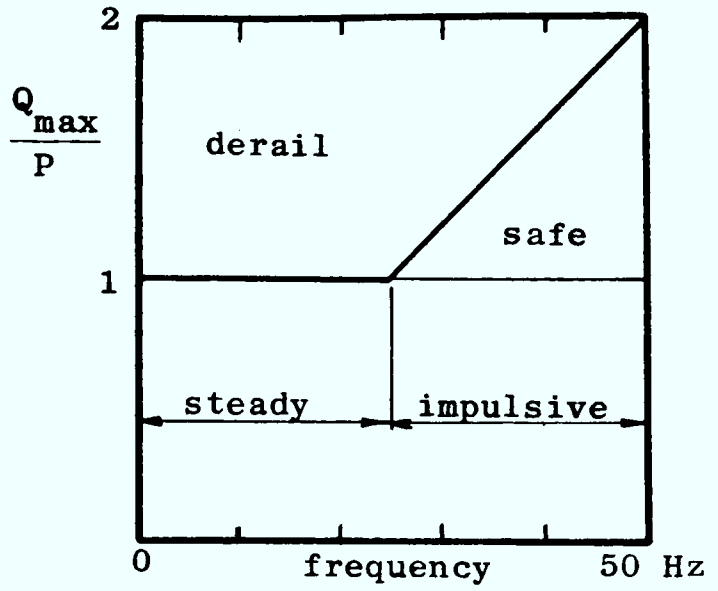

Fig 4.14 Likelihood of derailment for vehicles travelling along railways in coal mines

4.3.6 Wheel lift criterion

When the flange of a wheel lifts above the level of the rail a derailment can easily occur. It is clear that this type of derailment will be associated with a reduction in the vertical wheel load, and this will be used as the criterion for assessing this type of derailment. The loss of wheel load may be expressed as:

$$\frac{\Delta P}{P} = 1 \qquad (4.27)$$

where,

P = wheel load

ΔP = reduction of load

If a limit of 80% of this value is used:

$$\frac{\Delta P}{P} = 0.8 \qquad (4.28)$$

Equation (4.28) is used by JNR (see Ikemori (24)) to assess the likelihood of wheel lift derailment. The ratio $\Delta P/P$ is referred to as the "wheel load reduction ratio" by the Japanese and this term will also be used in this work.

4.3.7 Application of wheel lift criterion

Reduction in wheel load will generally occur due to uneven track (see section 4.38) or as a result of excessive pitching or rolling of

a vehicle. When the movement of the vehicle occurs as a result of resonance the wheel load reduction ratio can be obtained using a similar technique to that explained in section 4.3.6, with the reduction in load being determined from the rms accelerations using the expression,

$$\Delta P = \sqrt{2}\, m_e\, a_{rms} \qquad (4.29)$$

where,

a_{rms} = vertical rms acceleration of wheel
m_e = effective mass

This ratio can be compared directly with equation (4.28) to assess the likelihood of derailment.

In the case of a locomotive with a short wheelbase and a long overhang (see Fig 4.5) the load on the wheel can be reduced to zero when the locomotive pitches and bumps the track. This was first analysed in connection with an investigation of the likelihood of derailment of such a vehicle during heavy braking (see Van Manen (25)), and has since been extended to account for such a derailment due to track undulation (see Clibborn (17)).

4.3.8 Wheel lift caused by track irregularities

When a track has large amounts of undulation or twist a vehicle can derail due to purely kinematic effects. Criteria have been developed in connection with the development of the track monitoring equipment (see Clibborn(17)) and these relate the geometry of a vehicle to the track irregularities. The criteria are used to detect unacceptable sections of track and, although not germane to this work, are briefly explained below.

When a suspensionless vehicle travels over twisted track a wheel may lose contact with the rail as shown in Fig 4.15. When the flange lifts above the level of the rail a derailment can easily occur, and this forms the criterion for establishing the acceptability of a section of track. If the amount of wheel lift equals the flange depth, h, a relationship between cross-level and lift can be established (see equation (4.30).

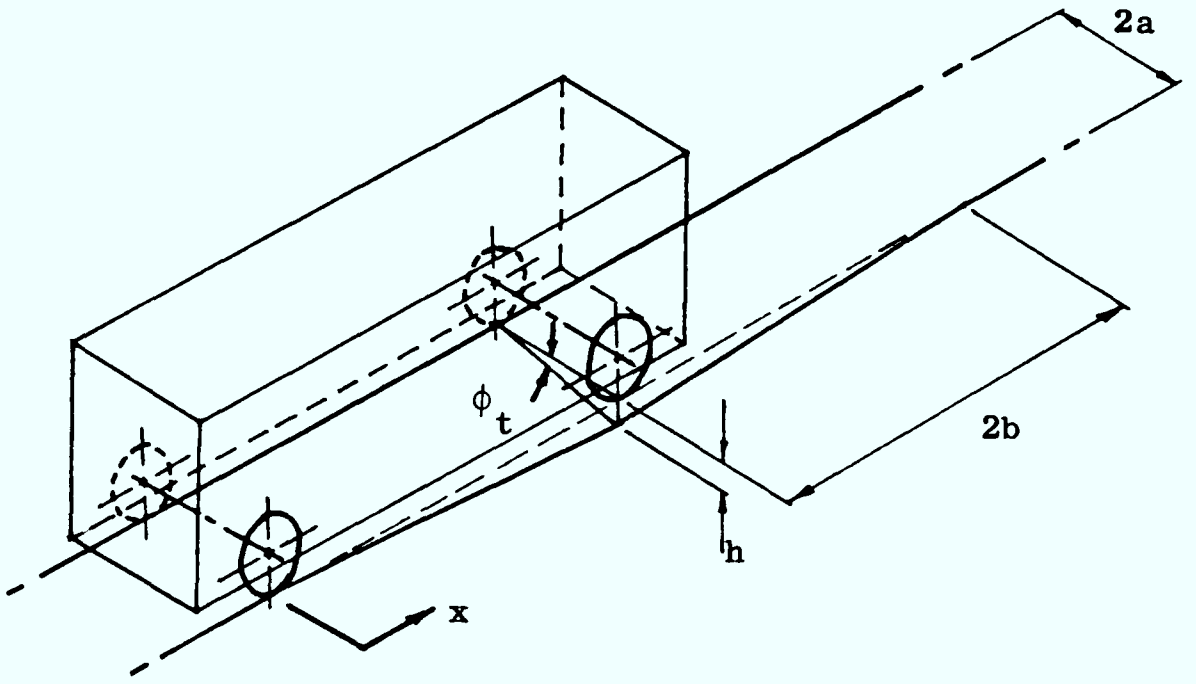

Fig 4.15 Rate of change of cross-level

$$\tan \phi_t \simeq \phi_t = {}^{h}/_{2a} \qquad (4.30)$$

where,

ϕ_t = cross-level (in radians)

2a = gauge

The rate of change of cross-level (or twist) corresponding to imminent wheel lift is:

$$\frac{d\phi_t}{dx} \simeq \frac{\phi_t}{2b} \simeq \frac{h}{4ab} \qquad (4.31)$$

For a typical two axle manrider,

h = 0.025 m

2a = 0.76 m

2b = 2.5 m (4.32)

A track that twists in excess of 1 degree in 1.33 metres is unacceptable.

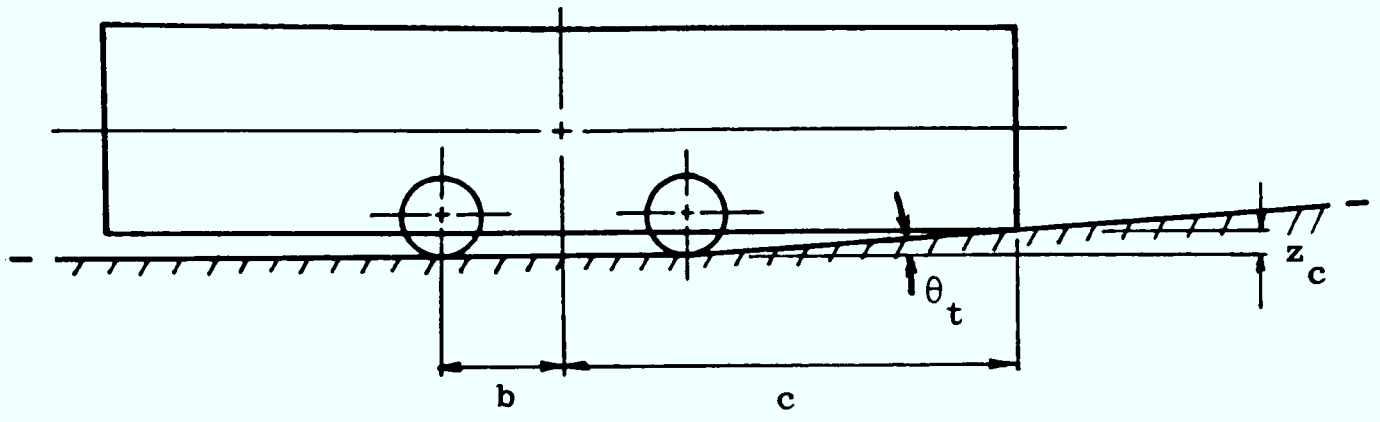

Fig 4.16 Gradient relative to overhang

The criterion for track undulation has been established for locomotives with long overhangs (see Fig 4.16) to locate sections along which the locomotives might bump the track. The rate of change of track gradient, θ_t, corresponding to imminent wheel lift is:

$$\frac{d\theta_t}{dx} \simeq \frac{\theta_t}{c} \simeq \frac{z_c}{c^2} \qquad (4.33)$$

where,

θ_t = track gradient (in radians)
c $\simeq$ overhang

An additional margin of safety has been incorporated leading to the criterion:

$$\frac{d\theta_t}{dx} \simeq \frac{z_c}{2c^2} \qquad (4.34)$$

For a typical locomotive of this type,

z_c = 0.1 m
c = 2.26 m

A track where the gradient changes in excess of 1 degree in 1.78 metres is unacceptable.

Chapter 5

Behaviour of a Single Wheelset

5.1 Introduction

The response of a vehicle to track irregularities depends on the interaction between the wheels and the rails, and so an examination of the motion of a single wheelset (or pair of wheels) provides a valuable insight into overall vehicle behaviour. A great deal of work has been carried out to explain the stability and curving performance of conventional wheelsets for mainline applications (eg see Wickens (26) and Newland (27)). However little has been done to examine the behaviour of wheels that revolve independently on a fixed axle, except with regard to trains fitted with wheels possessing extraordinary profiles (see Kaplan et al (28)). There is a need for a clear comparison of the two configurations, and this is the primary object of this chapter.

The comparison is made for the gondola manriding car shown in Fig 1.4. The production version of this vehicle has wheels that revolve independently on a fixed axle, and a new car has been developed which is fitted with conventional wheelsets (see section 6.5.4). The vehicle itself is discussed in greater detail in Chapter 6. A simple model is proposed and this is used to predict the responses of both configurations to track inputs; these predictions are assessed against the results of tests in section 5.2. The guidance and the likelihood of derailment of the two configurations are compared in section 5.3, and the effects of changing the wheel profiles and the suspension characteristics are examined. In addition, the stability of conventional wheelsets is discussed briefly in section 5.4.

5.2 Model of a single wheelset

5.2.1 Modelling decisions

The model is constructed to predict the sway and yaw of a single wheelset in response to changes in track lateral alignment. The wheelset is connected by linear suspension elements to a bogie which moves at constant speed along the track centreline. This is illustrated in Fig 5.1.

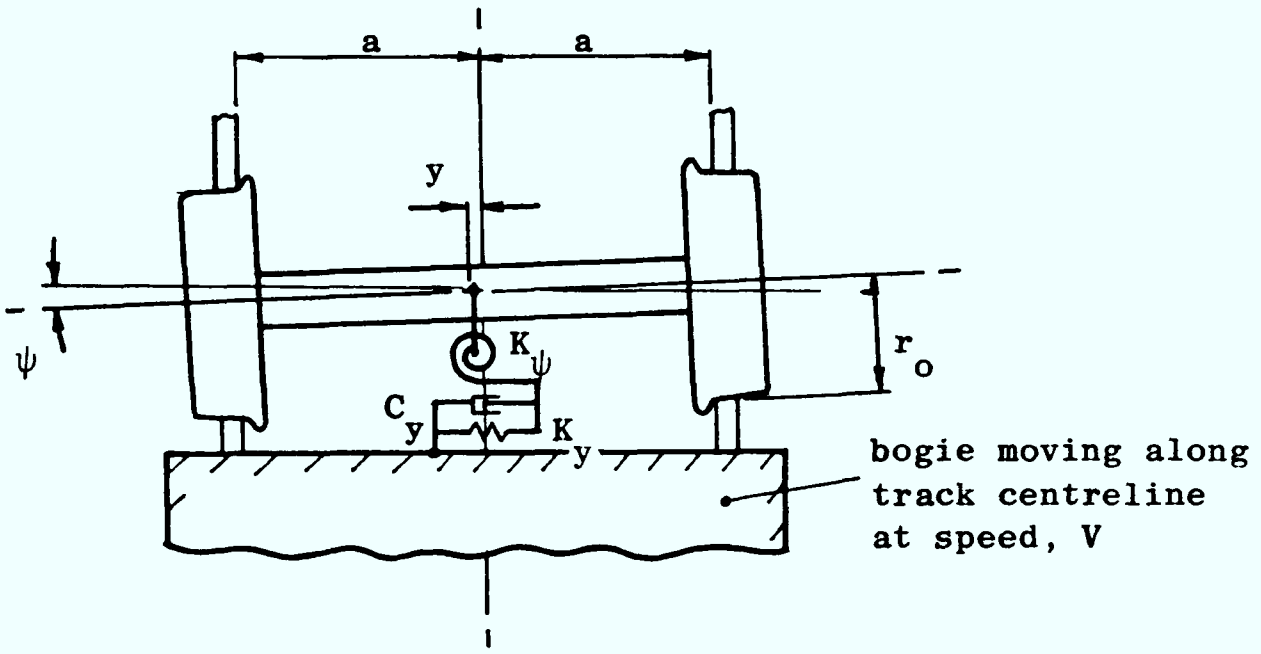

Fig 5.1 Model of a single wheelset (plan view)

The decision to ignore any lateral or vertical motion of the bogie is based on the test results (see Appendix 4) which suggest that the suspension stiffness is low enough for the wheels to move independently of the bogie. If the model is used to examine stiffer suspensions inaccuracies will arise as a result of the wheels and bogie moving together.

The geometry of the wheels and the rails are as shown in Fig 2.3 (ie new 14 inch diameter mine car wheels on 30 kg/m rails), and the gravitational stiffness forces are modelled on the basis of the results obtained for these profiles (see Fig 2.6). This model is shown in Fig 5.2 (b). By deciding to treat gravitational stiffness in this way a non-linearity is introduced and this is removed by employing a describing function technique (see section 5.2.3). The creep forces for a displaced wheelset have already been derived in equations (2.24) and (2.25) (see section 2.3.4) and are used in this form in the model. Creep coefficients are evaluated in section 5.2.4 using Kalker's linear creep theory.

5.2.2 Equations of motion

The lateral movement (sway) and yaw of an elastically restrained wheelset (as shown in Fig 5.1) can be expressed mathematically as shown in equations (5.1) and (5.2).

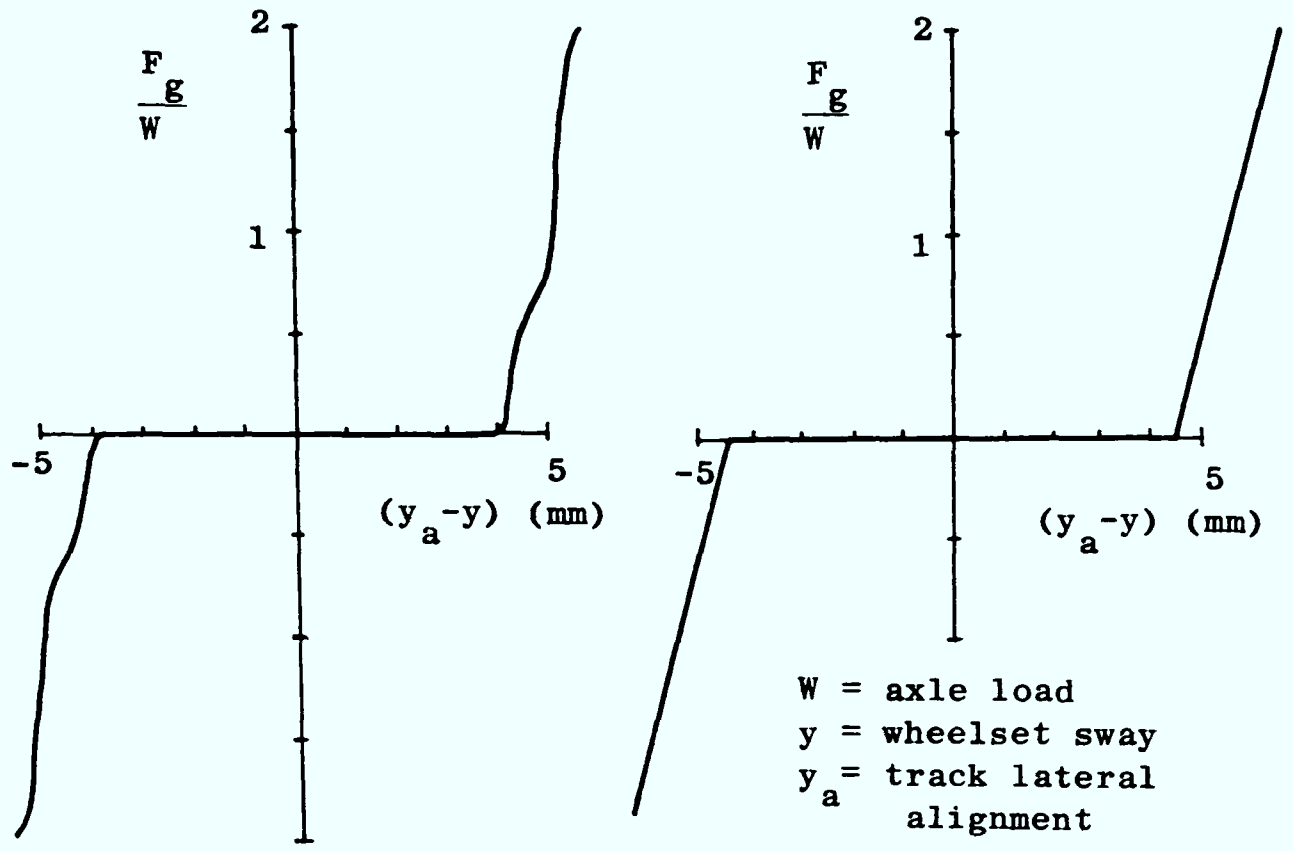

Fig 5.2 Variation of gravitational stiffness force, F_g with lateral displacement

(a) New wheel on 30 kg/m rail (Fig 2.6)

(b) Model

$$m\ddot{y} + \left(\frac{2f_{22}}{V} + C_y\right)\dot{y} + (K_y + K_g)\,y - 2f_{22}\psi = K_g\,y_a \qquad (5.1)$$

$$I_{zz}\ddot{\psi} + \frac{2f_{11}a^2}{V}\dot{\psi} + K_\psi\,\psi + \frac{2f_{11}a\lambda_o}{r_o}\,y = \frac{2f_{11}a\lambda_o}{r_o}\,y_a \qquad (5.2)$$

where,

y = sway

ψ = yaw

y_a = lateral alignment of track

m = mass

I_{zz} = yawing moment of inertia

K_g = gravitational stiffness

f_{11} = longitudinal creep coefficient

f_{22} = lateral creep coefficient

λ_o = conicity (see section 5.3.3)

(The remaining notation is shown in Fig 5.1)

The equations of motion are written for a conventional wheelset. However they can be applied to a pair of independently revolving wheels if the terms relating to longitudinal creep of the wheels are removed. This is done by making the longitudinal creep coefficient equal to zero.

5.2.3 Treatment of gravitational stiffness

The gravitational stiffness varies with the relative lateral positions of the wheels and the rails, and this is modelled as shown in Fig 5.2 (b). The gravitational stiffness is the slope of the curve in the figure and has two distinct values. For flange contact,

$$K_{gf} = 1000\ W \qquad (5.3)$$

where,

K_{gf} = gravitational stiffness (flange)
W = axle load

For tread contact,

$$K_{gt} = 5\ W \qquad (5.4)$$

where,

K_{gt} = gravitational stiffness (tread)

The r.h. side of the equation (5.4) is somewhat larger than would be expected for an undisplaced wheelset, having been obtained by averaging the small values of stiffness that occur with an undisplaced wheelset with the much larger values that exist when the root of the flange is near the rail. A pair of independently revolving wheels will tend to run with the root of the flange in the vicinity of the rail (see section 1.1.2 for preliminary discussion of guidance), and so this simplification would appear to be reasonable. For the case of a conventional wheelset the creep forces have a greater influence on behaviour than the gravitational stiffness, and so the simplification will have little effect on the accuracy of the model.

To incorporate gravitational stiffness in equation (5.1) the non-linearity associated with flange contact must be removed. This is done using a describing function approach (see Raven (12)) which is explained below.

Consider a sinusoidal input to the non-linearity to be:

$$(y_a - y) = B \sin \omega t \qquad (5.5)$$

where,

B = a constant

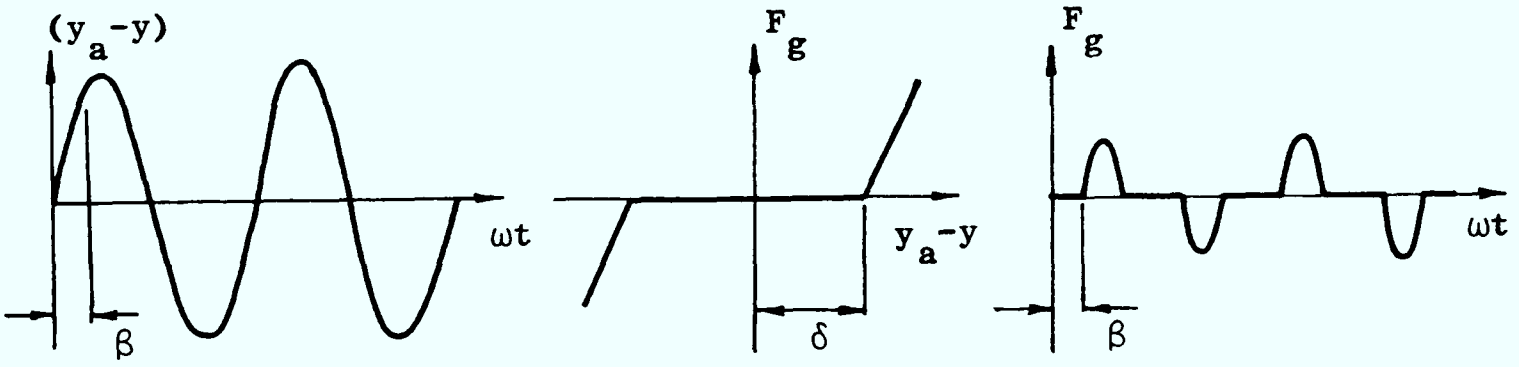

input non-linearity response

Fig 5.3 Response of non-linearity to a sinusoidal input

The response is shown in Fig 5.3, and this can be described in the following manner.

When, $|y_a - y| > \delta$

$$F_g = B \{(K_{gt} - K_{gf}) \sin \beta + K_{gf} \sin \omega t\} \qquad (5.6)$$

where,

$$\beta = \sin^{-1} \left(\frac{\delta}{B} \right)$$

When, $|y_a - y| < \delta$

$$F_g = B \{K_{gt} . \sin \omega t\} \qquad (5.7)$$

The response is periodic, and so may be expressed in terms of a Fourier series which, in this case, is given by:

$$F_g = \sum_{n-1}^{\infty} F_n \sin(n\omega t) \qquad (5.8)$$

where,

$$F_n = \frac{2}{\pi} \int_0^{\pi} F_g \sin(n\omega t)\, d(\omega t)$$

$$= \text{Fourier coefficients } (n = 1, 2, 3.....)$$

Equation (5.8) can be rewritten in the form:

$$F_g = F_1 \sin \omega t + \sum_{n=2}^{\infty} F_n \sin(n\omega t) \qquad (5.9)$$

where,

$F_1 \sin \omega t$ = fundamental harmonic

If equation (5.9) is divided by equation (5.5) an expression for gravitational stiffness is obtained:

$$K_g = \frac{F_g}{(y_a - y)} = N(B) + \sum_{n=2}^{\infty} \frac{F_n \sin(n\omega t)}{(y_a - y)} \qquad (5.10)$$

where,

$$N(B) = \frac{F_1}{B} = \text{describing function} \qquad (5.11)$$

When $B > \delta$, the Fourier coefficient F_1 is obtained using equations (5.6), (5.7) and (5.8), leading to the result:

$$F_1 = B\left\{(K_{gt} - K_{gf})\frac{2}{\pi}(\sin^{-1}\gamma + \gamma\sqrt{1 - \gamma^2}) + K_{gf}\right. \qquad (5.12)$$

where,

$$\gamma = {}^{\delta}/_{B}$$

When $B < \delta$ (using equation (5.7) and (5.8)),

$$F_1 = B\, K_{gt} \qquad (5.13)$$

Combining these results with equation (5.11) yields:

$$N(B) \simeq K_{gf} - K_{gf} \frac{2}{\pi} (\sin^{-1}\gamma + \gamma\sqrt{1 - \gamma^2}) \quad (\text{for } \gamma < 1)$$

$$= K_{gt} \quad (\text{for } \gamma > 1) \qquad (5.14)$$

Equations (5.3), (5.4) and (5.11) combine to give:

$$N(B) = \frac{-2000\ W}{\pi} (\sin^{-1}\gamma + \gamma\sqrt{1 - \gamma^2}) + 1000\ W \quad (\text{for } \gamma < 1)$$

$$= 5\ W \quad (\text{for } \gamma > 1) \qquad (5.15)$$

The results of equation (5.15) are shown in Fig 5.4.

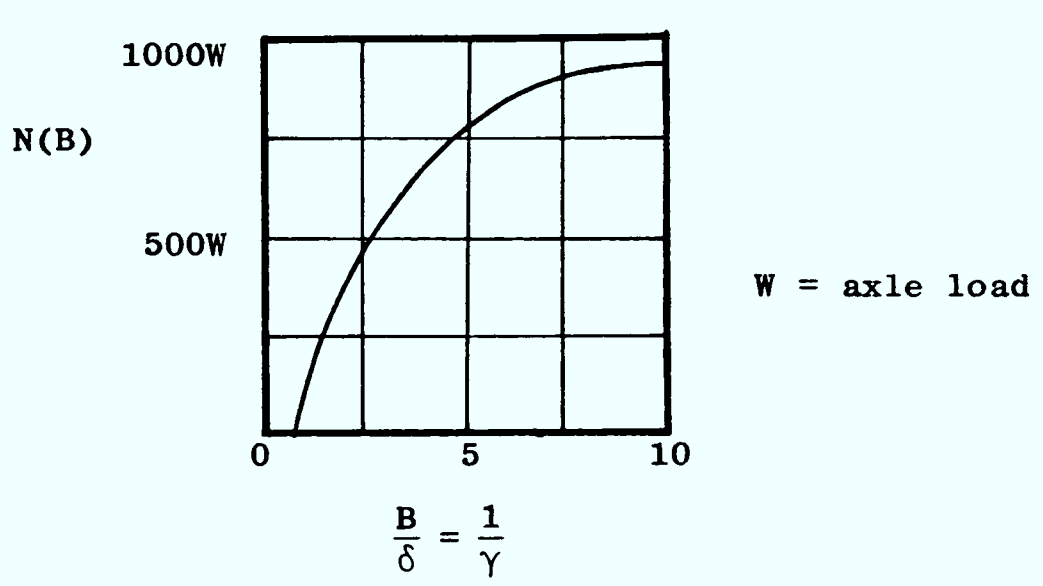

Fig 5.4 Describing function corresponding to non-linearity shown in Fig 5.3

By neglecting the higher order terms in equation (5.10) the describing function becomes an expression of the gravitational stiffness, and this has a constant value for any given input, B. In this form it can be incorporated into equation (5.1) without loss of linearity, which allows the solution explained in section 2.5 to be used. It should be noted that the input is a function of the wheelset sway as well as the track lateral alignment (see equation (5.5)), and so equations (5.1) and (5.2) require an iterative

solution: this is discussed further in section 5.2.5.

5.2.4 Evaluation of creep coefficients

The creep coefficients are evaluated by the linear creep theory explained in section 2.3.4 (see Kalker (9)), and specifically, by using equation (2.1.3),

$$f_{11} = G(ab)\, C_{11}$$
$$f_{22} = G(ab)\, C_{22}$$

where,

C_{11} and C_{22} = tabulated creep coefficients (see Kalker (7))

G = shear modulus of elasticity

a and b = semi-axes of contact ellipse

The dimensions of the contact ellipse are calculated on the basis of Hertz's theory of contact (see Timoshenko and Goodier (11)) which, for normal running, leads to the result:

$$a = (8.7 \times 10^{-5})\, W^{1/3} \text{ (metres)}$$
$$b = (7.1 \times 10^{-5})\, W^{1/3} \qquad (5.16)$$

where,

W = axle load (Newtons)

When contact at the tread is lost and the wheel travels on its flange:

$$a = (6.0 \times 10^{-5})\, W^{1/3} \text{ (metres)}$$
$$b = (2.4 \times 10^{-5})\, W^{1/3} \qquad (5.17)$$

The wheels will travel with the treads in contact with the rails for most of the time and so equation (5.16) will be generally applicable.

Kalker's tabulated coefficients are dependent on the relative values of a and b (specifically, the ratio a/b) which are obtained from equation (5.16). By incorporating these coefficients in equation (2.13) expressions are obtained for the creep coefficients:

$$f_{11} = 2114\ W^{2/3} \text{ (Newtons)}$$
$$f_{22} = 1919\ W^{2/3} \qquad (5.18)$$

Equation (5.18) can be simplified to give:

$$f_{11} = f_{22} = 2000\ W^{2/3} \text{ (Newtons)} \qquad (5.19)$$

5.2.5 Solution of equations

The solution of the equations of motion (equations (5.1) and (5.2)) is based on the method explained in section 2.5.2, in which the transfer function is evaluated for sinusoidal inputs over a range of frequencies. The original technique is for a linear system and the solution is independent of the magnitude of the inputs, however, the magnitude must be incorporated here owing to the way in which gravitational stiffness is treated (see section 5.2.3). In addition, an iterative solution is required. This is because the describing function which represents the gravitational stiffness is dependent on both the track alignment and the sway of the wheelset, which is in turn a solution of equations (5.1) and (5.2).

The track lateral alignment has been described previously in terms of the spectral density (see section 3.3.6), and specifically as:

$$S_a(\Omega) = {}^{A}/_{\Omega^2} \qquad (5.20)$$

where,

$S_a(\Omega)$ = spectral density describing track lateral alignment

A = roughness coefficient

Ω = spatial frequency

The mean square alignment is obtained using a variation of equation (2.59):

$$\langle y_a^2(x) \rangle = \int_0^\infty S_a(\Omega)\, d\Omega \qquad (5.21)$$

If the spectral density describes a single sinusoidal input, the mean square value of that input is given by:

$$\langle y_a^2 (x) \rangle = \int_0^\infty S_a (\Omega)\, d\Omega$$

$$= \int_{\Omega}^{\infty} {A}/{\Omega^2}\, d\Omega$$

$$= {A}/{\Omega} \qquad (5.22)$$

This sinusoidal input can be written as:

$$y_a (x) = \sqrt{{2A}/{\Omega}} \sin 2\pi\Omega x \qquad (5.23)$$

Equation (5.23) can be expressed in terms of temporal frequencies with respect to a wheelset moving along the track at constant speed, leading to the result:

$$y_a (t) = B_a \sin \omega t \qquad (5.24)$$

where,

$$B_a = \sqrt{\frac{2AV}{f}}$$

$$\omega = 2\pi f$$

This equation is similar to equation (5.5) and provides an estimate for the describing function representing gravitational stiffness (by substituting B_a for B in equation (5.15)). This estimate is incorporated in equations (5.1) and (5.2) which are solved using equation (2.38) to yield the transfer function. The response of the wheelset is now given by equation (2.39), which can be written in the form:

$$\underset{\sim}{q} = H(f)\, y_a \qquad (5.25)$$

where,

$\underset{\sim}{q}$ = wheelset co-ordinate vector = $\{{}^{y}_{\psi}\}$

$$H(f) = \text{transfer function} = \begin{Bmatrix} h_1 \\ h_2 \end{Bmatrix}$$

The sway of the wheelset is thus given by:

$$y = h_1 \cdot y_a \qquad (5.26)$$

Equations (5.24) and (5.26) are combined to give the expression:

$$(y_a - y) = (1 - h_1)\, B_a \sin \omega t \qquad (5.27)$$

This equation is used to revise the estimate for the describing function (by substituting $(1 - h_1)\, B_a$ for B in equation (5.15)) which leads to a revised transfer function. Thus, by iteration, the equations of motion are solved.

Consider the behaviour of the leading pair of wheels of a gondola car travelling along track with the lateral alignment described by the expression:

$$S_a(\Omega) = \frac{5 \times 10^{-6}}{\Omega^2} \ m^2 \cdot \text{m/cyc} \qquad (5.28)$$

Representative values for the quantities in equations (5.1) and (5.2) are:

m	=	150 kg	f_{11}	=	0
I_{zz}	=	35 kg m^2	f_{22}	=	2000 $W^{2/3}$ N
K_y	=	2×10^6 N/m	a	=	0.38 m
K_ψ	=	6×10^4 Nm/rad	r_o	=	0.178 m
C_y	=	100 Ns/m	δ	=	0.0045 m
W	=	6500 N			

(5.29)

The sway of the wheels is determined by solving the equations of motion, and this is shown in Fig 5.5 for the vehicle travelling at a speed of 17.5 mph.

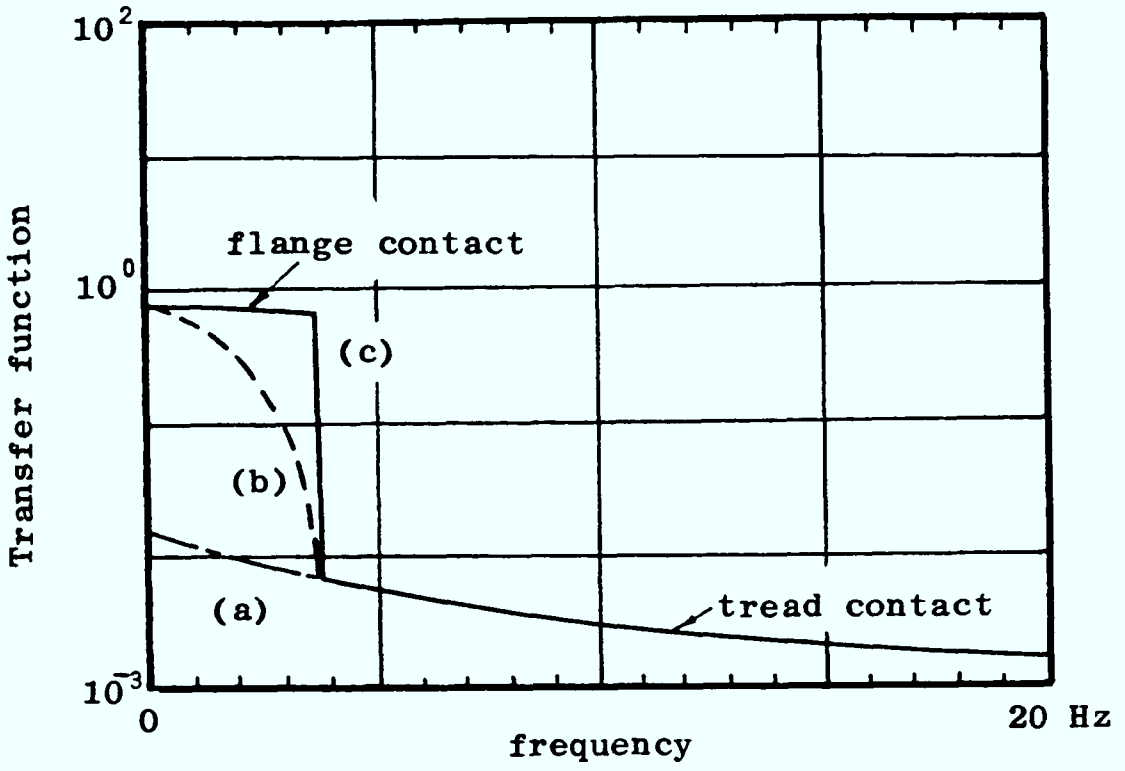

Fig 5.5 Transfer functions for a pair of wheels travelling at 17.5 mph.

(a) Not considering flange contact

(b) Flange contact: describing function technique without iteration

(c) Flange contact: describing function technique with iteration

Three solutions are presented in this figure, these being obtained by:

(a) neglecting flange contact

(b) using a describing function technique without iteration

(c) using a describing function technique with iteration

For frequencies greater than about 4 Hz the three solutions are identical and this is when the flange is not in contact with the rail. At lower frequencies the describing function approach takes into account the flange touching the rail, although the non-iterative solution underestimates the extent of this contact. It is clear that the iterative solution must be used when flange contact is being considered. A program to carry out this solution is included in Appendix 2.

5.2.6 Comparison of model and test results

The validity of the mathematical model is assessed in this section

against measurements taken on a gondola manriding vehicle. The tests were carried out using a vehicle in service which travelled at speed along a section of underground track. The motion was monitored with accelerometers and the measurements are presented in the form of acceleration spectral densities in Appendix 4. An explanation of the test procedure is included in section 6.3.

The sway of the wheels in response to an estimated level of lateral alignment has already been evaluated and presented as a transfer function in Fig 5.5 (c).

In order to express the sway in terms of the acceleration spectral density, equations (2.63), (3.38) and (5.20) are combined to give:

$$S_{\ddot{q}}(f) = (2\pi)^4 AVf^2 |H(f)|^2 \qquad (5.30)$$

where,

$$A = 5 \times 10^{-6} \ m^2 cyc/m \qquad \text{(see equation (5.28))}$$

Applying equation (5.30) leads to the results shown in Fig 5.6. The test results are also shown on this figure.

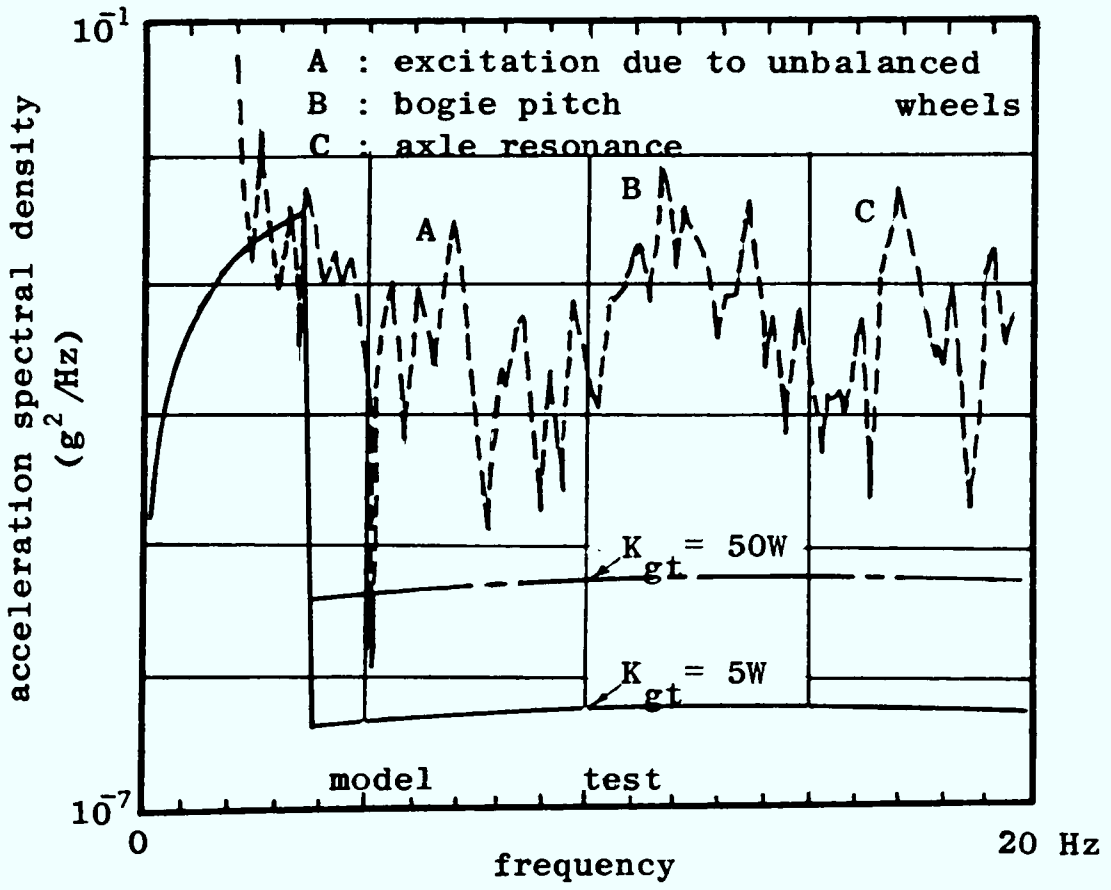

Fig 5.6 Comparison of model and test results for leading pair of wheels of gondola manriding cars (speed = 17.5 mph)

There are peaks in the measured spectral density due to excitation from unbalanced wheels and resonance of the bogie and wheelset, but these effects are not incorporated in the model (they are discussed further in Chapter 6). The outcome of the modelling compares favourably with the observed motion of the wheels at low frequencies when the flange is in contact with the rail. At higher frequencies the model underestimates the levels of oscillation which suggests that the value chosen for the gravitational stiffness at the tread is too small (see equation (5.4)). This implies that the root of the flange remains in contact with the rail during normal running. The effect of increasing this value of gravitational stiffness is shown in the figure.

With the exception of this stiffness, and the conicity, λ_o, the values of the quantities in the equations of motion may be used with confidence as they are either measured or derived from measured quantities. The conicity affects the motion of conventional wheelsets only and is discussed further in section 5.3.3.

5.2.7 Limitations of the model

The model presented can be used to explain dynamic behaviour. However it has certain specific limitations. The motion of the bogie is ignored and so the effects of bogie resonance are not incorporated; this is examined further in Chapter 6. In addition, this simplification means that stiffer primary suspensions, which lead to mutual sway of the wheels and bogie, may not be examined with the model (see section 5.2.1).

The treatment of gravitational stiffness (see Fig 5.2 (b)) ignores entirely the complex geometry of the wheel when it travels with the flange close to the rail. The analysis of the model is of a statistical nature in this work, in that only the general behaviour of the vehicle is being considered, and so this simplification is not crucial. Large inaccuracies can result, however, if the same model is analysed with a different technique, such as a time stepping integration method.

5.3 Guidance and likelihood of derailment

5.3.1 General considerations

The ability of a pair of wheels to follow the track is dependent on the restoring force generated when the wheels are displaced laterally. For a conventional wheelset the force occurs as a result of the differential creep which arises from having tapered wheel profiles (see section 2.3.4). For a pair of independently revolving wheels the force is generated during flange contact. It is clear that the magnitude of the restoring force reflects the guiding abilities of each configuration, and this is chosen as a basis for comparing the guidance of a wheelset and a pair of independently revolving wheels.

The lateral force is also a measure of the safety of the vehicle. When the flange touches the rail the ratio of the lateral force and the vertical wheel load can be compared against acceptability limits (see section 4.3.4) to ascertain the likelihood of wheel climb derailment. With the model of a single wheelset introduced in section 5.2 the effects of resonance and unbalanced wheels cannot be included, however, a tentative assessment of the safety can be made.

The restoring force is evaluated from the acceleration spectral density describing the sway of a pair of wheels by way of the method explained in section 4.3.5. The rms acceleration is determined using equation (4.1),

$$a_{rms} = \sqrt{S_{\ddot{q}}(f)\ \Delta f}$$

and the lateral force is evaluated using equations (4.24) and (4.25),

$$a_{peak} = \sqrt{2}\ .\ a_{rms}$$

$$Q = m a_{peak}$$

where,

Q = lateral force

m = mass of a pair of wheels

A single force is determined for the entire frequency range of the spectral density (ie Δf = 20 Hz) which, for a pair of independently

revolving wheels, corresponds approximately to the force occurring during flange contact.

5.3.2 Derailment of a pair of independently revolving wheels

The ratio of the lateral force and the vertical wheel load are shown in Fig 5.7 for the leading pair of wheels of a gondola manriding vehicle. The limiting values of this ratio for assessing the likelihood of wheel climb derailment, as proposed in section 4.3.4, are also shown on this figure.

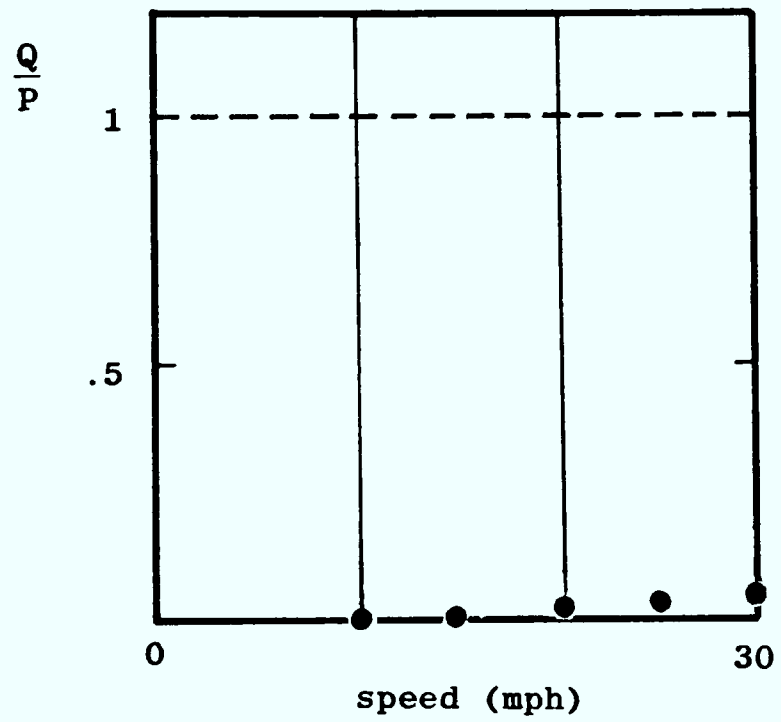

Fig 5.7 Likelihood of wheel climb derailment

On the basis of the results shown the pair of wheels may be considered safe from wheel climb derailment. As stated previously, the model takes no account of such things as resonance of the bogie or the effect of unbalanced wheels, however, the margin of safety indicates that the vehicle should be safe during normal running.

5.3.3 Effect of conicity

As a wheelset is displaced laterally there is a difference in the rolling radii of the two wheels, and this causes a conventional wheelset to steer back towards the middle of the track. The speed of response to such a disturbance is clearly dependent upon the rate of change of rolling radii difference with lateral displacement, and

this depends on the positions of the points of contact and the mutual geometries of the wheels and rails. The rate of change of rolling radii difference is called the conicity and corresponds to the gradient of the curve in Fig 2.4 (a).

For a new wheel the conicity corresponds approximately to the cone angle which, for manriding cars, is generally given by:

$$\lambda_o = 0.05 \text{ radians} \qquad (5.31)$$

After a wheel has been in service for a time the wheel will wear, and a "hollow" appears on the tread. This occurs because of the wheel swaying slightly about an equilibrium position, and results in an increase in the conicity. In addition, as a rail becomes worn the point of contact can change suddenly as a wheel is displaced laterally, and this will affect the conicity. This latter occurrence may also result in a sudden increase in the contact angle, but this will not be considered here.

The effect of conicity on the sway of a wheelset is shown in Fig 5.8.

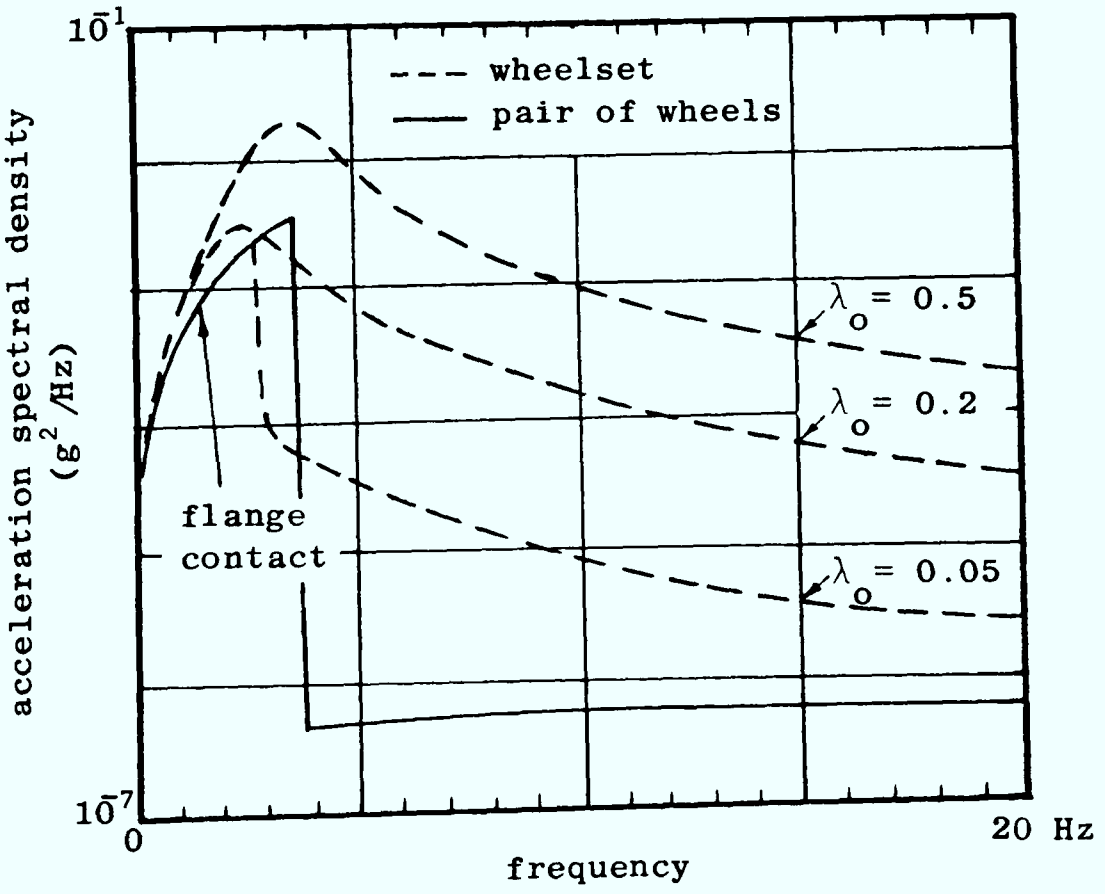

Fig 5.8 Effect of conicity on the sway of the leading wheelset of a gondola manriding car (speed = 17.5 mph)

The lateral forces may be evaluated from the acceleration spectral density using the method outlined in section 5.3.1, and this is done for a range of operating speeds in Fig 5.9. The force associated with a pair of independently revolving wheels is also included in this figure.

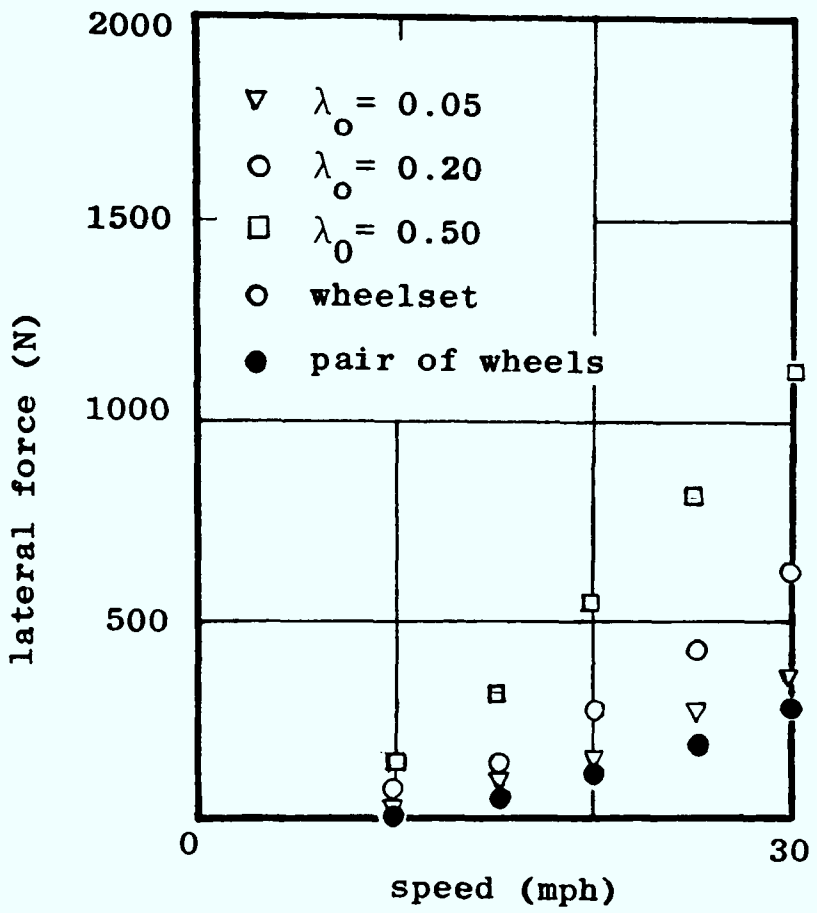

Fig 5.9 Effect of conicity on lateral guidance force of a wheelset

The forces reflect the guidance of the wheelsets (see section 5.3.1), and on this basis the wheels with a higher conicity appear to follow the track more closely. The values of acceleration spectral density are considerably larger at high frequencies for wheels with large conicities (see Fig 5.8) which indicates that more oscillation takes place following lateral disturbance. As the speed increases the oscillation becomes more pronounced, and this ultimately leads to instability. This is discussed further in section 5.4.

The benefits of using conventional wheelsets to improve guidance are only marginal for a new wheelset (λ_o = 0.05) as flange contact is

still the principal mechanism for guidance in this case. As the wheel wears the conicity increases and so the guidance improves. The average conicity of wheels used on British Rail trains has been measured (see Gilchrist (29)) and is generally in the range:

$$\lambda_o \simeq 0.1 \text{ to } 0.2 \qquad (5.32)$$

These conicities correspond to slightly worn wheels travelling along worn track. In the absence of measured data for wheelsets on manriding cars, an average conicity of,

$$\lambda_o = 0.2 \qquad (5.33)$$

will be used for a worn profile. This value can be revised when measured data becomes available.

On the basis of equation (5.33) and the results shown in Figs 5.8 and 5.9, it is clear that the restoring force associated with a displaced wheelset is about twice the magnitude of that generated with a pair of independently revolving wheels, and this is with little or no flange contact taking place.

5.3.4 Recommendation for change of tyre profile

When conventional wheelsets are used on high speed manriding vehicles the conicity should be large enough to ensure adequate guidance without flange contact. It has been shown in the previous section how the existing coned wheels fail to provide this guidance when new, and on this basis a revision of the profile is indicated. This can be achieved by adopting a so-called hollow tread profile that is closer to the final worn shape of the tyre (see Koffman (30)). This will provide a reasonable value of conicity for guidance, and ensure a more consistent motion of the vehicle.

5.3.5 Influence of primary suspension

The sway and the yaw of a pair of wheels is restricted by the presenee

of the primary suspension, and so the suspension characteristics must be considered when assessing guidance. The motion of wheels that revolve independently on a fixed axle will be dependent upon the lateral stiffness (see equation (5.1)), and the motion of conventional wheelsets will also be affected by yaw stiffness (see equation (5.2)). The effects of changing both of these quantities are illustrated in Fig 5.10.

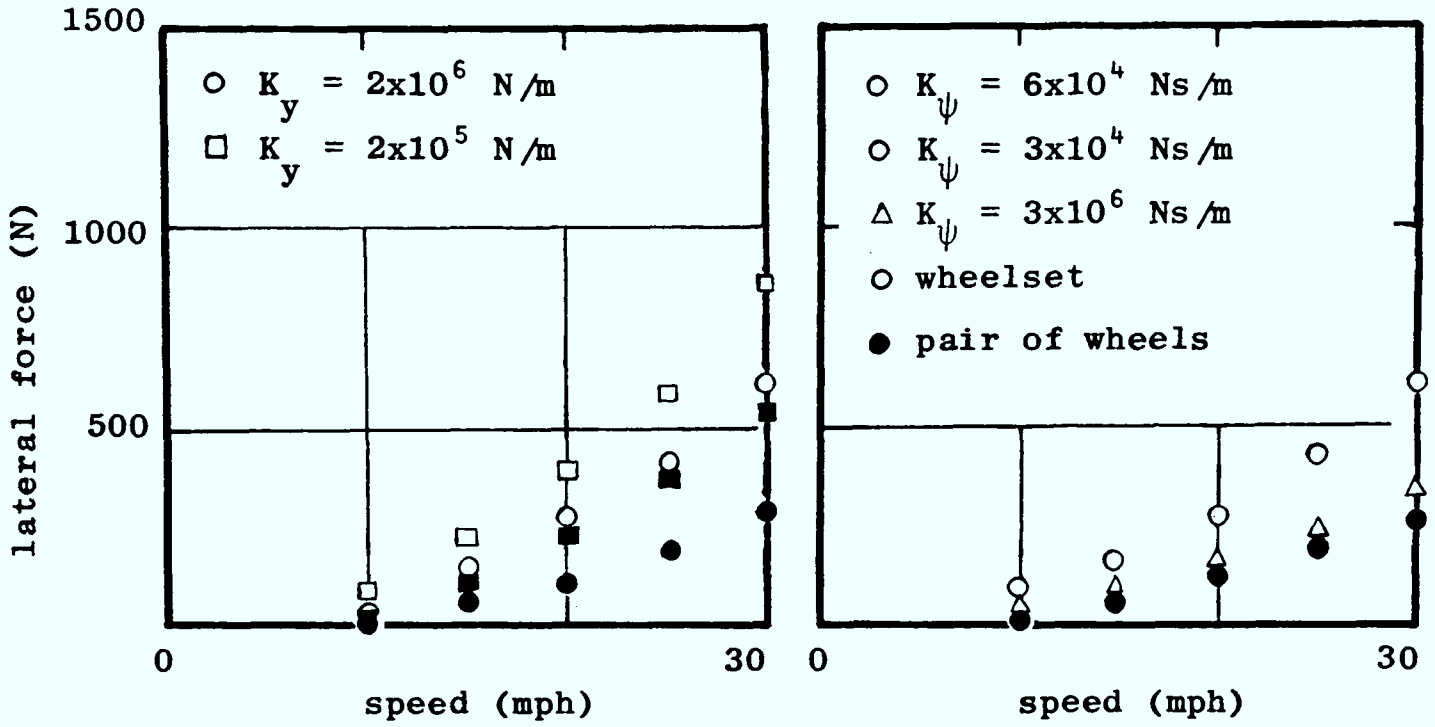

Fig 5.10 Influence of primary suspension on guidance force
(a) Changing lateral stiffness
(b) Changing yaw stiffness

It is clear that a more flexible lateral suspension allows the flange of the wheel to approach the rail more easily, and this leads to a higher guiding force for both configurations. This force is associated mainly with gravitational stiffness. A more flexible yaw suspension does little towards improving the guidance of either configuration, however, if this is made to be more rigid the steering capability associated with the differential creep of the wheels is reduced severely. Changing the damping in the primary suspension has little effect on the guidance.

5.3.6 Effect of axle load

For the leading pair of wheels of the gondola manriding vehicle, the axle load is given by:

$$W = 6500 \text{ N} \qquad (5.34)$$

For a pair of wheels in the middle of an unladen train,

$$W = 13250 \text{ N} \qquad (5.35)$$

For a fully laden train,

$$W = 23250 \text{ N} \qquad (5.36)$$

The effect of axle load on the guidance is illustrated in Fig 5.11.

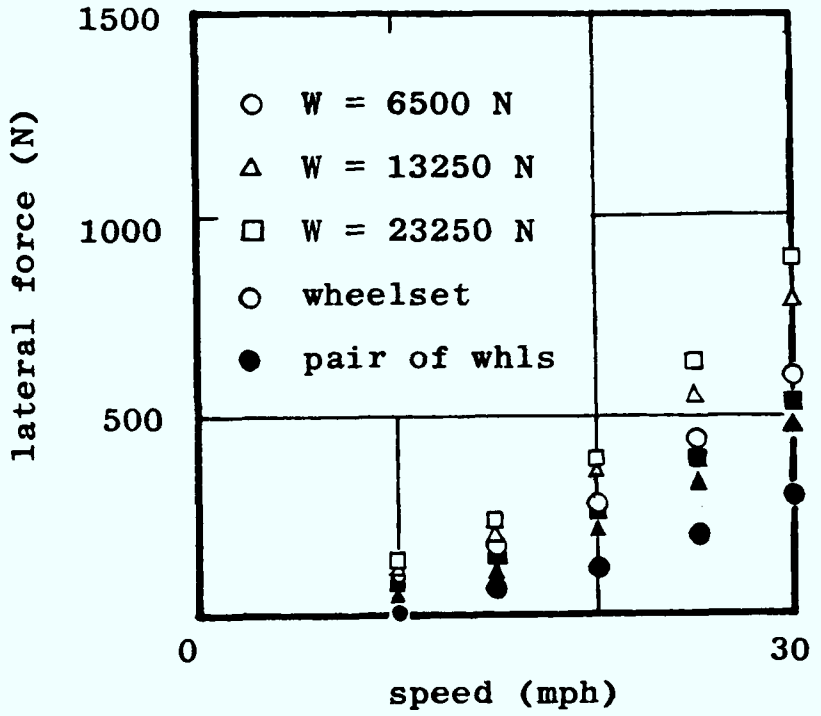

Fig 5.11 Effect of axle load on guidance force

Both the creep and the gravitational stiffness are dependent upon the axle load and this is evident in the results shown: a larger axle load leads to improved guidance for both configurations. For the case of independently revolving wheels the guidance is provided by flange contact and so the lateral flange force is increased. The likelihood of derailment decreases however, as the ratio of

lateral and vertical forces at the flange is smaller for a larger axle load.

5.3.7 Effect of gauge

The manner in which a section of track is laid, and the subsequent lateral loading that occurs as a result of normal traffic, both lead to a variation in the gauge. As the gauge becomes larger the wheels must be displaced further before the flange touches the rail, and this suggests a reduction in the guidance. This is illustrated in Fig 5.12.

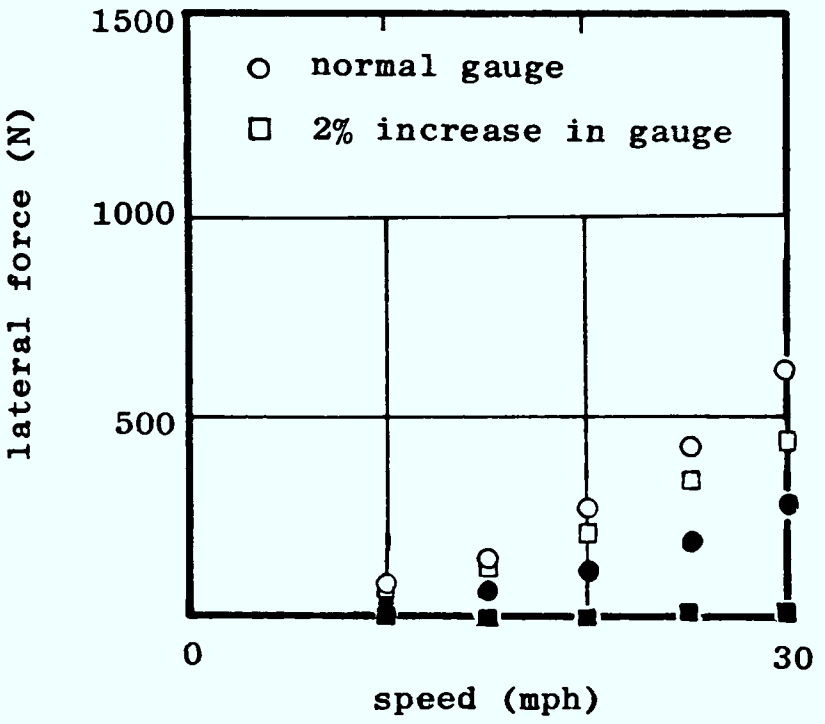

Fig 5.12 Effect of gauge

It can be seen from the figure that independently revolving wheels are quite sensitive to gauge, whereas conventional wheelsets retain the ability to steer towards the centre of the track. An implication of the results is that the incidence of flange contact will eventually reduce to zero as the gauge widens, however, this is clearly not the case. In the absence of bias (such as track cant) the lateral position of a pair of wheels at any given time will be an indeterminant quantity, and the model copes with this by always choosing a condition of zero lateral displacement as equilibrium. In considering the general behaviour of the pair of wheels this is an acceptable simplification, but errors may easily arise if different analysis

techniques are applied to the model (see section 5.2.7).

5.4 Stability of a conventional wheelset

5.4.1 Reason for instability

When a conventional wheelset is displaced laterally it will steer back towards the middle of the track. This occurs as a result of the difference in rolling radii of the two wheels, and is essentially a kinematic phenomenon. If the effects of creep are neglected, an isolated wheelset will continue to oscillate once disturbed, and the wavelength of the oscillation will be given by:

$$\lambda = 2\pi\sqrt{\frac{r_o\, a}{\lambda_o}} \qquad (5.37)$$

where,

λ = wavelength

a = semi-gauge

λ_o = conicity

r_o = rolling radius

This is known generally as the kinematic wavelength (see Wickens (26)).

The motion of a wheelset is modified by the creeping of the wheels and the presence of suspension, and both will damp out oscillation over a certain speed range. However, as the operating speed increases the frequency of the oscillation also gets higher, and eventually it begins to excite the wheelset resonance. When this occurs the oscillation no longer decays away after a disturbance, and the wheelset has an unstable motion which is constrained only by the presence of the flanges. The instability is known as wheelset hunting, and the speed at which it occurs is referred to as the "critical speed".

5.4.2 Technique for evaluating critical speed

The critical speed may be evaluated by considering equations (5.1) and (5.2) in the absence of excitation terms due to track irregularities. The equations become:

$$m\ddot{y} + \left(\frac{2f_{22}}{V} + C_y\right)\dot{y} + (K_y + K_g)\,y - 2f_{22}\psi = 0 \qquad (5.38)$$

$$I_{yy}\ddot{\psi} + \frac{2f_{11}a^2}{V}\dot{\psi} + K_\psi\psi + \frac{2f_{11}a\lambda_o}{r_o}\,y = 0 \qquad (5.39)$$

Which may be rewritten as:

$$\underset{\sim}{M}\ddot{\underset{\sim}{q}} + \underset{\sim}{L}\dot{\underset{\sim}{q}} + \underset{\sim}{K}\underset{\sim}{q} = 0 \qquad (5.40)$$

where,

M = inertia matrix

L = damping matrix

K = stiffness matrix

$\underset{\sim}{q}$ = wheelset co-ordinate vector

This equation is similar to the general form of the equations of motion used to determine the response (see section 2.4.2: equation (2.27)) and is called the "characteristic equation".

Equation (5.4) is linear (flange contact is not being considered here), and will have a solution of the form:

$$\underset{\sim}{q} = J_1 e^{\Lambda t} \qquad (5.41)$$

where,

J_1 = a matrix

Λ = eigenvalues (complex)

= a + jb

Equation (5.41) can be rewritten as:

$$\underset{\sim}{q} = J_1 e^{at} \cdot e^{jb}$$

$$= J_1 e^{at} (\cos bt + j \sin bt) \qquad (5.42)$$

It is clear that the motion will be stable whenever the real part of an eigenvalue, a, has a negative value, as this will lead to an

exponential decay of any oscillation resulting from displacement of the wheelset. The speed at which this real part takes a positive value corresponds to the critical speed.

In order to determine the eigenvalues, equation (5.40) can be rearranged by making the substitution:

$$\underset{\sim}{r} = \dot{\underset{\sim}{q}} \tag{5.43}$$

This leads to the equation,

$$\begin{bmatrix} -I & 0 \\ 0 & M \end{bmatrix} \begin{bmatrix} \dot{\underset{\sim}{q}} \\ \dot{\underset{\sim}{r}} \end{bmatrix} + \begin{bmatrix} 0 & I \\ K & L \end{bmatrix} \begin{bmatrix} \underset{\sim}{q} \\ \underset{\sim}{r} \end{bmatrix} = 0 \tag{5.44}$$

which has a solution of the form:

$$\begin{bmatrix} \underset{\sim}{q} \\ \underset{\sim}{r} \end{bmatrix} = J_2 e^{\Lambda t} \tag{5.45}$$

Combining equations (5.44) and (5.45) leads to the result:

$$A \begin{bmatrix} \underset{\sim}{q} \\ \underset{\sim}{r} \end{bmatrix} = \Lambda \begin{bmatrix} \underset{\sim}{q} \\ \underset{\sim}{r} \end{bmatrix} \tag{5.46}$$

where,

$$A = -\begin{bmatrix} -I & 0 \\ 0 & M \end{bmatrix}^{-1} \cdot \begin{bmatrix} 0 & I \\ K & L \end{bmatrix}$$

Equation (5.46) can be solved using a standard library subroutine (see NAG (31)) over a range of operating speeds. A listing of the program used for this work, which is suitable for examining the stability of any system with a characteristic equation in the form of equation (5.40), is included in Appendix 2. The program is called EIGEN.F77.

5.4.3 Critical speed of a wheelset

The critical speed of a wheelset will be lowest when the conicity is high as the kinematic oscillation is most pronounced in such a case. Using the technique explained in section 5.4.2 the critical speed corresponding to a conicity of $\lambda_o = 0.5$ is evaluated, and this

is shown in Fig 5.13. The frequency of oscillation, which corresponds to the imaginary part of the eigenvalue for wheelset yaw (see equation 5.4)) is also shown in the figure.

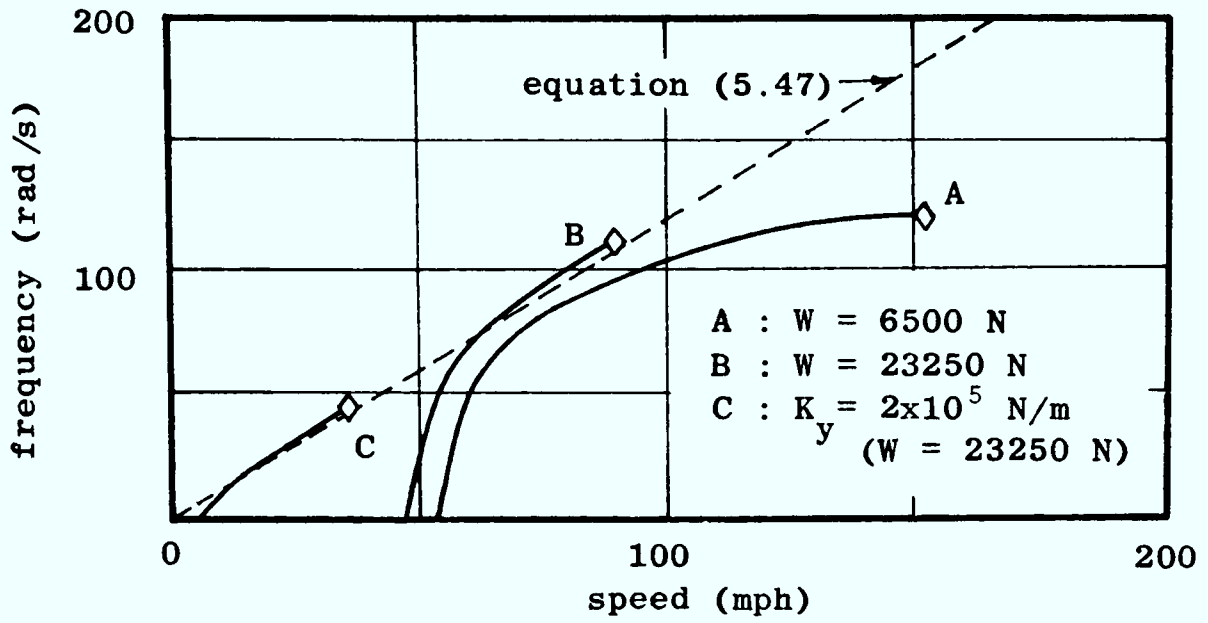

Fig 5.13 Critical speed of a conventional wheelset (λ_o = 0.5)

The critical speed is always above the operating speed range of the vehicle even when the suspension is ten times more flexible, and this indicates that wheelset hunting will not be a problem with the gondola vehicle. For large creep coefficients (cases B and C) the curves on the figure converge to a line marking a linear relationship between frequency and speed and this is the "kinematic frequency":

$$\omega = \sqrt{V \frac{\lambda_o}{r_o a}} \qquad (5.47)$$

The critical speed corresponds approximately to the frequency at which the sway resonance of the wheelset is excited, and so for large creep coefficients this may be evaluated using the expression:

$$V_c \simeq \sqrt{\frac{r_o a}{\lambda_o} \frac{K_y}{m}} \qquad (5.48)$$

As the creep coefficient gets smaller the steering ability of the wheelset reduces and so the critical speed increases. The creep

coefficients evaluated from Kalker's Theory will generally be larger than experimentally obtained coefficients (see Fig 2.9) and so the critical speeds shown in Fig 5.13 represent limiting cases.

Chapter 6

The Gondola Manriding Car

6.1 Introduction

The gondola manriding car (see Fig 6.1) is the fastest manriding vehicle in service in British coal mines, and currently travels at speeds up to 25 mph.

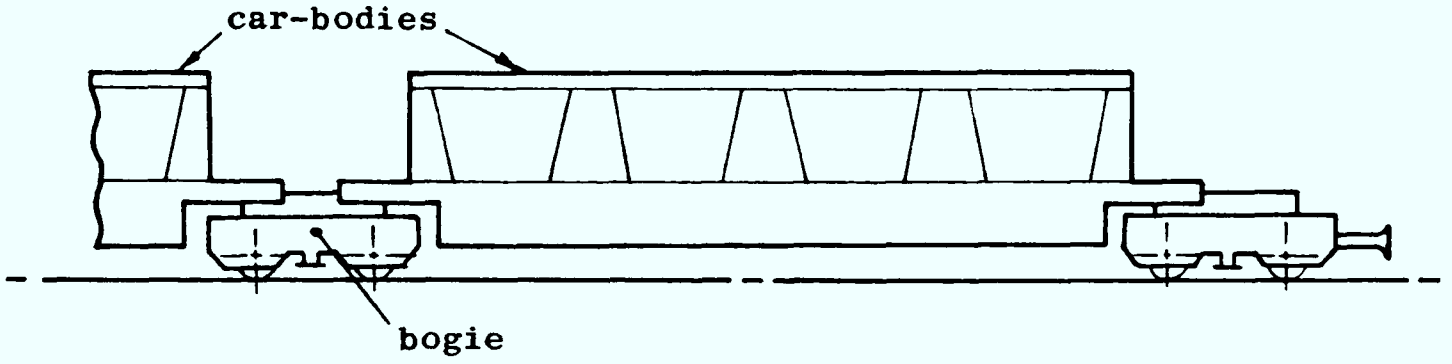

Fig 6.1 The gondola manriding car
(Photograph is shown in Fig 1.4)

The behaviour of the vehicle depends on the motion of the wheels, the motion of the rails, and on the suspension between the wheels and the body. The first of these features has been discussed in Chapter 5, and the behaviour as a consequence of the suspension is examined here. This is done by way of a mathematical model which looks at the response to track vertical profile irregularities. The model is introduced in section 6.2, and predictions are compared with test results in section 6.3. The model is used to investigate the effects on ride of different operating conditions in section 6.4. In addition, the effects of operating with unbalanced wheels is examined in section 6.5, and flange wear is discussed in section 6.6.

6.2 Model of the vertical dynamics

6.2.1 Modelling decisions

The model is constructed principally to predict the pitch and bounce of the leading (or trailing) bogie and car-body of a train in response to track irregularities. The motion of the locomotive is also

examined. This is illustrated in Fig 6.2.

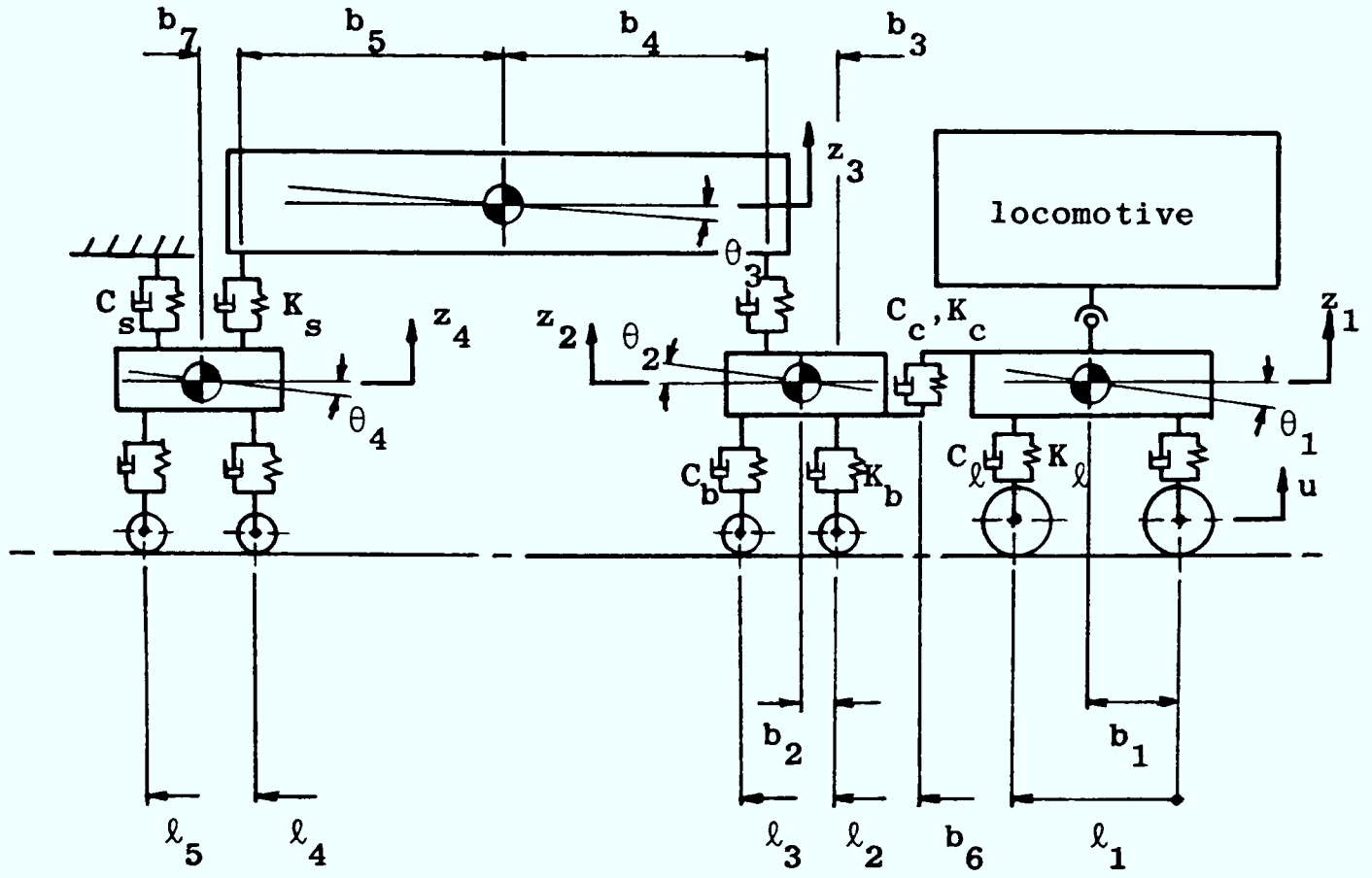

Fig 6.2 Model of the gondola manriding car being hauled by a Bo-Bo locomotive (photograph is shown in Fig 1.8)

The input to the model is the vertical profile of the track, and the wheels and rails are considered to remain in contact. The vehicle is examined when travelling at constant speed which allows the inputs to each of the wheels to be related by a time delay: the inputs may thus be expressed in terms of a single input at the front wheels.

Chevrons provide the primary suspensions for both the locomotive and manriding cars. The secondary suspension of the manriding car is provided by coil springs which connect the bogie and car-body via linkages (see Fig 6.3). The suspension elements are treated as shown in Fig 6.2 and are considered to be linear.

The track is taken to be rigid in the model, however, resilience can be included by considering the track stiffness to act in series with the primary suspension stiffnesses of the locomotive and manrider. This results in a reduction of these stiffnesses.

$$\mathbf{M} = \begin{bmatrix} m_1 + m_t & 0 & 0 & 0 & 0 & 0 & 0 & 0 \\ 0 & I_1 & 0 & 0 & 0 & 0 & 0 & 0 \\ 0 & 0 & m_2 & 0 & 0 & 0 & 0 & 0 \\ 0 & 0 & 0 & I_2 & 0 & 0 & 0 & 0 \\ 0 & 0 & 0 & 0 & m_3 & 0 & 0 & 0 \\ 0 & 0 & 0 & 0 & 0 & I_3 & 0 & 0 \\ 0 & 0 & 0 & 0 & 0 & 0 & m_4 & 0 \\ 0 & 0 & 0 & 0 & 0 & 0 & 0 & I_4 \end{bmatrix}$$

$$\mathbf{L} = \begin{bmatrix} 2C_t+C_a & (b_6-b_1)C_c & -C_a & (l_2+b_2-b_6)C_a & 0 & 0 & 0 & 0 \\ (b_6-b_1)C_c & 2b_1^2C_t+(b_6-b_1)^2C_a & -(b_6-b_1)C_c & (b_6-b_1)(l_2+b_2-b_6)C_c & 0 & 0 & 0 & 0 \\ -C_c & -(b_6-b_1)C_c & 2C_b+C_a+C_c & (l_3-l_2-2b_2)C_b+(b_3-b_2)C_a-(l_2+b_2-b_6)C_c & -C_a & b_4C_a & 0 & 0 \\ (l_2+b_2-b_6)C_c & (b_6-b_1)(l_2+b_2-b_6)C_c & (l_3-l_2-2b_2)C_b+(b_3-b_2)C_a-(l_2+b_2-b_6)C_c & (l_3-l_2-b_2)^2C_b+b_2^2C_b+(b_3-b_2)^2C_a+(l_2+b_2-b_6)^2C_c & -(b_3-b_2)C_a & (b_3-b_2)b_4C_a & 0 & 0 \\ 0 & 0 & -C_a & -(b_3-b_2)C_a & 2C_a & (b_5-b_4)C_a & -C_a & b_7C_a \\ 0 & 0 & b_4C_a & (b_3-b_2)b_4C_a & -(b_3-b_2)C_a & (b_4^2+b_5^2)C_a & -b_5C_a & b_5b_7C_a \\ 0 & 0 & 0 & 0 & -C_a & -b_5C_a & 2C_a+2C_b & 0 \\ 0 & 0 & 0 & 0 & b_7C_a & b_5b_7C_a & 0 & 2b_7C_a+\frac{1}{2}(l_5-l_4)^2C_b \end{bmatrix}$$

$$\mathbf{K} = \begin{bmatrix} 2K_t+K_a & (b_6-b_1)K_c & -K_a & (l_2+b_2-b_6)K_a & 0 & 0 & 0 & 0 \\ (b_6-b_1)K_c & 2b_1^2K_t+(b_6-b_1)^2K_c & -(b_6-b_1)K_c & (b_6-b_1)(l_2+b_2-b_6)K_c & 0 & 0 & 0 & 0 \\ -K_c & -(b_6-b_1)K_c & 2K_b+K_a+K_c & (l_3-l_2-2b_2)K_b+(b_3-b_2)K_a-(l_2+b_2-b_6)K_c & -K_a & b_4K_a & 0 & 0 \\ (l_2+b_2-b_6)K_c & (b_6-b_1)(l_2+b_2-b_6)K_c & (l_3-l_2-2b_2)K_b+(b_3-b_2)K_a-(l_2+b_2-b_6)K_c & (l_3-l_2-b_2)^2K_b+b_2^2K_b+(b_3-b_2)^2K_a+(l_2+b_2-b_6)^2K_c & -(b_3-b_2)K_a & (b_3-b_2)b_4K_a & 0 & 0 \\ 0 & 0 & -K_a & -(b_3-b_2)K_a & 2K_a & (b_5-b_4)K_a & -K_a & b_7K_a \\ 0 & 0 & b_4K_a & (b_3-b_2)b_4K_a & -(b_3-b_2)K_a & (b_4^2+b_5^2)K_a & -b_5K_a & b_5b_7K_a \\ 0 & 0 & 0 & 0 & -K_a & -b_5K_a & 2K_a+2K_b & 0 \\ 0 & 0 & 0 & 0 & b_7K_a & b_5b_7K_a & 0 & 2b_7K_a+\frac{1}{2}(l_5-l_4)^2K_b \end{bmatrix}$$

$$\mathbf{C} = \begin{bmatrix} C_t & C_t & 0 & 0 & 0 & 0 \\ -b_1C_t & b_1C_t & 0 & 0 & 0 & 0 \\ 0 & 0 & C_b & C_b & 0 & 0 \\ 0 & 0 & -b_2C_b & (l_3-l_2-b_2)C_b & 0 & 0 \\ 0 & 0 & 0 & 0 & 0 & 0 \\ 0 & 0 & 0 & 0 & 0 & 0 \\ 0 & 0 & 0 & 0 & C_b & C_b \\ 0 & 0 & 0 & 0 & -\frac{1}{2}(l_5-l_4)C_b & \frac{1}{2}(l_5-l_4)C_b \end{bmatrix}$$

$$\mathbf{D} = \begin{bmatrix} K_t & K_t & 0 & 0 & 0 & 0 \\ -b_1K_t & b_1K_t & 0 & 0 & 0 & 0 \\ 0 & 0 & K_b & K_b & 0 & 0 \\ 0 & 0 & -b_2K_b & (l_3-l_2-b_2)K_b & 0 & 0 \\ 0 & 0 & 0 & 0 & 0 & 0 \\ 0 & 0 & 0 & 0 & 0 & 0 \\ 0 & 0 & 0 & 0 & K_b & K_b \\ 0 & 0 & 0 & 0 & -\frac{1}{2}(l_5-l_4)K_b & \frac{1}{2}(l_5-l_4)K_b \end{bmatrix}$$

$$\mathbf{T}(s) = \begin{bmatrix} 1 \\ e^{-l_1 s/V} \\ e^{-l_2 s/V} \\ e^{-l_3 s/V} \\ e^{-l_4 s/V} \\ e^{-l_5 s/V} \end{bmatrix} \qquad \underset{\sim}{q} = \begin{bmatrix} z_1 \\ \theta_1 \\ z_2 \\ \theta_2 \\ z_3 \\ \theta_3 \\ z_4 \\ z_5 \end{bmatrix}$$

Fig 6.4 Matrices for equations of motion

of the vehicle. The general purpose computer program (see section 2.6.1) may be used to carry out the solution, and listings of the subroutines containing the information in Fig 6.4 are included in Appendix 2. The solutions are presented and compared with test results in section 6.3.3.

6.2.3 Parameter values

Values are given below for the masses, inertias, stiffness and damping elements, and dimensions of the gondola car as used in the model. The notation is shown in Fig 6.2.

m_ℓ	= 9000 kg *	C_b	= 3500 Ns/m
m_1	= 2000 kg *	C_s	= 2×10^4 Ns/m
I_1	= 1300 kg m^2 *	C_c	= 0
m_2	= 1018 kg *	b_1	= 0.9 m *
I_2	= 200 kg m^2 *	b_2	= 0.5 m
m_3	= 1850 kg *	b_3	= 0.8 m *
I_3	= 6500 kg m^2 *	b_4	= 2.96 m *
m_4	= 865 kg *	b_5	= 2.96 m *
I_4	= 130 kg m^2 *	b_6	= 2.9 m *
K_1	= 3.5×10^6 N/m	b_7	= 0.31 m *
K_b	= 1.6×10^6 N/M *	ℓ_1	= 1.6 m *
K_s	= 1.6×10^5 N/m *	ℓ_2	= 3.46 m *
K_c	= 2×10^5 N/m	ℓ_3	= 4.45 m *
C_ℓ	= 2×10^4 Ns/m	ℓ_4	= 9.98 m *
		ℓ_5	= 10.97 m * (6.1)

Where a value has been measured or derived from measured quantities it is indicated by an asterisk. Other values have been estimated.

6.2.4 Resonant frequencies

The resonant frequencies may be determined by considering the

equations of motion in the absence of excitation from the track. The equations are thus written in the form of equation (5.40):

$$M\ddot{q} + L\dot{q} + Kq = 0$$

The eigenvalues for this equation are evaluated using equation (5.46) (see section 5.4.2) and the resonant frequencies correspond to the imaginary parts of the eigenvalues. A listing of the program EIGEN.F77, which may be used to evaluate the eigenvalues, is included in Appendix 2. The resonant frequencies of the gondola manriding car are determined on this basis, and these are shown in Table 6.1.

Resonance	Frequency (Hz)
Locomotive	
Bounce	4.0
Bogie pitch	10
Manrider	
Car-body bounce	1.3
Car-body pitch	-
Leading bogie bounce	8.3
Leading bogie pitch	12

Table 6.1 Resonant frequencies of gondola manriding car

6.3 Vehicle testing

6.3.1 Tests at Ellington Colliery

A series of tests was carried out with the gondola manriding cars travelling along the main underground railway at Ellington Colliery. The train consisted of eleven cars being hauled by a Bo-Bo locomotive (see Fig 1.8). The motions of the trailing bogie of the locomotive, and of the leading bogie and car-body of the manriding car, were monitored by means of accelerometers (see Fig 6.5) as the train travelled along the track, and the results were recorded on magnetic tape. The motions of the trailing bogie and car-body of the manriding car were also recorded. Tests were carried out at

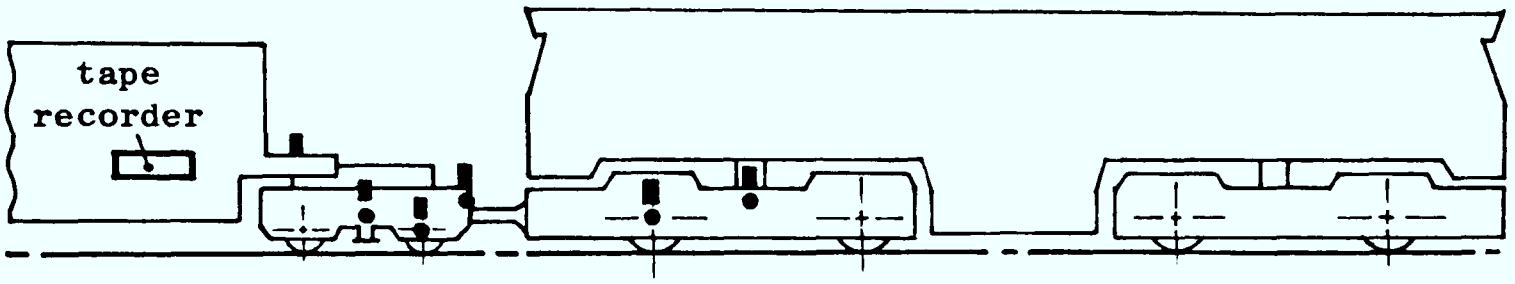

accelerometers

- monitoring z direction (vertical)
- monitoring y direction (lateral)

Fig 6.5 Instrumentation for tests

two nominal speeds (16 mph and 21 mph) travelling principally on track laid in concrete. Several tests were carried out on track laid on ballast.

6.3.2 Data processing

The test data was recorded in the form of a variation of acceleration with time and processed using a FFT spectrum analyser. This type of analyser uses the technique explained in section 3.3.2 (based on temporal rather than spatial co-ordinates) and yields the acceleration spectral densities describing the motion of the vehicle. These spectral densities are included in Appendix 4.

6.3.3 Comparison of model and test results

The validity of the mathematical model is assessed in this section against the measured acceleration spectral densities. The input to the model is the track vertical profile which is evaluated using the method described in section 3.2.3: the wheels of the locomotive are considered to remain in contact with the rails and measurements of the vertical movement of the axle are thus considered to correspond to the profile of the track. This leads to a description of the track in terms of a spectral density as illustrated in Fig 3.10, which may be expressed in the form of equation (3.38):

$$S_u(f) = \frac{AV^{n-1}}{f^n}$$

where,

$S_u(f)$ = spectral density describing input

A = roughness coefficient
= 5×10^{-8} $m^2 cyc^3/m^3$

n = integer exponent = 4

f = frequency

The acceleration spectral densities are evaluated from the model using equation (2.63):

$$S_{\ddot{q}}(f) = |H(f)|^2 \omega^4 S_u(f)$$

where,

H(f) = transfer function

ω = $2\pi f$

This may be done using the general purpose plotting program (see section 2.6.2).

The predicted vertical motion of the rear wheels of the locomotive corresponds quite closely to the test results (see Fig 6.6) for the train travelling both on track laid in concrete and track laid on ballast. The track resilience is incorporated in the latter case by considering a nominal track stiffness ($K_t = 2 \times 10^6$ N/m: see Appendix 4) to act in series with the primary suspension. The results shown in this figure substantiate the discussion in section 3.2.3 regarding the inaccuracy of describing vertical profile for resilient track on the basis of measurements of axle acceleration.

In general the outcome of the modelling of the manriding car compares favourably with measured results (see Figs 6.6 to 6.11). However there are instances where the results diverge. The model does not incorporate the roll of any vehicle components and, as a result, neither the resonances associated with the roll of the bogie or of the pair of wheels appear in the predictions. These occur at 15 Hz and 17 Hz respectively and are indicated by the letters A and B in the figures. In addition, there are peaks in the test results owing to the cars being fitted with unbalanced wheels (indicated by

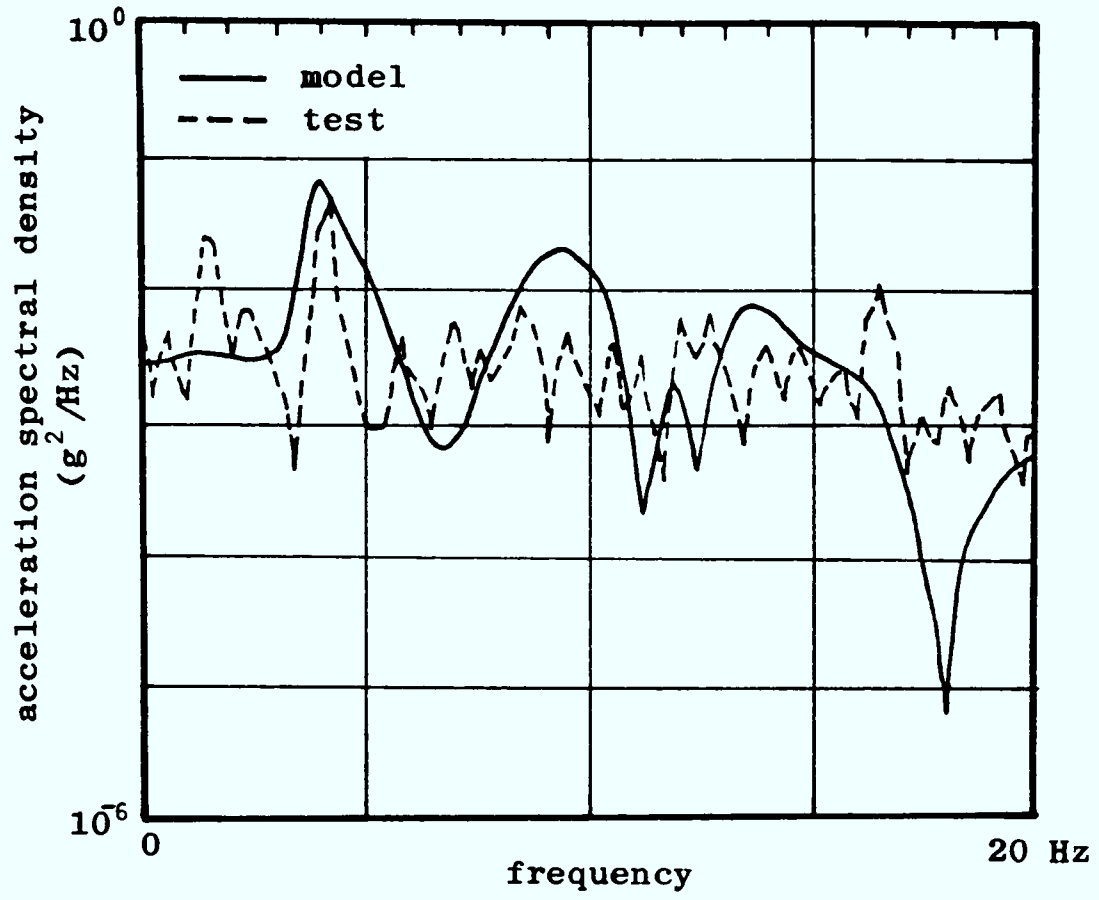

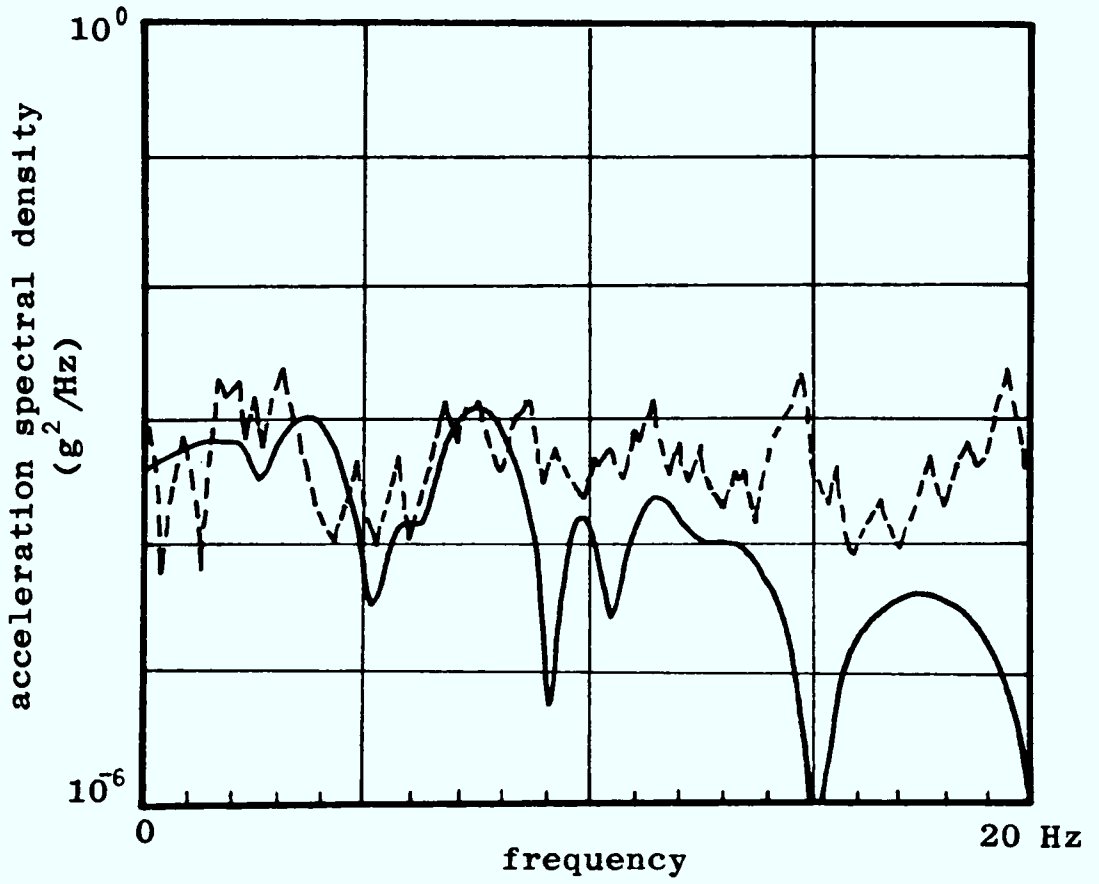

Fig 6.6 Bounce of locomotive rear wheels (speed = 21 mph)
(a) Rigid track (laid in concrete)
(b) Resilient track (laid on ballast)

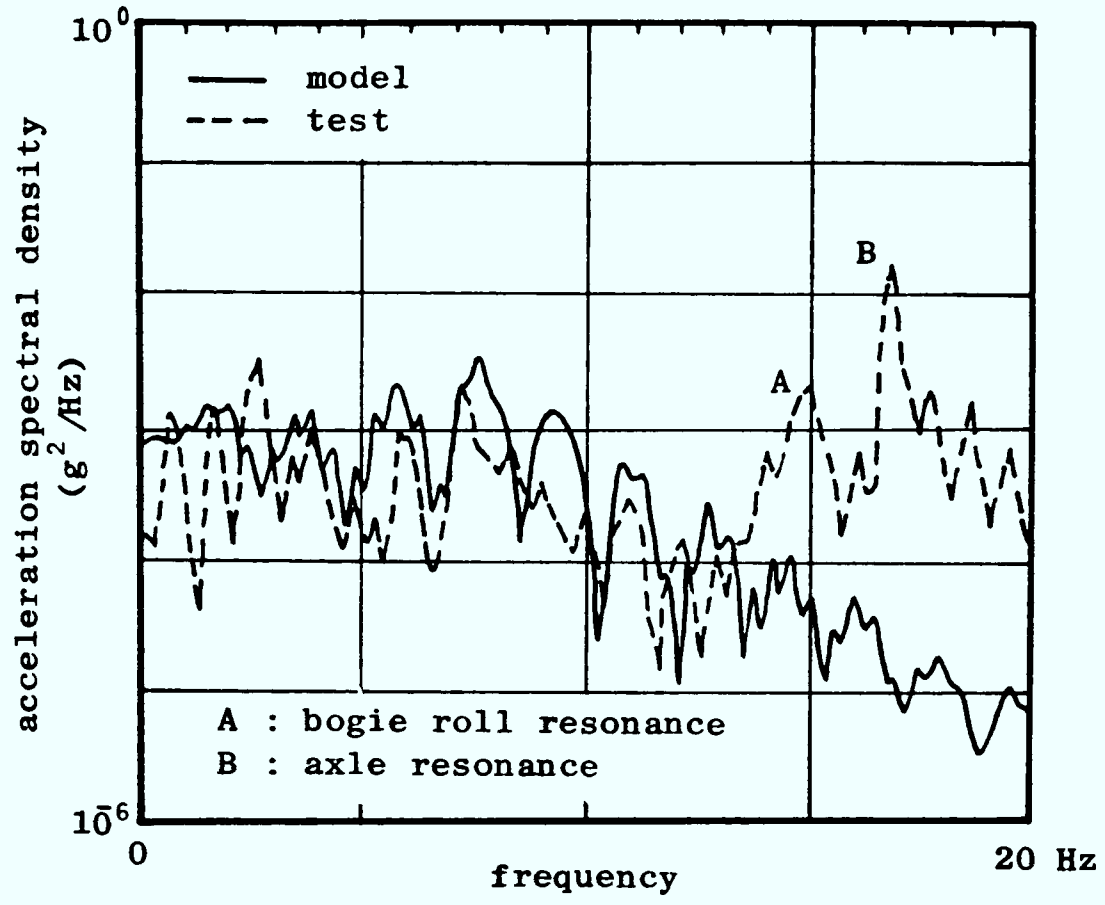

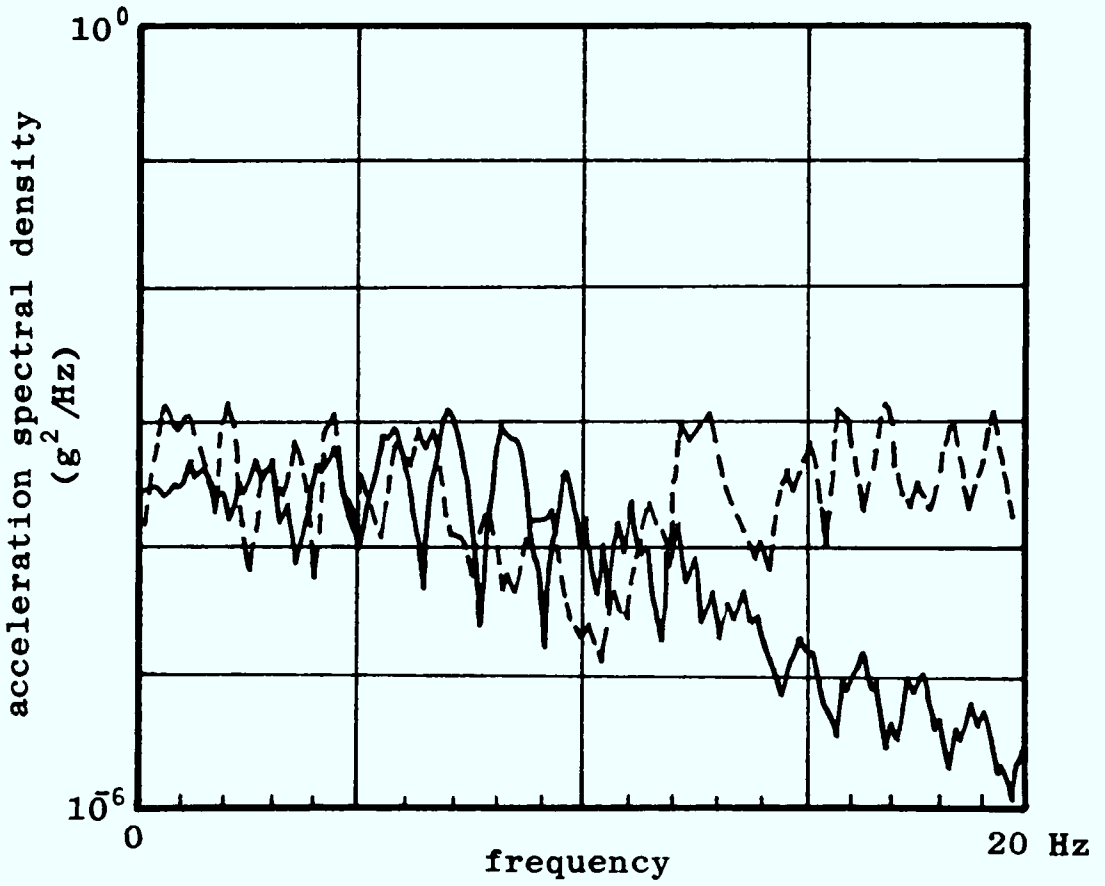

Fig 6.7 Vertical motion at front of leading car-body on rigid track
(a) speed = 21 mph
(b) speed = 16 mph

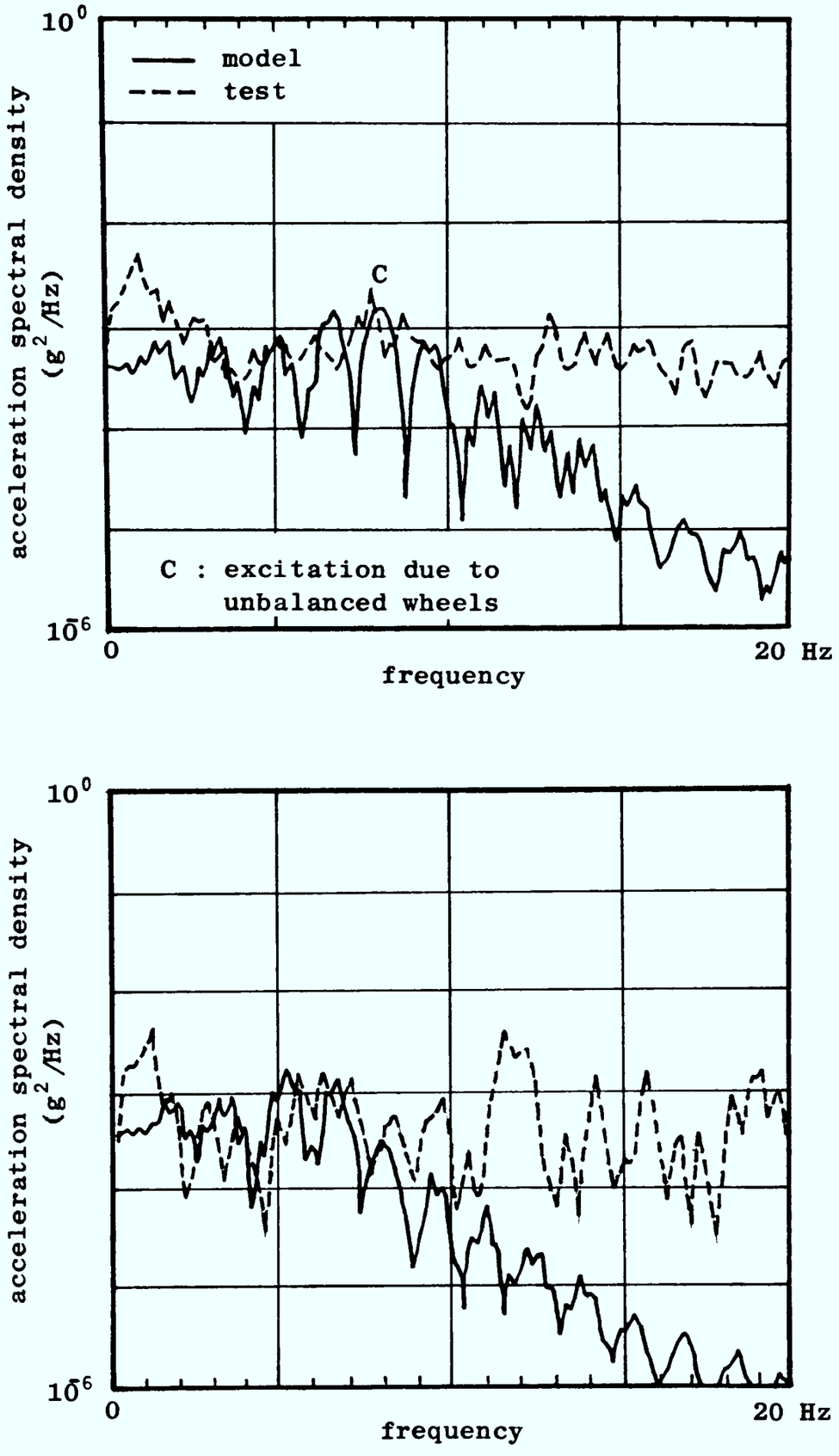

Fig 6.8 Vertical motion (speed = 18 mph)
(a) Rear of trailing car-body (rigid track)
(b) Front of leading car-body (resilient track)

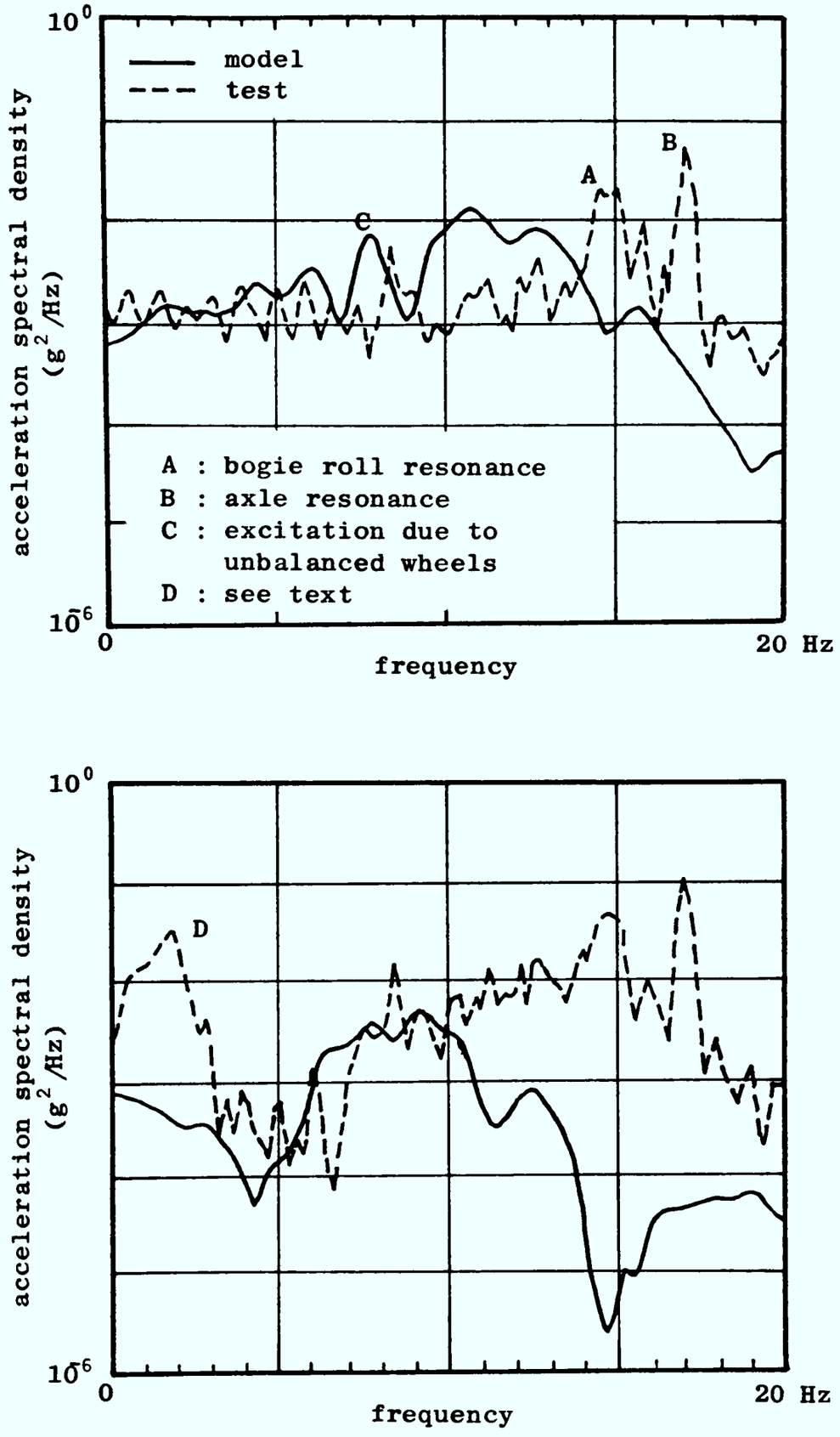

Fig 6.9 Vertical motion on rigid track (speed = 21 mph)
(a) Front of leading bogie
(b) Middle of leading bogie

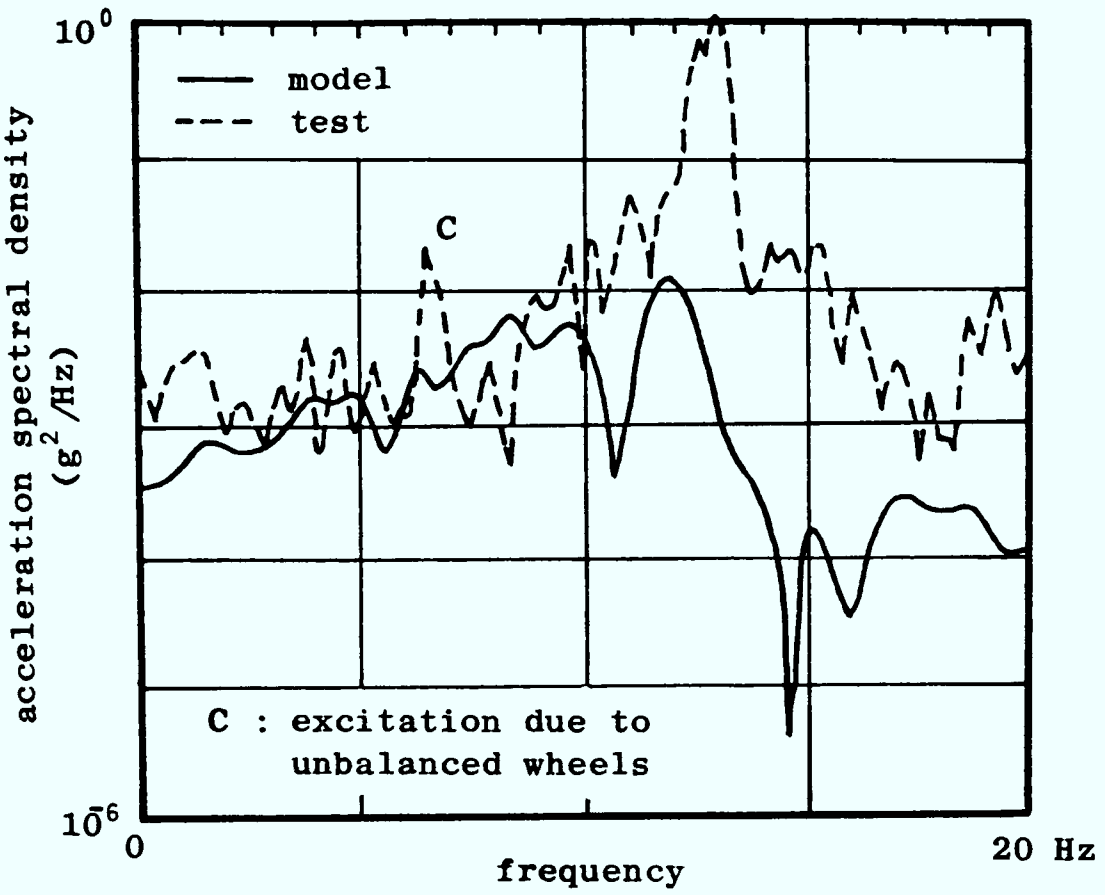

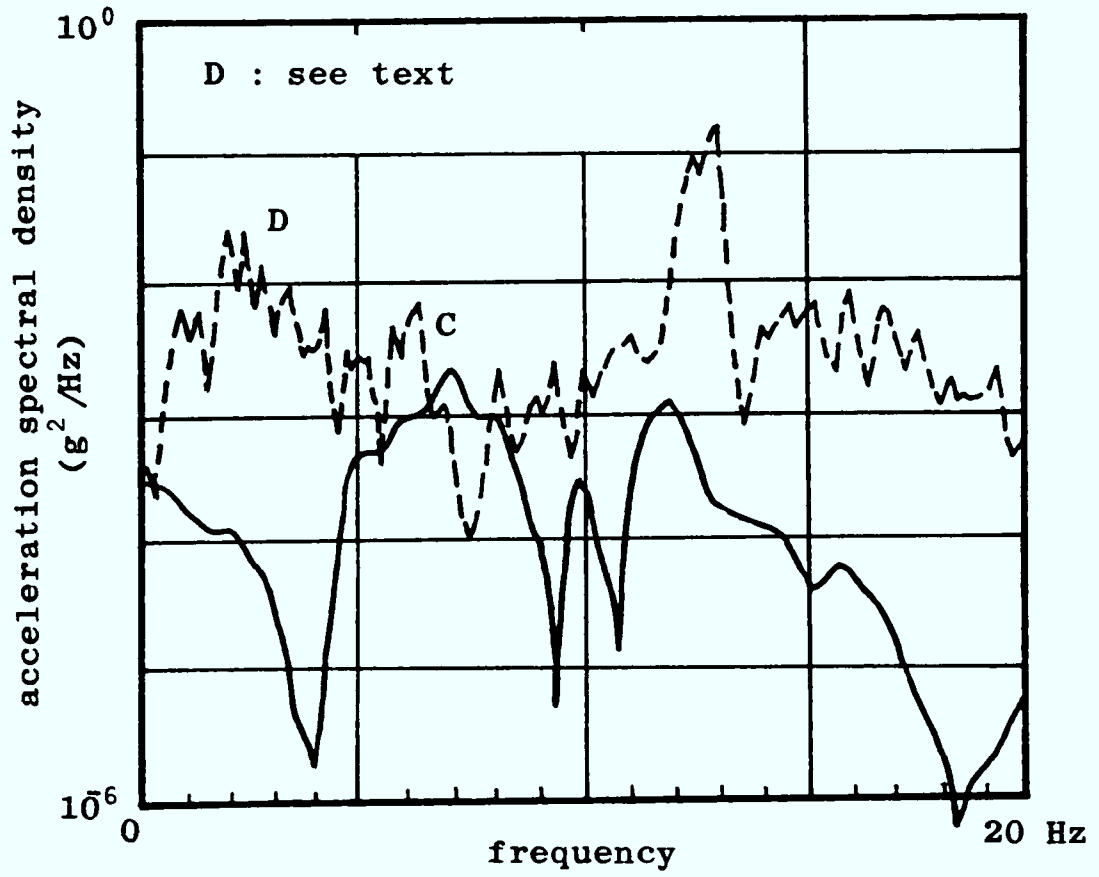

Fig 6.10 Vertical motion on rigid track(speed = 16 mph)
(a) Front of leading bogie
(b) Middle of leading bogie

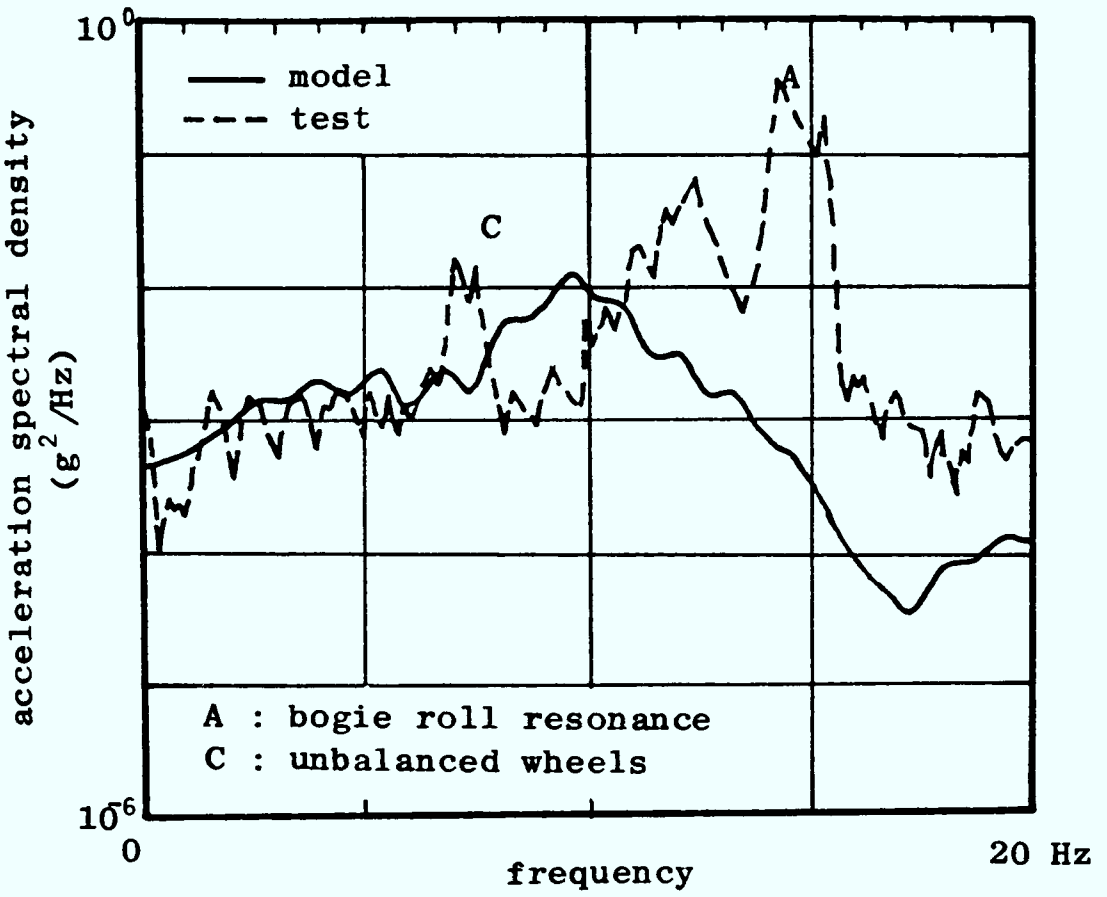

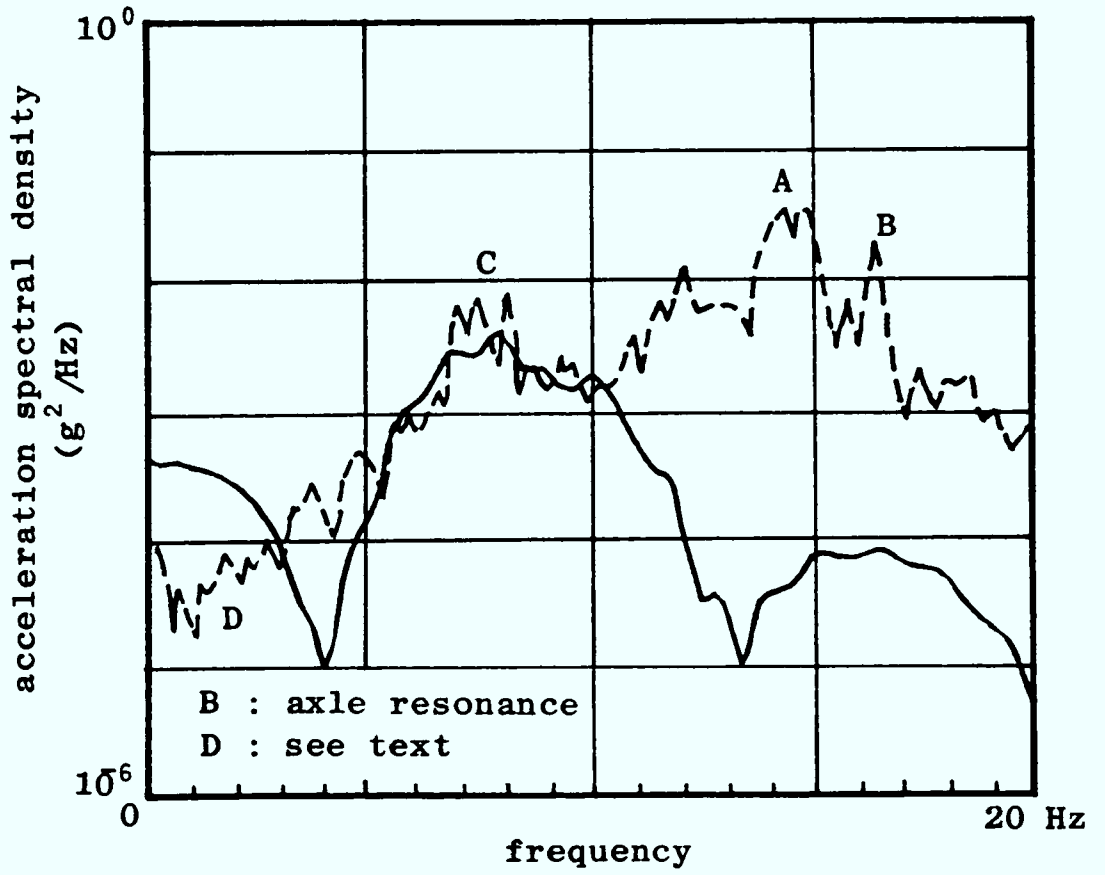

Fig 6.11 Vertical motion on rigid track (speed = 18 mph)
(a) Rear of trailing bogie
(b) Middle of trailing bogie

the letter C in the figures) and these are also absent from the predictions. The frequency at which a peak occurs is related to the forward speed of the vehicle by the expression:

$$f = \frac{\omega}{2\pi} = \frac{1}{2\pi} \left(\frac{V}{r_o}\right) \qquad (6.2)$$

where,

V = forward speed

r_o = wheel radius

The forces which occur as a result of the unbalanced wheels act to excite the resonances due to bogie and axle roll when the train travels at 21 mph (see Fig 6.9), and they excite the bogie pitch resonance when the train travels at 16 mph (see Fig 6.10). The effects of operating with unbalanced wheels is discussed further in sections 6.5 and 6.6.

Finally, the simple treatment of the secondary suspension (see section 6.2.1) takes no account of the transmission of car-body motion to the bogie via the pivot on the connecting linkage (see Fig 6.3). Although this has little effect on the predictions of car-body and locomotive behaviour, it does tend to distort the low frequency results for the middle of the bogie (indicated by the letter D in Figs 6.9, 6.10 and 6.11). The model has been developed principally to look at the ride of the car-body and so these inaccuracies are acceptable.

6.4 The ride of the vehicle

6.4.1 General considerations

The ride of the vehicle is assessed by applying the criterion introduced in section 4.2.3 to the model predictions. This criterion is based on permitted times of exposure to vibration. The vibration is expressed in terms of rms accelerations measured over third octave bands which are evaluated from the acceleration spectral densities using equation (4.1):

$$a_{rms} = \sqrt{S_{q}..(f)\ \Delta f}$$

where,

Δf = third octave frequency band

These are determined from the model using the general purpose plotting program (see section 2.6.2). No account is taken in this section of the effects on ride of using unbalanced wheels, but these are examined in section 6.5.3.

6.4.2 Effect of speed

On the basis of the results shown in Fig 6.12, the ride of the gondola car is acceptable at speeds in excess of 30 mph when the vehicle travels on track of a comparable standard to the track laid in concrete at Ellington Colliery ($A = 5 \times 10^{-8}$ $m^2 cyc^3/m^3$: see Fig 3.10). The ride of the locomotive is also acceptable (see Fig 6.13).

6.4.3 Effect of condition of track

The ride of the vehicle depends on the condition of the track and this is described in the mathematical model by the value of the roughness coefficient. Increasing this coefficient simulates a poorer quality track, and this leads to a poorer ride. The model of the vehicle is linear and so multiplying the roughness coefficient by a constant has the effect of multiplying the rms acceleration by the square root of that constant. In Figs 6.12 and 6.13, in which the rms accelerations are plotted logarithmically, this results in the acceleration values being displaced upwards. It is clear that for any given speed there will be a maximum value of the roughness coefficient for which the ride is only marginally acceptable, and these values can be evaluated from Figs 6.12 and 6.13. This leads to the results shown in Fig 6.14, which provides a relationship between the maximum permissible roughness coefficient and speed for both the manriding car and Bo-Bo locomotive.

6.4.4 Effect of secondary suspension

The effect of the secondary suspension is assessed by comparing the ride of the existing vehicle (see Fig 6.12) with the ride of a vehicle with a very stiff secondary suspension (see Fig 6.15). The latter case corresponds to a vehicle with a pivot connection between

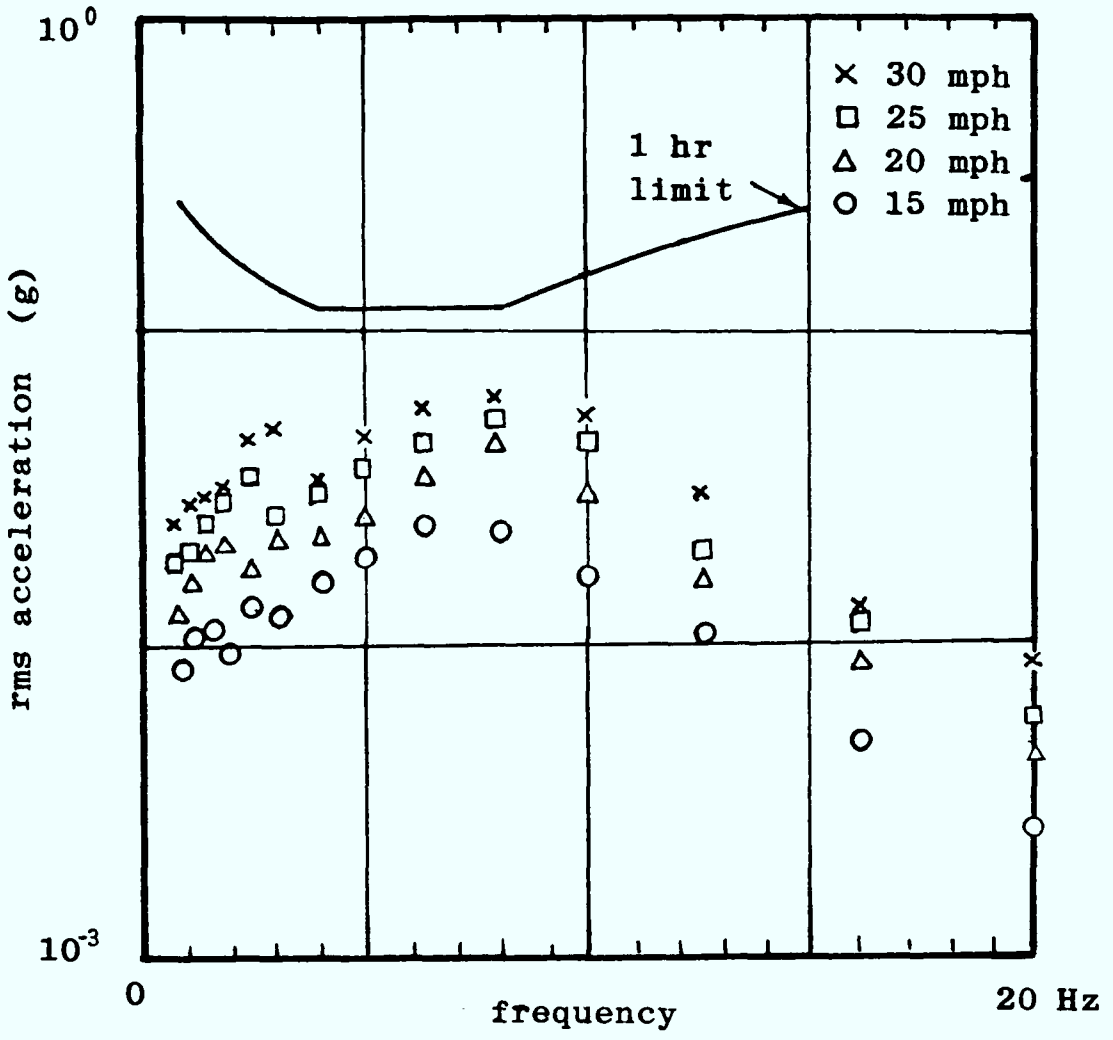

Fig 6.12 Rms accelerations at front of leading car-body

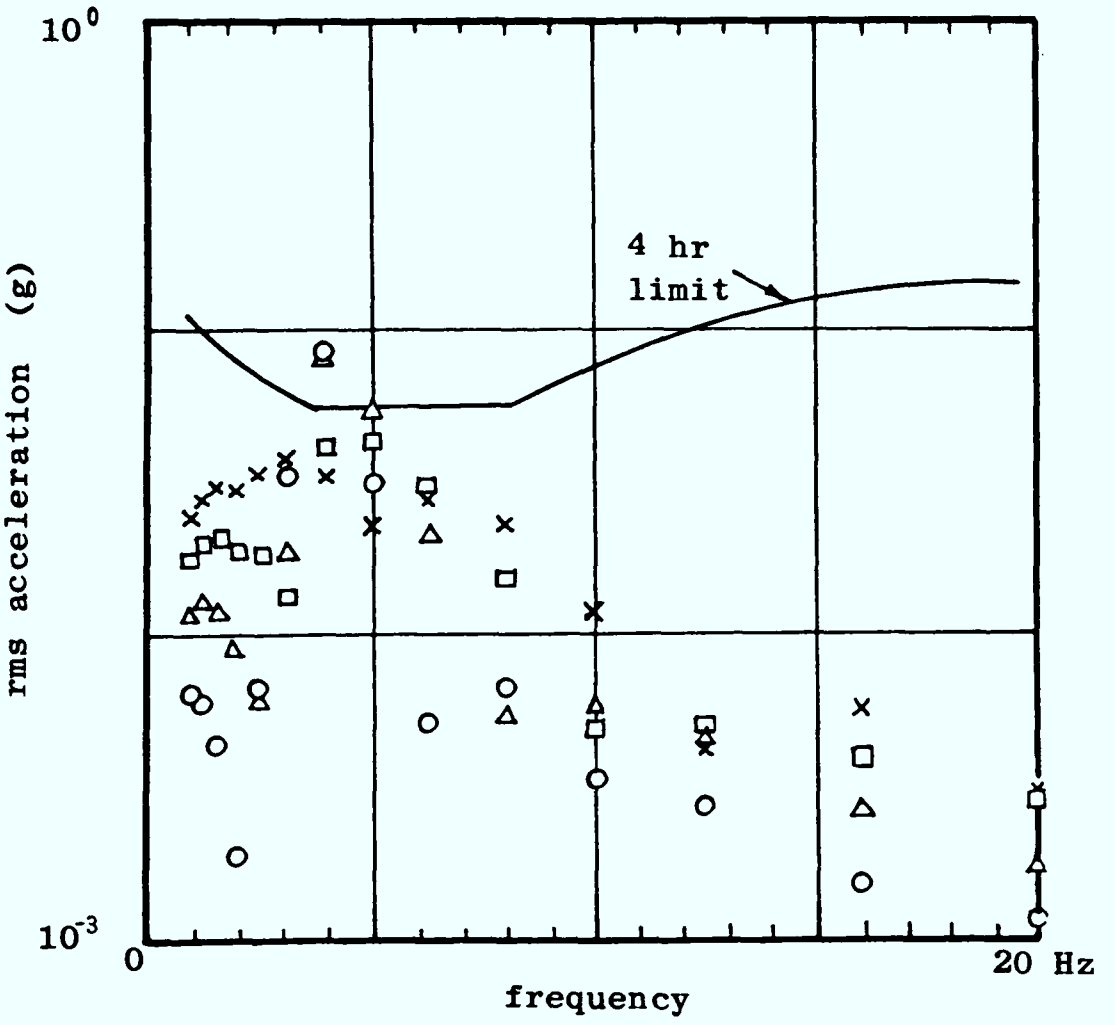

Fig 6.13 Rms accelerations at driver's seat of Bo-bo locomotive

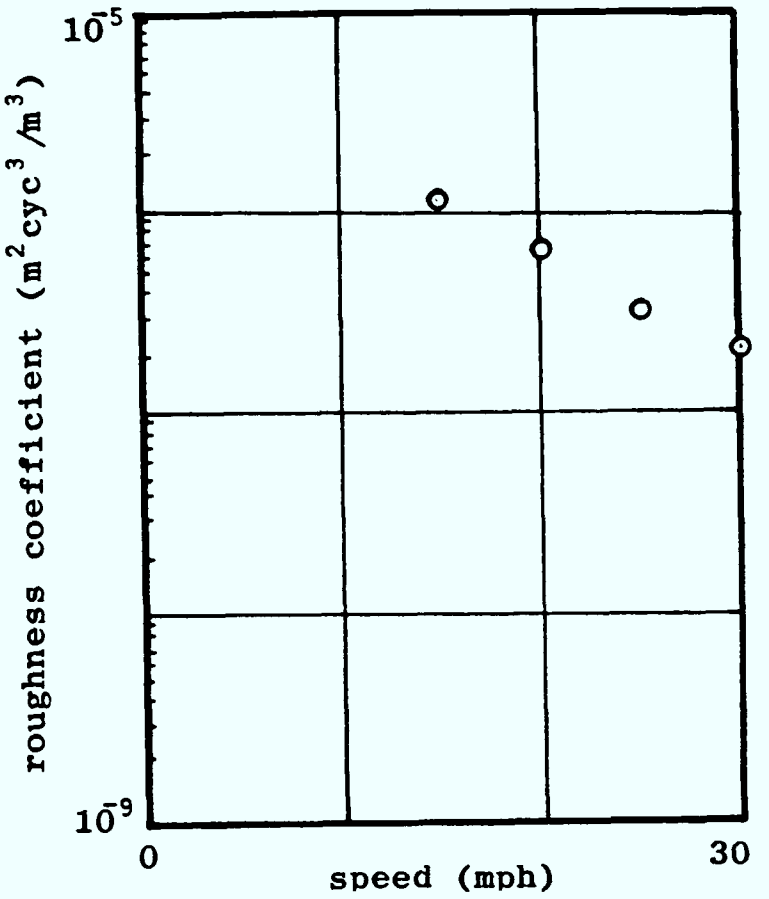

(a)

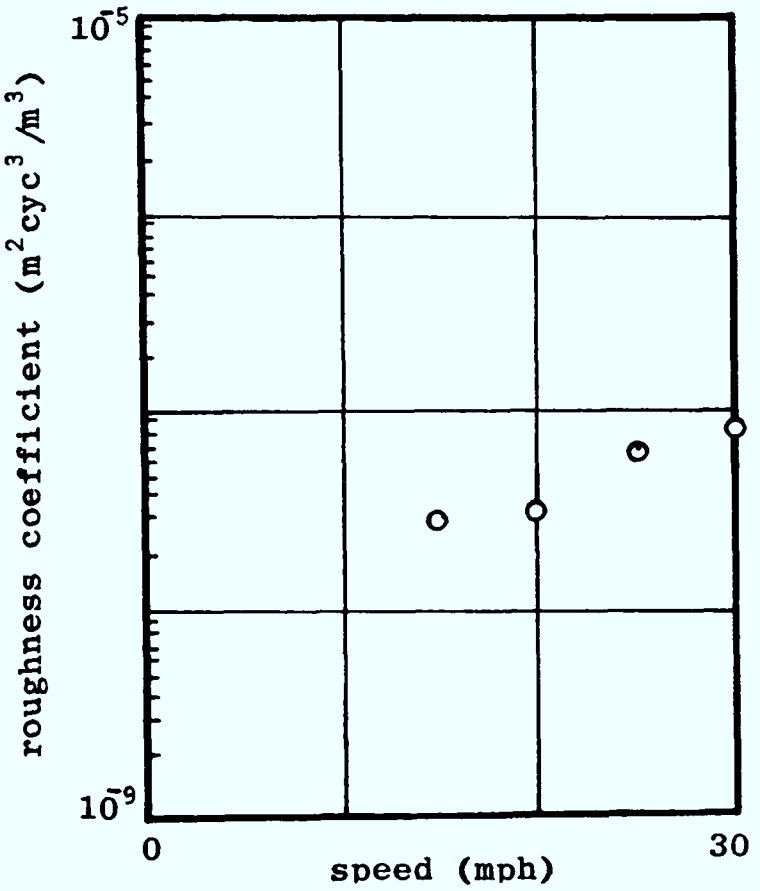

(b)

Fig 6.14 Relationship between the maximum permissible values of roughness coefficient, A, and speed for an acceptable ride.
(a) Front of leading car-body
(b) Driver's seat of Bo-bo locomotive

the bogie and car-body.

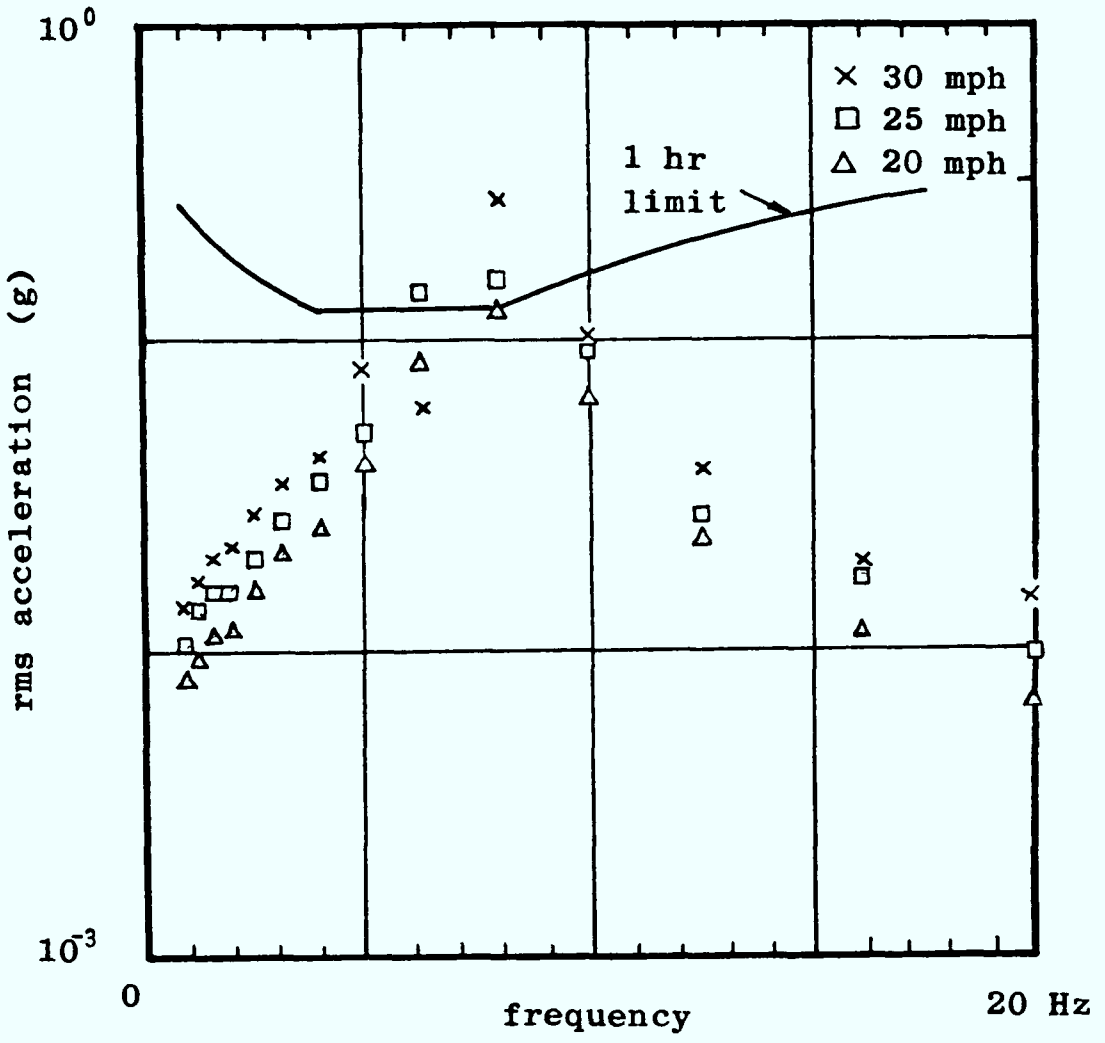

Fig 6.15 Rms accelerations at front of car-body of gondola manriding vehicle (stiff secondary suspension)

It is clear that the ride is unacceptable at high speeds in the absence of the secondary suspension.

6.5 Effects of unbalanced wheels

6.5.1 Reasons for wheels being unbalanced

The wheels on the gondola manriding vehicle are based on those used on mine cars, and these wheels are not balanced (see BS 4854:1972 (5)). This is because there is no need to fit balanced wheels for the low speeds at which mine cars operate. The wheels are cast, and then the hub, the tread, and the rail side of the flange are machined. There will be thickness variations produced in the casting and machining which will lead to unbalanced wheels, but there is a further source of unbalance. The wheels are greased, and a boss is cast on the hub at the root of one of the spokes to accommodate a large grease nipple. It is clear that unbalance will

be inevitable. However, the want of balance will vary from wheel to wheel.

6.5.2 Forces arising from the use of unbalanced wheels

The use of unbalanced wheels leads to the generation of out-of-balance forces which produce peaks in the measured acceleration spectral densities (see section 6.3.3). The peaks occur at frequencies which are given by equation (6.2):

$$f = \frac{\omega}{2\pi} = \frac{1}{2\pi}\left(\frac{V}{r}\right)$$

where,

V = forward speed of the wheel

The tests carried out at Ellington Colliery show that both vertical and lateral forces are generated, and these are shown in Fig 6.16. The forces shown in this figure are evaluated from the measured peaks (see Appendix 4) using equation (4.1), (4.24), and (4.25) (see section 4.3.5):

$$a_{rms} = \sqrt{S_{\ddot{q}}(f)\ \Delta f}$$

$$a_{peak} = \sqrt{2}\ .\ a_{rms}$$

$$F = m_e\ a_{peak} \qquad (6.3)$$

where,

a = acceleration (rms or peak)

$S_{\ddot{q}}(f)$ = acceleration spectral density

Δf = width of peak

m_e = effective mass

F = out-of-balance force

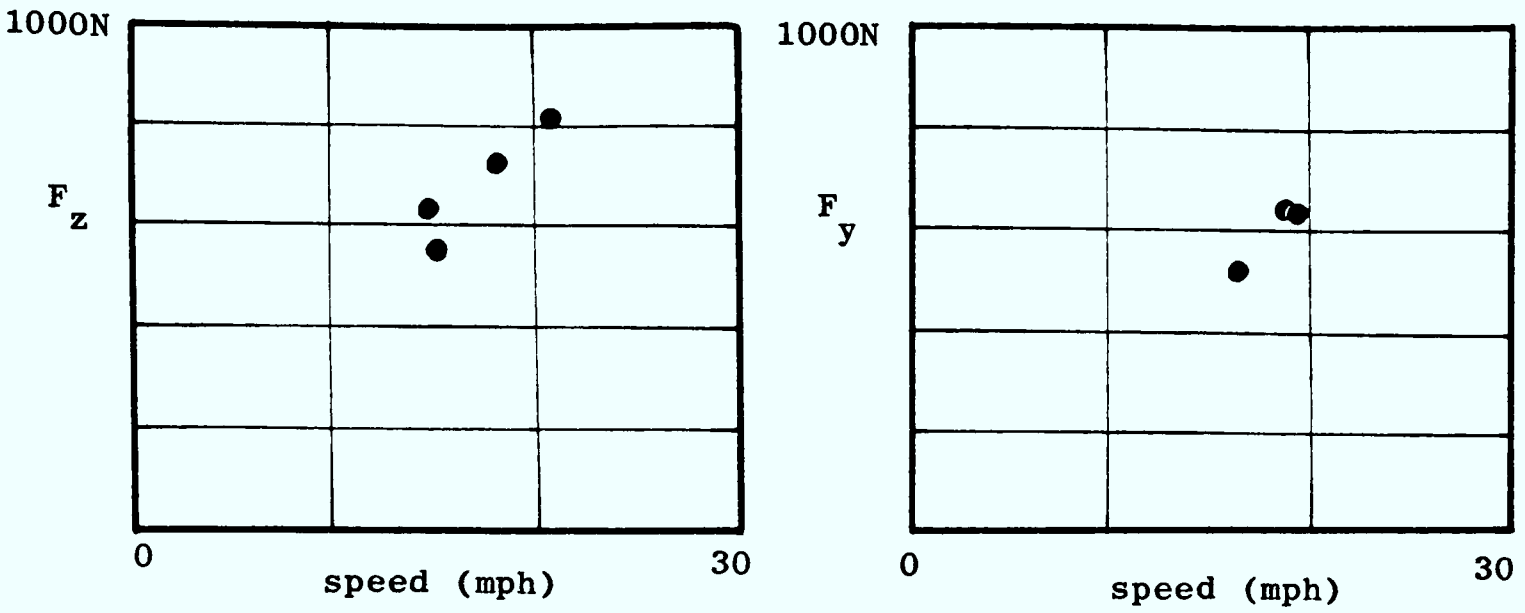

Fig 6.16 Forces occurring as a result of having unbalanced wheels fitted to gondola car.

6.5.3 Effect on ride

The rms accelerations for the front of the car-body are evaluated for third octave bands from the test results (see Fig 6.7) and shown in Fig 6.17. The use of unbalanced wheels leads to an increase in the levels of vibration. However, the ride is still acceptab le on the basis of the chosen acceptability limits (see section 4.2.3).

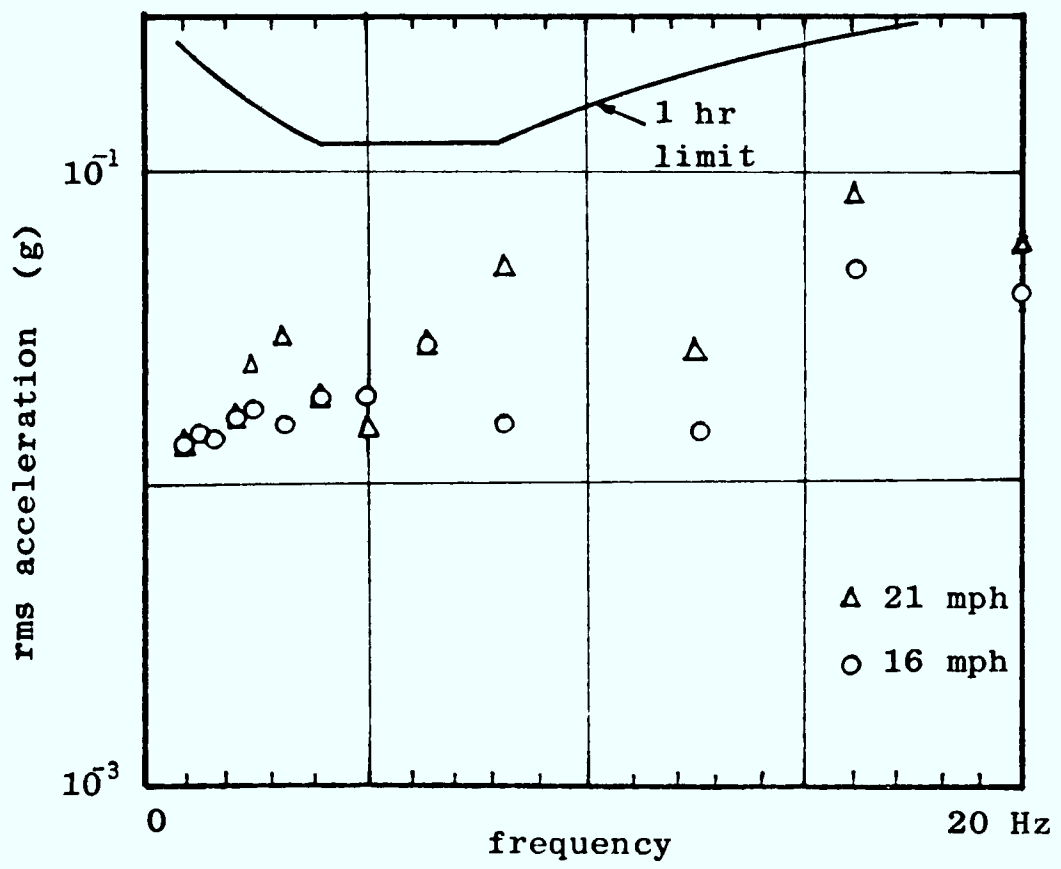

Fig 6.17 Rms acceleration for the front of the leading car-body of the gondola manriding car.

6.5.4 Effect on the likelihood of derailment

The use of unbalanced wheels leads to lateral forces being generated between the wheel and the rail (see Fig 6.16). If resonance is ignored the effects of these forces on the safety of the leading pair of wheels is shown in Fig 6.18.

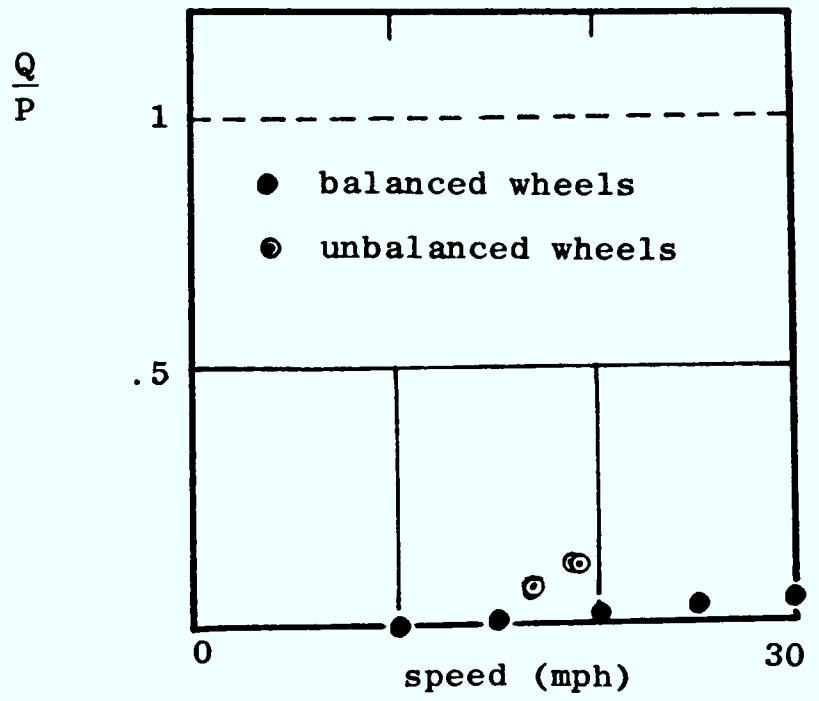

Fig 6.18 Likelihood of wheel climb derailment of the leading pair of wheels

Although the wheel climb derailment ratios (Q/P) are increased, the results indicate that a derailment is still unlikely. However, at particular speeds the bogie resonances (pitch and roll) are excited and these lead to significant reductions in wheel load. The test results indicate that the worst case occurs at a speed of 16 mph when the bogie pitch resonance is excited (see Fig 6.10). In this case the peak acceleration of the bogie above the leading pair of wheels is 0.7 g, and the wheel load reduction ratio is thus given by:

$$\frac{\Delta P}{P} = 0.7 \qquad (6.4)$$

The value is very close to the limiting value of 0.8 (see section 4.3.6) indicating that running the vehicle with a severly unbalanced wheel could easily lead to the likelihood of derailment.

6.6 Flange wear

6.6.1 General description

The gondola manriding cars operating at Easington and Gedling

Collieries have shown severe wear of the flanges when travelling at high speed (the maximum operating speeds are 18 mph and 25 mph respectively). This is illustrated in Fig 6.19 which shows the change in profile of a wheel over a period of one month at Easington Colliery (see Atkinson (32)), and Fig 6.20 which is a photograph of a worn wheel taken from Gedling Colliery.

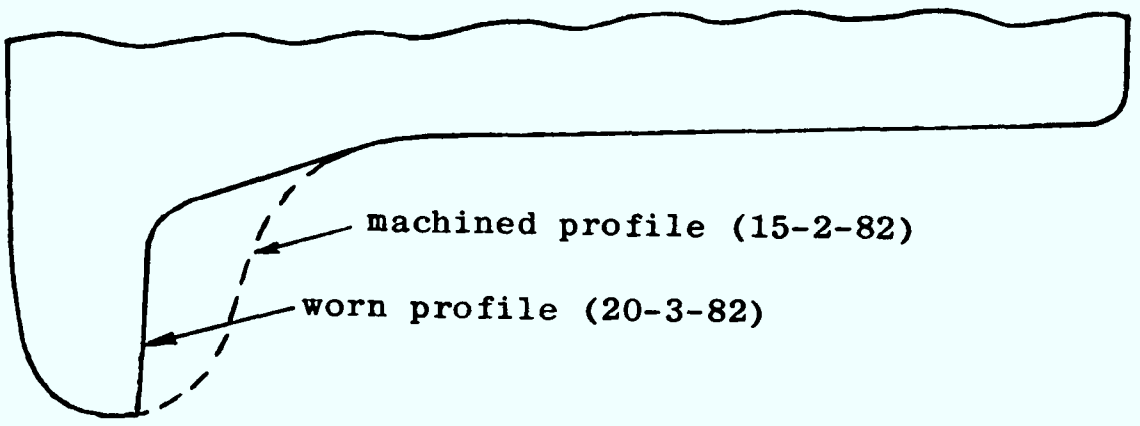

Fig 6.19 Change in profile of wheel operating at Easington Colliery

The only other British colliery in which the gondola cars travel at equivalent speeds to those achieved at Easington and Gedling is Ellington Colliery (the maximum operating speed is 23 mph) and here there is no evidence of flange wear. The track at Ellington is laid in concrete and at Easington and Gedling on ballast.

6.6.2 Observations at Gedling Colliery

Qualitative testing has been carried out on the manriding train at Gedling Colliery in order to examine the possibility of a relationship between the use of unbalanced wheels and rapid flange wear. The train consists of six gondola vehicles which are hauled at a maximum speed of 25 mph by electric trolley locomotives at the front and rear of the train (see Fig 1.9). The worn wheels on a bogie exhibiting severe flange wear on one side were replaced with balanced ones and observed after being in service for one month. Although all wheels were slightly worn, the wear was most pronounced on the wheels which had not been balanced. Another bogie showing rapid flange wear was completely re-fitted with balanced wheels and, again, only slight wear could be ovserved after operating for a month (see Clemson (33)). After being in service for a further four months the wheels on this

bogie had worn uniformly, but the rate of wear was about half the previous rate.

The observations indicate that the use of balanced wheels does inhibit wear, but it cannot stop it completely. It has been shown previously how independently revolving wheels rely upon flange contact for guidance, and this will clearly be accompanied by wear. On the basis of the analysis in Chapter 5 the lateral flange force, and thus the wear, can be reduced with a reduction of speed of the vehicle or an improvement of the standard of track (particularly, the lateral alignment and cross-level of the track). Alternatively, the use of conventional wheelsets will significantly reduce wear by removing the need of flange contact for guidance (see section 5.3.3).

6.3.3 Observations at Easington Colliery

The effects of using conventional wheelsets to reduce flange wear have been tested on a single bogie of a gondola manriding car at Easington Colliery. The original wheels of the bogie had previously exhibited severe wear (see Fig 6.19), and were replaced with prototype wheelsets. With the new arrangement there has been no flange wear (see Atkinson (32)) although a slight hollow has been worn in the tyre of the wheel (see section 5.3.3). A production version of the wheelset is currently being developed for use at both Easington and Gedling Collieries.

Chapter 7

The Unit Train

7.1 Introduction

Unit trains have been developed in recent years specifically for high speed manriding. They are generally smaller than more conventional manriding trains and carry fewer men.

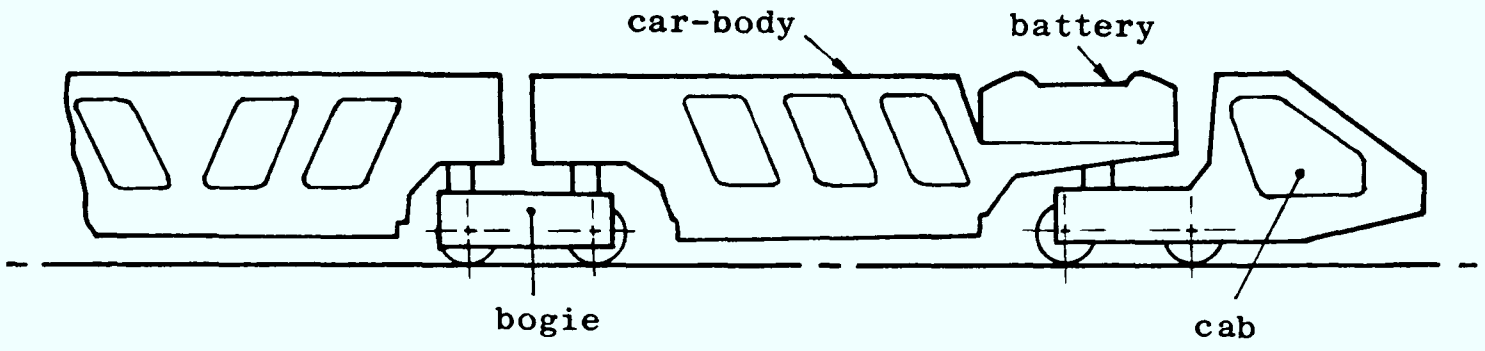

Fig 7.1 Unit train (tare = 15000 kg)

The prototype train shown in Fig 7.1 (see also Fig 1.7) is designed to carry a team of 24 men for the complete journey from the shaft to the coal face along both arterial and subsidiary roads. The trains are permanently coupled, and consist of three car-bodies with driving cabs at both the front and the rear. It is driven at a maximum speed of 25 mph by electric traction motors which are fitted on each axle (see NCB (34)).

The behaviour of the train is examined by means of two mathematical models. The first of these is a model of the vertical dynamics which predicts the response of the front half of the train to track vertical profile irregularities (see section 7.2). These predictions are compared with test results in section 7.3, and are used to assess the ride of the vehicle in section 7.4. The second model is of the lateral dynamics of the cab, and this predicts the response to lateral alignment irregularities in the track (see section 7.5). This model is also assessed against test results, and used to examine further the ride of the unit train.

Much of the work concerned with the model of the vertical dynamics also appears in two published papers (see Van Manen & Brickle (35), (36)).

7.2 Model of the vertical dynamics

7.2.1 Modelling decisions

The model is constructed principally to predict the bounce and pitch of the leading cab and leading car-body in response to track vertical profile irregularities. This is illustrated in Fig 7.2.

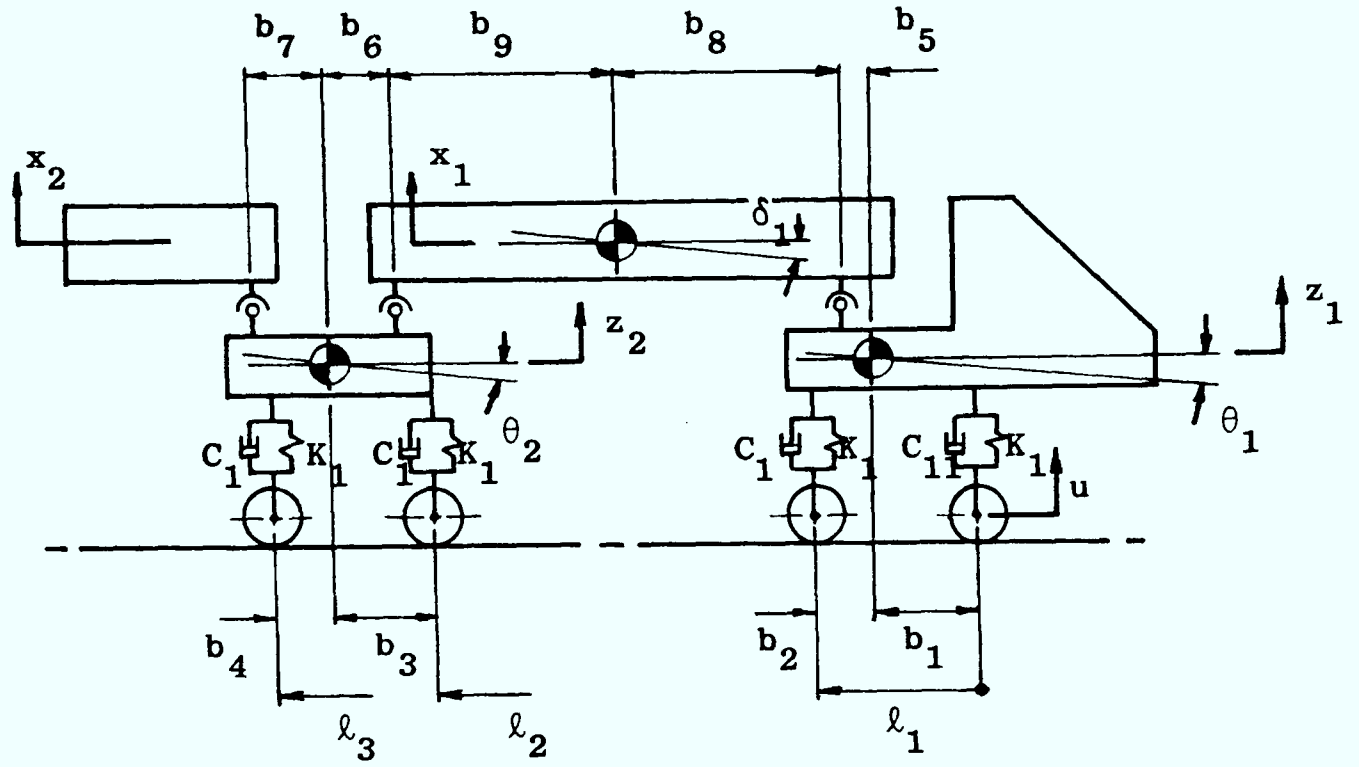

Fig 7.2 Model of the unit train (photograph is shown in Fig 1.7)

The vehicle is examined when travelling at constant speed along rigid track, and the inputs to the wheelsets are expressed in terms of a single input at the front wheels and a time delay. The wheels are considered to remain in contact with the rails, and the suspension elements are taken as being linear. Track resilience may be included by considering a track stiffness to act in series with the primary suspension.

7.2.2 Equations of motion

The positions of the vehicle components are described by seven equations of motion which are expressed in the general form of equation (2.33):

$$(Ms^2 + Ls + K)\underset{\sim}{q} = (Cs + D)\,T(s)u$$

The matrices for this equation are shown in Fig 7.3, and equation

$$M = \begin{bmatrix} m_3 & 0 & 0 & 0 & 0 & 0 & 0 \\ 0 & I_3 & 0 & 0 & 0 & 0 & 0 \\ 0 & 0 & m_4 & 0 & 0 & 0 & 0 \\ 0 & 0 & 0 & m_1 & 0 & 0 & 0 \\ 0 & 0 & 0 & 0 & I_1 & 0 & 0 \\ 0 & 0 & 0 & 0 & 0 & m_2 & 0 \\ 0 & 0 & 0 & 0 & 0 & 0 & I_2 \end{bmatrix}$$

$$L = \begin{bmatrix} 2C_2 & (b_9-b_8)C_2 & 0 & -C_2 & -b_8C_2 & -C_2 & b_6C_2 \\ (b_9-b_8)C_2 & (b_9^2+b_8^2)C_2 & 0 & b_8C_2 & b_5b_8C_2 & -b_9C_2 & b_6b_9C_2 \\ 0 & 0 & C_2 & 0 & 0 & -C_2 & -b_7C_2 \\ -C_2 & b_8C_2 & 0 & C_1+C_{11}+C_2 & b_2C_1-b_1C_{11}+b_8C_2 & 0 & 0 \\ -b_6C_2 & b_8b_6C_2 & 0 & b_2C_1-b_1C_{11}+b_6C_2 & b_2^2C_1+b_1^2C_{11}+b_8^2C_2 & 0 & 0 \\ -C_2 & -b_9C_2 & -C_2 & 0 & 0 & 2C_1+2C_2 & (b_4-b_3)C_1+(b_7-b_6)C_2 \\ b_6C_2 & b_9b_6C_2 & -b_7C_2 & 0 & 0 & (b_4-b_3)C_1+(b_7-b_6)C_2 & (b_4^2+b_3^2)C_1+(b_7^2+b_6^2)C_2 \end{bmatrix}$$

$$K = \begin{bmatrix} 2K_2 & (b_9-b_8)K_2 & 0 & -K_2 & -b_8K_2 & -K_2 & b_6K_2 \\ (b_9-b_8)K_2 & (b_9^2+b_8^2)K_2 & 0 & b_8K_2 & b_5b_8K_2 & -b_9K_2 & b_6b_9K_2 \\ 0 & 0 & K_2 & 0 & 0 & -K_2 & -b_7K_2 \\ -K_2 & b_8K_2 & 0 & 2K_1+K_2 & (b_2-b_1)K_1+b_8K_2 & 0 & 0 \\ -b_6K_2 & b_6b_8K_2 & 0 & (b_2-b_1)K_1+b_6K_2 & (b_2^2+b_1^2)K_1+b_6^2K_2 & 0 & 0 \\ -K_2 & -b_9K_2 & -K_2 & 0 & 0 & 2K_1+2K_2 & (b_4-b_3)K_1+(b_7-b_6)K_2 \\ b_6K_2 & b_9b_6K_2 & -b_7K_2 & 0 & 0 & (b_4-b_3)K_1+(b_7-b_6)K_2 & (b_4^2+b_3^2)K_1+(b_7^2+b_6^2)K_2 \end{bmatrix}$$

$$C = \begin{bmatrix} 0 & 0 & 0 & 0 \\ 0 & 0 & 0 & 0 \\ 0 & 0 & 0 & 0 \\ C_{11} & C_1 & 0 & 0 \\ -b_1C_{11} & b_2C_1 & 0 & 0 \\ 0 & C & C_1 & C_1 \\ 0 & 0 & -b_3C_1 & b_4C_1 \end{bmatrix}$$

$$D = \begin{bmatrix} 0 & 0 & 0 & 0 \\ 0 & 0 & 0 & 0 \\ 0 & 0 & 0 & 0 \\ K_1 & K_1 & 0 & 0 \\ -b_1K_1 & b_2K_1 & 0 & 0 \\ 0 & 0 & K_1 & K_1 \\ 0 & 0 & -b_3K_1 & b_4K_1 \end{bmatrix}$$

$$T(s) = \begin{bmatrix} 1 \\ e^{-L_1s/V} \\ e^{-L_2s/V} \\ e^{-L_3s/V} \end{bmatrix} \qquad \underset{\sim}{q} = \begin{bmatrix} x_1 \\ \phi_1 \\ z_2 \\ x_1 \\ \theta_1 \\ z_2 \\ \theta_2 \end{bmatrix}$$

Fig 7.3 Matrices for equations of motion

(2.38) is used to yield the transfer function of the vehicle (see section 2.5). The general purpose computer program described in section 2.6.1 may be used to carry out this solution, and listings of the subroutines containing the information in Fig 7.3 are included in Appendix 2. The solutions are presented in section 7.3.2.

7.2.3 Parameter values

Values are given below for the masses, inertias, stiffness and damping elements, and dimensions of the unit train as used in the model. The notion is shown in Fig 7.2.

m_1	= 1060 kg *	ℓ_1	= 1.0 m *
I_1	= 350 kg m^2 *	ℓ_2	= 5.1 m *
m_2	= 520 kg *	ℓ_3	= 6.1 m *
I_2	= 45 kg m^2 *	b_1	= 0.5 m *
m_3	= 2610 kg *	b_2	= 0.5 m *
I_3	= 7000 kg m^2 *	b_3	= 0.5 m *
m_4	= 1200 kg *	b_4	= 0.5 m *
k_1	= 6×10^5 N/m *	b_5	= 0.24 m *
c_1	= 6×10^3 Ns/m	b_6	= 0.4 m *
c_{11}	= 6×10^3 Ns/m	b_7	= 0.73 m *
k_2	= 5×10^8 N/m	b_8	= 2.25 m *
c_2	= 6×10^3 Ns/m	b_9	= 2.25 m * (7.1)

Where a value has been measured or derived from measured quantities it is indicated by an asterisk. The remaining values are estimated.

7.2.4 Resonant frequencies

The resonant frequencies are determined using the method explained in section 6.2.4, and are shown in Table 7.1.

Resonance	Frequency (Hz)
Cab	
Bounce	3.2
Pitch	4.0
Bogie	
Bounce	2.7
Pitch	5.3

Table 7.1 Resonant frequencies of unit train

7.3 Vehicle testing

7.3.1 Tests at Bevercotes Colliery

A series of tests was carried out with the unit train travelling along the test track at Bevercotes Colliery. This track is on the surface and has a 110 metre straight section with a gradient of 1 in 15. The motions of the leading cab, front car-body and bogie were monitored by means of accelerometers (see Fig 7.4), and the results were recorded on magnetic tape. Three nominal speeds were considered: 7 mph, 11.5 mph, and 15 mph. The tests at the slowest speed were carried out travelling up the gradient, and the latter tests were carried out travelling down. There was some difficulty in maintaining a constant speed of 15 mph on the short section of test track available, and so a stationary sample of an adequate length could not

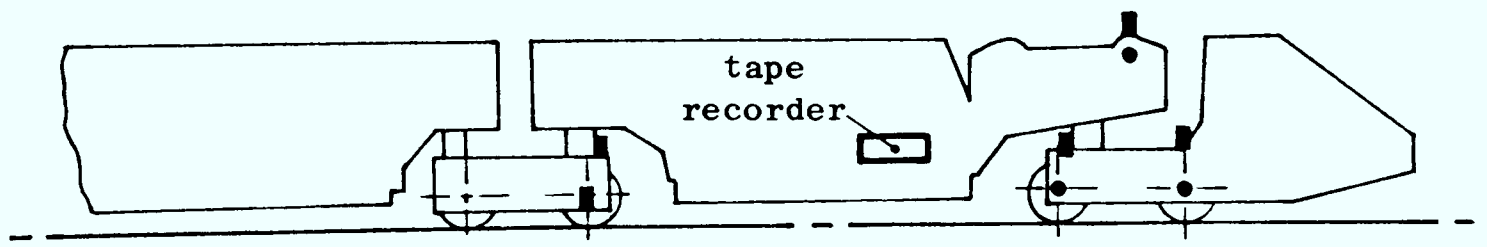

Fig 7.4 Instrumentation for tests

be obtained (see section 3.3.2). The reliability of the results at the fastest speed is thus questionable. The test data was processed using a spectrum analyser (see section 6.3.2) which yielded acceleration spectral densities describing the motion of the train. These spectral densities are included in Appendix 4.

7.3.2 Comparison of model and test results

The validity of the mathematical model is assessed against the test results by comparing acceleration spectral densities (see section 6.3.3). The vertical profile of the test track is the input to the mathematical model, and this is determined from measurements of the vertical acceleration of the axle (see section 3.2.3). This leads of a description of the track in terms of a spectral density as illustrated in Fig 7.5.

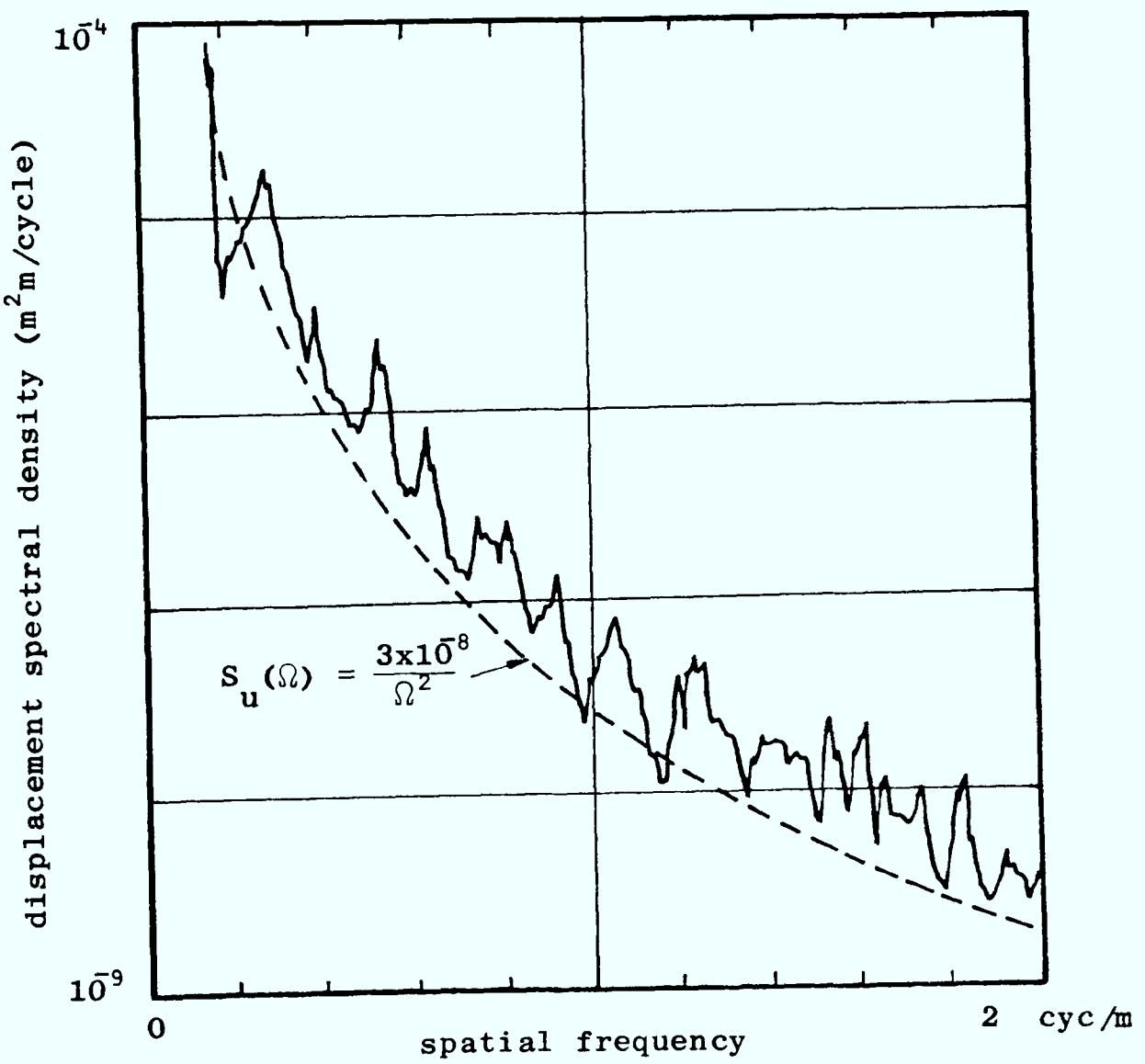

Fig 7.5 Spectral density describing vertical profile for surface test track at Bevercotes Colliery (17.3.83)

This may be expressed in the form of equation (3.38):

$$S_u(f) = \frac{AV^{n-1}}{f^n}$$

where,

$S_u(f)$ = spectral density describing input

A = roughness coefficient
= 3×10^{-8} $m^2 cyc^3/m^3$

n = integer exponent = 4

f = frequency

The acceleration spectral density is evaluated from the model using equation (2.63):

$$S_{\ddot{q}}(f) = |H(f)|^2 \omega^4 S_u(f)$$

where,

H(f) = transfer function

This is done using the general purpose plotting program (see section 2.6.2).

The outcome of the modelling compares favourably with the test results at the two slower speeds (see Fig 7.6) even though there is some divergence at frequencies greater than about 10 Hz. The vibration levels at these higher frequencies are not large enough to affect significantly the ride of the train, and so this divergence may be ignored. The comparison between model and test results at the fastest speed is not particularly satisfactory (see Fig 7.7) due to the difficulties in maintaining a constant speed of 15 mph on the short section of test track (see section 7.3.1).

7.4 The ride of the train

7.4.1 General considerations

The ride of the train is assessed on the basis of permissible exposure times to vibration (see section 4.2.3). The vibration is expressed in terms of rms accelerations measured in third octave bands, and these are evaluated from the model using the general

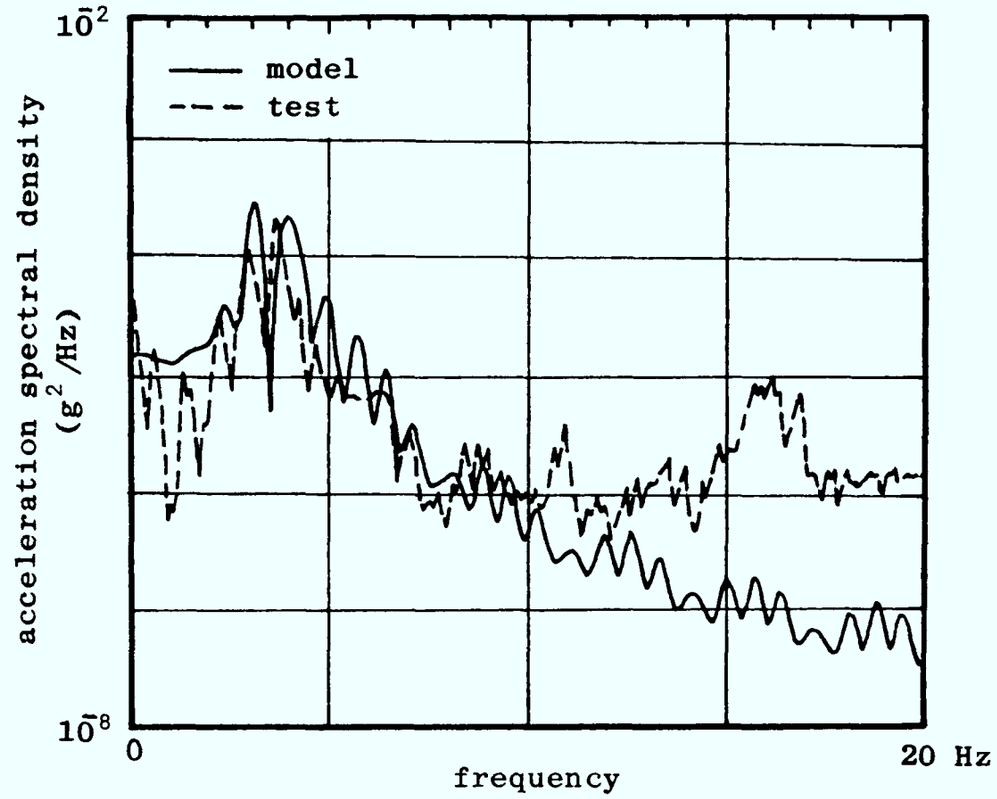

(a)

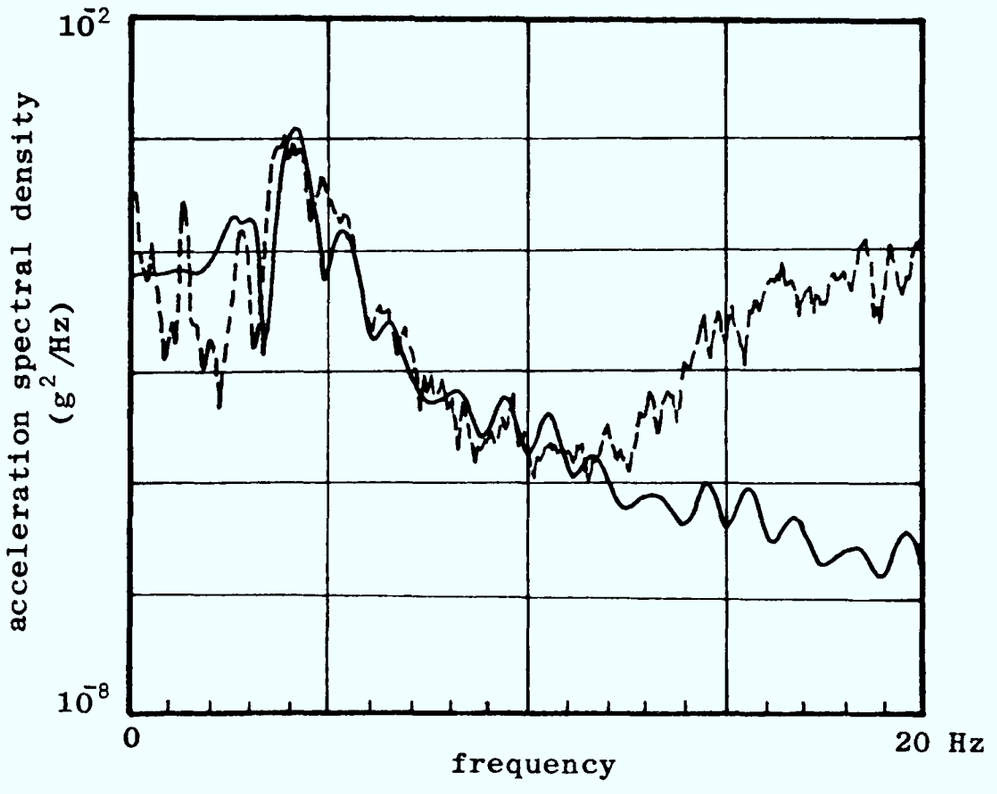

(b)

Fig 7.6 Vertical motion at front of car-body

(a) speed = 7 mph

(b) speed = 11.5 mph

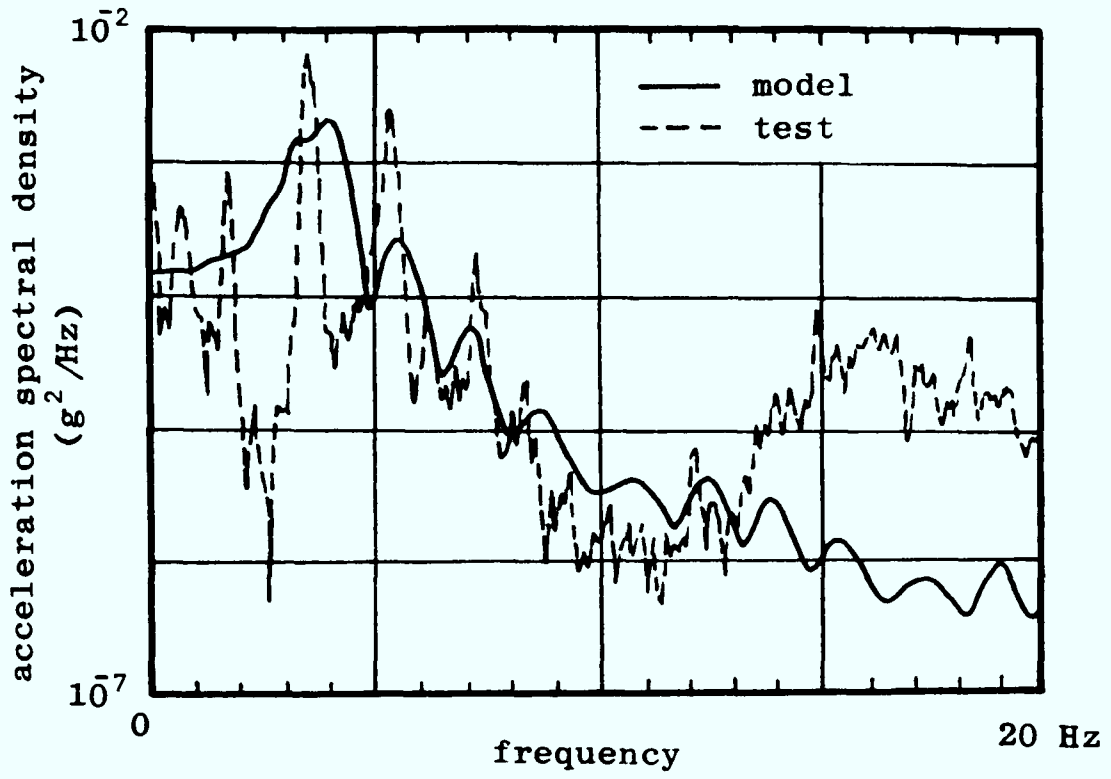

Fig 7.7 Vertical motion at front of car-body (speed = 15 mph)

purpose plotting program (see section 2.6.2).

7.4.2 Effect of speed and condition of track

The rms accelerations for the cab and car-body are shown in Figs 7.8 and 7.10 for the unit train travelling at different speeds along track of a reasonable standard ($A = 5 \times 10^{-8}$ $m^2 cyc^3/m^3$). Relationships between maximum roughness coefficients and speed are shown in shown in Figs 7.9 and 7.11, and these may be used to examine the effect of travelling along track of an inferior quality. These relationships are determined from Figs 7.8 and 7.10 by displacing the rms accelerations upwards until a marginally acceptable ride is indicated (see section 6.4.3).

The ride in the cab is poor as a result of the pitching motion being amplified by the long overhang. The existing design is both unsuitable for travelling at high speeds along arterial roads, and for travelling at low speeds along subsidiary roads. As this is a prototype vehicle there is clearly a case for modifying the design. Suggestions for modifications to the suspension are discussed in section 7.4.3. The ride in the car-body is acceptable for the operating speeds of the train.

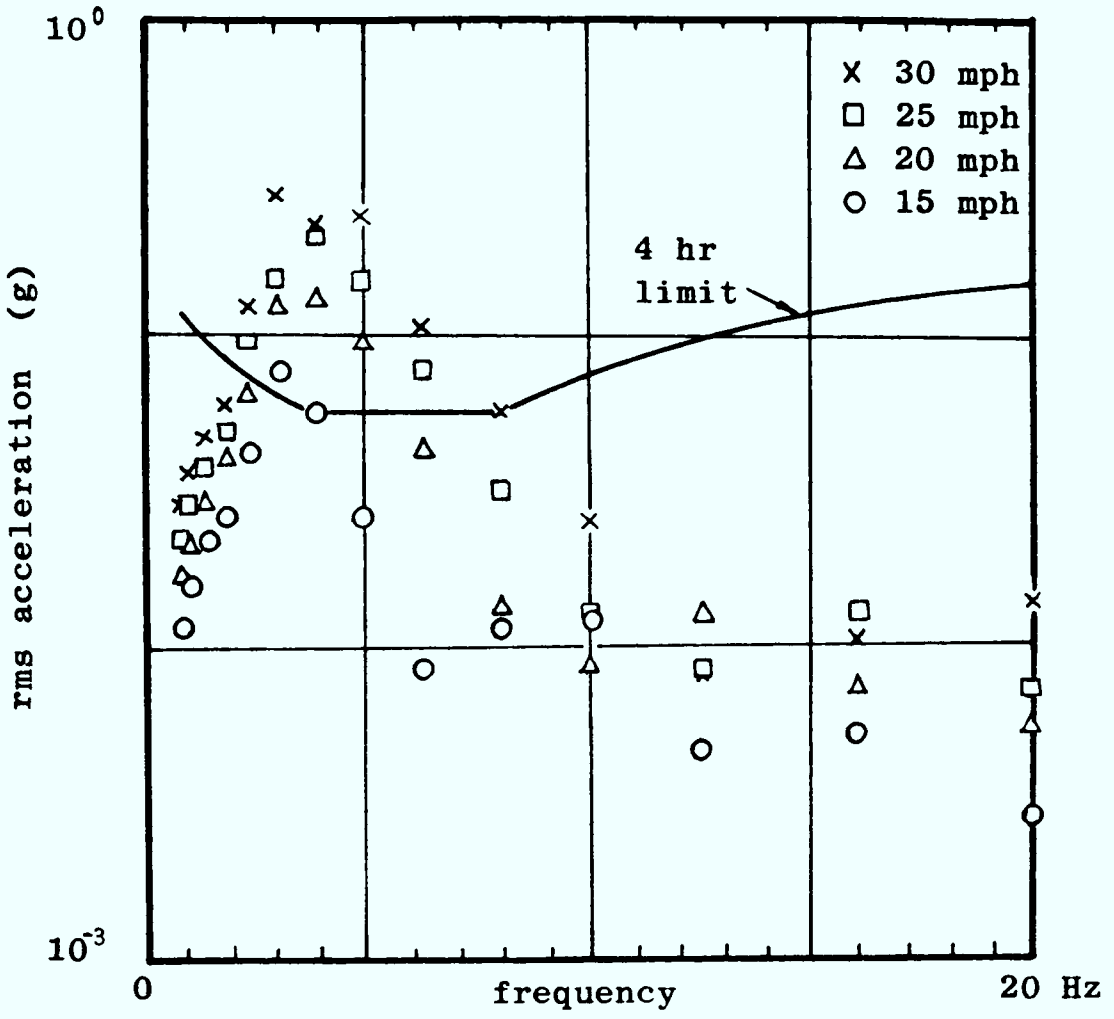

Fig 7.8 Rms accelerations at driver's seat of the cab

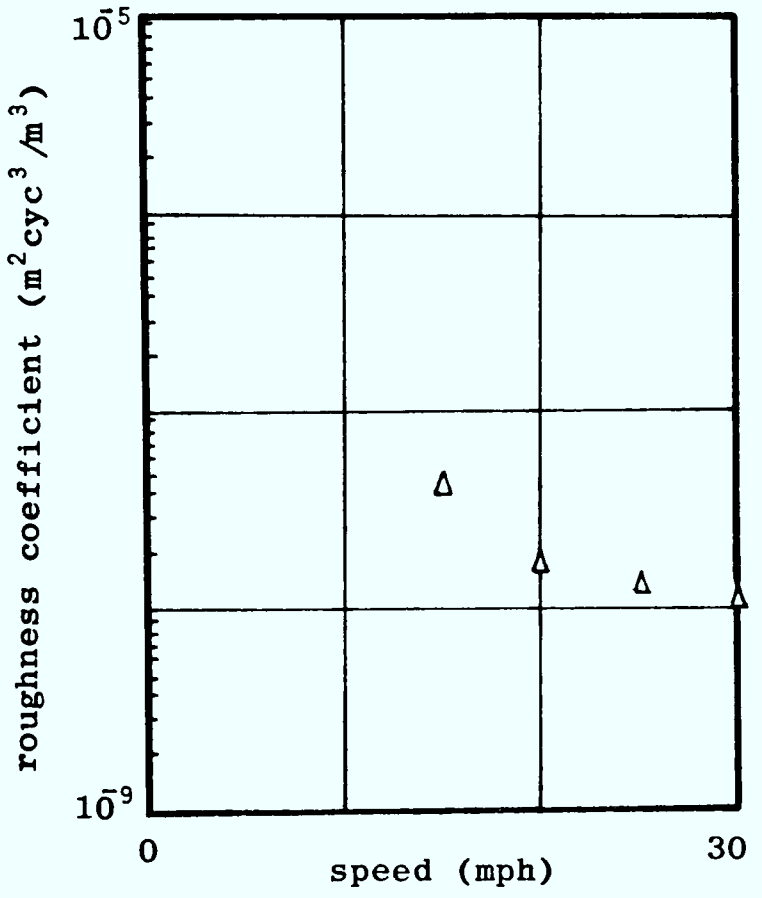

Fig 7.9 Relationship between the maximum permissible values of roughness coefficient, A, and speed for an acceptable ride at the driver's seat of the cab

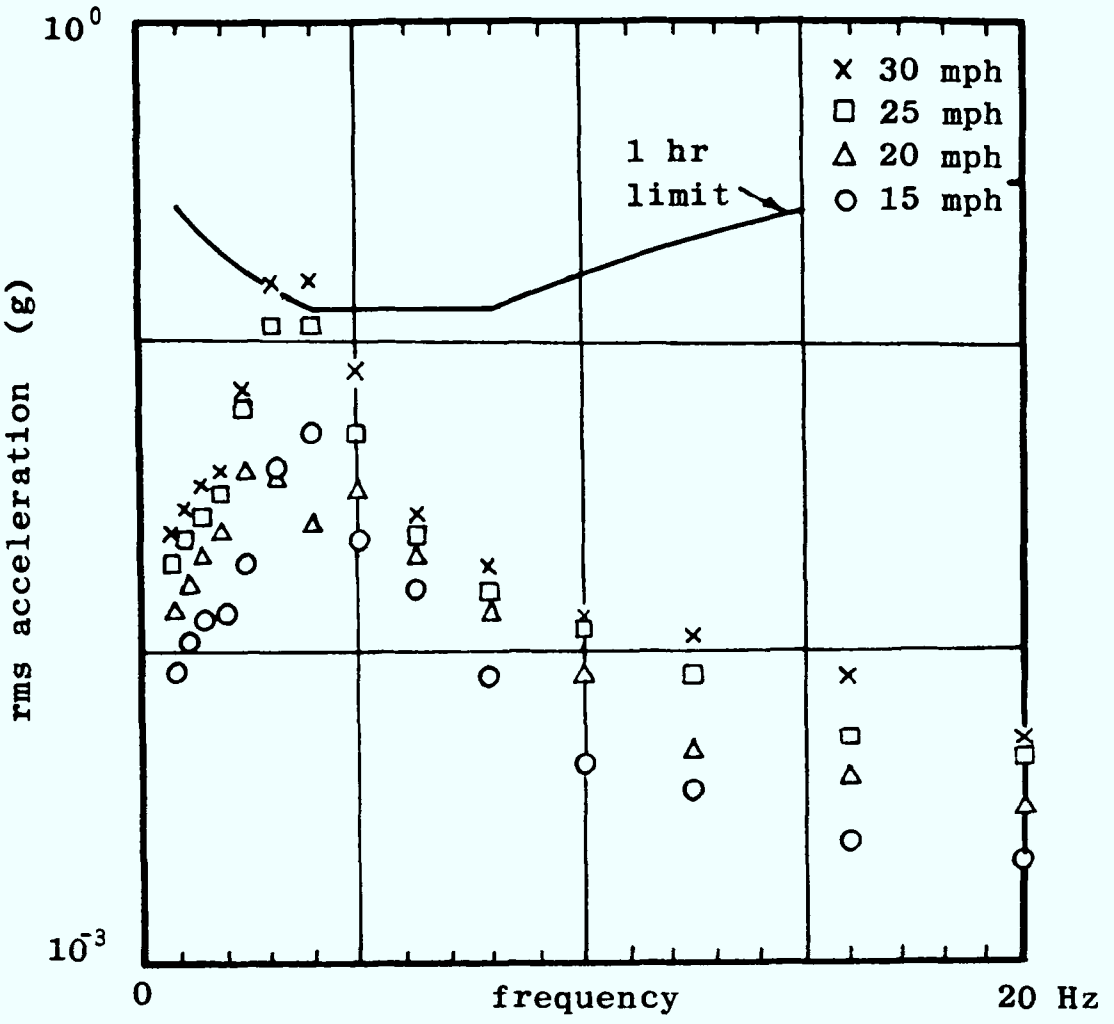

Fig 7.10 Rms accelerations at the front of the leading car-body

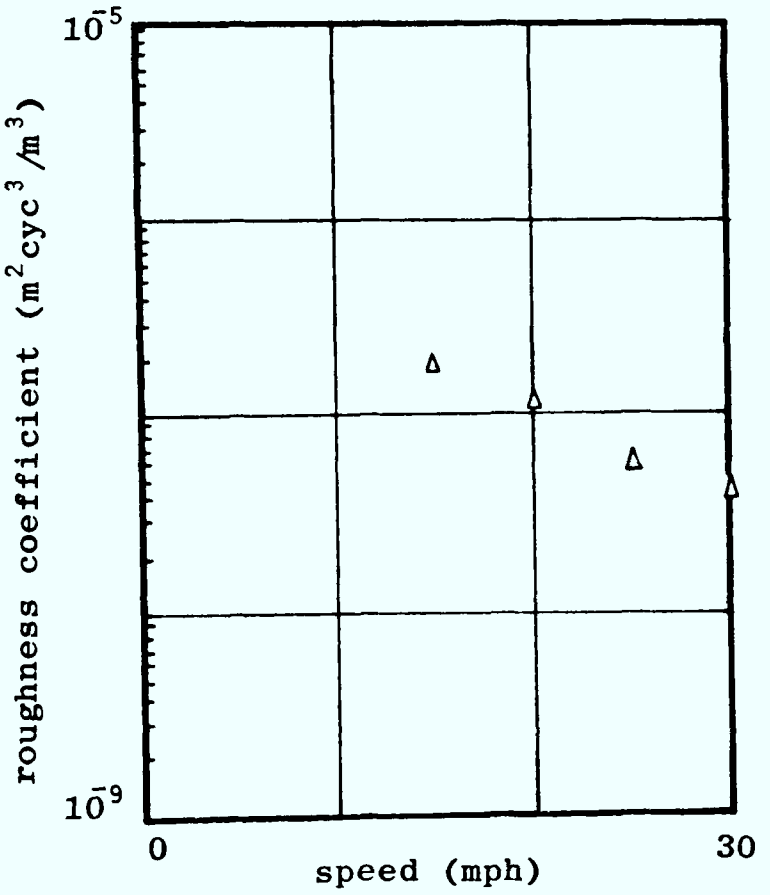

Fig 7.11 Relationship between the maximum permissible values of roughness coefficient, A, and speed for an acceptable ride at the front of the leading car-body

7.4.3 Effect of dampers

The effect on the ride in the cab of increasing the amount of damping in the primary suspension is illustrated in Fig 7.12.

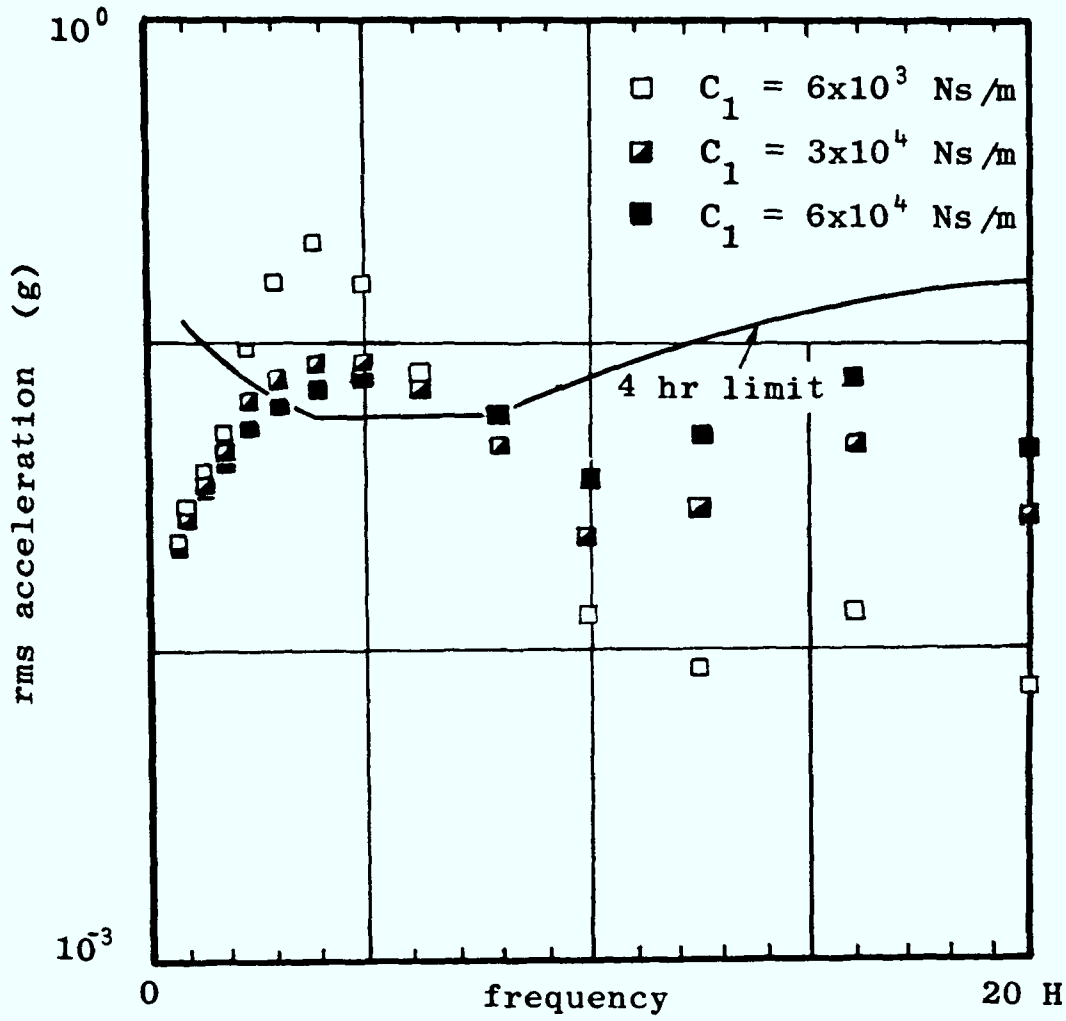

Fig 7.12 Rms accelerations at driver's seat of the cab (25 mph)

Ensuring a reasonable ride for the driver requires significant damping of the pitching oscillation of the cab, and this suggests that shock absorbers should be used. These should be fitted to both wheelsets on the cab, as fitting the shock absorbers to the front wheelset only has little effect on the ride.

7.5 Model of the lateral dynamics

7.5.1 Modelling decisions

The model is constructed principally to predict the sway and yaw of the leading cab in response to lateral alignment irregularities in the track, but it also takes account of the roll and yaw of the leading car-body. The primary suspension is quite stiff in the lateral direction and is treated as being rigid. The model is shown in Fig 7.13.

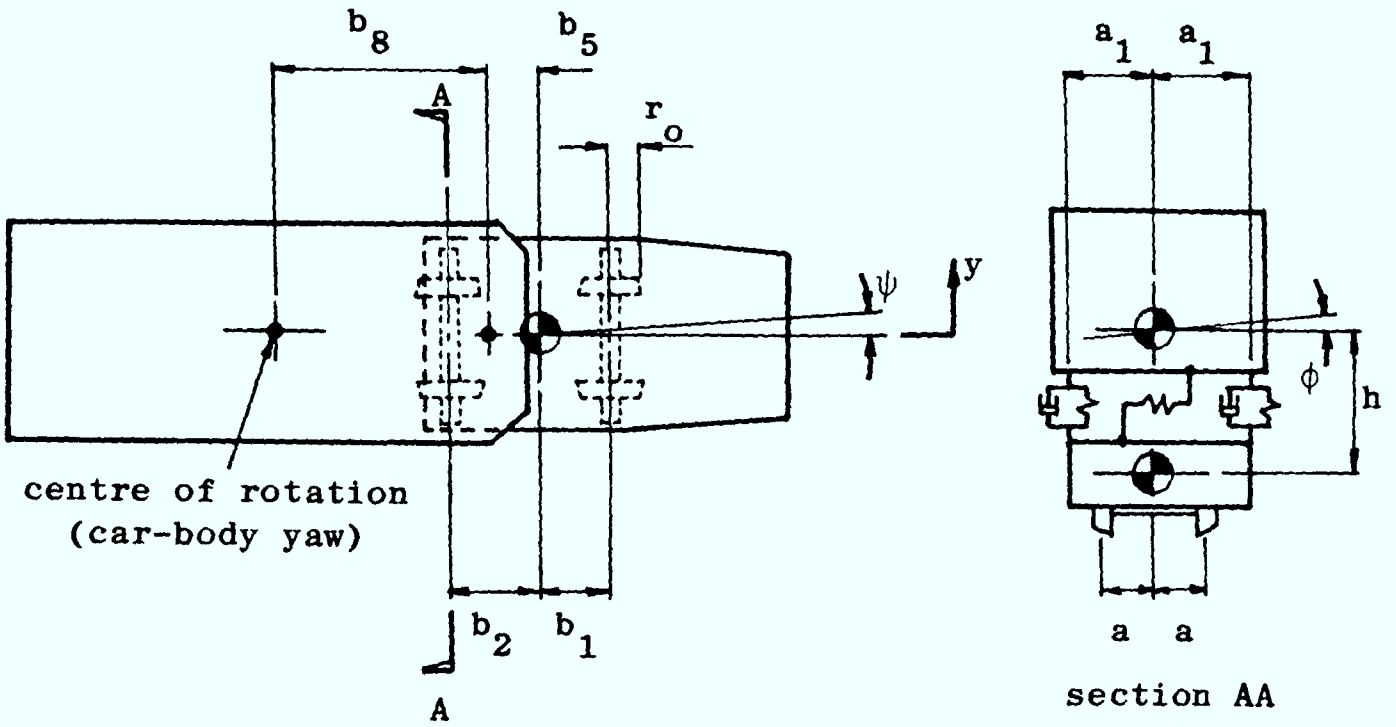

Fig 7.13 Model of the unit train (plan view)

The train is fitted with conventional wheelsets and, when displaced laterally, these behave in a similar way to the wheelset described in section 2.3.4 (see equations (2.24) and (2.25)). Creep coefficients are evaluated on the basis of Kalker's linear creep theory, but as every wheelset is driven, these coefficients are factored. This is because the wheels will also creep as a result of driving. No account is taken in the model for the flanges touching the rails.

The vehicle is considered when travelling at constant speed, and the inputs to the two wheelsets are expressed as an input and a time delay.

7.5.2 Equations of motion

The position of the cab is described by three equations of motion:

$$(m + \frac{I_b}{b_8^2})\ddot{y} + \frac{4f_{22}}{V}\dot{y} + 2K_g y + \frac{2f_{22}}{V}(b_1 - b_2)\dot{\psi}$$

$$+ (K_g(b_1 - b_2) - 4f_{22})\psi - Kh\phi = K_g(y_{aF} + y_{aR}) \qquad (7.2)$$

$$(I_{zz} + I_b \left(\frac{b_5}{b_8}\right)^2)\ddot{\psi} + \frac{4f_{11}a^2}{V}\dot{\psi} + \frac{2f_{11}a\lambda_o}{r_o}(b_1 - b_2)\psi$$

$$+ \frac{4f_{11}a\lambda_o}{r_o} y + Khb_5\phi = \frac{2f_{11}a\lambda_o}{r_o}(y_{aF} + y_{aR}) \qquad (7.3)$$

$$J\ddot{\phi} + 2C_r a_1^2\dot{\phi} + 2K_r a_1^2\phi - Khy + Khb_5\psi = 0 \qquad (7.4)$$

where,

y = sway of cab

ψ = yaw of cab

y_{aF} = lateral alignment (front wheelset)

y_{aR} = lateral alignment (rear wheelset)

m = mass of cab

I_{zz} = yawing moment of inertia of cab

I_b = yawing moment of inertia of car-body

J = roll moment of inertia of car-body

K = lateral stiffness of secondary suspension

K_r = stiffness of pair of roll support springs

C_r = damping value of roll support suspension

f_{11} & f_{22} = creep coefficients

λ_o = conicity

(The remaining notation is shown in Fig 7.13)

These may be written in the general form of equation (2.33) and solved to yield the transfer function using equation (2.38) (see section 2.5). This is done using the general purpose computer program (see section 2.6.1).

7.5.3 Parameter values

The values for the masses, inertias, and dimensions used in the model are given overleaf. Where a value has been measured or derived from a measured quantity it is indicated by an asterisk.

$$
\begin{aligned}
m &= 1060 \text{ kg } * & b_1 &= 0.5 \text{ m } * \\
I_{zz} &= 350 \text{ kg m}^2 * & b_2 &= 0.5 \text{ m } * \\
I_b &= 7000 \text{ kg m}^2 * & b_5 &= 0.24 \text{ m } * \\
J &= 260 \text{ kg m}^2 * & b_8 &= 2.25 \text{ m } * \\
K &= 4 \times 10^5 \text{ N/m} & a &= 0.356 \text{ m } * \\
K_r &= 4 \times 10^5 \text{ N/m } * & a_1 &= 0.38 \text{ m } * \\
C_r &= 9 \times 10^3 \text{ Ns/m} & r_o &= 0.178 \text{ m } * \\
h &= 0.5 \text{ m} & \lambda_o &= 0.2
\end{aligned}
\qquad (7.4)
$$

Values for the parameters associated with the interaction between the wheels and rails are based on the ones used in Chapter 5. The wheel profile of the unit train is slightly different to that of the gondola car, but the differences are near the flange which is not being considered in this analysis. The gravitational stiffness is thus given by equation (5.4):

$$Kg = 5W$$

where,

$$W = \text{axle load} \simeq 18000 \text{ N}$$

The creep coefficients are obtained by multiplying equation (5.19) by a factor of 0.5 to account for the effect of driving (see section 7.5.1).

$$f_{11} = f_{22} = 1000\, W^{2/3} \text{ (Newtons)} \qquad (7.5)$$

7.5.4 Comparison of model and test results

The predictions of the mathematical model are compared here with results obtained from the 7 mph tests at Bevercotes Colliery (see section 7.3.1). In the absence of any measurements of the lateral alignment of the track, the following estimate of the spectral density is used as the input to the model:

$$S_a(\Omega) = \frac{2 \times 10^{-6}}{\Omega^2} \text{ m}^2 \text{ m/cycle} \qquad (7.6)$$

The acceleration spectral densities are evaluated on the basis of this input using the general purpose plotting program (see section 2.6.2).

The correlation between the model and the test results is quite close (see Figs 7.14 and 7.15), with the only significant divergence occurring as a result of the drop-outs which are produced by the model at regular frequency intervals. These drop-outs occur as a result of the simple way in which the motion of the cab has been treated, and may be related to the wheelbase and operating speed of the train.

If neither the yaw of the cab or the effects of primary suspension are taken into consideration, the lateral motions of the front and rear wheelsets can be represented as:

$$y_F(t) = y_{cab}(t + \frac{b_1}{V})$$

$$y_R(t) = y_{cab}(t - \frac{b_2}{V}) \qquad (7.7)$$

where,

y_{cab} = sway of cab

y_F = lateral motion of front wheelset

y_R = lateral motion of rear wheelset

The model predicts the sway on the basis of the average lateral motion of the two wheelsets, which may be expressed as:

$$y = \tfrac{1}{2}(y_F + y_R) \qquad (7.8)$$

where,

y = predicted sway of the cab

Combining equations (7.7) and (7.8) produces the result:

$$y(t) = \tfrac{1}{2}(y_{cab}(t + \frac{b_1}{V}) + y_{cab}(t - \frac{b_2}{V})) \qquad (7.9)$$

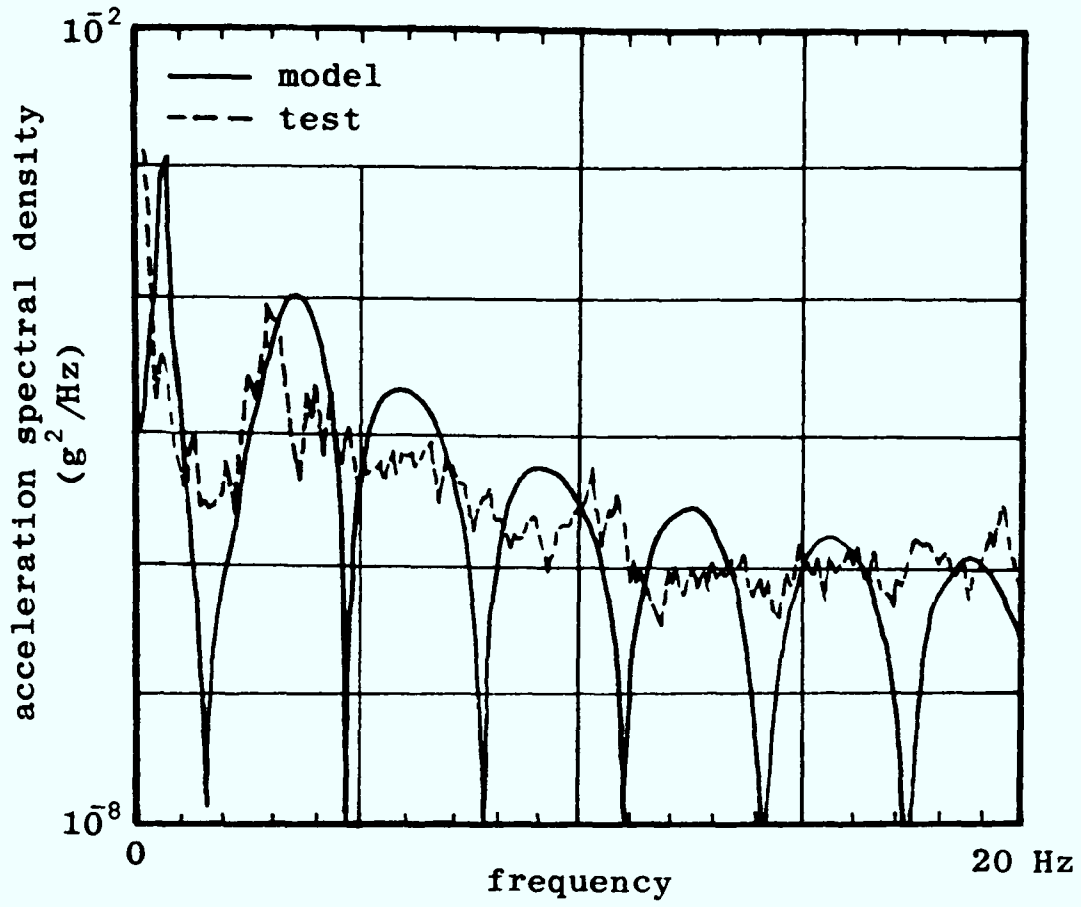

Fig 7.14 Front of leading car-body (top) (speed = 7 mph)

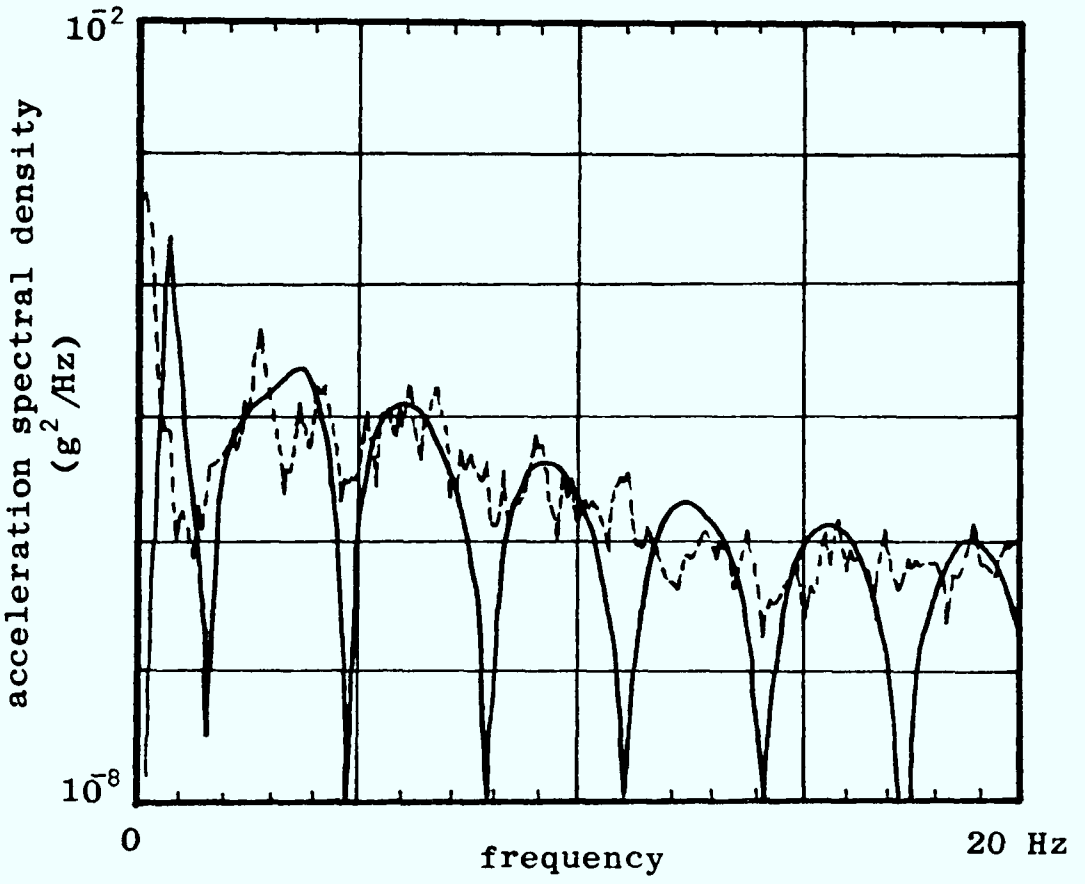

Fig 7.15 Above rear wheelset of leading cab (speed = 7 mph)

Using the method of Laplace transforms (see section 3.2.1), and putting $b = b_1 = b_2$ yields:

$$y = y_{cab} \left(\cos \left(\frac{2\pi bf}{V}\right)\right) \qquad (7.10)$$

This is similar to the result obtained in equation (3.12) in relation to the measurement of track cross-level from a moving vehicle. On the basis of equation (7.10) the drop-out frequencies correspond to the condition:

$$f = \frac{NV}{4b} \qquad (7.11)$$

$$(N = 1, 3, 5 \ldots..)$$

where,

V = speed of vehicle

This is consistent with the results shown in Figs 7.14 and 7.15. The simple model thus provides no information about the vehicle motion at the drop-out frequencies, and only limited information in the immediate vicinity of the drop-outs. However, the main features of the motion are predicted.

The test results (see Fig 7.15) indicate a sharp peak at a very low frequency, and this suggests that the flange is touching the rail. Flange contact is not taken into consideration in the model, but this peak is still predicted. This is because the value used for gravitational stiffness corresponds with the premise that the root of the flange is always in the vicinity of the rail (see section 5.2.3). Further evidence of flange contact is provided by the fact that the model is quite insensitive to changes in the values of creep coefficients and conicity, which suggests that little steering action is provided by the wheelsets. This implies that the guidance must be provided by flange contact. On the basis of the discussion in Chapter 5 (eg see Fig 5.9) the flange contact may be expected to increase as the train travels faster. The steering action, which is inhibited by the very stiff primary lateral suspension, will only assist in guiding the train if the suspension is more flexible (see

section 5.3.5).

7.5.5 Effect of lateral oscillation on ride

The ride in the leading cab is shown in Fig 7.16 for a train travelling along track of a reasonable standard ($A = 2 \times 10^{-6}$ m^2 cyc/m).

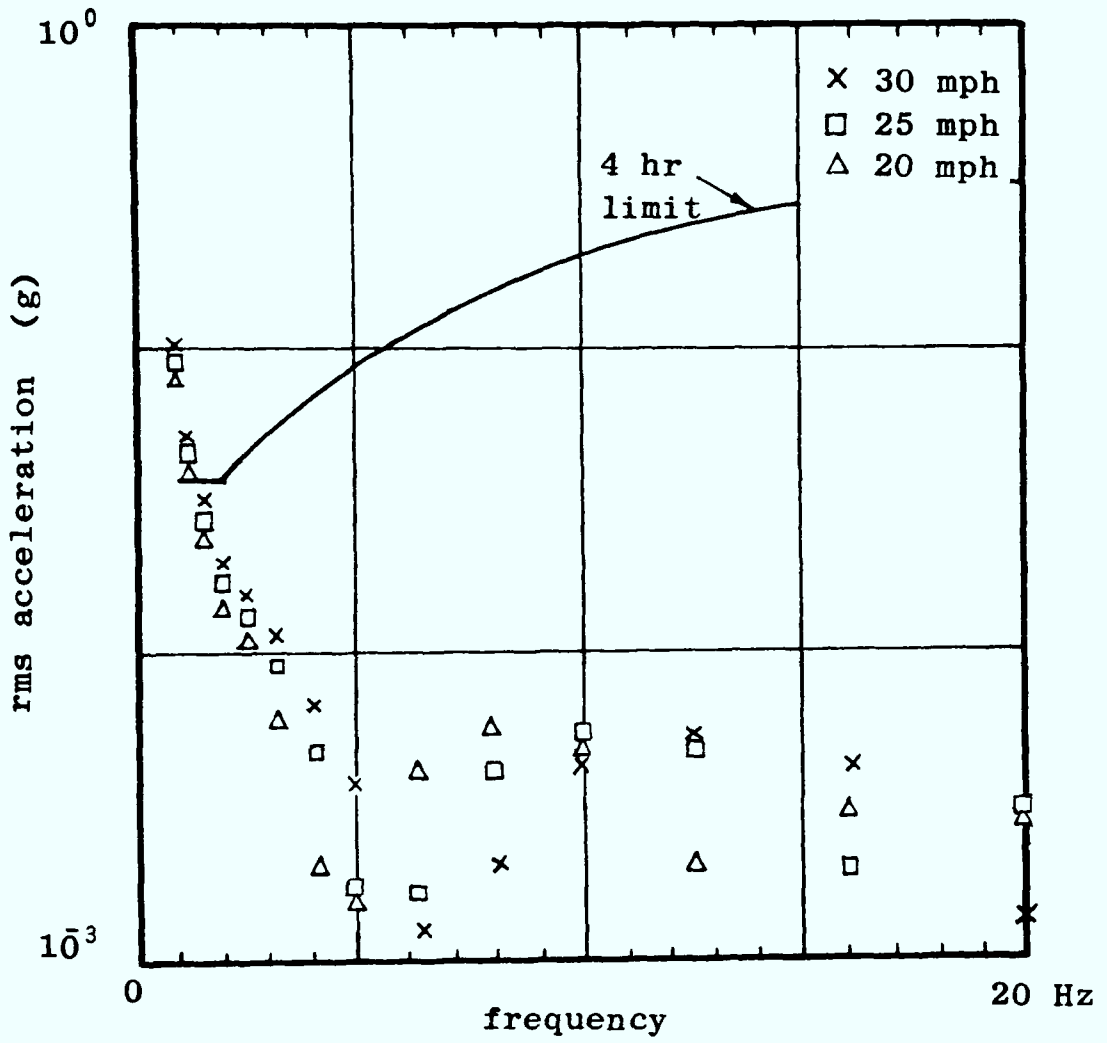

Fig 7.16 Lateral rms accelerations at driver's seat of cab

The rms accelerations are quite high at very low frequencies which leads to an unacceptable ride. These high accelerations can be reduced by using a more flexible lateral primary suspension.

Chapter 8

The Two Axle Vehicle

8.1 Introduction

Two axle manriding cars (see Fig 1.5) and two axle locomotives (see Figs 1.1 and 1.9) are used widely in British coal mines, although often at lower operating speeds than either gondola cars or unit trains. These vehicles generally have little or no suspension and thus exhibit a fairly uncomplicated dynamic behaviour.

The general purpose manriding car shown in Fig 1.5 is the main subject of this chapter and has an identical arrangement of wheels, axle, and primary suspension to that of the gondola manriding car. The results and discussion presented in Chapter 5 about the behaviour of a pair of wheels is thus generally applicable. The motion of the vehicle body is examined by way of the simple model introduced in Chapter 2 (see Fig 2.12 and equation (2.28)) which predicts the bounce and pitch of the vehicle in response to vertical profile irregularities in the track. This model has already been used to illustrate certain aspects of the work throughout the thesis.

The model of the vehicle is described in section 8.2 and an alternative method of solving the equations of motion is introduced in section 8.3. This is a time stepping integration technique which may be used to examine the time response to particular irregularities (such as points and dipped joints). The predictions of the model are compared with results obtained by running a vehicle over a known step in a track in section 8.4, and the behaviour of the manriding car for different operating conditions is examined in section 8.5. Two axle locomotives are discussed briefly in section 8.6.

8.2 Model of the vertical dynamics

8.2.1 Description of the model

The vehicle is modelled as shown in Fig 8.1. It is examined when travelling at constant speed and the inputs to each pair of wheels are expressed in terms of a single input at the front wheels and a time delay. The track is modelled as if it is rigid, but resilience may be included by considering the track stiffness to act in series with the primary stiffness. The position of the car-body is described by two equations of motion (see equation (2.28)) which are

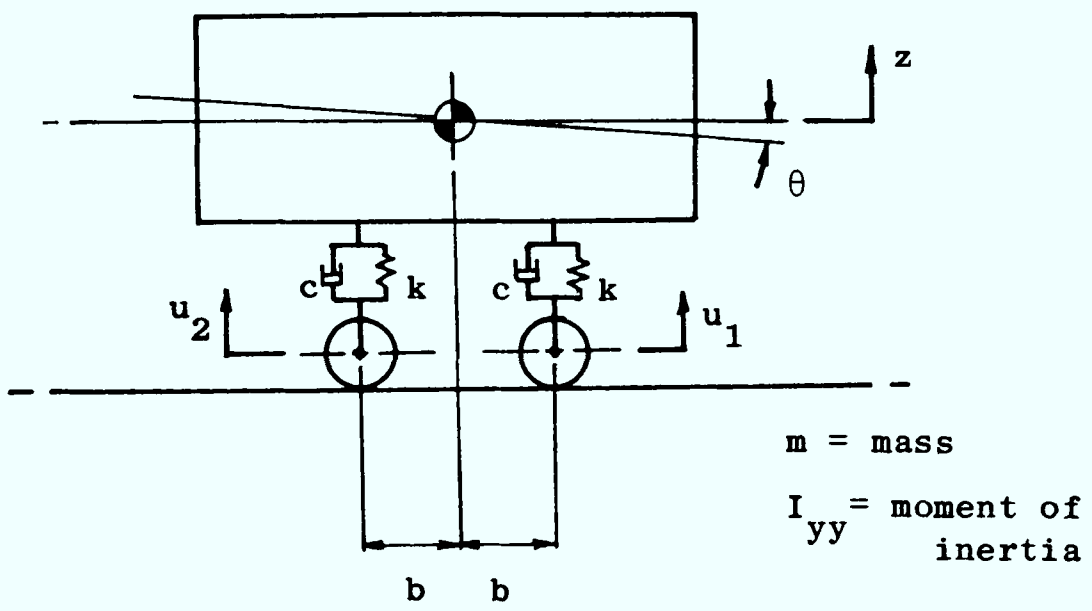

Fig 8.1 Model of a two axle vehicle
(Photograph is shown in Fig 1.5)

reproduced below:

$$m\ddot{z} + 2c\dot{z} + 2kz = c(\dot{u}_1 + \dot{u}_2) + k(u_1 + u_2)$$

$$I_{yy}\ddot{\theta} + 2b^2c\dot{\theta} + 2b^2k\theta = b^2c(\dot{u}_2 - \dot{u}_1) + b^2k(u_2 - u_1) \qquad (8.1)$$

where,

$$u_1 = u(t)$$

$$u_2 = u(t - {}^{2b}/V)$$

$$V = \text{forward speed} \qquad (8.2)$$

8.2.2 Parameter values

Values are given below for the mass, inertia, stiffness, damping value, and wheelbase of the vehicle being modelled. These values are all measured or derived from measured quantities.

$$m = 1134 \text{ kg (unladen)}$$

$$I_{yy} = 1100 \text{ kg m}^2$$

$$k = 2 \times 10^6 \text{ N/m}$$

$$c = 1.5 \times 10^4 \text{ Ns/m}$$

$$b = 0.69 \text{ m} \qquad (8.3)$$

8.2.3 Resonant frequencies

The resonant frequencies are determined using the method of section 6.2.4, and these are shown in Table 8.1. The pitch dominates the vertical motion and is the only resonant frequency detected.

Resonance	Frequency (Hz)
Car-body bounce	-
Car-body pitch	6.6

Table 8.1 Resonant frequencies of two axle manriding vehicle

8.3 Time stepping integration solution technique

Time stepping integration is used to provide an approximate solution to the differential equations which describe vehicle motion (see equation (8.1)). It leads to simulation in the time domain, and may be explained with reference to Fig 8.2. This shows the variation of the vehicle coordinate vectors ($\ddot{\underset{\sim}{q}}$, $\dot{\underset{\sim}{q}}$, $\underset{\sim}{q}$) with time.

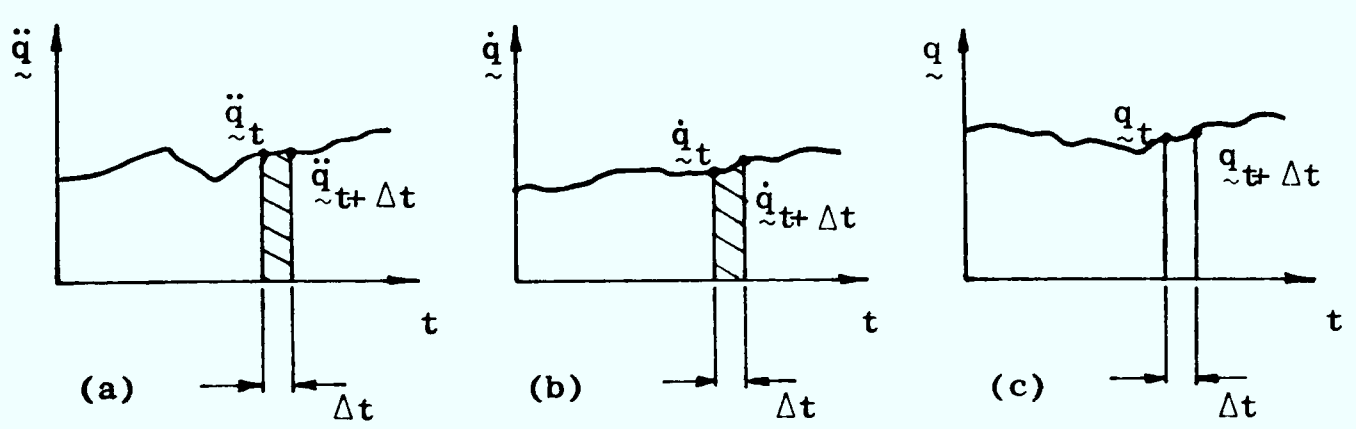

Fig 8.2 Time-stepping integration

If the quantities, $\ddot{\underset{\sim}{q}}_{t+\Delta t}$, $\ddot{\underset{\sim}{q}}_t$, $\dot{\underset{\sim}{q}}_t$, and $\underset{\sim}{q}_t$ are initially known, then:

$$\dot{\underset{\sim}{q}}_{t+\Delta t} = \dot{\underset{\sim}{q}}_t + \int_t^{t+\Delta t} \ddot{\underset{\sim}{q}}(\tau)\, d\tau \qquad (8.4)$$

where,

$$\int_t^{t+\Delta t} \ddot{\underset{\sim}{q}}(\tau)\, d\tau = \text{area of shaded strip in Fig 8.2(a)}$$

and,

$$\underset{\sim}{q}_{t+\Delta t} = \underset{\sim}{q}_t + \int_t^{t+\Delta t} \dot{\underset{\sim}{q}}(\tau)\, d\tau \qquad (8.5)$$

where,

$\int_{t}^{t+\Delta t} \dot{\underset{\sim}{q}}(\tau)\, d\tau$ = area of shaded strip in Fig 8.2(b).

These two equations may be simplified by approximating the shaded strips to rectangles, and this leads to the result:

$$\dot{\underset{\sim}{q}}_{t+\Delta t} = \dot{\underset{\sim}{q}}_{t} + \frac{\Delta t}{2}(\ddot{\underset{\sim}{q}}_{t+\Delta t} + \ddot{\underset{\sim}{q}}_{t})$$

$$\underset{\sim}{q}_{t+\Delta t} = \underset{\sim}{q}_{t} + \frac{\Delta t}{2}(\dot{\underset{\sim}{q}}_{t+\Delta t} + \dot{\underset{\sim}{q}}_{t}) \qquad (8.6)$$

This is known as the Trapezoidal integration method.

Consider the equations of motion written in the form:

$$M\ddot{\underset{\sim}{q}} + L\dot{\underset{\sim}{q}} + K\underset{\sim}{q} = C\dot{\underset{\sim}{u}} + D\underset{\sim}{u} \qquad (8.7)$$

where,

M = inertia matrix

L = damping matrix

K = stiffness matrix

C,D = input matrices

For a small time increment, Δt:

$$\ddot{\underset{\sim}{q}}_{t+\Delta t} \simeq M^{-1}(C\dot{\underset{\sim}{u}}_{t} + D\underset{\sim}{u}_{t} - L\dot{\underset{\sim}{q}}_{t} - K\underset{\sim}{q}_{r}) \qquad (8.8)$$

The time response may be evaluated for a given input ($\dot{\underset{\sim}{u}}_{t}$, $\underset{\sim}{u}_{t}$) using equations (8.8) and (8.6), provided that suitable initial values of $\ddot{\underset{\sim}{q}}_{t}$, $\dot{\underset{\sim}{q}}_{t}$, and $\underset{\sim}{q}_{t}$ are chosen.

The Trapezoidal method (equation (8.6)) is based on a very simple approximation of the integrals in equations (8.4) and (8.5) and may be inappropriate for solving complex equations of motion: this is discussed further in section 8.4.2. A computer program which is suitable for determining the time response by this method is included in Appendix 2, and solutions for a two axle vehicle travelling over a step in a track are presented in section 8.4.2.

8.4 Vehicle testing

8.4.1 Tests at Swadlincote test site

Tests were carried out with the two axle manriding vehicle travelling along the surface track at MRDE Swadlincote test site. A 12 mm vertical step was put into the left-hand rail, and the vehicle travelled down this step at a nominal speed of 13 mph , and reversed up the step at a nominal speed of 5 mph. The motions of the front and rear ends of the car-body were monitored by means of accelerometers, and the relative motions of the front wheels were monitored by displacement transducers (see Fig 8.3). The results were recorded on magnetic tape and later transferred to chart paper using a UV recorder (see Appendix 4).

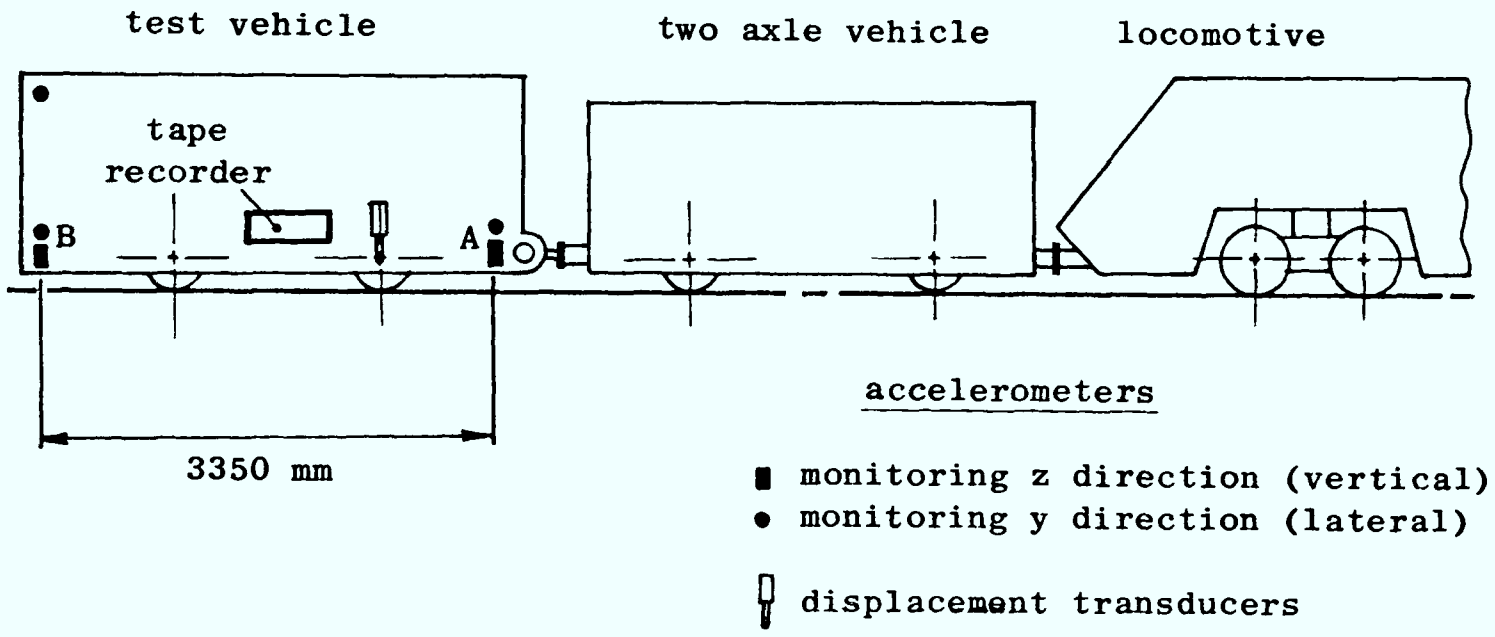

Fig 8.3 Instrumentation for tests

8.4.2 Comparison of model and test results

The validity of the mathematical model is assessed by comparing the outcome of the modelling with the observed behaviour of the vehicle. The input to the model is a 12 mm vertical step in the left-hand rail, and this was introduced by means of an irregular fishplate. This is shown in Fig 8.4.

The test vehicle was at the rear of the train (see Fig 8.3), and when it travelled down the step the rails were already pressed firmly into the ballast. The resilience of the track is thus included in the modelling for this case. When the test vehicle reversed up the step there was little movement of the track owing to

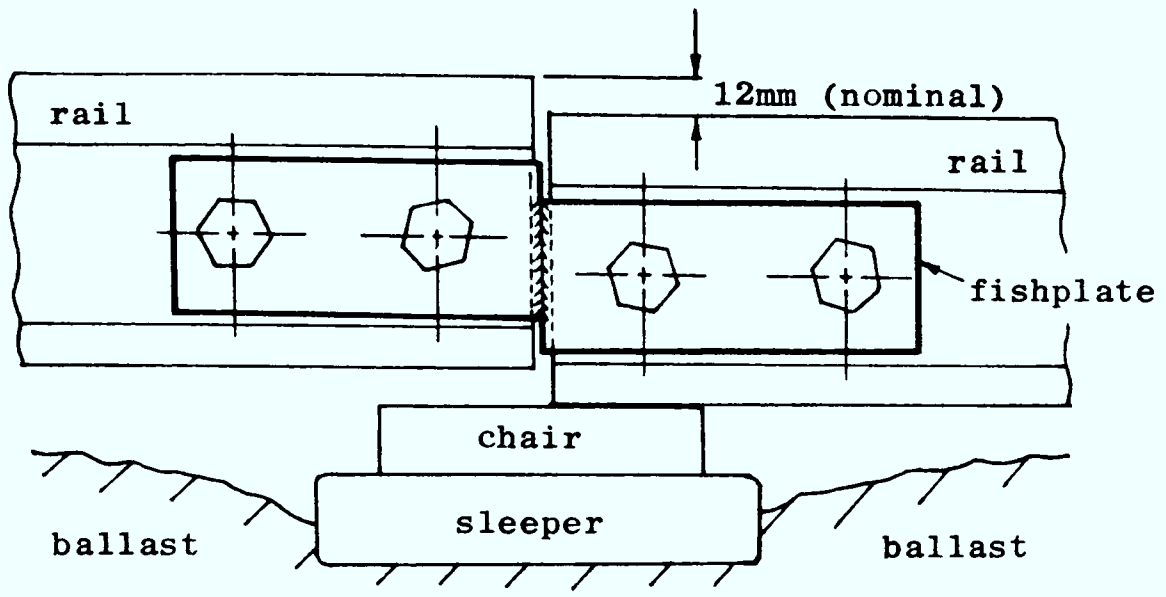

Fig 8.4 Step in left-hand rail

the small axle loads, and track resilience is thus ignored in the modelling.

The motion of the car-body as predicted by the model is similar to the test results (see Fig 8.5). There is some divergence of the results at the faster speed, but considering the very simple manner in which the vehicle and track have been treated, the agreement is quite good. The relative motion of the front wheels are also predicted reasonably well by the model (see Fig 8.6). The test results here are the average relative motions of the left and right wheels.

The agreement shown in Figs 8.5 and 8.6 occurs largely as a result of the uncomplicated nature of both the vehicle and the input. As more complex track irregularities are considered it becomes increasingly more difficult to define the input correctly, and this leads to problems in comparing the outcome of modelling with tests. This problem is largely avoided with the method of comparison used in the earlier chapters, where a statistical description of both the track and vehicle motion is used. More sophisticated models are needed to explain complicated aspects of vehicle behaviour (such as the motion of a laterally displaced wheelset as a result of the tapered profiles of the wheels) and the simple integrating method introduced in section 8.3 is then often inappropriate.

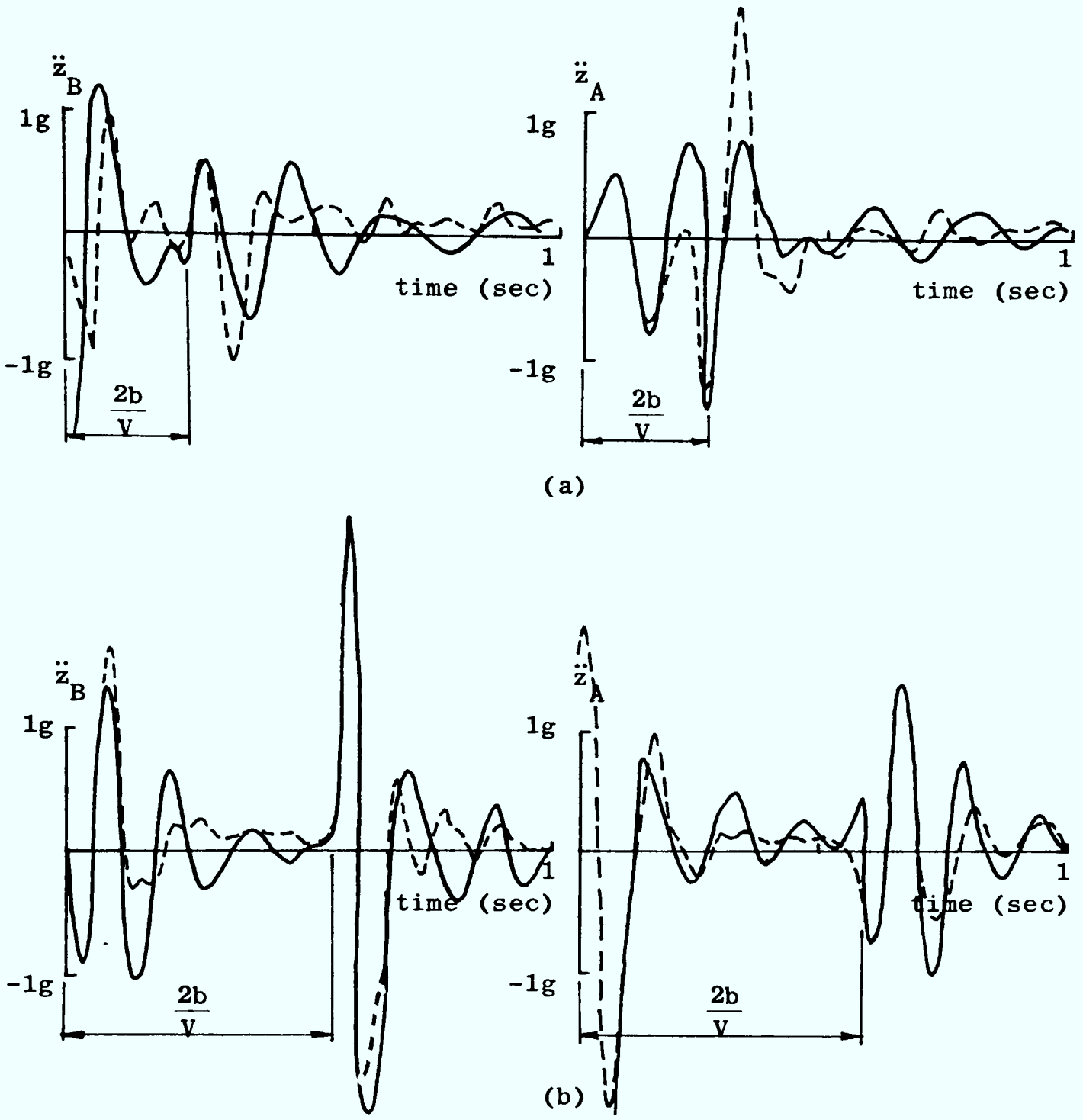

Fig 8.5 Vertical response to a step in the track
(a) travelling down the step (speed = 13 mph)
(b) reversing up the step (speed = 5.5 mph)

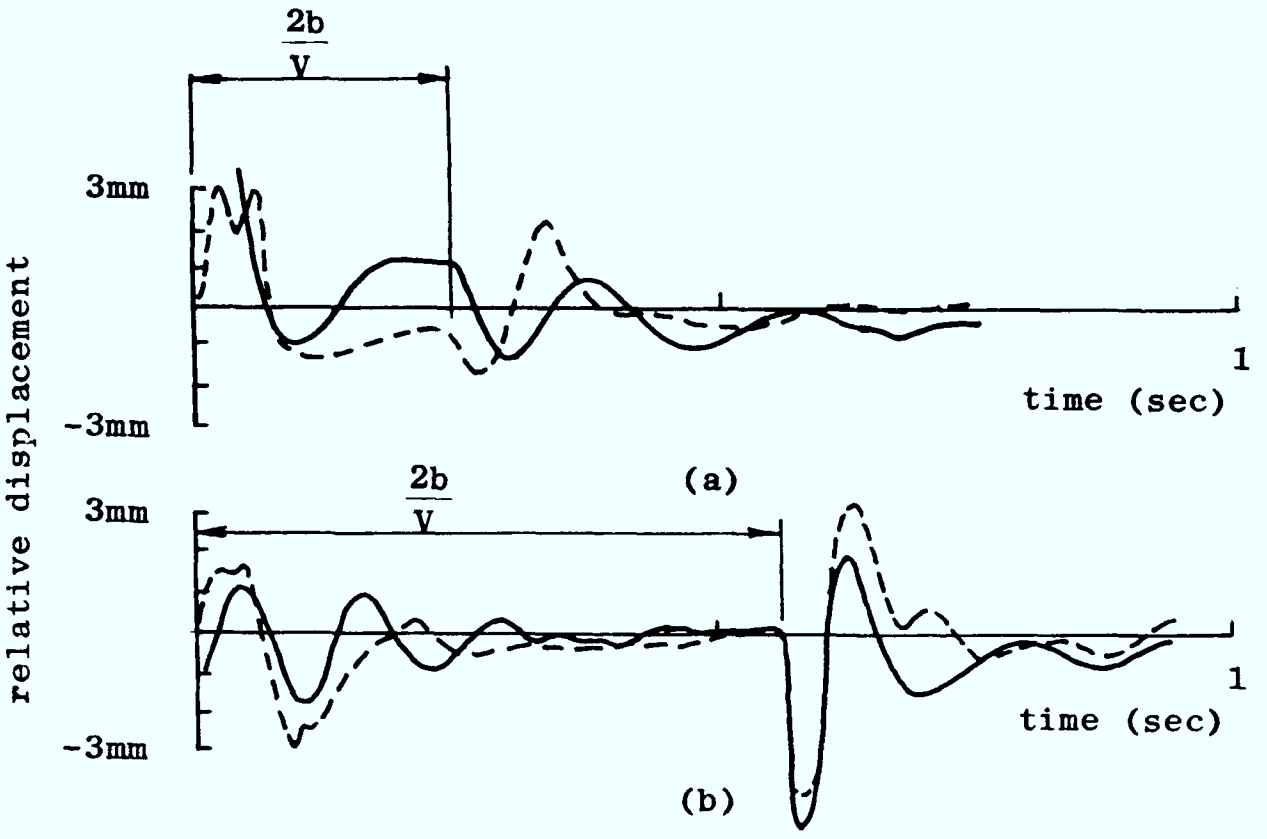

Fig 8.6 Relative motion of front wheels

(a) travelling down the step (speed = 13 mph)

(b) reversing up the step (speed = 5.5 mph)

8.5 The ride of the two axle manriding car

8.5.1 General considerations

In the previous section, equations (8.1) and (8.2) were shown to describe adequately the motion of the two axle manriding car in response to a known vertical step in the track. The model can be further exploited if these equations are now solved in the frequency domain (see section 2.5) which allows assessment of the ride in terms of the acceptability limits defined in section 4.2.3. Such a solution has been carried out earlier in the thesis resulting in a description of the response of the manrider in terms of transfer function (see Fig 2.14), and in terms of the acceleration spectral density and rms accelerations (see Fig 2.18). The latter figure is reproduced overleaf (Fig 8.7).

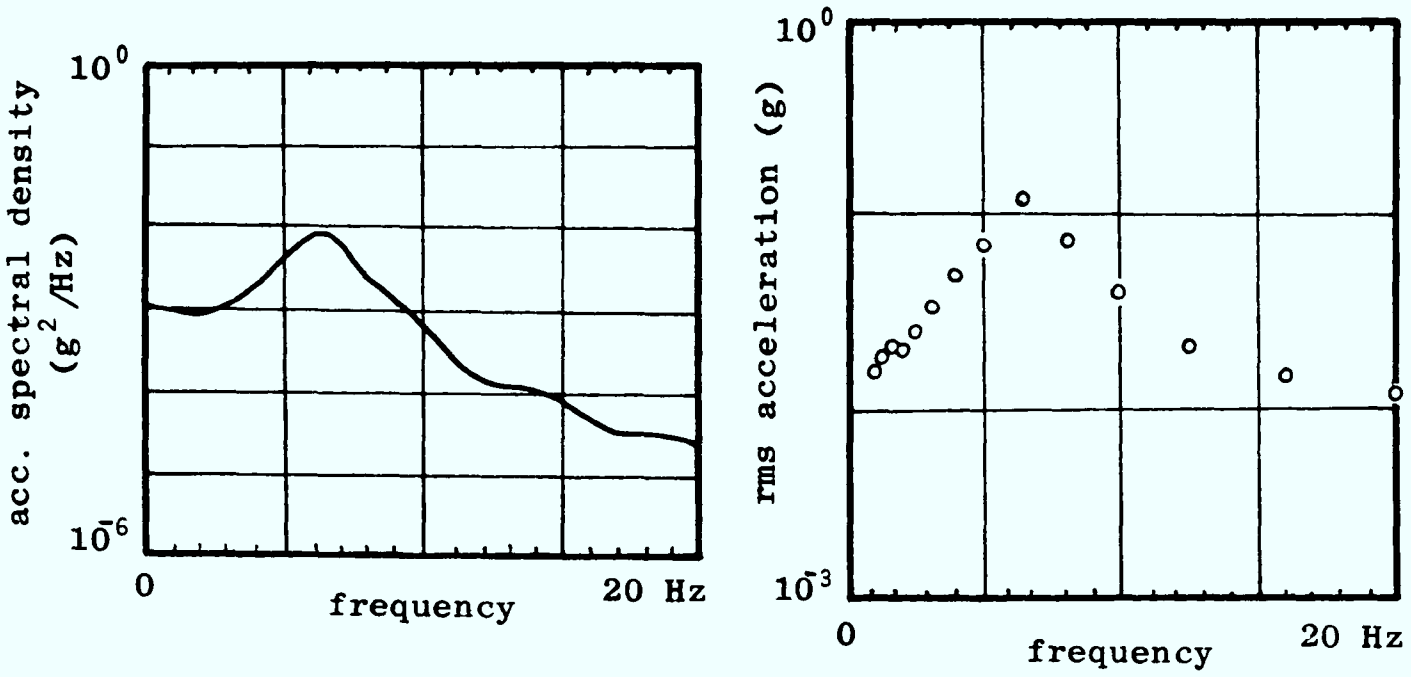

Fig 8.7 (a) Acceleration spectral density

(b) Rms accelerations

Two axle vehicle - response at front of vehicle to track vertical input (speed = 15 mph)

8.5.2 Effect of speed and condition of track

The rms accelerations for a two axle vehicle travelling along rigid track of a reasonable standard ($A = 5 \times 10^{-8}$ $m^2 cyc^3/m^3$) are shown in Fig 8.8 for a number of different speeds. By displacing these accelerations upwards the effect of a poorer track can be examined (see section 6.4.3), and this leads to the relationship between maximum permissible roughness coefficient and speed shown in Fig 8.9. The results for the car-bodies of the gondola manriding vehicle and unit train are also presented in this figure.

The ride of the two axle car is quite inferior to that of the other manriding vehicles, and is clearly unacceptable at high speeds. On poor quality track ($A = 5 \times 10^{-7}$ $m^2 cyc^3/m^3$) a fairly low maximum permissible speed of 8 mph is recommended on the basis of the acceptability limits. The ride improves on resilient track as a result of the vibrations being more readily damped, and this is illustrated on the figure. The motion of the rails and sleepers in the ballast is complex, but the treatment it is given in the model is quite simple and only partially tested. The relationship shown

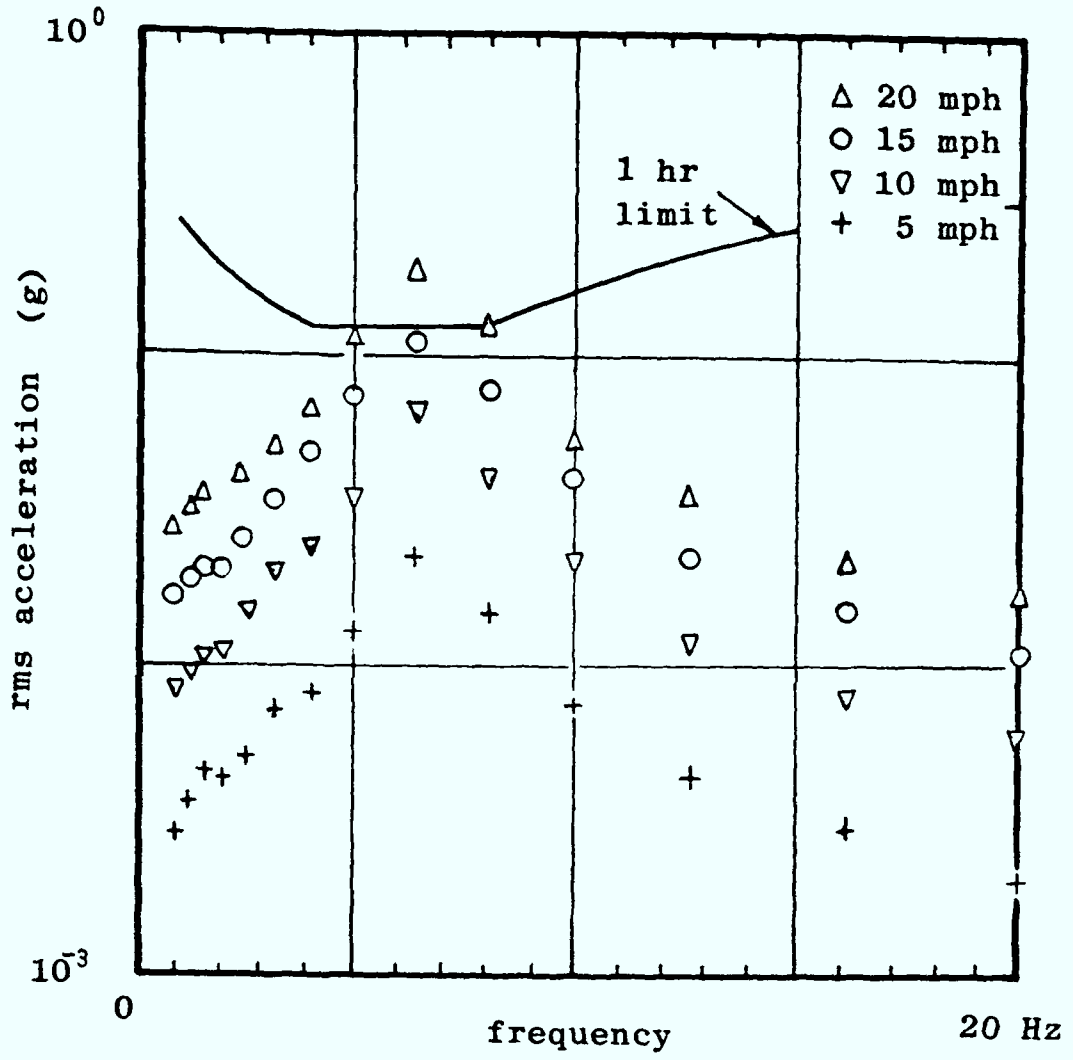

Fig 8.8 Rms accelerations at front of car-body

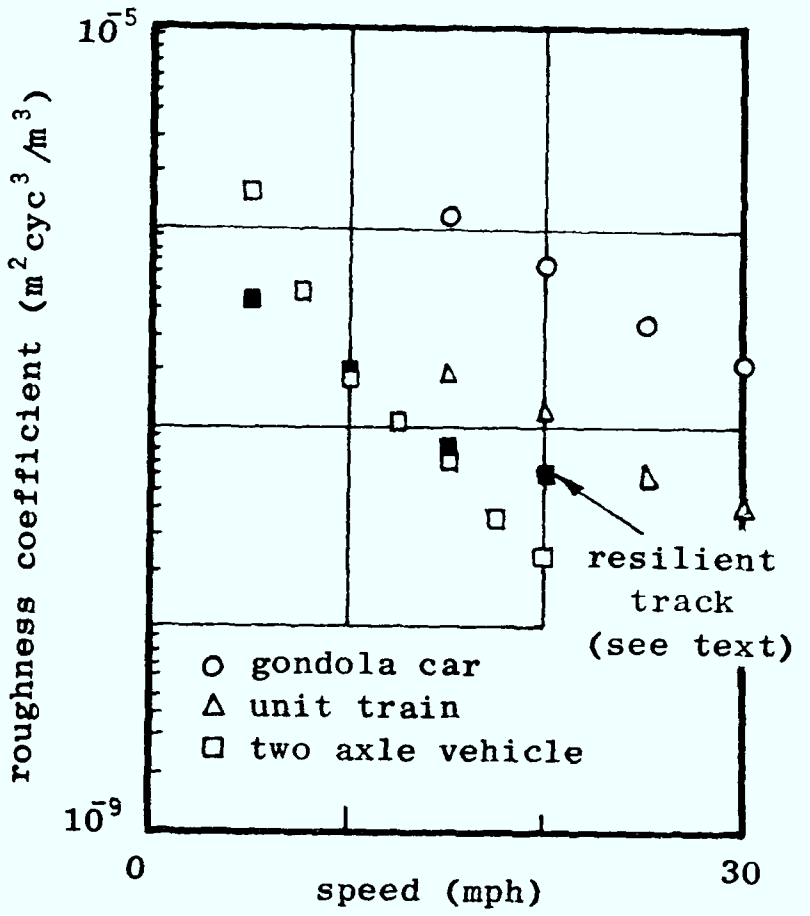

Fig 8.9 Relationship between the maximum permissible values of roughness coefficient, A, and speed for an acceptable ride in car-bodies of each class of manriding car.

in the figure for resilient track, which is based on the model, should thus be used with care.

8.5.3 Effect of primary suspension

The effect of the primary suspension is assessed in Fig 8.10 by comparing the ride of the existing vehicle with that of a vehicle with a more flexible suspension, and with one without suspension (see section 4.2.5). The comparison is made for the vehicles travelling at a speed of 15 mph along rigid track of a reasonable standard ($A = 5 \times 10^{-8}\ m^2 cyc^3/m^3$).

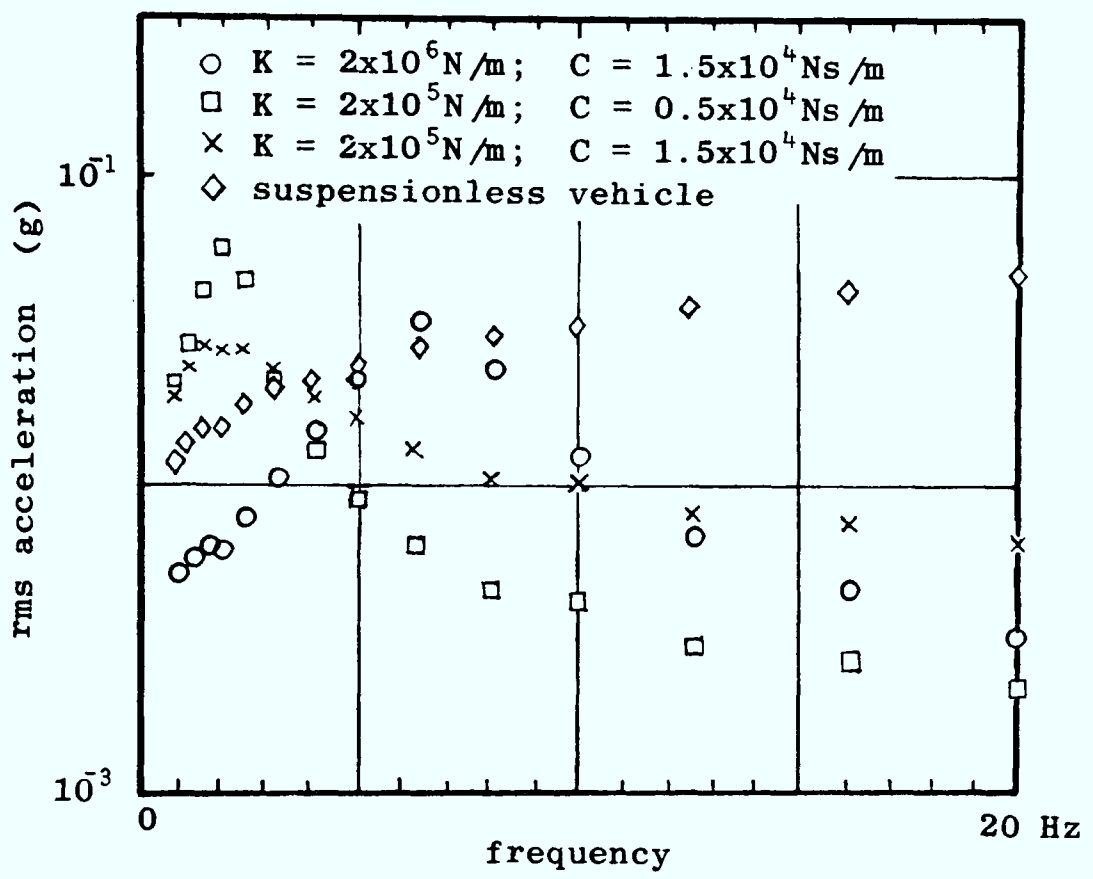

Fig 8.10 Rms accelerations at the front of the two axle manriding car (15 mph)

The results suggest that a superior ride is obtained when there is no suspension, and this is due to the fact that such a vehicle is not influenced by kinetic effects when travelling along normal track. However, it responds very badly to sudden changes in the track (such as dipped joints), and these reduce the ride quality and may affect the safety. The modelling technique used here cannot accommodate such irregularities.

The results for the vehicle with a flexible suspension indicate a slight reduction in the levels of vibration, and a shift in the

peak accelerations to a lower frequency. The ride is improved significantly only when additional damping is introduced into the suspension and this would appear to be the most effective method of improving the vehicles for high speed operation.

8.6 The ride of a two axle locomotive

8.6.1 Description of the locomotive

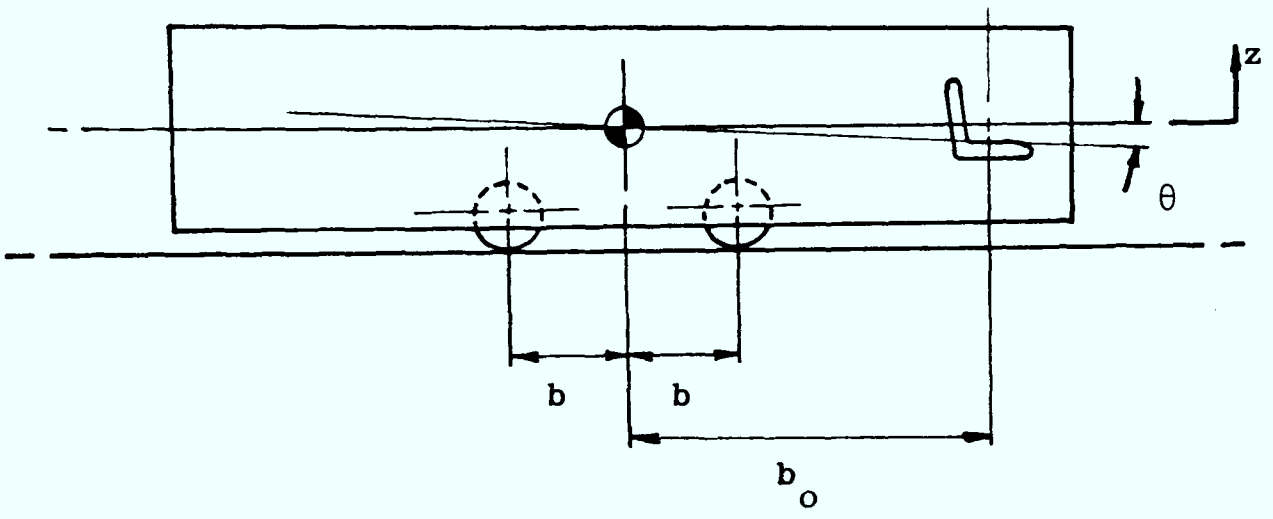

Fig 8.11 Two axle locomotive

The class of locomotive shown in Fig 8.11, which is widely used in British coal mines, is the subject of this section. It has a short wheelbase and a long overhang and, as a result, the pitching and yawing motions are amplified both at the driver's seat and the rear coupling. The motion of an isolated locomotive in response to vertical profile irregularities of the track is considered here using the model of a two axle vehicle. The ride is assessed on the basis of the chosen acceptability limits (see section 4.2.3).

8.6.2 Parameter values and resonant frequencies

Values are given below for the mass, inertia, stiffness, damping value, wheelbase, and overhang for a typical diesel locomotive.

$$\begin{aligned} m &= 15000 \text{ kg} \\ I_{yy} &= 20000 \text{ kg m}^2 \\ K &= 3.5 \times 10^6 \text{ N/m} \\ C &= 5.0 \times 10^4 \text{ Ns/m} \\ b &= 0.6 \text{ m} \\ b_o &= 2.25 \text{ m} \end{aligned} \qquad (8.8)$$

The resonant frequencies are evaluated (see section 6.2.4) and presented in Table 8.2.

Resonance	Frequency (Hz)
Locomotive bounce	2.4
Locomotive pitch	1.8

Table 8.2 Resonant frequencies of two axle locomotive

8.6.3 Effect of speed and condition of track

The rms accelerations for the locomotive travelling along rigid track of a reasonable standard ($A = 5 \times 10^{-8}$ $m^2 cyc^3/m^3$) are shown in Fig 8.12 for a number of different operating speeds. A relationship

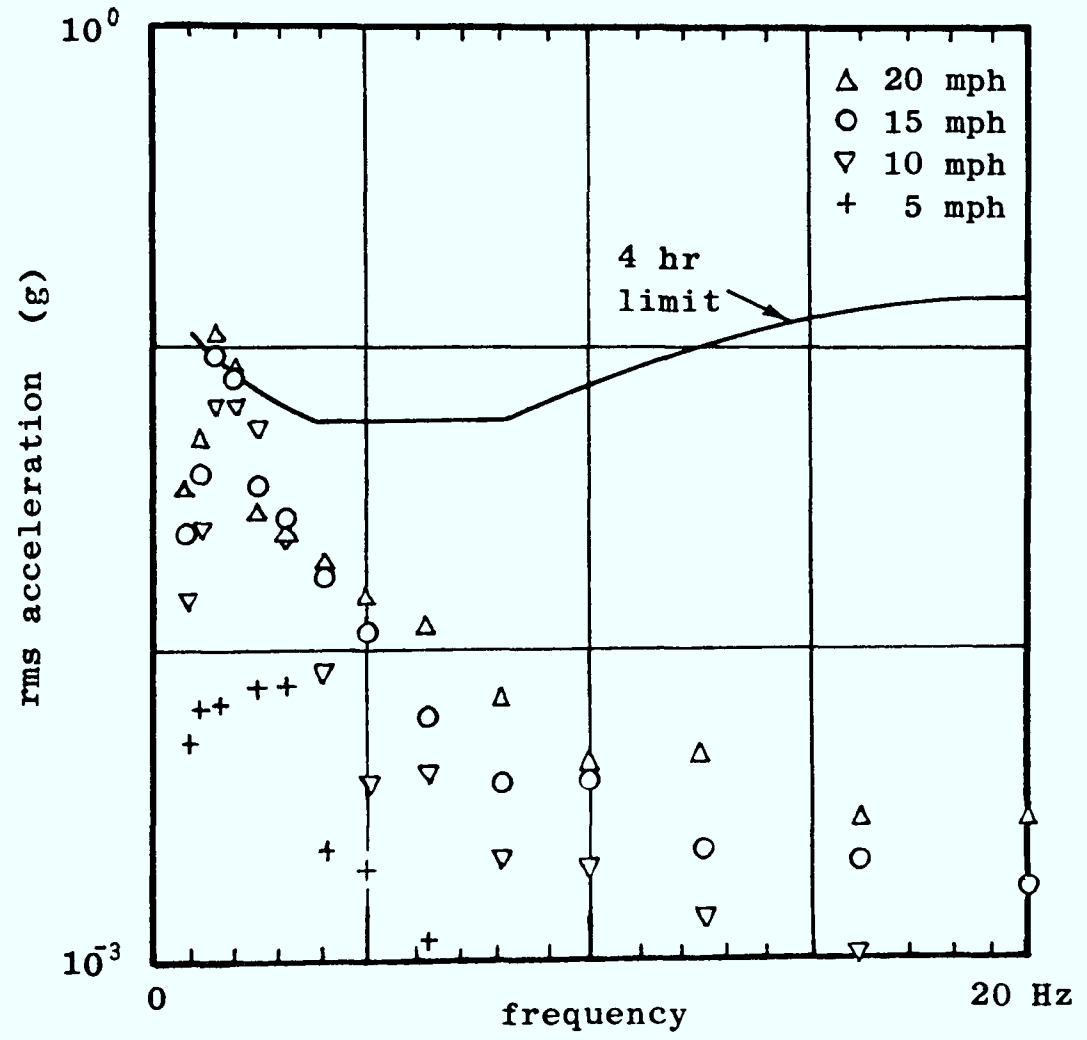

Fig 8.12 Rms accelerations at driver's seat of two axle locomotive

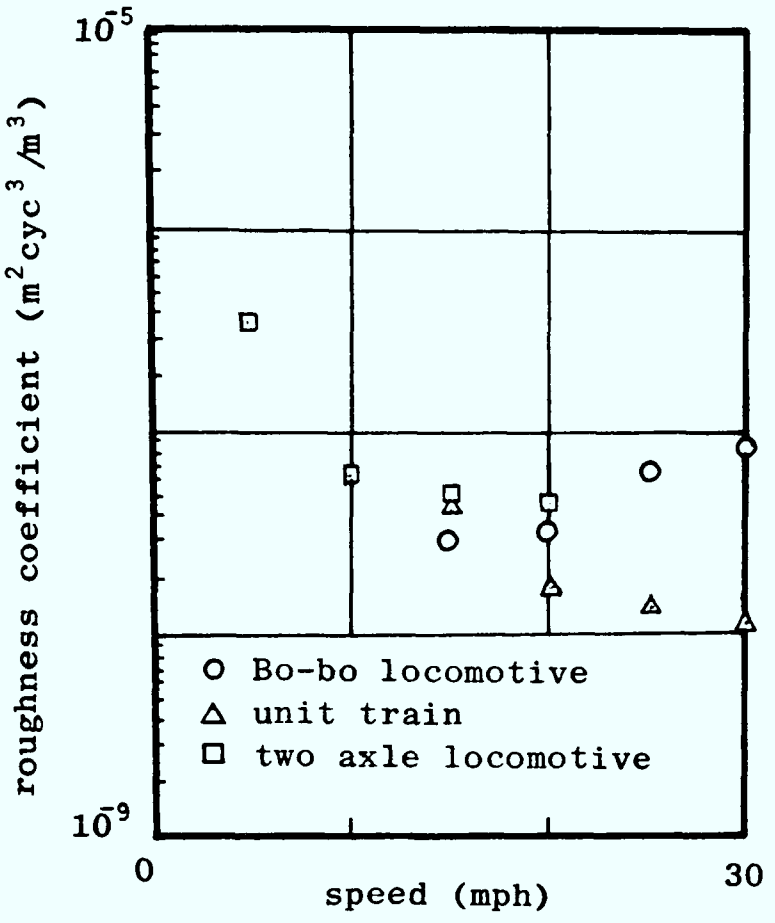

Fig 8.13 Relationship between the maximum permissible values of roughness coefficient, A, and speed for an acceptable ride in driver's seats of each class of locomotive.

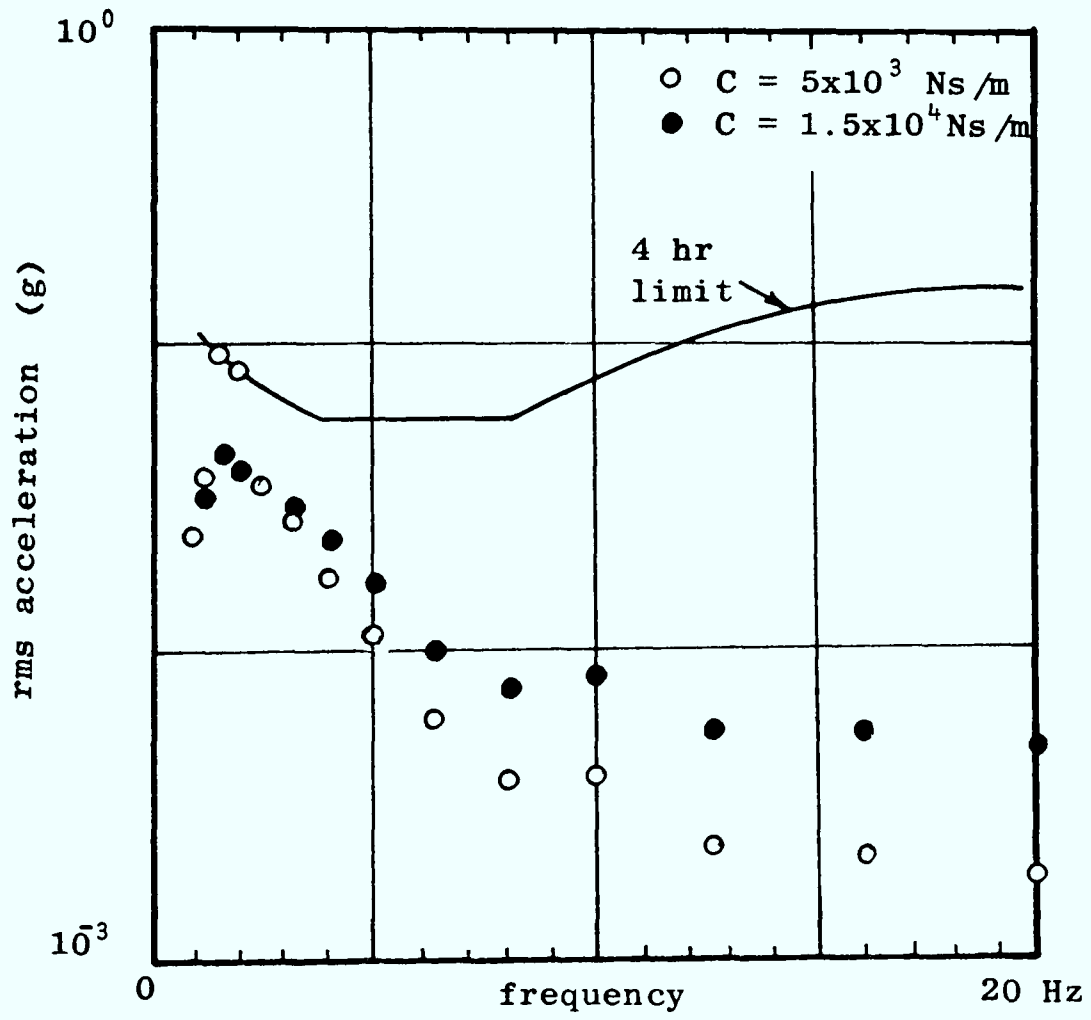

Fig 8.14 Rms accelerations at driver's seat of a two axle locomotive.

between the maximum permissible roughness coefficient and speed is shown in Fig 8.13, together with results for the Bo-bo locomotive and driving cab of the unit train.

The results indicate that the vehicle is not really suitable for travelling at high speeds, particularly when the track is of an inferior standard. This substantiates the conclusions made previously for a suspensionless locomotive of this type (see section 4.2.6).

8.6.4 Effect of dampers

Increasing the damping in the primary suspension improves the ride significantly and this is illustrated in Fig 8.14. Again this would appear to be the most effective method of improving the vehicles for high speed operation.

Chapter 9

Conclusion

9.1 Mine railways

The behaviour of a vehicle depends upon the state of the track it runs on, and this is particularly apparent with the manriding trains operating in coal mines. Even a good section of mine railway will appear to undulate, twist and wind (see Fig 1.8), and these features of the track geometry ultimately limit the safe speed at which any design of train may travel.

In mines, the rails are supported on chairs attached to sleepers, and there are irregularities associated with such things as joints, the lengths of rails, sleeper spacing, and points. The rail joints generally consist of a fish plate connection, although continuously welded track is occasionally used. Newly laid track may be observed with quite large spaces between adjacent rails at the joints (up to 15 mm), and these will clearly influence the behaviour of trains. Small vertical steps are also common. The rail lengths are quite short (18 ft rail lengths are common), and the action of ordinary traffic causes each rail to drop at the ends and become raised in the middle. This hogging is permanent and leads to periodic undulation and a dip in every joint. The sleeper spacing can also lead to periodic irregularities.

The tracks are laid on beds which vary from colliery to colliery: on ballast, directly on the floor, and in concrete. A track laid in concrete (eg Ellington Colliery) is not distorted greatly by the action of ordinary traffic and thus needs little maintenance, but the rigidity of the track causes large forces to be applied to the suspensions of the trains. A track laid on ballast has resilience, but the sizes of irregularities may be expected to increase when used by normal traffic. The occurrence of irregularities, although principally due to the large forces which are generated between the wheels and rails, is aggravated by the fact that the tracks are laid on floors which are subject to geological movement. The relationship between different bed construction, the resultant track irregularities and the behaviour of the vehicles has been discussed briefly in this thesis (see sections 3.4 and 8.5.2), but it clearly warrants further attention.

Because there are many different types of irregularities, the description of track geometry is never a straightforward task. Meticulous inspection along the entire length of a track is time consuming, and may well be impractical in many situations. This is, however, the only way in which isolated irregularities such as a rapid change in cross-level or a raised rail joint may be identified (see section 4.3.8). Description by spectral densities is a convenient alternative when only the average state of the track is required. The spectral density describes both random and periodic irregularities statistically in the form of the average sizes of the irregularities over a range of spatial frequencies (see section 3.3), and may be obtained from measurements of a relatively short section of track. The spectral density can be described by a simple algebraic relationship (equation (3.32)) which is found to compare favourably with measured data.

$$S_u(\Omega) = \frac{A}{\Omega^n}$$

where,

$S_u(\Omega)$ = spectral density describing irregularity

A = roughness coefficient

n = integer exponent (2, 3, or 4)

This relationship is used generally in the characterisation of main-line railways and is a convenient basis of comparison of different tracks: a large value of the roughness coefficient corresponds to a poor quality track. Using this description, a good section of mine railway is found to have irregularities which are about ten times larger than British mainline track (see section 3.4).

9.2 Manriding trains

The trains used in coal mines are quite different to those used on mainline railways: the weights, dimensions and suspension characteristics have all evolved to suit the extraordinary environment in which they operate. The vehicles are reasonably light (the axle load of the heaviest locomotive is about 10 tonnes, and of a typical

laden manrider is about 2 tonnes) and they have short wheelbases to enable the negotiation of curves with very small radii. As a result of this, there are many vehicles which have long overhangs, and where bogies are used they are generally shared between adjacent car-bodies (eg gondola car and unit train). The suspension is undeveloped and appears to have been designed to prevent derailment from kinematic effects. It is generally stiff and has little damping.

With the exception of those used for driving, the wheels revolve independently on a fixed axle which means that the flanges have to touch the rails to guide the vehicle. Although this causes few problems at slow speeds, it can lead to rapid flange wear and larger track irregularities at high speeds. Wear has already been observed on the gondola manriding cars, where it is also attributable to the use of unbalanced wheels (see section 6.6). The flange wear can be reduced by balancing the wheels, but if the existing wheel configurations are retained, further reduction in the wear depends on lowering the speeds of the vehicles or significantly improving the condition of the track. Both of these solutions are quite unsuitable, and so the clear implication is that conventional wheelsets should be fitted to manriding trains that travel at high speeds.

9.3 Recommendation for using conventional wheelsets

The tapered wheels of a conventional wheelset revolve at the same speed and tend to steer towards the middle of the track when displaced laterally. Provided that the yaw stiffness is low enough (see section 5.3.5), and an appropriate tyre profile is chosen for the wheels (see section 5.3.4), the vehicle will follow the track with little flange contact taking place. The advantages of using conventional wheelsets increase as trains travel faster and wheelsets should be fitted to any vehicle which is designed to travel at a speed greater than about 15 mph. This is a nominal speed chosen on the basis of the discussion in Chapter 5 (see Fig 5.9). Hunting instability, as a result of the steering action of wheelsets, is unlikely to occur (see section 5.4.3).

9.4 Likelihood of derailment

The existing vehicles operate with the flanges always in the vicinity of the rails, and so the wheels might be expected to "climb" up the rail and leave the track. This is unlikely to occur during normal running (see section 5.3.2), but it may occur as a result of sudden changes in the track geometry. The use of conventional wheelsets will reduce any danger of wheel climb derailment.

The use of unbalanced wheels on the gondola car can, under certain normal operating conditions, lead to a danger of derailment. When the train travels at a speed of 16 mph the pitch resonance of the leading bogie is excited, and this can lead to the front wheels lifting from the track (see section 6.5.4).. This is a further indication of the need for balanced wheels.

9.5 The ride of manriding trains

Little attention has been given in the past to the ride of mining trains. The levels of vibration increase as trains travel faster, and this leads to both greater loading of the track and vehicles, and a reduction of the comfort and working efficiency of the driver and passengers. Assessing any physiological response to vibration is difficult, and no universally accepted criterion has yet evolved. In this work the acceptability of the ride is assessed on the basis of permissible exposure times to known levels of acceleration measured in third octave frequency bands. In the absence of data collected specifically for mining transport, the permissible times are based on an international standard which sets general limits for maintaining working efficiency (see section 4.2.3). As more data becomes available these limits may be reviewed.

Designing vehicle suspensions to provide an adequate ride is more difficult than designing them to ensure safety from derailment and, in consequence, many of the exisiting vehicles are found to have an unacceptable ride. The vehicles with long overhangs (eg two axle locomotive and the cab of the unit train) generally provide a poor ride as a result of the amplification of the pitching motion, and these vehicles could be improved with an increase in the damping (see sections 7.4.3, 8.5.3, and 8.6.4). The ride in the gondola car, which has a secondary suspension, is quite acceptable when assessed

against this criterion.

9.6 Mathematical modelling of rail vehicles

In general, mathematical models are used to provide explanations of the motion of trains under a variety of different operating conditions. The models need to be elaborate enough to reflect the aspects of vehicle behaviour which are of interest, and constructed in such a way that the effects of design changes can be realistically assessed.

The models proposed in this thesis, although not sophisticated, fulfil these two requirements. They are constructed in order to predict the response to measured track irregularities, and produce results which compare favourably with the results of tests on all the main classes of rail vehicles used for manriding in British coal mines. The models have been used successfully to explain certain aspects of vehicle behaviour and, used in conjunction with the chosen acceptability criteria, have provided certain guidelines for changes in design (eg the requirement for conventional wheelsets).

There is little to be gained in creating more elaborate models of the existing vehicles travelling along normal track. As the vehicles evolve, such as when conventional wheelsets are fitted, the need for more detailed modelling will arise.

9.7 Permissible speeds of existing vehicles

Relationships are shown in Fig 9.1 between the maximum permissible speed of each class of manriding vehicle and the roughness coefficient describing the vertical profile of the track upon which it travels. The relationships are based on the predictions of the models and the ride acceptability limits.

Similar relationships to the ones shown can be evaluated for particular vehicles by changing the parameter values in the models (see section 6.4.3).

9.8 Suggestions for further work

Mining and mainline railways have different characteristics and, in the past, little of the data gathered from mainline experience has been readily transferrable to the mining application. As a result of

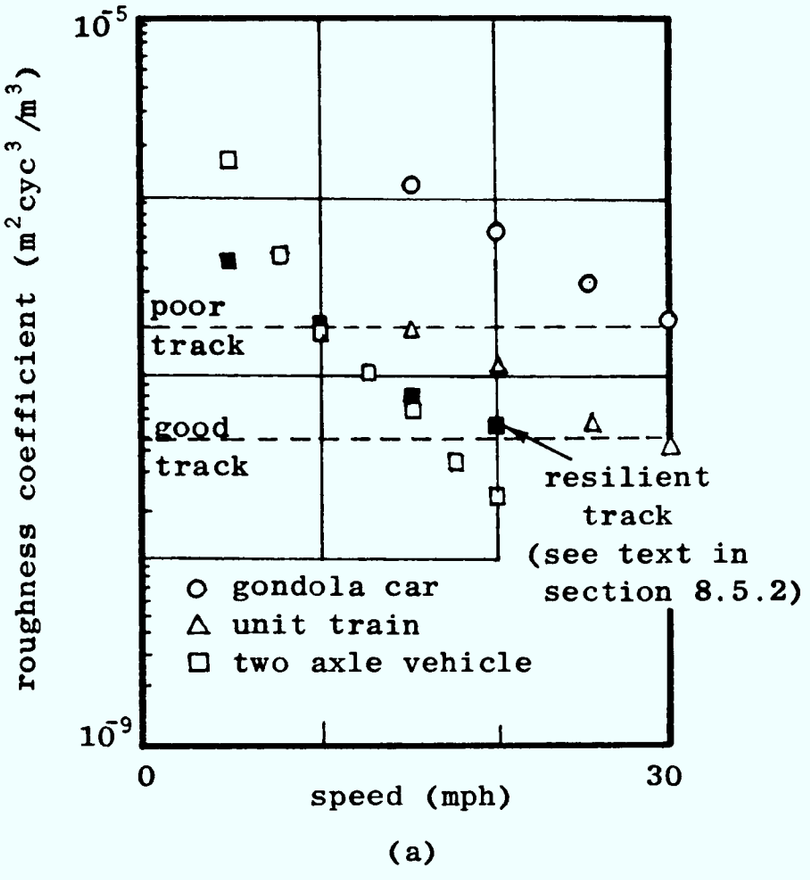

(a)

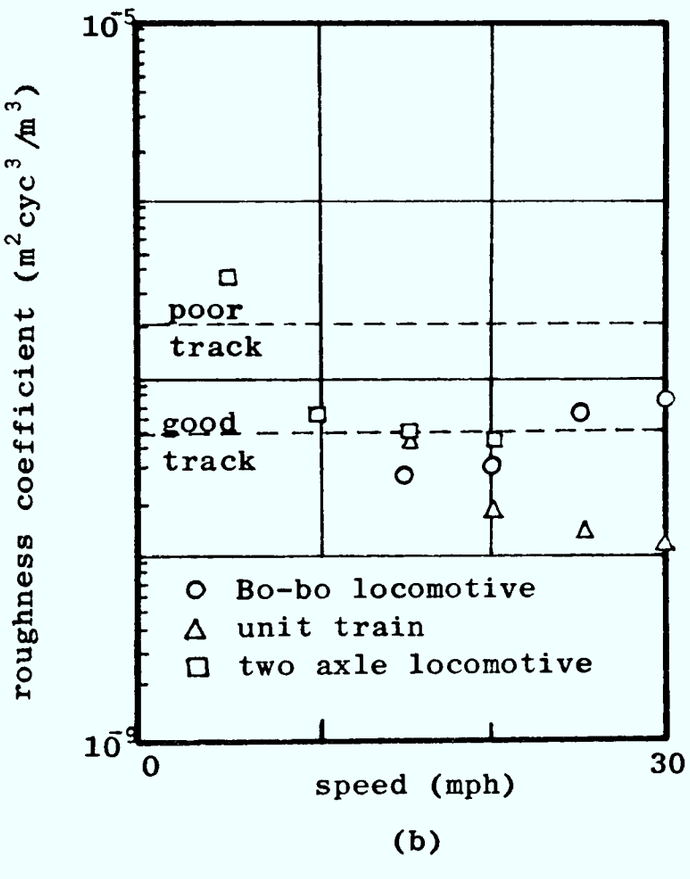

(b)

Fig 9.1 Relationship between the maximum permissible values of roughness coefficient, A, and speed for an acceptable ride
(a) car-bodies
(b) driver's seats of locomotives

this work it is now possible to apply much of the existing knowledge of wheelset design and vehicle behaviour to mine railways. However, there are aspects of the work still needing amplification.

The behaviour of manriding trains travelling over isolated irregularities, such as dipped joints and rapid changes in cross-level, has not been fully explored. Typical irregularities need to be identified, and ways of describing them, preferably by a single parameter, must be devised. The motion of vehicles in the vertical plane may then be investigated with only minor modifications of the models presented in this thesis (see sections 8.3 and 8.4), but any modelling of the lateral motion will require a more precise description of the geometries of the wheels and rails (see section 5.2.7). A device for measuring wheel and rail profiles is thus needed, and the design of the device must satisfy the stringent safety regulations used in coal mines. Modelling of the response of a rail vehicle to a particular irregularity can be used to ascertain any likelihood of derailment and, to this end, the criteria proposed in Chapter 4 (see section 4.3.4 and 4.3.6) can be used.

Another area requiring further work concerns the deterioration of track as a result of normal use. The action of mine trains, used for both manriding and the movement of materials, leads to the formation of quite large irregularities in the track, and these ultimately limit the safe speeds at which trains may travel. If a relationship is determined between the bed construction, the behaviour of the vehicles, and the resultant irregularities, a criterion could be devised for designing vehicles for safe use on track designed for minimum maintenance. The development of such a design criterion could lead to both a general improvement in the condition of the track, and a significant increase in the permissible speeds of mine trains.

References

(1) Curl, S.J., "Underground transport in coal mines", IEA Coal Research, Report No. ICTIS/TROI, April 1978.

(2) Stephenson, G., "Observations on edge and tram railways", 19th May 1821.

(3) Wickens, A.H., & Gilchrist, A.O., "Railway vehicle dynamics - the emergence of a practical theory", CEI MacRobert Award Lecture, 1977.

(4) ISO, "Proposal for ISO standard on characterization of rail-track irregularities", ISO/TC 108/SC 2/WG4-4, ANS2 S2-67, June 1979.

(5) BS 4854:1972, "Specification for cars for manriding in mines", British Standard, 1972.

(6) Carter, F.W., "On the action of a locomotive driving wheel", Proc. R.Soc., 1926.

(7) Kalker, J.J., "Survey of wheel-rail rolling contact theory", Veh. Sys. Dyn.5, 1979, pp 317-358.

(8) Hertz, H., "Über die Berührung fester elastischer Körper" (On the contact of elastic solids), J. Keine und Angewandte Mathematik, 1882, pp 156-171.

(9) Kalker, J.J., "On the rolling contact of two elastic bodies in the presence of dry friction", Doc. dissert., Tech University of Delft, 1967.

(10) Hobbs, A.E.W., "A survey of creep", BR Tech. note DYN 52, April 1967.

(11) Timoshenko, S.P., & Goodier, J.N., "Theory of elasticity", 3rd edit., McGraw-Hill, 1970, section 141.

(12) Raven, F.H., "Automatic control enginering", McGraw-Hill Kogakusha Ltd., NY, 1978.

(13) Newland, D.E., "An introduction to random vibrations and spectral analysis", Longman, 1975.

(14) NAG, Subroutine F04 ADF, Numerical Algorithms Group

(15) Lewis, R.B., Cook, W.L., & Forsyth, R.J., "The high speed track recording coach", BR Tech note TRIS 1, 260-82-1, Feb 1981.

(16) BS1259:1958, "Intrinsically safe electrical apparatus and circuits for use in explosive atmospheres", British Standard, 1958.

(17) Clibborn, J.S., "Underground rail transport monitoring", Mining Tech., Nov 1982, pp 473-477.

(18) Pollard, M.G., "Power spectra of track roughness obtained from the APT survey", BR Tech note DT2, Oct 1969.

(19) ISO, "Guide for the evaluation of human exposure to whole-body vibration", ISO 2631-1978 (E).

(20) Nadal, M.J., "Theorie de la stabilite des locomotives Part II: mouvement de lacet" Annls Mines 1896, 10, 2.

(21) Gilchrist, A.O., & Brickle, B.V., "A re-examination of the proneness to derailment of a railway wheelset", J.Mech.Eng.Sc., Vol. 18, No. 3, 1976, pp 131-141.

(22) Matsui, N., "On the derailment quotient, Q/P", JNR Car Dyn. Lab., Railway Tech. Research Inst., 1966.

(23) Arai, S., & Yokose, K., "Simulation of lateral motion of 2-axle railway vehicle in running", The Dyn. of Vehicles on Roads and Railway tracks, ed. Pacejka, Swets & Zeitlinger, Amsterdam, 1976.

(24) Ikemori, M., "A study of track maintenance for the derailment due to the interaction between track and vehicle", JNR Quart. Reports, Vol. 19, No. 1, 1978, pp 1-6.

(25) Van Manen, P., "Investigation of the derailments of the Hunslet 90 hp diesel locomotive at Blidworth colliery", Report to the NCB Mining Res. & Development Est., March 1982.

(26) Wickens, A.H., "The dynamic stability of railway vehicle wheelsets and bogies having profiled wheels", Int.J. Solids Structures, Vol. 1, 1965, pp 319-341.

(27) Newland, D.E., "Steering characteristics of bogies", The Railway Gazette, 4 Oct 1968.

(28) Kaplan, A., Hasselman, T.K., & Short, S.A., "Independently rotating wheels for high speed trains", SAE Paper No 700841, Oct 5-9, 1970.

(29) Gilchrist, A.O., "Variation along the track of conicity and rolling line offset", BR Tech. note DYN 62, July 1967.

(30) Koffman, J.L., "Heumann tyre profile tests on British Railways", The Railway Gazette, 2 April 1965, pp 279-283.

(31) NAG, Subroutine F02 AFF, Numerical Algorithms Group.

(32) Atkinson, W., "Easington 11 car gondola manriding cars", NCB Internal memo., 11th May 1982.

(33) Clemson, P., Visit report No. TT(84) 19, NCB Mining Res. & Development Est., 29 March 1984.

(34) NCB, "NCB-Clayton 24 seat unit train", Information brochure, NCB Mining Res. & Development Est., Eng. Principles Branch, Aug 1982.

(35) Van Manen, P., & Brickle, B.V., "The dynamic behaviour of a railway mine vehicle", The Mining Engineer, June 1983, pp 653-656.

(36) Van Manen, P., & Brickle, B.V., "The interaction between railway mine vehicles and track in coal mines, Proc 8th IAVSD Symposium, MIT, Cambridge, Ma., USA, 15-19 Aug 1983.

Appendix 1

Fourier Transforms

The Fourier transform evaluates the harmonic content of a waveform using the relationship:

$$X(f) = \int_{-\infty}^{\infty} x(t)e^{-j2\pi ft}dt \qquad \text{(A1.1)}$$

where,

$x(t)$ = waveform

$X(f)$ = Fourier transform

t = time

f = frequency

This is defined whenever:

$$\int_{-\infty}^{\infty} |x(t)|\, dt < \infty \qquad \text{(A1.2)}$$

If the waveform is represented as a series of N points, equally spaced by a time, Δt, the discrete Fourier transform is used:

$$X_k = \frac{1}{N} \sum_{r=0}^{N-1} x_r e^{-j2\pi kr/N} \qquad \text{(A1.3)}$$

(k = any integer)

where,

X_k = Fourier coefficient

($X_k(f)$ is located at the frequency, $f = {}^{K}/_{N\Delta t}$)

This may be solved using a fast Fourier transform (see Fig A1.1)

```
1000 ! FFT SUBROUTINE
1010 FOR J=1 TO N8
1020 A1(J)=A1(J)/N8
1030 A2(J)=A2(J)/N8
1040 NEXT J
1050 N2=N8/2
1060 N1=N8-1
1070 J=1
1080 FOR L=1 TO N1
1090 IF L>=J THEN 1160
1100 T1=A1(J)
1110 T2=A2(J)
1120 A1(J)=A1(L)
1130 A2(J)=A2(L)
1140 A1(L)=T1
1150 A2(L)=T2
1160 K=N2
1170 IF K>=J THEN 1210
1180 J=J-K
1190 K=K/2
1200 GOTO 1170
1210 J=J+K
1220 NEXT L
1230 FOR M=1 TO N
1240 U1=1
1250 U2=0
1260 M1=2^M
1270 K=M1/2
1280 W1=COS(PI/K)
1290 W2=-SIN(PI/K)
1300 FOR J=1 TO K
1310 FOR L=J TO N8 STEP M1
1320 L1=L+K
1330 T1=A1(L1)*U1-A2(L1)*U2
1340 T2=A1(L1)*U2+A2(L1)*U1
1350 A1(L1)=A1(L)-T1
1360 A2(L1)=A2(L)-T2
1370 A1(L)=A1(L)+T1
1380 A2(L)=A2(L)+T2
1390 NEXT L
1400 U1=U1*W1-U2*W2
1410 U2=U1*W2+U2*W1
1420 NEXT J
1430 NEXT M
1435 BEEP @ BEEP @ BEEP
1440 RETURN
```

Fig A1.1 Basic computer program to calculate the discrete Fourier Transform of a sequence A1(1), A1(2),..A1(N8) by the fast Fourier Transform technique (see Newland (13)).

where,

A1(R) = x_r in equation (A1.3)

N8 = N in equation (A1.3)

Appendix 2

Computer Programs

A2.1 Evaluation of transfer function

The program TF.F77 evaluates the transfer function of any vehicle with a motion described by equations in the form:

$$(Ms^2 + Ls + K)\underset{\sim}{q} = (Cs + D)T(s)u$$

where,

M, L, K	=	inertia, damping and stiffness matrices
C, D	=	input matrices
$\underset{\sim}{q}$	=	vehicle co-ordinate vector
u	=	track co-ordinate at front wheels
T(s)	=	time delay vector
s	=	differential operator

The program is written in FORTRAN 77, and uses a library subroutine (see NAG (14)) to evaluate the transfer function a 0.1 Hz intervals over a frequency range of 0 to 20 Hz. The inertia, damping, stiffness and input matrices are defined in the subroutine PARAM, and the time delay vector is defined in the subroutine INPUT. The transfer function is expressed in the form of real and imaginary vectors (see equation 2.40) which are written into an output file designated by the user. The speed of the vehicle and the number of variables in the equations of motion (max 10 variables) are also written into this file.

A listing of the main program is shown in Fig A2.1, and listings of the subroutines containing the matrices and vectors for each of the vehicle models are shown in Figs A2.2 to A2.6. The program is also explained in the text (see section 2.6.1).

A2.2 Evaluation of wheelset transfer function

The program TFW.F77 evaluates the transfer function for a single wheelset and includes the non-linear effects of the flange touching the rail. It is essentially the same as the program TF.F77, except for the fact that it includes a describing function description of gravitational stiffness (see section 5.2.5).

The program, which is listed in Fig A2.7, is only applicable to the model of a single wheelset described in Chapter 5.

A2.3 Plotting of variables

The transfer function data can be plotted in the following ways by the program PLOT.F77: as an acceleration spectral density, as rms accelerations in third octave bands, or as a transfer function. The program creates the plots for a track input expressed in the form:

$$S_u(\Omega) = \frac{A}{\Omega^n}$$

where,

$S_u(\Omega)$ = spectral density describing track irregularity

Ω = spatial frequency

A = roughness coefficient

n = integer exponent (2,3, or 4)

The values of the roughness coefficient and the exponent are defined by the user and a single variable, or combination of two variables, is then plotted. The program is written in FORTRAN 77 and uses Benson plotter library subroutines.

A listing of the program is shown in Fig A2.8. The program is also explained in the text (see section 2.6.2).

A2.4 Evaluation of eigenvalues

The program EIGEN.F77 evaluates the solutions (eigenvalues) for the characteristic equation:

$$\underset{\sim}{M}\ddot{q} + \underset{\sim}{L}\dot{q} + \underset{\sim}{K}q = 0$$

The program is written in FORTRAN 77, and uses a library subroutine (see NAG (31)) to evaluate the eigenvalues over a range of operating speeds. The inertia, damping, and stiffness matrices are defined in the subroutine PARAM (see section A2.1).

A listing of the program is shown in Fig A2.9. The solution technique is explained in more detail in the text (see section 5.4.2).

```
 10 GCLEAR ! PITCH & BOUNCE
 15 LOCATE 0,58,0,86
 20 SCALE 0,1,-1.5,1.5
 30 XAXIS 0,.1
 40 YAXIS 0,.5
 50 H=.001
 60 M=1134
 70 I=1100
 80 K=2000000
 90 C=15000
100 V=2.45
110 B=.69
120 Y2=0 @ Y1=0 @ Y0=0
130 Z2=0 @ Z1=0 @ Z0=0
140 V2=0 @ V1=0 @ V0=0
150 W2=0 @ W1=0 @ W0=0
160 U1=0 @ U2=0
170 FOR T=0 TO 1 STEP H
180 U1=.006
190 IF T>2*B/V THEN U2=.006
200 Z2=K*(U1+U2)-2*K*Y0-2*C*Y1
210 Z2=Z2/M
220 W2=B*B*(K*(U2-U1)-2*K*V0-2*C
    *V1)/I
230 Z1=Y1+H/2*(Y2+Z2)
240 Z0=Y0+H/2*(Y1+Z1)
250 W1=V1+H/2*(V2+W2)
260 W0=V0+H/2* V1+W1)
270 Y2=Z2 @ Y1=Z1 @ Y0=Z0
280 V2=W2 @ V1=W1 @ V0=W0
290 PLOT T,(-(1.675*W2)+Z2)/9.8
300 NEXT T
310 END
```

where,

$$Z2 = \ddot{z}_{t+\Delta t} \qquad Y2 = \ddot{z}_{t}$$

$$Z1 = \dot{z}_{t+\Delta t} \qquad Y1 = \dot{z}_{t}$$

$$Z0 = z_{t+\Delta t} \qquad Y0 = z_{t}$$

$$W2 = \ddot{\theta}_{t+\Delta t} \qquad V2 = \ddot{\theta}_{t}$$

$$W1 = \dot{\theta}_{t+\Delta t} \qquad V1 = \dot{\theta}_{t}$$

$$W0 = \theta_{t+\Delta t} \qquad V0 = \theta_{t}$$

Fig A2.10 Simulation of two axle vehicle (AXLE2)

Appendix 4

Test Results

A4.1 The gondola manriding car

The test results are presented in the form of spectral densities which describe the accelerations at various positions of the vehicle. The notation is defined in Fig A4.1.

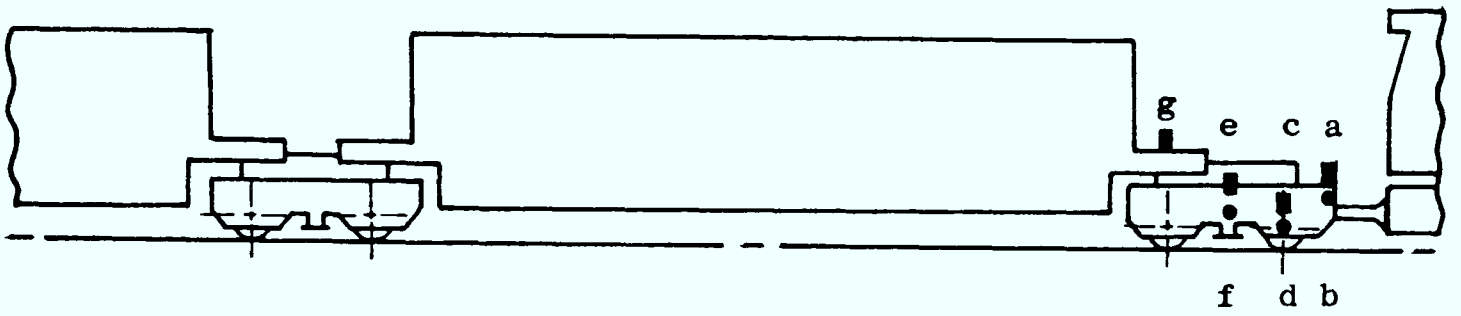

Fig A4.1 Tredomen gondola manriding car

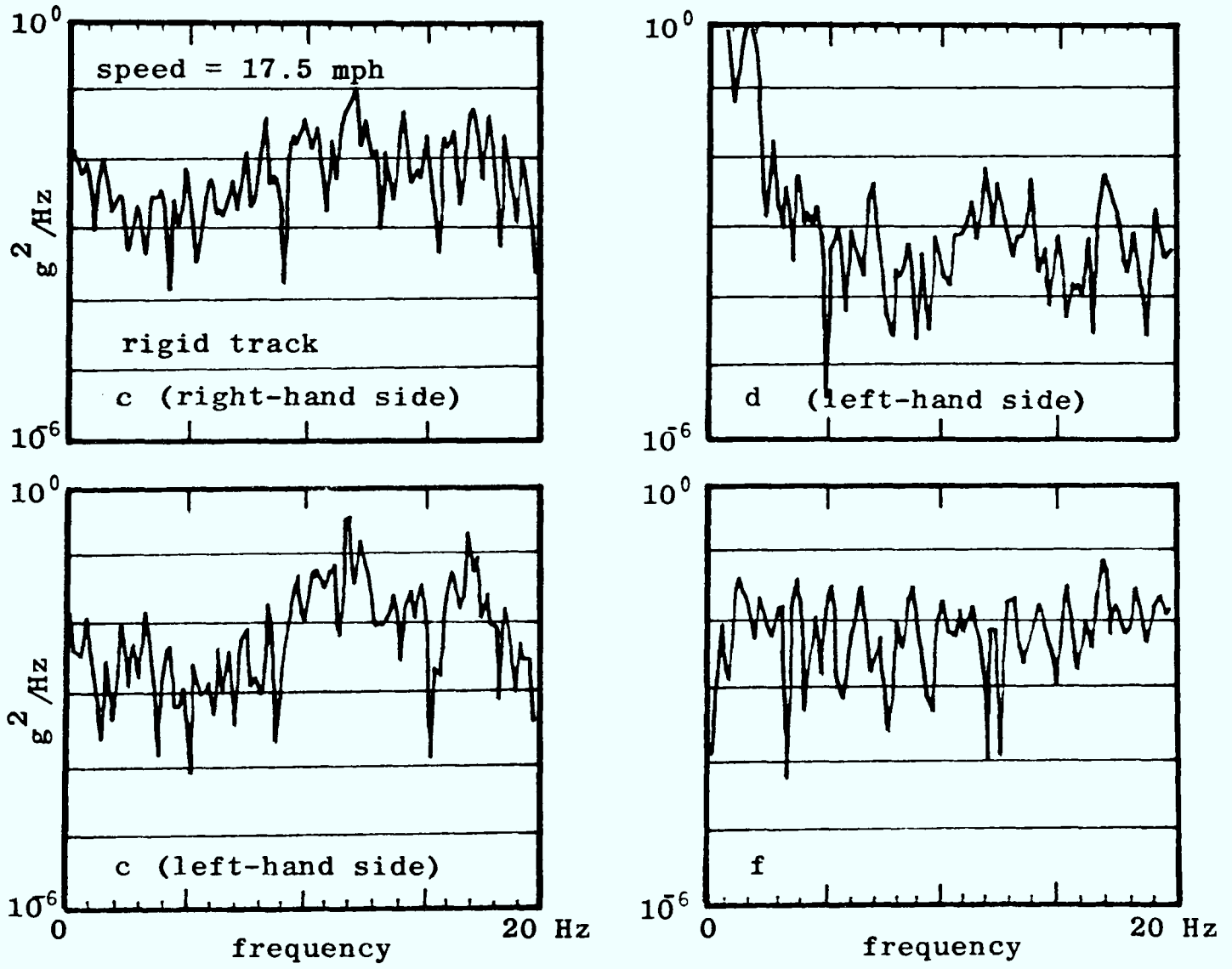

Fig A4.2 Acceleration spectral densities

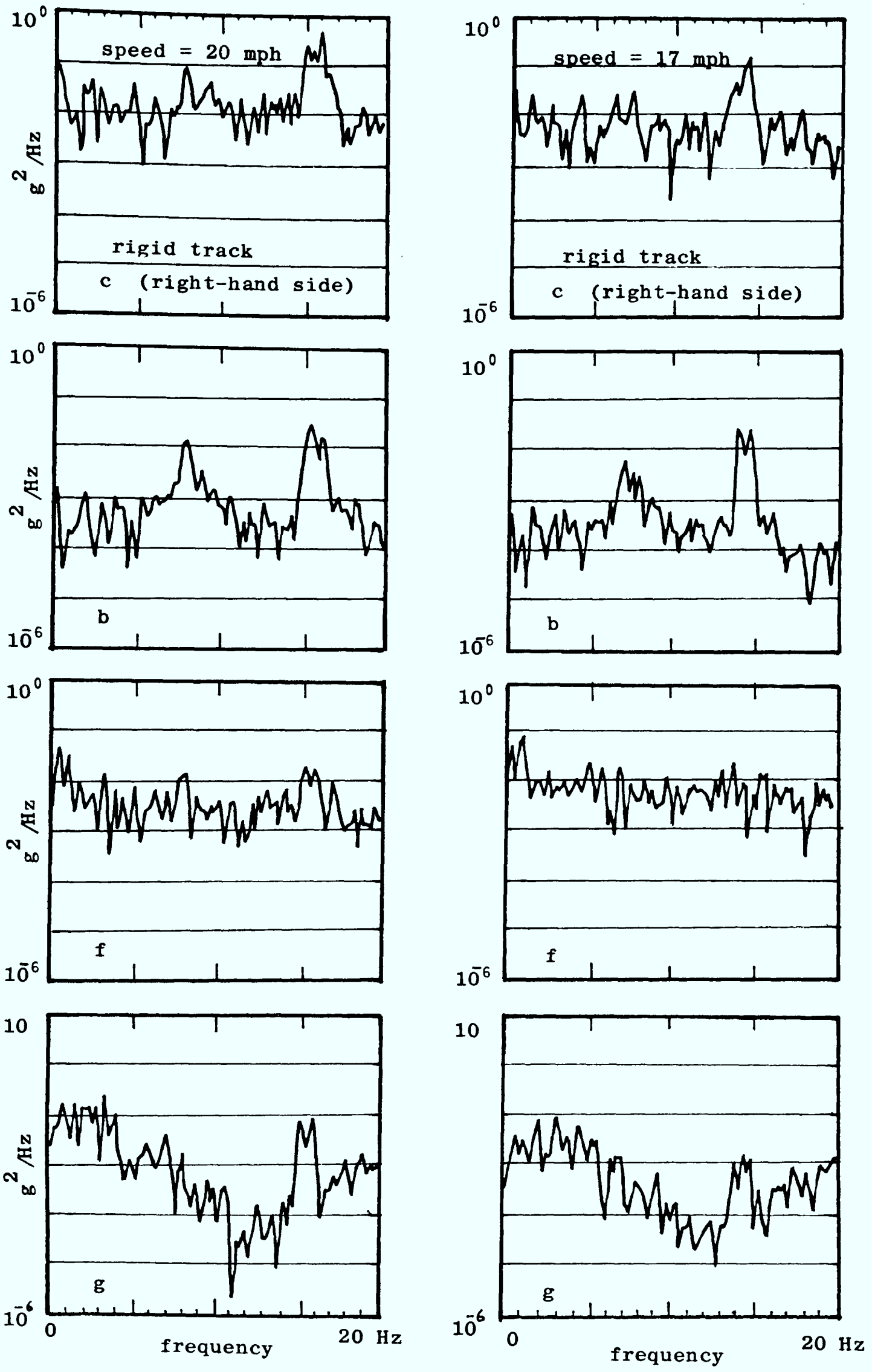

Fig A4.3 Acceleration spectral densities

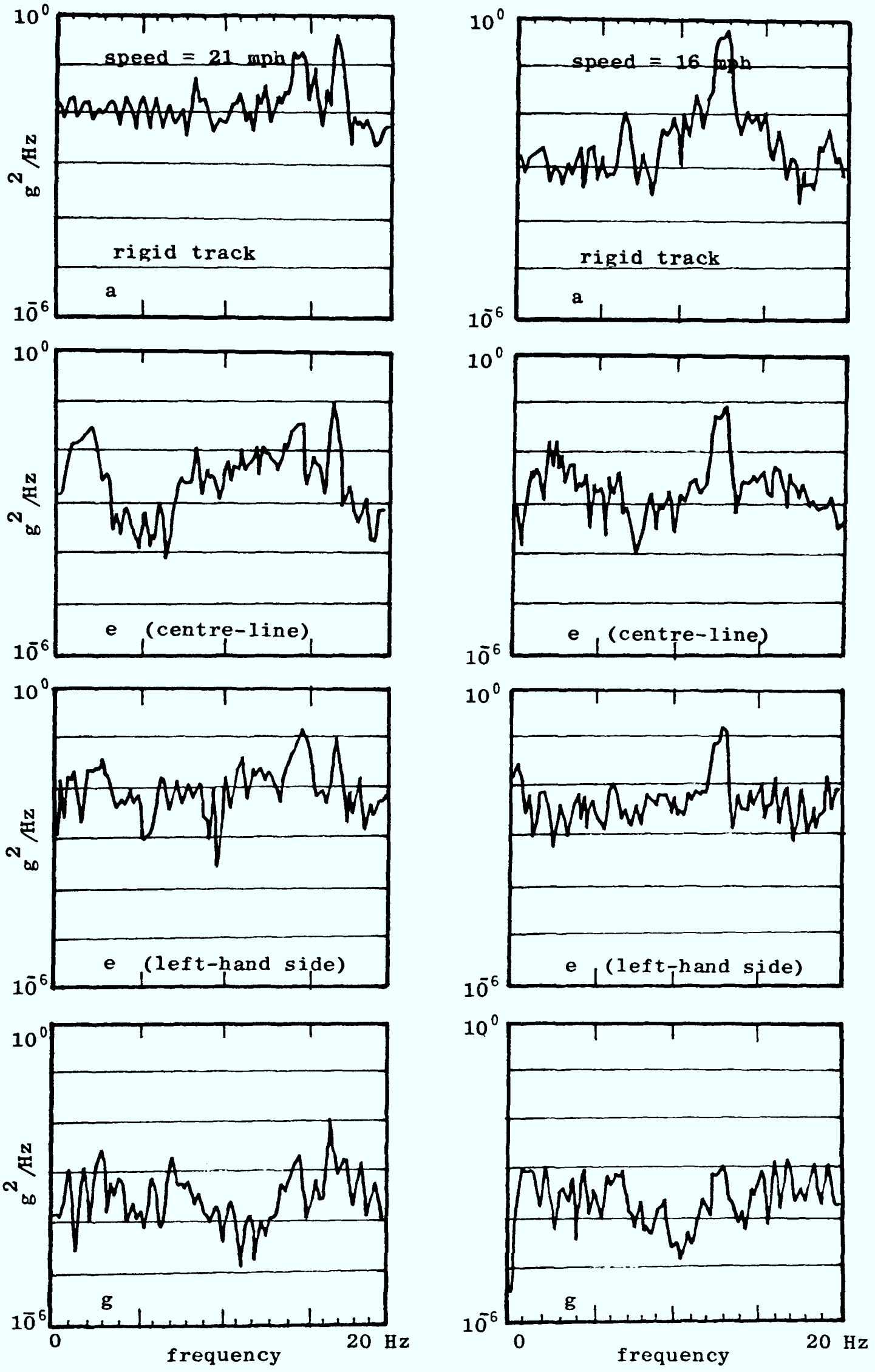

Fig A4.4 Acceleration spectral densities

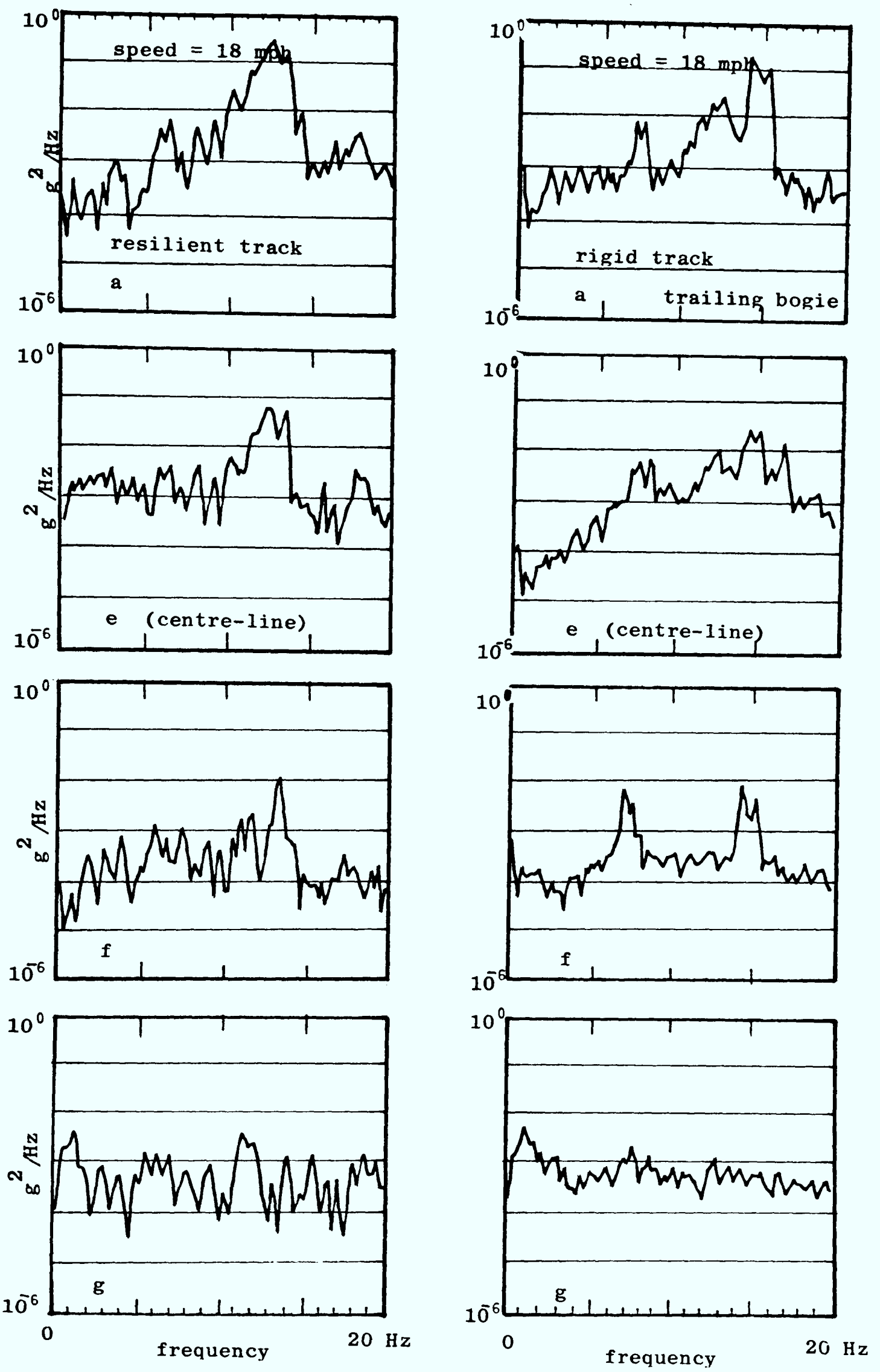

Fig A4.5 Acceleration spectral densities

A4.2 The Bo-bo locomotive

The test results are presented in the form of spectral densities which describe the accelerations at various positions of the vehicle. The notation is defined in Fig A4.6.

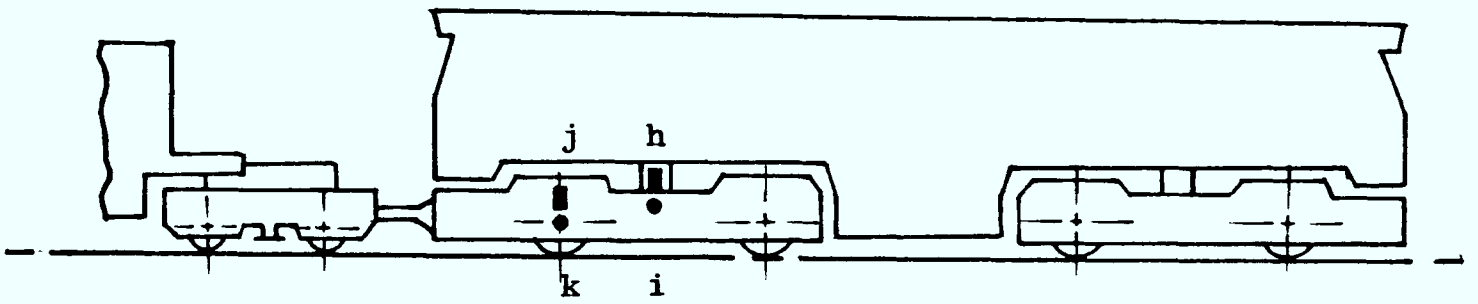

Fig A4.6 Hunslet 225 kW Bo-bo locomotive

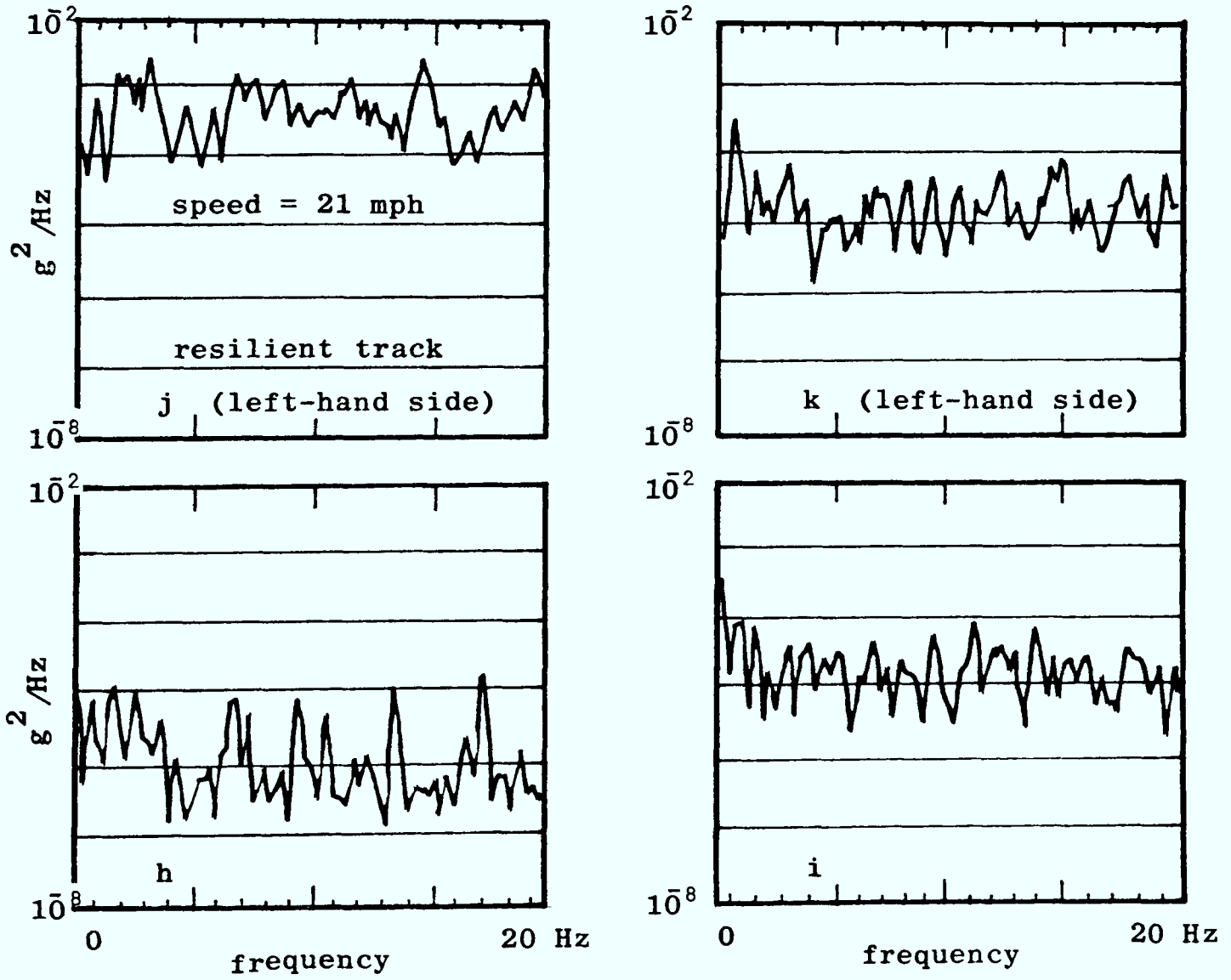

Fig A4.7 Acceleration spectral densities

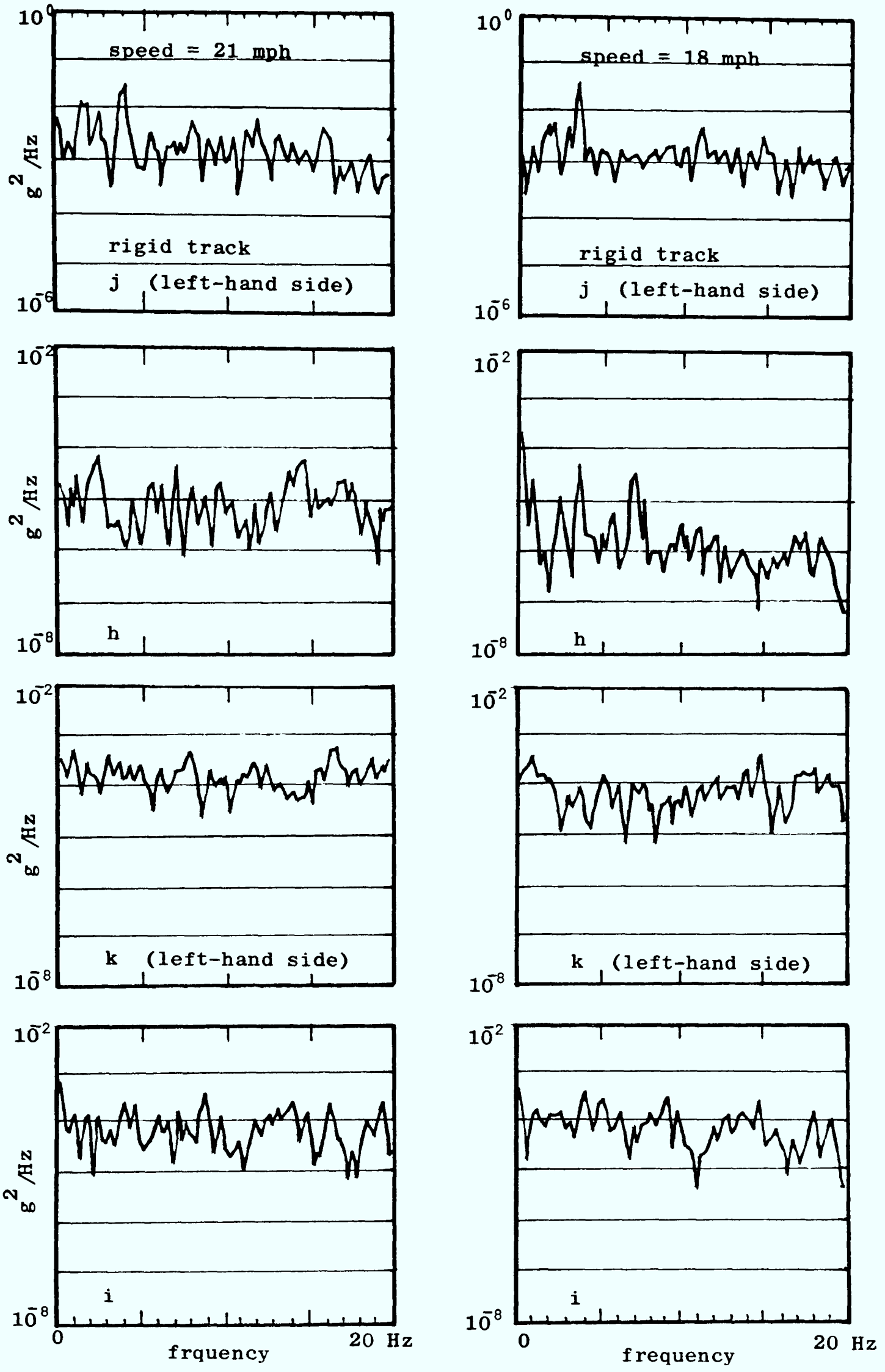

Fig A4.8 Acceleration spectral densities

A4.3 The unit train

The test results are presented in the form of spectral densities which describe the accelerations at various positions of the vehicle. The notation is defined in Fig A4.9

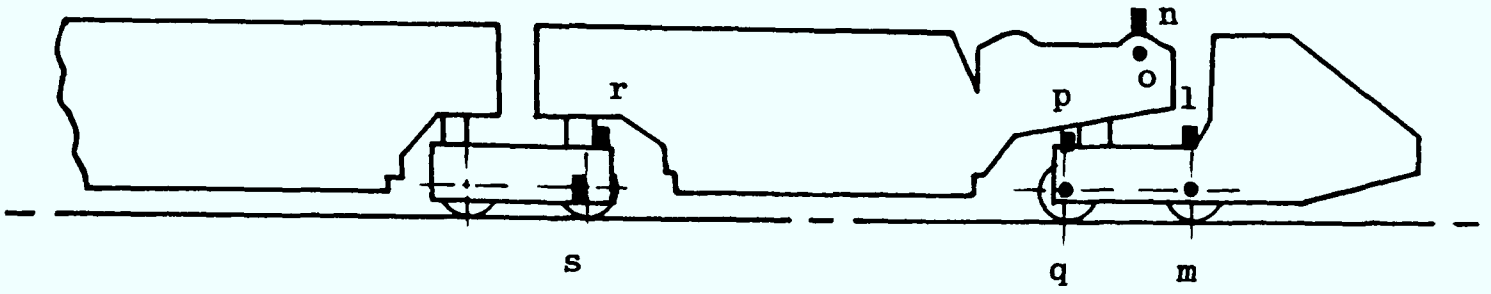

Fig A4.9 NCB-Clayton 24 seat unit train

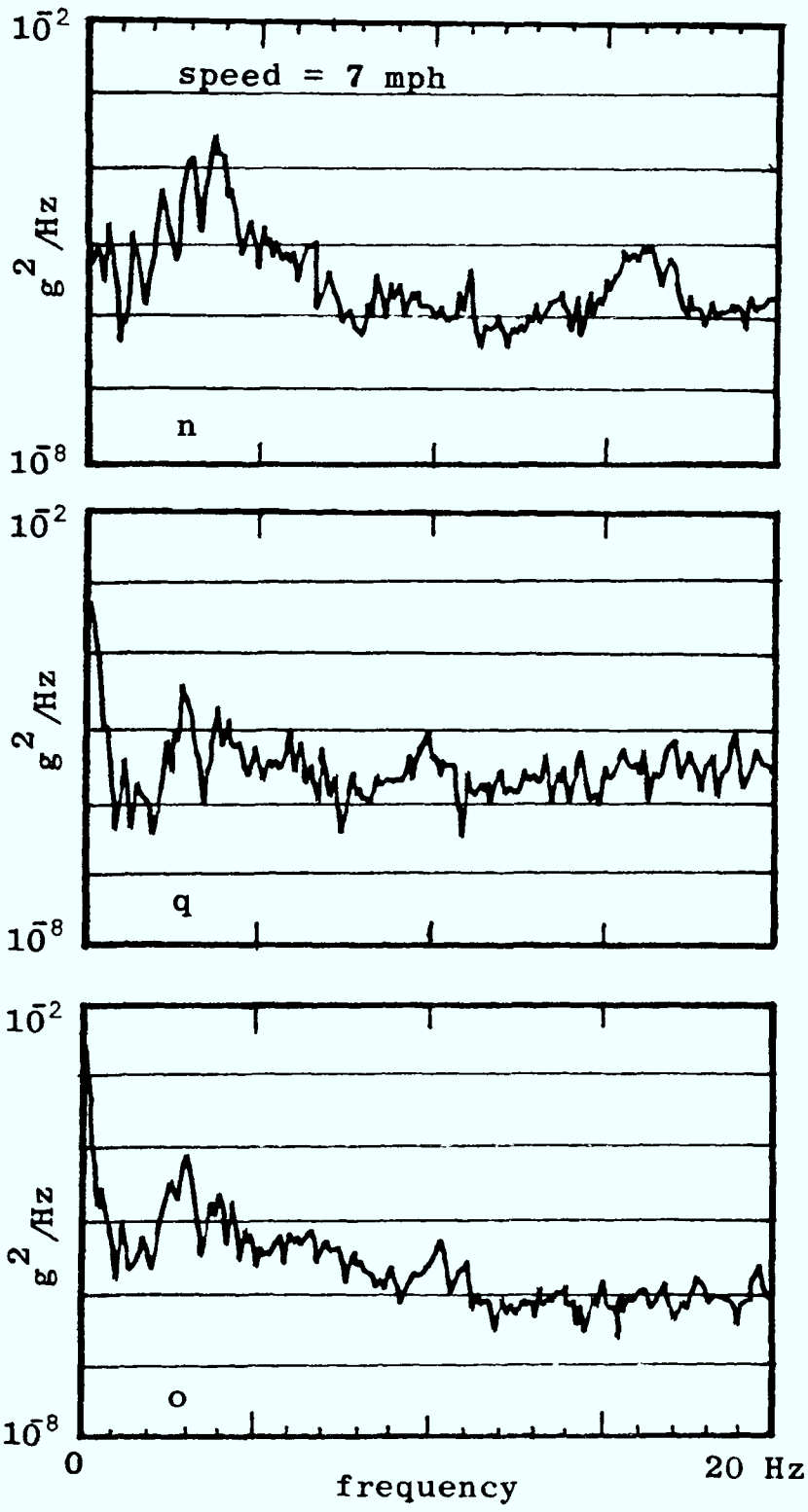

Fig A4.10 Acceleration spectral densities

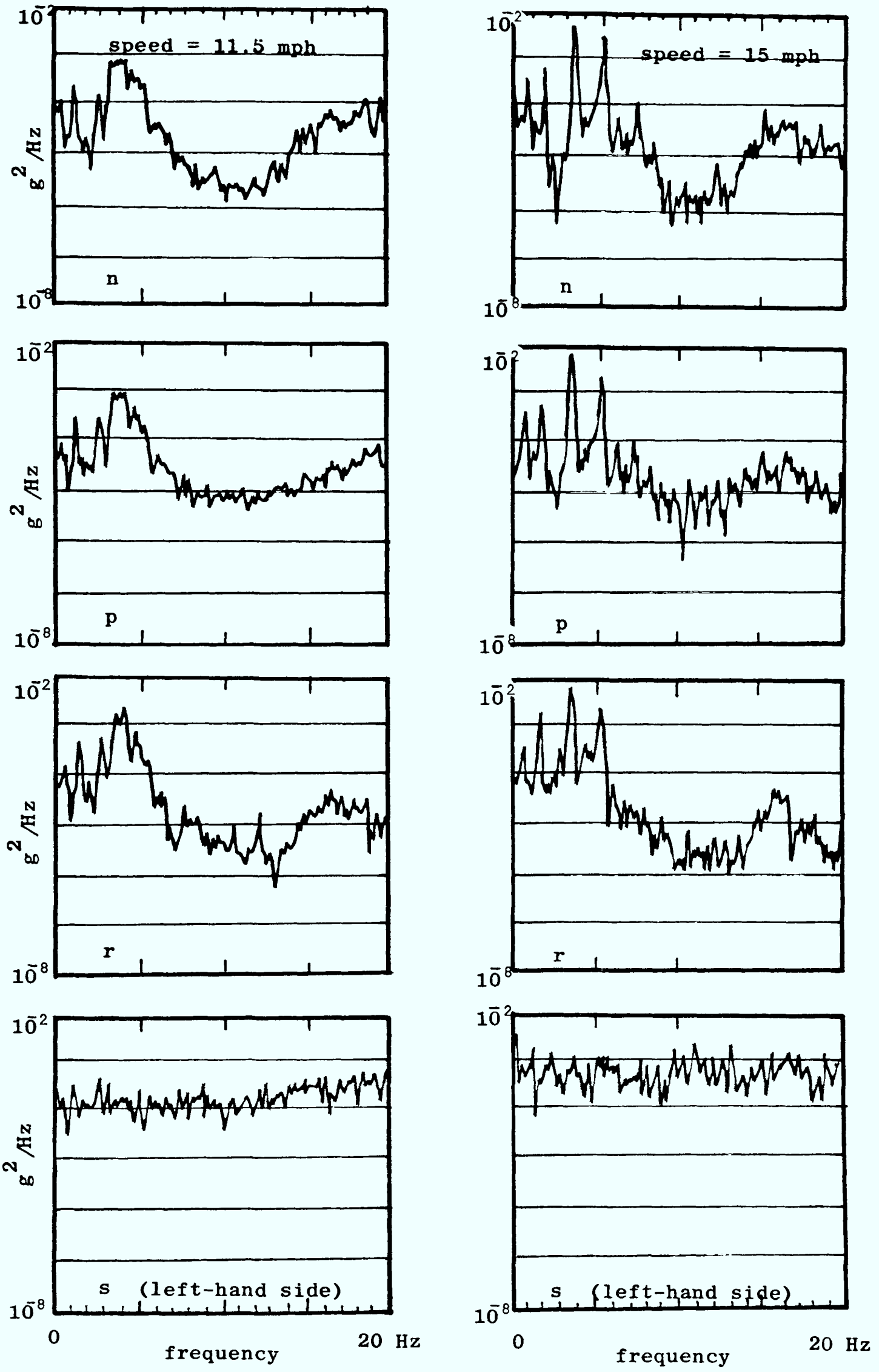

Fig A4.11 Acceleration spectral densities

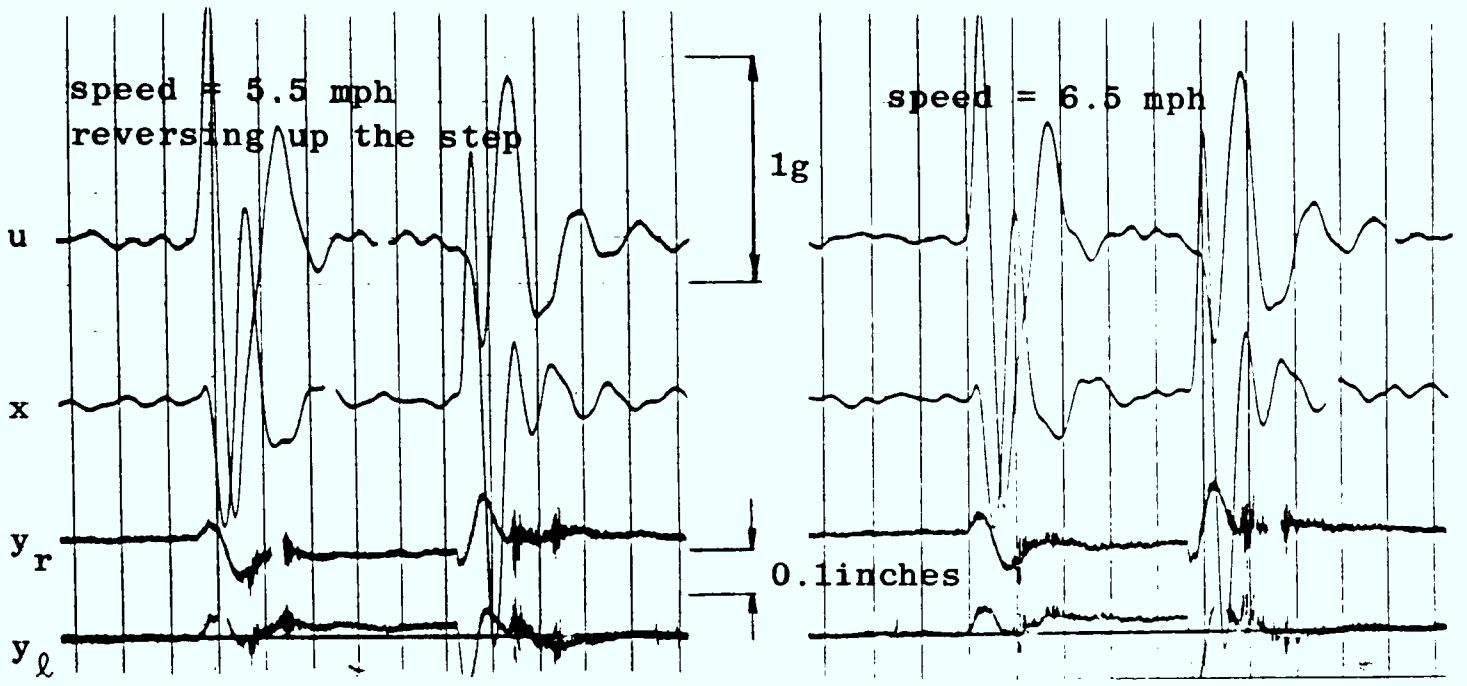

Fig A4.14 Response to a 12mm step in the left rail

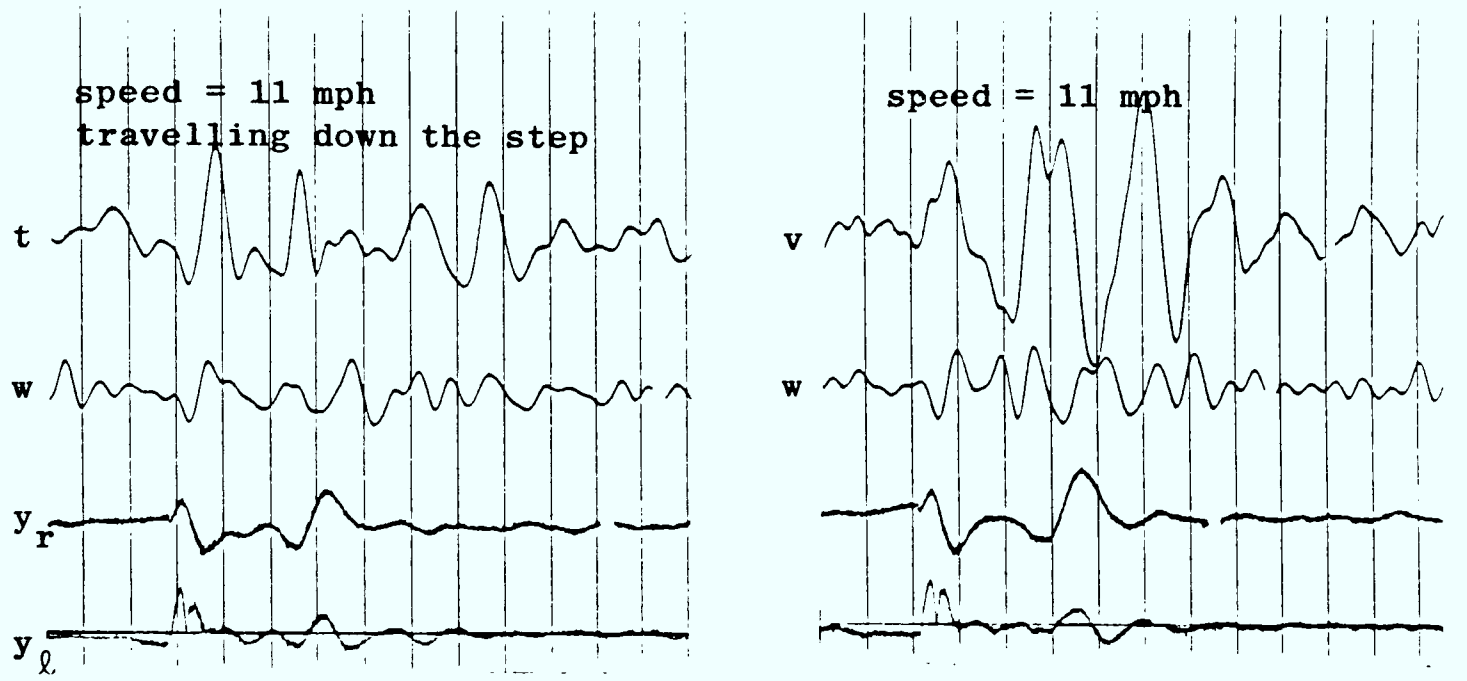

Fig A4.15 Response to a 12mm step in the left rail

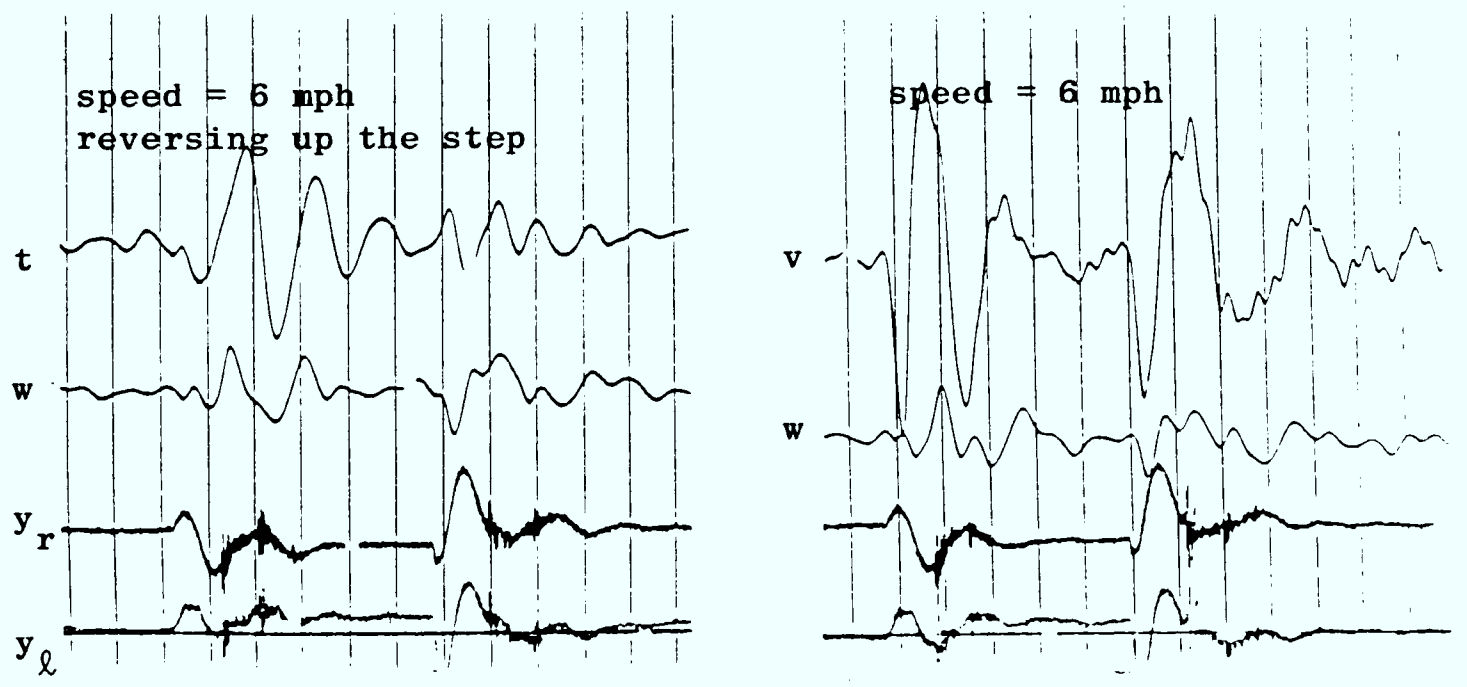

Fig A4.16 Response to a 12mm step in the left rail

A4.5 Track resilience

While the tests on the two axle vehicle were being carried out, the vehicle was parked with the rear wheels above the step in the track and the static deflection of the left-hand rail was measured. On this basis an approximate value for the vertical stiffness of the Swadlincote test track was obtained:

$$K_t \simeq 2 \times 10^6 \text{ N/m} \qquad \text{(A4.1)}$$